

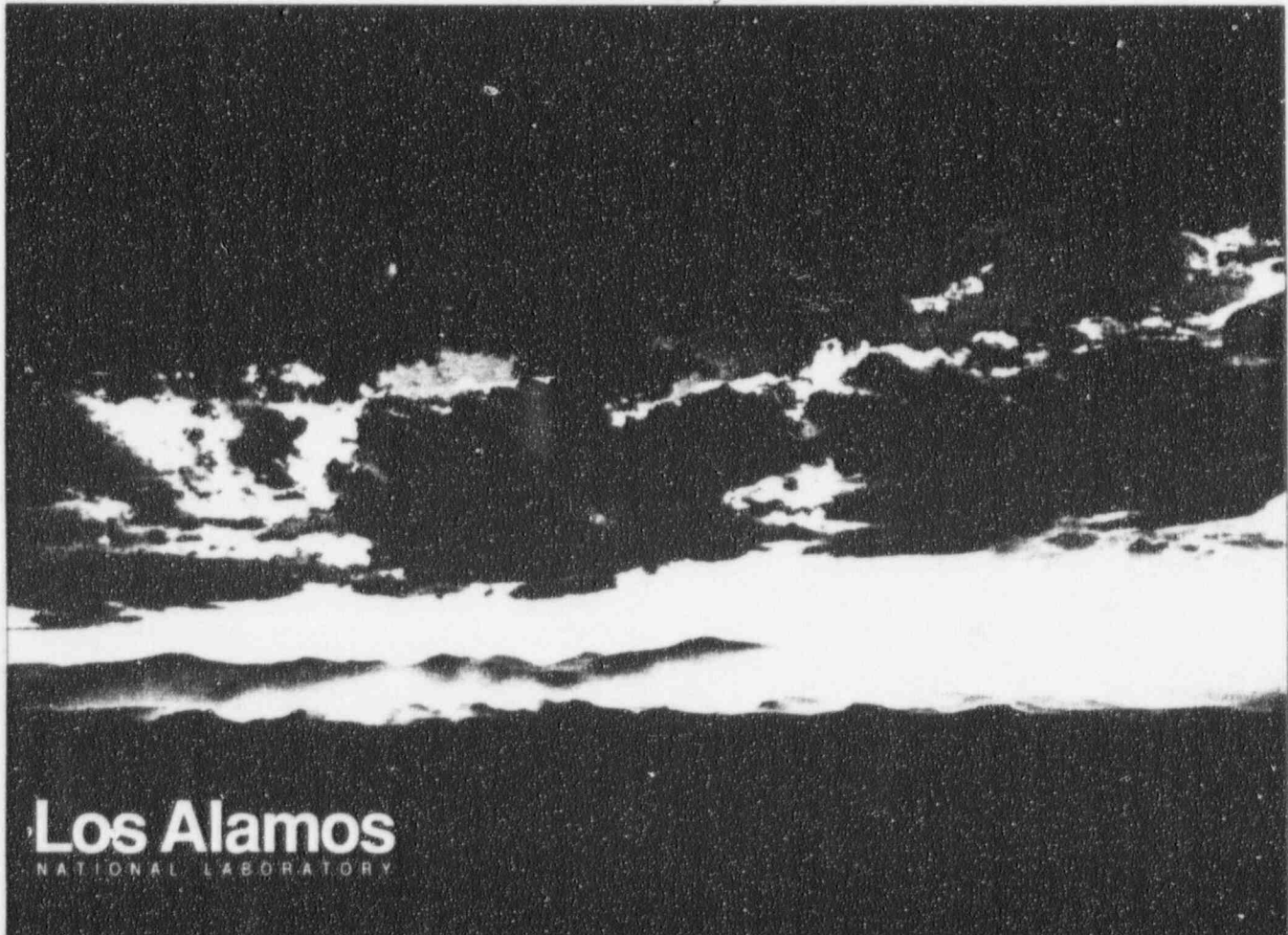
LA-UR-95-4431

UPDATED TRAC ANALYSIS OF 80% DOUBLE-ENDED COLD-LEG BREAK
FOR THE AP600

Jan 26, 1996

by

James F. Lime
Brent E. Boyack



Photograph by Chris J. Lindberg

Los Alamos National Laboratory, an affirmative action/equal opportunity employer, is operated by the University of California for the U.S. Department of Energy under contract W-7405-ENG-36. By acceptance of this article, the publisher recognizes that the U.S. Government retains a nonexclusive, royalty-free license to publish or reproduce the published form of this contribution, or to allow others to do so, for U.S. Government purposes. The Los Alamos National Laboratory requests that the publisher identify this article as work performed under the auspices of the U.S. Department of Energy. Los Alamos National Laboratory strongly supports academic freedom and a researcher's right to publish; therefore, the Laboratory as an institution does not endorse the viewpoint of a publication or guarantee its technical correctness.

Form No. 836 R5; ST 2629 10/95

9607010234 960626
PDR ADOCK 05200003
A PDR

Attachment 2

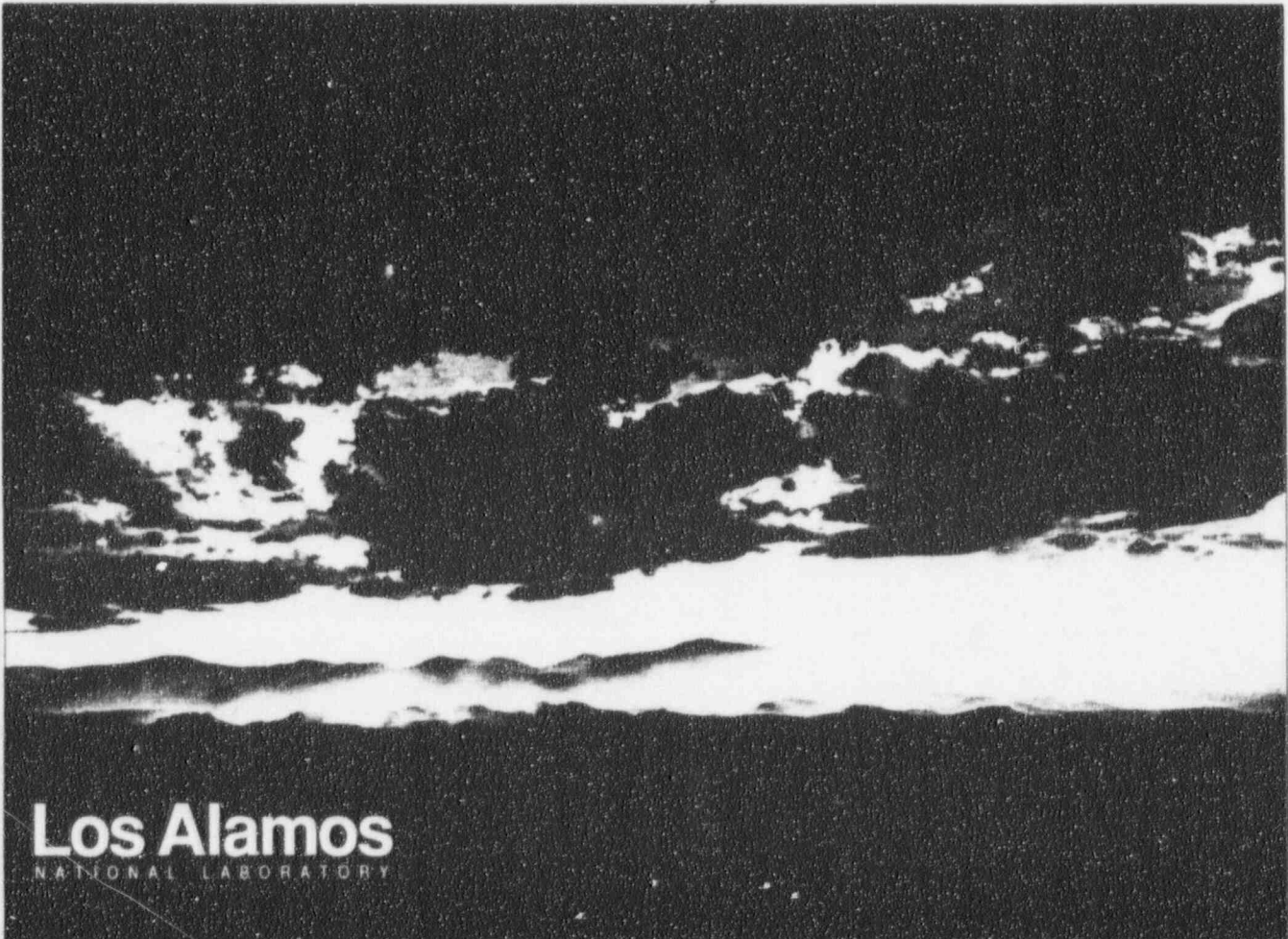
LA-UR-95-4431

UPDATED TRAC ANALYSIS OF 80% DOUBLE-ENDED COLD-LEG BREAK
FOR THE AP600

Jan 26, 1996

by

James F. Lime
Brent E. Boyack



Photograph by Chris J. Lindberg

Los Alamos
NATIONAL LABORATORY

Los Alamos National Laboratory, an affirmative action/equal opportunity employer, is operated by the University of California for the U.S. Department of Energy under contract W-7405-ENG-36. By acceptance of this article, the publisher recognizes that the U.S. Government retains a nonexclusive, royalty-free license to publish or reproduce the published form of this contribution, or to allow others to do so, for U.S. Government purposes. The Los Alamos National Laboratory requests that the publisher identify this article as work performed under the auspices of the U.S. Department of Energy. Los Alamos National Laboratory strongly supports academic freedom and a researcher's right to publish; therefore, the Laboratory as an institution does not endorse the viewpoint of a publication or guarantee its technical correctness.

Form No. 836 R5; ST 2629 10/95

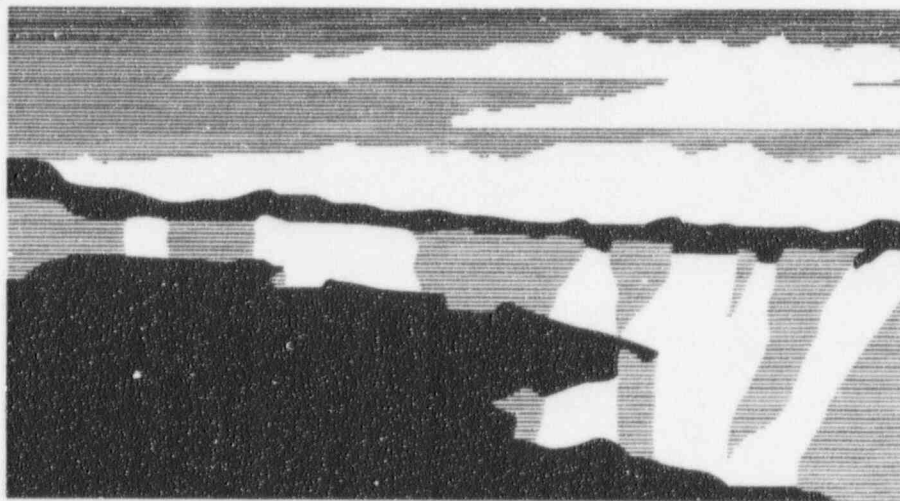
9607010234 960626
PDR ADOCK 05200003
A PDR

LA-UR-95-4431

Title: **UPDATED TRAC ANALYSIS OF 80% DOUBLE-ENDED COLD-LEG BREAK FOR THE AP600**

Author(s): **James F. Lime
Brent E. Boyack**

Submitted to: **For USNRC Distribution**



Los Alamos
NATIONAL LABORATORY

Los Alamos National Laboratory, an affirmative action/equal opportunity employer, is operated by the University of California for the U.S. Department of Energy under contract W-7405-ENG-36. By acceptance of this article, the publisher recognizes that the U.S. Government retains a nonexclusive, royalty-free license to publish or reproduce the published form of this contribution, or to allow others to do so, for U.S. Government purposes. The Los Alamos National Laboratory requests that the publisher identify this article as work performed under the auspices of the U.S. Department of Energy. Los Alamos National Laboratory strongly supports academic freedom and a researcher's right to publish; therefore, the Laboratory as an institution does not endorse the viewpoint of a publication or guarantee its technical correctness.

LA-UR-95-4431

Los Alamos National Laboratory is operated by the University of California for the United States Department of Energy under contract W-7405-ENG-36

TITLE: UPDATED TRAC ANALYSIS OF AN 80% DOUBLE-ENDED COLD-LEG BREAK FOR THE AP600 DESIGN

AUTHOR(S): J. F. Lime and B. E. Boyak

SUBMITTED TO:

By acceptance of this article, the publisher recognizes that the U.S. Government retains a nonexclusive, royalty-free license to publish or reproduce the published form of this contribution, or to allow others to do so, for U.S. Government purposes.

The Los Alamos National Laboratory requests that the publisher identify this article as work performed under the auspices of the U.S. Department of Energy.

Los Alamos

Los Alamos National Laboratory
Los Alamos, New Mexico 87545

FORM NO. 836 R4
ST NO 2529 5/81

**UPDATED TRAC ANALYSIS OF AN 80% DOUBLE-
ENDED COLD-LEG BREAK FOR THE AP600 DESIGN**

J. F. Lime and B. E. Boyack

**Technology and Safety Assessment Division
Los Alamos National Laboratory
Los Alamos, New Mexico 87545**

CONTENTS

NOMENCLATURE	xii
EXECUTIVE SUMMARY	1
ABSTRACT	4
1.0. INTRODUCTION	4
2.0. PLANT DESCRIPTION	5
2.1. AP600 Description.....	5
2.2. Key AP600 Features—LBLOCA Response	7
2.3. Comparison with Current Generation Westinghouse PWRs	7
3.0. TRAC MODEL DESCRIPTION	7
3.1. Plant Model Database	7
3.2. Reactor Vessel	8
3.3. Loop Components	9
3.4. Passive Safety Systems	10
3.5. Updated Model Changes	10
4.0. TRAC CODE DESCRIPTION	12
5.0. LBLOCA CALCULATION RESULTS	13
5.1. Blowdown Period (0 to 12.3 s)	14
5.2. Refill Period (12.3 to 43 s)	22
5.3. Reflood Period(43 to 240 s)	26
5.4. Long-Term Cooling Period (240 s and Beyond)	31
6.0. COMPARISON WITH <u>W</u> COBRA/TRAC	33
7.0. CONCLUSIONS AND RECOMMENDATIONS	35
REFERENCES	36
APPENDIX A. CORE-INLET MASS FLOWS	A-1
APPENDIX B. CORE-OUTLET MASS FLOWS	B-1
APPENDIX C. AVERAGE-ROD CLADDING TEMPERATURES	C-1
APPENDIX D. HOT-ROD CLADDING TEMPERATURES.....	D-1
APPENDIX E. AVERAGE-ROD CLADDING TEMPERATURES VS ROD ELEVATION AT SELECTED TRANSIENT TIMES	E-1
APPENDIX F. HOT-ROD CLADDING TEMPERATURES VS ROD ELEVATION AT SELECTED TRANSIENT TIMES	F-1
APPENDIX G. LBLOCA TIMESTEP AND CPU TIME INFORMATION	G-1

TABLES

I.	EXTENDED LBLOCA SEQUENCE OF EVENTS	37
II.	COMPARISON TO <u>W</u> COBRA/TRAC 80% DEGB LOCA	38

FIGURES

1.	AP600 plant isometric.....	39
2.	AP600 containment cutaway view	40
3.	Schematic of AP600 reactor coolant system and passive safety systems	41
4.	Isometric view of reactor vessel model	42
5.	Elevation view of reactor vessel model, including downcomer nodding.....	43
6.	Plan views of reactor vessel model.....	44
7.	Reactor vessel heat structures	44
8.	Reactor coolant loop-1 model overview	45
9.	Reactor coolant loop-2 model overview	45
10.	Passive Safety Systems model overview	46
11.	Vessel-collapsed liquid levels.....	47
12.	System pressures	47
13.	Fuel-rod maximum cladding temperatures	48
14.	Pressurizer mass flows	48
15.	Accumulator mass flows	49
16.	Accumulator liquid level	49
17.	Accumulator liquid volume fraction	50
18.	Core makeup tank mass flows	50
19.	Core makeup tank liquid levels	51
20.	PRHRS mass flows	51
21.	Core makeup tank-pressure balance-line mass flows	52
22.	Break mass flows	52
23.	Break exit voiding	53
24.	Steam-generator primary-outlet mass flows	53
25.	Cold-leg mass flows	54
26.	Intact cold-leg voiding.....	54
27.	Hot-leg 1 mass flows.....	55

FIGURES (CONT)

28.	Hot-leg 2 mass flows	55
29.	Hot-leg 1 voiding	56
30.	Hot-leg 2 voiding	56
31.	Total makeup flow	57
32.	Net-system mass-flow loss	57
33.	Integrated net-system mass-flow loss	58
34.	Heated core-average vapor fraction	58
35.	Core-inlet mass flows	59
36.	Core-outlet mass flows	59
37.	Core-outlet liquid-mass flows	60
38.	Core-outlet vapor-mass flows	60
39.	Fuel-rod reactivities	61
40.	Stored-energy distribution in fuel rod with time	61
41.	Average-rod temperatures in cell 1 ($r = 1, \theta = 1$)	62
42.	Average-rod temperatures in cell 4 ($r = 1, \theta = 4$)	62
43.	Hot-rod temperatures in cell 1 ($r = 1, \theta = 1$)	63
44.	Hot-rod temperatures in cell 4 ($r = 1, \theta = 4$)	63
45.	Average-rod temperatures in cell 9 ($r = 2, \theta = 1$)	64
46.	Average-rod temperatures in cell 12 ($r = 2, \theta = 4$)	64
47.	Cell 4 average-rod temperatures vs rod elevation, 0 to 10 s	65
48.	Cell 4 average-rod temperatures vs rod elevation, 20 to 140 s	65
49.	Cell 4 hot-rod temperatures vs rod elevation, to 10 s	66
50.	Cell 4 hot-rod temperatures vs rod elevation, 20 to 140 s	66
51.	Downcomer average vapor fraction	67
52.	Total guide tube flow	67
53.	Lower-plenum average vapor fraction	68
54.	Lower-plenum coolant temperatures	68
55.	Upper-head average vapor fraction	69
56.	Upper-plenum average vapor fraction	69
57.	Steam and feedwater mass flows	70
58.	Total upper-head support-plate drain-hole mass flow	70
59.	Downcomer-to-upper-head mass flow	71
60.	Reactor-coolant pump-rotor speeds	71

FIGURES (CONT)

61.	Comparison of <u>W</u> COBRA/TRAC and TRAC upper-plenum pressure	72
62.	Comparison of <u>W</u> COBRA/TRAC and TRAC accumulator mass flow	72
63.	Comparison of <u>W</u> COBRA/TRAC and TRAC lower-plenum liquid level	73
64.	Comparison of <u>W</u> COBRA/TRAC and TRAC downcomer liquid level	73
65.	Comparison of <u>W</u> COBRA/TRAC and TRAC hot-rod peak cladding temperatures	74
66.	Comparison of <u>W</u> COBRA/TRAC and TRAC hot-rod cladding temperatures at 6-ft rod elevation.....	74
67.	Comparison of <u>W</u> COBRA/TRAC and TRAC hot-rod cladding temperatures at 8.5-ft rod elevation.....	75
68.	Comparison of <u>W</u> COBRA/TRAC and TRAC hot-rod cladding temperatures at 10-ft rod elevation.....	75
69.	Comparison of <u>W</u> COBRA/TRAC and TRAC average-rod cladding temperatures at 6-ft rod elevation	76
70.	Comparison of <u>W</u> COBRA/TRAC and TRAC average-rod cladding temperatures at 8.5-ft rod elevation	76
71.	Comparison of <u>W</u> COBRA/TRAC and TRAC average-rod cladding temperatures at 10-ft rod elevation	77
72.	Comparison of <u>W</u> COBRA/TRAC peripheral-rod cladding temperatures to TRAC outer-ring average-rod cladding temperatures at 6-ft rod elevation	77
73.	Comparison of <u>W</u> COBRA/TRAC peripheral-rod cladding temperatures to TRAC outer-ring average-cladding temperatures at 8.5-ft rod elevation	78
74.	Comparison of <u>W</u> COBRA/TRAC peripheral-rod cladding temperatures to TRAC outer-ring average-rod cladding temperatures at 10-ft rod elevation	78
A-1.	Core-inlet mass flow, core sector cell 1 ($r = 1, \theta = 1$)	A-1
A-2.	Core-inlet mass flow, core sector cell 2 ($r = 1, \theta = 2$)	A-2
A-3.	Core-inlet mass flow, core sector cell 3 ($r = 1, \theta = 3$)	A-2
A-4.	Core-inlet mass flow, core sector cell 4 ($r = 1, \theta = 4$)	A-3
A-5.	Core-inlet mass flow, core sector cell 5 ($r = 1, \theta = 5$)	A-3
A-6.	Core-inlet mass flow, core sector cell 6 ($r = 1, \theta = 6$)	A-4
A-7.	Core-inlet mass flow, core sector cell 7 ($r = 1, \theta = 7$)	A-4
A-8.	Core-inlet mass flow, core sector cell 8 ($r = 1, \theta = 8$)	A-5
A-9.	Core-inlet mass flow, core sector cell 9 ($r = 2, \theta = 1$)	A-5
A-10.	Core-inlet mass flow, core sector cell 10 ($r = 2, \theta = 2$)	A-6
A-11.	Core-inlet mass flow, core sector cell 11 ($r = 2, \theta = 3$)	A-6
A-12.	Core-inlet mass flow, core sector cell 12 ($r = 2, \theta = 4$)	A-7
A-13.	Core-inlet mass flow, core sector cell 13 ($r = 2, \theta = 5$)	A-7

FIGURES (CONT)

A-14.	Core-inlet mass flow, core sector cell 14 ($r = 2, \theta = 6$).....	A-8
A-15.	Core-inlet mass flow, core sector cell 15 ($r = 2, \theta = 7$).....	A-8
A-16.	Core-inlet mass flow, core sector cell 16 ($r = 2, \theta = 8$).....	A-9
B-1.	Core-outlet mass flow, core sector cell 1 ($r = 1, \theta = 1$).....	B-1
B-2.	Core-outlet mass flow, core sector cell 2 ($r = 1, \theta = 2$).....	B-1
B-3.	Core-outlet mass flow, core sector cell 3 ($r = 1, \theta = 3$).....	B-2
B-4.	Core-outlet mass flow, core sector cell 4 ($r = 1, \theta = 4$).....	B-2
B-5.	Core-outlet mass flow, core sector cell 5 ($r = 1, \theta = 5$).....	B-3
B-6.	Core-outlet mass flow, core sector cell 6 ($r = 1, \theta = 6$).....	B-3
B-7.	Core-outlet mass flow, core sector cell 7 ($r = 1, \theta = 7$).....	B-4
B-8.	Core-outlet mass flow, core sector cell 8 ($r = 1, \theta = 8$).....	B-4
B-9.	Core-outlet mass flow, core sector cell 9 ($r = 2, \theta = 1$).....	B-5
B-10.	Core-outlet mass flow, core sector cell 10 ($r = 2, \theta = 2$).....	B-5
B-11.	Core-outlet mass flow, core sector cell 11 ($r = 2, \theta = 3$).....	B-6
B-12.	Core-outlet mass flow, core sector cell 12 ($r = 2, \theta = 4$).....	B-6
B-13.	Core-outlet mass flow, core sector cell 13 ($r = 2, \theta = 5$).....	B-7
B-14.	Core-outlet mass flow, core sector cell 14 ($r = 2, \theta = 6$).....	B-7
B-15.	Core-outlet mass flow, core sector cell 15 ($r = 2, \theta = 7$).....	B-8
B-16.	Core-outlet mass flow, core sector cell 16 ($r = 2, \theta = 8$).....	B-8
C-1.	Average-rod cladding temperatures, core sector cell 1 ($r = 1, \theta = 1$).....	C-1
C-2.	Average-rod cladding temperatures, core sector cell 2 ($r = 1, \theta = 2$).....	C-1
C-3.	Average-rod cladding temperatures, core sector cell 3 ($r = 1, \theta = 3$).....	C-2
C-4.	Average-rod cladding temperatures, core sector cell 4 ($r = 1, \theta = 4$).....	C-2
C-5.	Average-rod cladding temperatures, core sector cell 5 ($r = 1, \theta = 5$).....	C-3
C-6.	Average-rod cladding temperatures, core sector cell 6 ($r = 1, \theta = 6$).....	C-3
C-7.	Average-rod cladding temperatures, core sector cell 7 ($r = 1, \theta = 7$).....	C-4
C-8.	Average-rod cladding temperatures, core sector cell 8 ($r = 1, \theta = 8$).....	C-4
C-9.	Average-rod cladding temperatures, core sector cell 9 ($r = 2, \theta = 1$).....	C-5
C-10.	Average-rod cladding temperatures, core sector cell 10 ($r = 2, \theta = 2$).....	C-5
C-11.	Average-rod cladding temperatures, core sector cell 11 ($r = 2, \theta = 3$).....	C-6
C-12.	Average-rod cladding temperatures, core sector cell 12 ($r = 2, \theta = 4$).....	C-6
C-13.	Average-rod cladding temperatures, core sector cell 13 ($r = 2, \theta = 5$).....	C-7
C-14.	Average-rod cladding temperatures, core sector cell 14 ($r = 2, \theta = 6$).....	C-7

FIGURES (CONT)

C-15.	Average-rod cladding temperatures, core sector cell 15 ($r = 2, \theta = 7$)	C-8
C-16.	Average-rod cladding temperatures, core sector cell 16 ($r = 2, \theta = 8$)	C-8
D-1.	Hot-rod cladding temperatures, core sector cell 1 ($r = 1, \theta = 1$)	D-1
D-2.	Hot-rod cladding temperatures, core sector cell 2 ($r = 1, \theta = 2$)	D-1
D-3.	Hot-rod cladding temperatures, core sector cell 3 ($r = 1, \theta = 3$)	D-2
D-4.	Hot-rod cladding temperatures, core sector cell 4 ($r = 1, \theta = 4$)	D-2
D-5.	Hot-rod cladding temperatures, core sector cell 5 ($r = 1, \theta = 5$)	D-3
D-6.	Hot-rod cladding temperatures, core sector cell 6 ($r = 1, \theta = 6$)	D-3
D-7.	Hot-rod cladding temperatures, core sector cell 7 ($r = 1, \theta = 7$)	D-4
D-8.	Hot-rod cladding temperatures, core sector cell 8 ($r = 1, \theta = 8$)	D-4
D-9.	Hot-rod cladding temperatures, core sector cell 9 ($r = 2, \theta = 1$)	D-5
D-10.	Hot-rod cladding temperatures, core sector cell 10 ($r = 2, \theta = 2$)	D-5
D-11.	Hot-rod cladding temperatures, core sector cell 11 ($r = 2, \theta = 3$)	D-6
D-12.	Hot-rod cladding temperatures, core sector cell 12 ($r = 2, \theta = 4$)	D-6
D-13.	Hot-rod cladding temperatures, core sector cell 13 ($r = 2, \theta = 5$)	D-7
D-14.	Hot-rod cladding temperatures, core sector cell 14 ($r = 2, \theta = 6$)	D-7
D-15.	Hot-rod cladding temperatures, core sector cell 15 ($r = 2, \theta = 7$)	D-8
D-16.	Hot-rod cladding temperatures, core sector cell 16 ($r = 2, \theta = 8$)	D-8
E-1a.	Average-rod cladding temperatures vs core elevation at selected transient times from 0 to 10 s for core cell 1	E-1
E-1b.	Average-rod cladding temperatures vs core elevation at selected transient times from 20 to 140 s for core cell 1	E-2
E-2a.	Average-rod cladding temperatures vs core elevation at selected transient times from 0 to 10 s for core cell 2	E-2
E-2b.	Average-rod cladding temperatures vs core elevation at selected transient times from 20 to 140 s for core cell 2	E-3
E-3a.	Average-rod cladding temperatures vs core elevation at selected transient times from 0 to 10 s for core cell 3	E-3
E-3b.	Average-rod cladding temperatures vs core elevation at selected transient times from 20 to 140 s for core cell 3	E-4
E-4a.	Average-rod cladding temperatures vs core elevation at selected transient times from 0 to 10 s for core cell 4	E-4
E-4b.	Average-rod cladding temperatures vs core elevation at selected transient times from 20 to 140 s for core cell 4	E-5

FIGURES (CONT)

E-5a.	Average-rod cladding temperatures vs core elevation at selected transient times from 0 to 10 s for core cell 5.....	E-5
E-5b.	Average-rod cladding temperatures vs core elevation at selected transient times from 20 to 140 s for core cell 5.....	E-6
E-6a.	Average-rod cladding temperatures vs core elevation at selected transient times from 0 to 10 s for core cell 6.....	E-6
E-6b.	Average-rod cladding temperatures vs core elevation at selected transient times from 20 to 140 s for core cell 6.....	E-7
E-7a.	Average-rod cladding temperatures vs core elevation at selected transient times from 0 to 10 s for core cell 7.....	E-7
E-7b.	Average-rod cladding temperatures vs core elevation at selected transient times from 20 to 140 s for core cell 7.....	E-8
E-8a.	Average-rod cladding temperatures vs core elevation at selected transient times from 0 to 10 s for core cell 8.....	E-8
E-8b.	Average-rod cladding temperatures vs core elevation at selected transient times from 20 to 140 s for core cell 8.....	E-9
E-9a.	Average-rod cladding temperatures vs core elevation at selected transient times from 0 to 10 s for core cell 9.....	E-9
E-9b.	Average-rod cladding temperatures vs core elevation at selected transient times from 20 to 140 s for core cell 9.....	E-10
E-10a.	Average-rod cladding temperatures vs core elevation at selected transient times from 0 to 10 s for core cell 10.....	E-10
E-10b.	Average-rod cladding temperatures vs core elevation at selected transient times from 20 to 140 s for core cell 10.....	E-11
E-11a.	Average-rod cladding temperatures v. core elevation at selected transient times from 0 to 10 s for core cell 11.....	E-11
E-11b.	Average-rod cladding temperatures vs core elevation at selected transient times from 20 to 140 s for core cell 11.....	E-12
E-12a.	Average-rod cladding temperatures vs core elevation at selected transient times from 0 to 10 s for core cell 12.....	E-12
E-12b.	Average-rod cladding temperatures vs core elevation at selected transient times from 20 to 140 s for core cell 12.....	E-13
E-13a.	Average-rod cladding temperatures vs core elevation at selected transient times from 0 to 10 s for core cell 13.....	E-13
E-13b.	Average-rod cladding temperatures vs core elevation at selected transient times from 20 to 140 s for core cell 13.....	E-14

FIGURES (CONT)

E-14a.	Average-rod cladding temperatures vs core elevation at selected transient times from 0 to 10 s for core cell 14.....	E-14
E-14b.	Average-rod cladding temperatures vs core elevation at selected transient times from 20 to 140 s for core cell 14.....	E-15
E-15a.	Average-rod cladding temperatures vs core elevation at selected transient times from 0 to 10 s for core cell 15.....	E-15
E-15b.	Average-rod cladding temperatures vs core elevation at selected transient times from 20 to 140 s for core cell 15.....	E-16
E-16a.	Average-rod cladding temperatures vs core elevation at selected transient times from 0 to 10 s for core cell 16.....	E-16
E-16b.	Average-rod cladding temperatures vs core elevation at selected transient times from 20 to 140 s for core cell 16.....	E-17
F-1a.	Hot-rod cladding temperatures vs core elevation at selected transient times from 0 to 10 s for core cell 1.....	F-1
F-1b.	Hot-rod cladding temperatures vs core elevation at selected transient times from 20 to 140 s for core cell 1.....	F-2
F-2a.	Hot-rod cladding temperatures vs core elevation at selected transient times from 0 to 10 s for core cell 2.....	F-2
F-2b.	Hot-rod cladding temperatures vs core elevation at selected transient times from 20 to 140 s for core cell 2.....	F-3
F-3a.	Hot-rod cladding temperatures vs core elevation at selected transient times from 0 to 10 s for core cell 3.....	F-3
F-3b.	Hot-rod cladding temperatures vs core elevation at selected transient times from 20 to 140 s for core cell 3.....	F-4
F-4a.	Hot-rod cladding temperatures vs core elevation at selected transient times from 0 to 10 s for core cell 4.....	F-4
F-4b.	Hot-rod cladding temperatures vs core elevation at selected transient times from 20 to 140 s for core cell 4.....	F-5
F-5a.	Hot-rod cladding temperatures vs core elevation at selected transient times from 0 to 10 s for core cell 5.....	F-6
F-5b.	Hot-rod cladding temperatures vs core elevation at selected transient times from 20 to 140 s for core cell 5.....	F-6
F-6a.	Hot-rod cladding temperatures vs core elevation at selected transient times from 0 to 10 s for core cell 6.....	F-7
F-6b.	Hot-rod cladding temperatures vs core elevation at selected transient times from 20 to 140 s for core cell 6.....	F-7
F-7a.	Hot-rod cladding temperatures vs core elevation at selected transient times from 0 to 10 s for core cell 7.....	F-8

FIGURES (CONT)

F-7b.	Hot-rod cladding temperatures vs core elevation at selected transient times from 20 to 140 s for core cell 7.....	F-8
F-8a.	Hot-rod cladding temperatures vs core elevation at selected transient times from 0 to 10 s for core cell 8.....	F-9
F-8b.	Hot-rod cladding temperatures vs core elevation at selected transient times from 20 to 140 s for core cell 8.....	F-9
F-9a.	Hot-rod cladding temperatures vs core elevation at selected transient times from 0 to 10 s for core cell 9.....	F-10
F-9b.	Hot-rod cladding temperatures vs. core elevation at selected transient times from 20 to 140 s for core cell 9.....	F-10
F-10a.	Hot-rod cladding temperatures vs core elevation at selected transient times from 0 to 10 s for core cell 10.....	F-11
F-10b.	Hot-rod cladding temperatures vs core elevation at selected transient times from 20 to 140 s for core cell 10.....	F-11
F-11a.	Hot-rod cladding temperatures vs core elevation at selected transient times from 0 to 10 s for core cell 11.....	F-12
F-11b.	Hot-rod cladding temperatures vs core elevation at selected transient times from 20 to 140 s for core cell 11.....	F-12
F-12.	Hot-rod cladding temperatures vs core elevation at selected transient times from 0 to 10 s for core cell 12.....	F-13
F-12b.	Hot-rod cladding temperatures vs core elevation at selected transient times from 20 to 140 s for core cell 12.....	F-13
F-13a.	Hot-rod cladding temperatures vs core elevation at selected transient times from 0 to 10 s for core cell 13.....	F-14
F-13b.	Hot-rod cladding temperatures vs core elevation at selected transient times from 20 to 140 s for core cell 13.....	F-14
F-14a.	Hot-rod cladding temperatures vs core elevation at selected transient times from 0 to 10 s for core cell 14.....	F-15
F-14b.	Hot-rod cladding temperatures vs core elevation at selected transient times from 20 to 140 s for core cell 14.....	F-15
F-15a.	Hot-rod cladding temperatures vs core elevation at selected transient times from 0 to 10 s for core cell 15.....	F-16
F-15b.	Hot-rod cladding temperatures vs core elevation at selected transient times from 20 to 140 s for core cell 15.....	F-16
F-16a.	Hot-rod cladding temperatures vs core elevation at selected transient times from 0 to 10 s for core cell 16.....	F-17
F-16b.	Hot-rod cladding temperatures vs core elevation at selected transient times from 20 to 140 s for core cell 16.....	F-17

FIGURES (CONT)

G-1.	Timestep size.....	G-3
G-2.	Total CPU time per calculation run.....	G-1

NOMENCLATURE

1D	One dimensional
3D	Three dimensional
ACC	Accumulator
ACC-A	Accumulator connected to broken direct vessel injection line A
ACC-B	Accumulator connected to intact direct vessel injection line B
ADS	Automatic depressurization system
CMT	Core makeup tank
CMT-A	Core makeup tank connected to direct vessel injection line A
CMT-B	Core makeup tank connected to direct vessel injection line B
DEGB	Double-ended guillotine break
DVI	Direct vessel injection
DVI-A	Direct vessel injection line A
DVI-B	Direct vessel injection line B
ECC	Emergency core coolant
ECCS	Emergency core coolant system
IBLOCA	Intermediate-break loss-of-coolant accident
IRWST	In-containment refueling water storage tank
JAERI	Japan Atomic Energy Research Institute
LBLOCA	Large-break loss-of-coolant accident
LSTF	Large Scale Test Facility
NRC	United States Nuclear Regulatory Commission
PBL-A	Pressure balance line connected to cold-leg A
PBL-B	Pressure balance line connected to cold-leg B
PCCS	Passive containment cooling system
PRHRS	Passive residual heat removal system
PSIS	Passive safety injection system
PWR	Pressurized water reactor
RCP	Reactor coolant pump
RCS	Reactor coolant system
ROSA	Rig of Safety Assessment, AP600 integral test facility, Japan
S	Safeguards
SBLOCA	Small-break loss-of-coolant accident

UPDATED TRAC ANALYSIS OF AN 80% DOUBLE-ENDED COLD-LEG BREAK FOR THE AP600 DESIGN*

J. F. Lime and B. E. Boyack

Technology and Safety Assessment Division
Los Alamos National Laboratory
Los Alamos, New Mexico 87545

EXECUTIVE SUMMARY

The AP600 is an advanced passive 600-MWe reactor design being developed by Westinghouse in conjunction with the US Department of Energy's Advanced Light Water Reactor Technology Program. The AP600 has been submitted for Nuclear Regulatory Commission (NRC) design certification. In accordance with 10CFR52.47 for design certification, advanced reactor applicants are required to submit neutronic and thermal-hydraulic safety analyses over a sufficient range of normal operation, transient conditions, and specified accident sequences. Review and confirmation of these analyses for the AP600 design constitute an important activity in the NRC's review for design certification. In support of its design certification review, the NRC is using best-estimate thermal-hydraulic codes to perform audit calculations. The NRC is using TRAC-PF1/MOD2 as its primary tool for confirmatory safety analyses of large-break loss-of-coolant accidents (LBLOCA). This report documents the results and analyses of a multidimensional TRAC-PF1/MOD2 calculation of an updated AP600 LBLOCA, an 80% double-ended guillotine cold-leg break next to the reactor-coolant pump. This analysis was performed with an AP600 plant model updated for model corrections and plant design changes, and supersedes an earlier TRAC AP600 LBLOCA analysis.¹

The TRAC model used for the LBLOCA calculation is finely noded. The reactor vessel is modeled with two multidimensional vessel components in order to preserve the AP600 vessel geometry. The first vessel component models the lower plenum, core, core bypass, reflector, upper plenum, and upper head. The second models the downcomer. One-dimensional (1D) components are used to model the remainder of the reactor coolant system. The passive safety systems are also modeled. The accumulators and core makeup tanks (CMT) are modeled with 1D components. Because this analysis focused on the first few minutes of a LBLOCA, models of the automatic depressurization system (ADS), passive residual heat removal system (PRHRS), and in-reactor refueling water storage tank (IRWST) were not included because they are not activated during the interval of the calculation. The containment is modeled as a constant back pressure of one atmosphere.

* This work was funded by the US Nuclear Regulatory Commission's Office of Nuclear Regulatory Research.

The TRAC AP600 plant model was updated for plant design changes and for model corrections identified from a peer review of the TRAC plant model at INEL on May 26-27, 1994. The plant design changes included deletion of the pressurizer pressure balance lines to the core makeup tanks, adding a venturi to the direct vessel injection (DVI) nozzle, and piping geometry changes in the CMT and accumulator injection lines. The modeling corrections included the modeling of counter-current flow limitation (CCFL) in the upper core plate, reactor power deposition to the reactor coolant flow, core azimuthal and radial power distribution, and other changes. In addition, the break location was changed from next to the vessel downcomer to between the reactor coolant pump and the CMT pressure balance line connection, to match the WCOBRA/TRAC break location.

The TRAC-PF1/MOD2 code version used was interim version 5.4.04. There were major code error fixes in this code version. Major code corrections include a blowdown heat transfer error fix, tee-component momentum source fix, and mass loss error fix, and a downcomer interfacial drag.

The transient thermal-hydraulic behavior of an LBLOCA can be characterized in major phases:

1. Blowdown Period, 0 to 12.3 s. During this phase, there is a rapid system depressurization and a high rate of flow out the break. By 6 s the core is over 90% voided. The rapid loss of coolant causes fuel cladding temperatures to increase rapidly; they reach a blowdown maximum at 7 s and then decrease slightly from an increase in cooling. The maximum-power fuel-rod peak clad temperature during this period reached 1021 K (1378°F). Increased cooling is the result of a decrease in net mass-flow loss out of the reactor vessel when two-phase flow occurs at the break exits.
2. Refill Period, 12.3 to 43 s. The system pressure decreases below 700 psia and the accumulators begin to discharge. The vessel net mass-flow loss decreases and by 20 s more flow begins to enter the vessel than is leaving. Fuel cladding temperatures, however, increase gradually as the core, upper plenum, and upper head regions continue to void and core cooling becomes less effective. In the latter phase of this period, the primary has stopped depressurizing and the break flow is essentially all vapor. The lower plenum starts to refill from accumulator flow injection. Fuel temperatures continue to increase.
3. Reflood, 43 s to 240 s The lower plenum has refilled and core reflood and quenching begins. The maximum-power fuel rod peak clad temperatures reach a maximum of 1197 K (1695°F) at 58 s and then decreased gradually thereafter. The average-power fuel rods are quenched by 165 s, and the maximum-power fuel rods are quenched by 240 s. The accumulators are completely empty of liquid at the same time that the maximum-power fuel rods are quenched.

4. Long-term cooling, 240 s and beyond. There is a short period, 240 to 265 s, during which there is no emergency core-coolant flow. The accumulators have completely emptied; however, the core makeup tanks and the IRWST have not yet started to inject because the pressure in the DVI line is still too high to allow the check valves to open. The pressure finally is low enough to allow all the core makeup tanks that they can drain at 265 s. The IRWST drain line check valves finally open at ~275 s. The core, still in a state of saturated nucleate boiling at the beginning of this period, eventually will revert to single-phase natural-convective cooling. There is sufficient water in the IRWST to cover the hot and cold legs completely and form a natural-circulation path between the containment and the reactor core.

The TRAC calculation results are compared with the Westinghouse WCOBRA/TRAC results presented in the AP600 Standard Safety Analysis Report (SSAR).¹⁰ The comparison shows reasonable agreement between the two calculations. The system depressurization was about the same in both calculations. The TRAC accumulator flows were higher than the WCOBRA/TRAC flows, so refill and reflood event times are earlier than WCOBRA/TRAC event times. We believe that the accumulators in the WCOBRA/TRAC analysis were calibrated to a lower flow than the accumulators in the TRAC analysis.

A significant similarity between the two calculations is in the calculation of the hot-rod peak cladding temperature (PCT). Both the TRAC and WCOBRA/TRAC calculations show the reflood PCT to be higher than the blowdown PCT. The TRAC and WCOBRA/TRAC calculated reflood PCTs compare within 50 K, although the TRAC-calculated peak occurred much earlier in the transient. The reason for the earlier PCT is being investigated. The TRAC-calculated hot-rod PCT is lower than the App. K limit of 2200°F, but near the cladding oxidation temperature of 1700°F. Should the calculated PCT exceed 1700°F, the TRAC-calculated PCT would no longer be accurate because TRAC does not account for oxidation effects.

A major difference between the two calculations is in the cooling of average-powered rods during the late blowdown period. The WCOBRA/TRAC calculation showed top-down rewetting and quenching of average-powered rods during the late-blowdown phase, with cladding temperatures being cooled down to saturation-temperature levels.

The TRAC calculation showed considerable radial and azimuthal variation in fuel cladding temperatures. Fuel rods near the break experienced less top-down quenching and higher cladding temperatures than the fuel rods opposite and away from the break. In addition, the fuel rods in radial ring 1 experienced less top-down quenching than the fuel rods in the outer radial ring 2, a consequence of CCFL. In general, the degree of top-down quenching and rewetting in the TRAC calculation was not as high as in the WCOBRA/TRAC calculation. This may be because the TRAC reflood model does not account for quenching resulting from a falling liquid film.

UPDATED TRAC ANALYSIS OF AN 80% DOUBLE-ENDED COLD-LEG BREAK FOR THE AP600 DESIGN*

J. F. Lime and B. E. Boyack

ABSTRACT

An updated TRAC 80% large-break loss-of-coolant accident (LBLOCA) has been calculated for the Westinghouse AP600 advanced reactor design. The updated calculation incorporates major code error corrections, model corrections, and plant design changes. The 80% break size was calculated by Westinghouse to be the most severe large-break size for the AP600 design. The LBLOCA transient was calculated to 280 s, which was the time of IWRST injection. All fuel rods were quenched completely by 240 s. Peak cladding temperatures (PCTs) were well below the App. K limit of 1478 K (2200°F) but very near the cladding oxidation temperature of 1200 K (1700°F). Transient event times and PCT for the TRAC calculation were in reasonable agreement with those calculated by Westinghouse using their WCOBRA/TRAC code. However, there were significant differences in the detailed phenomena calculated by the two codes, particularly during the blowdown phase. The reasons for these differences are still being investigated. Additional break sizes and break locations need to be analyzed to confirm the most severe break postulated by Westinghouse.

1.0. INTRODUCTION

The AP600 is an advanced passive 600-MWe reactor design being developed by Westinghouse in conjunction with the US Department of Energy Advanced Light Water Reactor Technology Program. The AP600 has been submitted for Nuclear Regulatory Commission (NRC) design certification. In accordance with 10CFR52.47 for design certification, advanced reactor applicants are required to submit neutronic and thermal-hydraulic safety analyses over a sufficient range of normal operation, transient conditions, and specified accident sequences. Review and confirmation of these analyses for the AP600 design constitute an important activity in the NRC's review for design certification. In the process of design certification, the NRC will use best-estimate, thermal-hydraulic codes to perform audit calculations. The best-estimate code selected by the NRC for analyzing large-break loss-of-coolant accident (LBLOCA) transients is TRAC-PF1/MOD2,² developed by Los Alamos National Laboratory. Los Alamos was requested by the NRC to perform LBLOCA analyses with TRAC in support of the design certification review of the AP600.

* This work was funded by the US Nuclear Regulatory Commission's Office of Nuclear Regulatory Research.

2.0. PLANT DESCRIPTION

A brief description of the AP600 system is provided with a review of those systems and components having the greatest impact on the course of the LBLOCA during the blowdown, refill, and reflood periods of the transient. Similarities and differences between the AP600 and the Westinghouse four-loop PWR safety systems and their impact on the LBLOCA are discussed.

2.1. AP600 Description

The AP600 is an advanced passive 600-MWe reactor design being developed by Westinghouse in conjunction with the US Department of Energy Advanced Light Water Reactor Technology Program. The AP600 is a two-loop design. Each loop contains one hot leg (HL), one steam generator (SG), two reactor coolant pumps (RCP), and two cold legs (CL). A pressurizer is attached to one of the hot legs. The reactor coolant pumps are a canned-motor design and are attached directly to the steam generator. The loop seal is eliminated an added safety feature in that core uncover caused by the existence of water-filled loop seals is eliminated during a postulated small-break (SB) LOCA. The core is designed for a low-power-density and consists of 145 fuel assemblies with an active fuel length of 12 ft. The fuel assembly is a 17 x 17 array of fuel and control rods.

The AP600 incorporates passive safety systems that rely only on redundant/fail-safe valving, gravity, natural circulation, and compressed gas. There are no pumps, diesels, or other active machinery in these safety systems. During plant shutdown, all the passive safety features will be tested to demonstrate system readiness, flow, and heat removal performance. These systems are shown in an isometric cutaway view of the AP600 reactor design in Fig. 1, containment cutaway in Fig. 2, and in a schematic diagram in Fig. 3. Two Passive Safety Injection System (PSIS) trains, each with an accumulator (ACC), a Core Makeup Tank (CMT), and an injection line from the In-containment Refueling Water Storage Tank (IRWST) and sump are connected directly to the reactor-vessel downcomer via a direct vessel injection (DVI) line.

Depressurization of the primary system is an essential process that is required to ensure long-term cooling of the AP600. For example, the accumulators inject coolant into the reactor coolant system (RCS) only after the primary pressure has dropped to 700 psia. Coolant injection from large, safety-class water pools, specifically the IRWST and sump, can occur only after the reactor coolant system pressure decreases below the gravitational head of each pool. An Automatic Depressurization System (ADS) permits a controlled pressure reduction of the RCS. The ADS has four stages. Each of the first three stages consists of two trains providing redundant flow paths between the top of the pressurizer and the IRWST. The coolant discharged to the IRWST is condensed and accumulated for later injection into the RCS. The actuation signal for first stage ADS is a reduction in the coolant inventory of one CMT to 67% of its initial value. ADS stage 2 is actuated 70 s after stage 1 actuation. ADS stage 3 is actuated 120 s after stage 2 actuation. The actuation signal for fourth-stage ADS is a reduction in the inventory of one CMT to 20% of its initial value and an interval of 120 s following third-stage ADS actuation. The fourth stage ADS consists of two trains, one train connecting the top of

the pressurizer hot leg (loop 1) and the containment, and the other train connecting the loop-2 hot leg and the containment. A direct discharge path to the containment is needed to ensure that the PCS pressure will equilibrate with the containment pressure so that the head-driven IRWST injection can proceed. The fractions of the total ADS discharge area for ADS stages 1-4 are 0.038, 0.171, 0.171, and 0.62, respectively. After the accumulators and CMTs are depleted and the primary system has depressurized and approached the containment pressure, water injection is provided from the IRWST. This tank empties after several days. Provisions are also made for recirculating coolant from a sump. IRWST and sump recirculation may occur at the same time for some transients.

The AP600 containment plays an essential role in the long-term cooling of the primary via the Passive Containment Cooling System (PCCS). Steam entering the containment, either through a break in the primary or through operation of the ADS, condenses on the inside of the steel containment shell. The condensate drains downward and a large fraction is delivered via gutters to either the IRWST or the sump. Heat transfer on the outside of the containment steel shell is by evaporation of liquid sprayed near the top of the steel reactor containment dome by the PCCS, and by convection to an air stream induced by buoyancy-driven flow (unforced). This air stream enters a high-elevation inlet, flows downward to an elevation near the bottom of the cylindrical portion of the steel reactor containment structure, passes upward through the annular gap between the steel reactor containment structure and the concrete shield building, and is exhausted to the atmosphere near the top of the concrete shield building. The PCCS spray inventory is eventually depleted. However, by the time the PCCS water supply is depleted, the decay heat has decreased sufficiently so that the buoyancy induced air flow through the air gap between the steel containment structure and the concrete shield building can remove the core decay heat.

For non-LOCA accidents, long-term heat removal is provided by a Passive Residual Heat Removal System (PRHRS) that removes core heat through natural circulation. The PRHRS receives water from the top of the hot leg to which the pressurizer is connected. The single PRHRS line connected to the hot leg divides into two lines, each feeding one of the two PRHRS heat exchangers residing in the IRWST. The two PRHRS discharge lines then rejoin and connect to the outlet plenum of the steam generator outlet in the same loop. When functioning as the heat sink for the PRHRS heat exchangers, the IRWST has sufficient water volume to remove decay heat for two hours before the inventory reaches saturation temperature. Isolation valves on the PRHRS lines open upon receipt of the safeguards (S) signal, and a buoyancy induced flow transports primary coolant through the PRHRS. The PRHRS may also contribute to the removal of energy from the primary system during LOCA events. However, operation of the PRHRS is interrupted when the PRHRS inlet void fraction becomes very high, degrading the energy transport to the PRHRS heat exchangers. Thus, the PRHRS is ineffective for LBLOCAs, has a limited interval of effectiveness for intermediate-break LOCAs, and has an extended period of effectiveness for SBLOCAs. The coolant in the PRHRS lines and heat exchangers will, however, contribute to the total makeup flow during a LOCA.

Westinghouse has changed several features of the AP600 design since it was submitted for design certification. Although only the final design is of interest when assessing safety, it is important to assure that the design information used in performing various safety assessments reflects either the current or final design. In performing the assessments presented in this document, we reflect the design features known to us as of November 15, 1994.

2.2. Key AP600 Features - LBLOCA Response

The selected scenario is an 80% break in a single cold leg between the RCP and the nozzle to which the cold-leg pressure balance line (PBL) is connected. For this PWR LBLOCA scenario, a large amount of primary coolant is discharged through the two-sided break, the core completely fills with vapor, the fuel rod cladding temperatures rapidly increase, emergency core coolant (ECC) is injected, and the core is quenched. This sequence of events occurs within the first five min following the break initiation. From break initiation through the time the entire core is quenched, the accumulators and core makeup tanks are the key and dominant components ensuring core cooling. After the accumulators have emptied and depressurized completely, the core makeup tanks start to inject along with IRWST injection. Although the ADS will be initiated on CMT level, they serve no purpose in depressurizing the system.

2.3. Comparison with Current Generation Westinghouse PWRs

Several design differences do enter into the early phases of the LBLOCA scenarios for the two plants. For example, in the AP600, ECC is injected directly into the downcomer through the two DVI lines of the PSIS. Thus a cold-leg break does not directly result in the loss of ECC from either accumulator. In the earlier Westinghouse designs, each of the four accumulator injection lines are connected to a different cold leg. Thus, the entire inventory of one accumulator is lost through the break and is unavailable for core cooling. In the AP600, a turning vane directs the flow from each DVI line downward into the downcomer, thereby affecting the amount of ECC bypass. The average linear power in the AP600 core is ~70% of that in the four-loop Westinghouse PWR. One manifestation of the lower power density core is that the internal diameter of the AP600 is fully 90% of that in the four-loop Westinghouse PWR and the internal vessel cross-sectional area is ~82%. The two accumulators contain about the same volume of boric water as three accumulators in the Westinghouse four-loop plant.

3.0. TRAC MODEL DESCRIPTION

The TRAC model of the AP600 is a finely noded, multidimensional model with 161 hydrodynamic components (752 3-D and 868 1-D computational fluid cells) and 45 heat-structure components in the model. The LBLOCA plant model has undergone an independent quality-assurance check.

3.1. Plant Model Database

The TRAC AP600 LBLOCA plant model reflected as accurately as possible the AP600 design based on the design information we had at the time the analysis was performed. Where design information was lacking, modeling assumptions had to be made or the

Component	TRAC Model Database
Reactor Vessel	
Vessel internal geometry	Westinghouse AP600 drawings.
Fuel-bundle geometry	Westinghouse AP600 drawings.
Fuel-rod reactivity coefficients	Assumption. Used USPWR plant model ⁴
Vessel flow and internal resistances	Westinghouse.
Reactor Coolant System	
Hot- and cold-leg piping	Westinghouse AP600 drawings.
Reactor coolant pumps	Westinghouse rated values and COBRA/TRAC homologous pump curves.
Steam generator	Internal geometry and thermal-hydraulic data-Westinghouse computer output.
Pressurizer and pressurizer surge line	Westinghouse AP600 drawings.
Passive Safety Injection System	
CMT and accumulator tank geometry	Westinghouse dimensions and volumes.
Injection line piping	Westinghouse reduced-size AP600 drawings. Dimensions approximated for non-legible values.
CMT pressure balance lines	Westinghouse AP600 drawings.
Check valves	0.4 psi to open, based on Westinghouse in-situ check valve tests, -0.4 psi to close, assumed
Flow resistances	Westinghouse, design-basis flows and resistances
Control systems	
Trips, set points, and delay times	Information provided by Westinghouse for some trips but not all.
Pressurizer pressure and level control	These and other plant control systems adapted from a TRAC model of a Westinghouse three-loop plant.
Steam generator level control	

modeling from a RELAP5 AP600 plant model³ had to be used. A summary of the database sources for the TRAC plant model is given below:

3.2. Reactor Vessel

The reactor vessel is modeled in three-dimensional (3D) cylindrical coordinates, with 4 radial rings, 8 azimuthal sectors, and 17 axial levels. An isometric view of the reactor vessel model is shown in Fig. 4. Elevation and plan views of the reactor vessel model

are also shown in Figs. 5 and 6, respectively. Two TRAC vessel components are needed to model the reactor vessel in order to preserve the elevations of the hot-leg, cold-leg, and PSIS connections to the vessel. Otherwise, there would have to be a compromise on modeling the vessel true geometry. The elevation differences of these piping connections to the reactor vessel are clearly seen in the elevation view of Fig. 5.

The first vessel component, component 10, models the lower plenum, core, upper plenum, and upper head. The core region is modeled with the first two radial rings. The third radial ring models the reflector region. The fourth radial ring is used in the lower plenum and in the upper head but in the axial levels modeling the core and upper plenum it is not used. The second vessel component, component 20, models the downcomer annulus and is noded into two radial rings, eight azimuthal sectors, and 13 axial levels. Radial ring 1 is a noncomputational ring and is used only to model the annular geometry of the downcomer. Where possible, the same axial-level noding heights are used in both vessel components. The two vessel components are connected together by short one-dimensional (1D) pipe components. Other 1D pipe components are used to model the fuel-assembly guide tubes, upper-head cooling spray flow, core bypass flow, and reflector-block cavity fluid regions.

A total of 33 TRAC heat structure components are used to model the core and reactor vessel structure, as shown in Fig. 7. There is heat conduction in the core barrel between the downcomer annulus and the core region. Outer heat-structure surfaces are treated adiabatically. The fuel rods are modeled with one powered heat structure. The fuel rods are combined and modeled as 16 lumped assemblies each with the same number of fuel rods, one for each of the active core sectors shown in Fig. 6. Supplemental hot-rod components are also modeled that represent the maximum-power fuel rods. The core decay power is calculated using reactivity feedback coefficients. Control-rod and reactivity feedback coefficients are from a 15 x 15-fuel large-break US/Japanese PWR model⁴ because we did not have sufficient reactivity information for the AP600 design at the time the TRAC model was developed. The reflector-block heat structure models 0.25% of the total core power during steady state. Power deposition of 2.35% to the core coolant flow was modeled with a very thin artificial heat structure that was coupled to each of the core hydro cells. When the reactor is scrammed, the reflector-block and coolant-deposited power are reduced to zero.

3.3. Loop Components

Figures 8 and 9 show a modeling overview of reactor coolant loops. Loop 1 is modeled with 33 hydro components and 181 1D computational cells. The pressurizer is connected to the hot leg of loop 1. The PRHRS is also connected to loop 1, with the PRHRS inlet line being connected to the hot leg of loop 1 and the PRHRS return line being connected to the steam generator outlet plenum (see Fig. 1). Loop 2 has 32 components and 162 1D cells, and is similar in noding to loop 1 except that there is no pressurizer, and instead of pressurizer spray sources, core makeup tank pressure balance lines connect to the cold legs. Loop 2 also models the broken cold leg, which is modeled with a series of TEE and VALVE components that allow for a more mechanistic modeling of a large break.

The reactor-coolant pump homologous performance curves are from the Westinghouse Cobra/TRAC input. The steam generator model reflects the AP600 $\Delta 75$ design, which is similar to the current Westinghouse Model F design, but has a taller tube bundle and redesigned secondary-side risers and separators. Where specific component design data were not available for the AP600, components from a Westinghouse three-loop plant were used. All external piping wall structures are modeled with an outer adiabatic boundary assumed.

3.4. Passive Safety Systems

Figure 10 shows a modeling overview of the AP600 passive safety systems, the PSIS, ADS, PRHRS, and IRWST. There are two separate trains in each of the systems and each of the trains are modeled separately. The TRAC LBLOCA plant model includes the components of the PSIS, the accumulators, core makeup tanks, pressure balance lines, and injection lines, as these are the only safety components activated in the first few minutes of a LBLOCA transient. Also included in the LBLOCA plant model are the PRHRS primary-side components, to account for its liquid inventory. In the latest AP600 plant design, the PRHRS isolation valve will open on an "S" signal, which will allow the PRHRS fluid to drain into the primary coolant system. The other passive safety systems, the ADS and IRWST, will be modeled for longer-term transients such as for intermediate- and small-break LOCAs, where the transient is calculated out to when the IRWST drains into the reactor coolant system (RCS).

Both PSIS trains are orificed to delivered the same amount of flow even though the piping geometry of the two trains are different. Separate stand-alone cases of both PSIS trains were used to calibrate the accumulator and CMT flows to Westinghouse specified values.

3.5. Updated Plant Model Changes

The plant model was updated for a number of design changes and model corrections. An AP600 Working Group Meeting was held at the Idaho National Engineering Laboratory to review the TRAC plant model and TRAC LOCA calculations with the NRC and Idaho National Engineering Laboratory staff.⁵ The plant model peer review identified a number of modeling changes that were incorporated into the plant model. These design and modeling changes are noted as follows:

1. DVI Injection Nozzle Venturi. A venturi was modeled in the DVI injection nozzle based on an AP600 design change.
2. Pressure Balance Line from Pressurizer. The pressure balance line from the pressurizer to the core makeup tank was removed based on an AP600 design change
3. Feedwater and Steam Lines. The feedwater and steam lines were modeled from AP600 drawings received at the INEL peer review meeting.

4. DVI Line Geometry Changes. Westinghouse changed the DVI line A to avoid piping stress problems. The previous piping arrangement had core makeup tank flow and accumulator flow coming together from opposite ends of the main pipe of a tee and then flowing through the side section of the tee to another tee before flowing into the main DVI line. This was changed so that the accumulator flow discharged through the main pipe and the CMT flow was from the side pipe.
5. Orificing in the PSIS Lines. The CMT, ACC, and IRWST lines are each orificed to deliver a specified flow at a given net driving head. The orifice locations are shown in the noding diagrams. We assumed the orifice to be a sharp-edge orifice, modeling the actual orifice area and applying a theoretical irreversible pressure loss coefficient for a sharp-edge orifice. Stand-alone flow calibration cases were used to adjust the orifice area and corresponding loss coefficient. The orifice area ratio used for each flow are noted in the modeling diagrams
6. Power deposition to reactor coolant. The Westinghouse database specified that 97.4% of the total reactor power is deposited in the fuel rods. The remaining power was assumed to be deposited into the reflector block and core coolant. The non-fuel power deposition was corrected so that 0.25% power was deposited in the reflector block and the remaining 2.35% was deposited into the moderator (coolant). The moderator deposited power was modeled with a very thin slab powered heat structure that coupled to each core sector fluid cell. The very thin slab allows a very rapid power deposition and transient response to the core coolant.
7. Core azimuthal power distribution. Westinghouse provided a fuel-bundle power distribution for a 1/8 core sector. This sector is offset 22.5° from the hydro sector. In modeling the average power distribution and accounting for the offset, alternate sectors will have slightly more power. The core sectors corresponding to the cold leg sectors will have slightly less power than the core sectors to the hot legs and DVI injection line.
8. Counter-Current Limiting Flow (CCFL). The TRAC CCFL modeling option was added to the AP600 plant model at several places, in the reactor vessel upper core plate, in the hot leg inclination, in the pressurizer surge line at the 90° elbow bend, and in the pressurizer heater upper support plate.
9. Check Valve Pressure Differential. All plant check valves were modeled to open on a 0.40 psi pressure differential across the valve, based on in-situ check valve testing by Westinghouse. We assumed that the valves would close on a -0.40 psi pressure differential.
10. Cold Leg Break Location. The break location was changed from next to the downcomer to between the reactor coolant pump and the pressure balance

line connection to conform with the break location assumed by Westinghouse in their WCOBRA/TRAC LBLOCA analyses.

11. Reflector Block Cavity Fluid. Four pipe components were added to the plant model to account for the reflector block cavity fluid. These pipe components were connected to the core by assuming the very thin gaps between reflector blocks formed a flow path. A flow resistance based on parallel flat plates gaps was assumed for the leakage paths between the cavity region and the core.

4.0. TRAC CODE DESCRIPTION

Analysis was performed with an interim version TRAC-PF1/MOD2, version 5.4.04. TRAC-PF1/MOD2, Ref. 2, is the latest TRAC version to be developed by Los Alamos National Laboratory. TRAC was developed to provide advanced, best-estimate predictions for postulated accidents in pressurized-water reactors. The fluid-dynamics solution is formulated in the six equation, two-fluid, nonequilibrium model with a staggered difference scheme. Multidimensional flow capability is available in the vessel component, either in cylindrical or Cartesian coordinates. One-dimensional flow capability is available in the other hydrodynamic modeling components.

TRAC-PF1/MOD2 features a 3D stability-enhancing two-step method, which removes the Courant time-step limit within the vessel solution. There are also internal code-structure vectorization changes to improve computational times. MOD2 also includes improvements to the interfacial drag and heat transfer constitutive relationships for stratified flow and air-water mixtures, a more efficient matrix solution method, and conservation of momentum flux. Other major features of TRAC include: (1) a two-phase, two-fluid, nonequilibrium hydrodynamics model with a noncondensable gas field; (2) flow-regime-dependent constitutive equations; (3) either a 1D or 3D reactor-vessel model; (4) complete control-systems modeling capability; and (5) a generalized heat-structure component.

A major modeling option in MOD2, exercised in the LBLOCA analysis, is an improved mechanistic reflood model based on the inverted annular flow regime mapping of Dejarlais and Ishii.⁶ This reflood model and its assessment against experimental data are reported in Ref. 2 and also in Refs. 7-9. Additional reflood model development efforts have been identified, such as the modeling of top-down quenching from a falling liquid film and applicability of the reflood model to high-power applications.

Another modeling option exercised in the LBLOCA is the counter-current flow limit option. The Bankoff CCFL correlation was applied at the core upper plate and at the pressurizer heater upper support plate. CCFL based on a Wallis diameter-dependence scaling was applied at the hot-leg inclinations and at the vertical elbow in the pressurizer surge line.

There were major code errors and problems corrected in version 5.4.04. These included correcting for asymmetric flow problems in TEE components, a post-CHF heat transfer error that significantly affected the blowdown heat transfer, and total mass-loss error,

5.0. LBLOCA CALCULATION RESULTS

The limiting LBLOCA has been identified as an 80% DEGB in a single cold-leg pipe between the primary coolant pump and the connecting point for the CMT PBL to the cold leg.¹⁰ Westinghouse has concluded that this hypothesized break will produce the maximum fuel rod cladding temperature. Table I gives the sequence of events that occur for the TRAC calculation of this limiting LBLOCA.

To facilitate analysis, the LBLOCA calculation is subdivided into four time periods that characterize events during the sequence. The format and period definitions of the LBLOCA in AP600 closely follow those of Ref. 11. These time periods, termed blowdown, refill, reflood, and long-term cooling are defined by the start of accumulator injection and by the core and lower plenum liquid mass fraction behaviors (Fig. 11). The first two periods and most of the third period have been calculated. Therefore, only the first three periods will be discussed in detail in this report.

The *blowdown period* is the result of a break in the coolant system through which the primary coolant is expelled. Blowdown physical processes/phenomena include critical flow at the break, fluid flashing and depressurization, redistribution of fuel-rod stored energy, and heating of the fuel rods due to degraded heat transfer. During blowdown, some components are affected more than others. In particular, the heat removal from the core results from the changing flow and heat transfer regimes in the core. The performance of the primary coolant pumps degrade as the coolant flashes. The steam generator heat transfer degrades after the steam-generator secondaries are isolated. The blowdown period ends when the intact-loop accumulator injection is initiated.¹¹

During the *refill period*, the reactor system starts to recover as the PSIS components (CMTs and accumulators) start to inject coolant into the primary system. The important refill components and processes/phenomena concern the introduction of water into the reactor vessel downcomer and its subsequent distribution. Refill physical processes/phenomena are the operation of the PSIS, including interactions between the accumulators and CMTs, bypassing injected water through the downcomer to the broken cold leg, and penetration of safety injection water into the lower plenum. The refill period ends when the mixture level in the lower plenum approaches the core inlet, and conditions are established for reflooding the core with coolant.

When sufficient water from the PSIS has entered the lower plenum and the core liquid inventory enters a period of sustained recovery, the *reflood period* is in progress and the hot fuel rods are being recovered with water. The reflood process is highly oscillatory but the overall trend with increasing time is increasing core coolant inventory, i.e., a sustained recovery. The reflood processes may be quite slow because much of the water is boiled and transported as steam and entrained droplets into the upper plenum

and hot-leg piping. The reflood period ends when the entire core is quenched, that is, all fuel rod cladding temperatures are at or below the coolant saturation temperature.

The *long-term cooling period* continues after total core quench. At the time the fuel rod cladding is completely quenched, the core is only partially full. The accumulators also have just emptied of liquid. However, the noncondensable gas in the accumulator continues to discharge into the DVI lines, which keeps the DVI line pressure up and delays CMT draining for ~30 s. Finally, the CMTs resume draining their inventory into the primary. A few seconds later, IRWST injection is initiated when the primary pressure decreases to a level less than the static head in the IRWST. CMT and IRWST draining may occur simultaneously because both are gravity-head driven. Draining of the IRWST is expected to take several days, after which water from the sump is recirculated indefinitely. For many accident scenarios, the depressurization process must be assisted by operation of the ADS. The ADS is actuated when the liquid volume of one CMT is reduced to 67% and the ADS valve-opening sequence is initiated. However, the LBLOCA produces sufficient area to depressurize the primary, even in the absence of ADS actuation.

For the TRAC calculation, the containment back pressure was specified to be a constant one atmosphere. The scenario description is supported by Figs. 11 through 60 that display significant calculational results. In some cases, the figure legends identify components with alphabetic or numeric descriptors, for example, DVI line A or CMT B. Figure 3, a schematic of the AP600 and its passive safety systems, shows the relationships between the plant components and the TRAC input model labels. With reference to Fig. 3, loop 1 contains hot leg 1 (HL 1) and cold legs 1A and 1B (CL 1A and 1B). The pressurizer is connected to HL 1. The PRHRS is connected between HL 1 and the outlet plenum of steam generator 1 (SG 1). One train of the fourth stage ADS attaches to the PRHRS inlet line which is in turn connected to HL 1. Loop 2 contains HL 2 and CL 2A and 2B. The second train of the fourth-stage ADS connects directly to HL 2. The PSIS has two trains which feed coolant directly to the downcomer through DVI lines A and B. Connected to DVI line A are CMT A, ACC A, and a IRWST drain line. Connected to DVI line B are CMT B, ACC B and a second IRWST drain line. DVI A is connected to CL 2A by PBL A. DVI B is connected to CL 2B by PBL B. The postulated 80% DEGB occurs in CL 2B between the PBL B connection to CL 2B and RCP 2B.

5.1. Blowdown Period (0 to 12.3 s)

Overview

The AP600 LBLOCA blowdown starts at the time the break opens, and ends when intact loop accumulator injection is initiated, a period of ~12.3 s. The initial break mass flows are high, reflecting subcooled critical flows at the break planes. The mass flow from the vessel side of the break is much larger than that from the pump side because of the high hydraulic resistances of the pump and the steam generator piping. Because coolant flows from the vessel to the break through both the hot and cold legs, core flow rapidly stagnates; the flow at the core inlet reverses shortly after the break occurs. Early in the

transient, flow from the intact loops is generally bypassed around the reactor vessel downcomer to the broken cold leg and out the break.

As the primary coolant system rapidly depressurizes (Fig. 12), flashing occurs first in the highest temperature parts of the system, starting in the pressurizer and rapidly progressing through the upper plenum, hot legs, and then proceeding through the core and the steam generator and finally the lower plenum, downcomer, and cold legs. The pressurizer starts flashing earliest, but because of the resistance to flow out of the surge line, it takes almost 10 s to empty. The highest pressure in the primary is in the pressurizer until 7 s (Fig. 12). The flow from the pressurizer also contributes to the flow of upper plenum liquid into the top of the core. The steam volume addition rate from flashing reduces the primary coolant depressurization rate in the higher temperature portions of the primary system. Flashing and nucleate boiling begin in the core. Because of the core radial power profile, voiding in the core is nonuniform. The core approaches a vapor-filled condition within 2 s and the accompanying reactor kinetic effects produce a core power reduction. The reactor is tripped at ~1 s on either low primary pressure (pressurizer) or containment high pressure. The fuel rod cladding temperatures increase rapidly because of the degrading rod-to-fluid heat transfer (Fig. 13)^a.

The pressure in the broken cold leg decreases rapidly and to a lower level than in the hotter parts of the primary system where the rate of pressure decrease is reduced by flashing (Fig. 12). The break flow regime changes from subcooled to saturated critical flow, voiding occurs in the break and increases the resistance to flow, and the break mass flow rate decreases rapidly.

Processes/phenomena in the primary coolant system are tightly coupled during the early part of the blowdown period. The decreasing pump-side break flow rapidly affects core cooling processes/phenomena. RCP 2A and RCP 2B share a common plenum in SG 2. Immediately following accident initiation, the flow through RCP 2B to the break is so high that flow delivered to RCP 2A is small. However, as the CL 2B break flow decreases, the flow delivered to RCP 2B recovers to a near-normal level. The increased flow through RCP 2A is delivered through CL 2A to the downcomer inlet annulus where it joins with the flows from CL 1A and CL 1B. With the additional flow from CL 2A, the coolant supplied through the intact cold legs (1A, 1B, and 2A) exceeds the bypass flow to the vessel side of the break through CL 2B for a brief interval. The excess coolant enters the still liquid-full downcomer and displaces liquid into the lower plenum, partially refilling the lower plenum, introducing some liquid into the core region, and restoring upward flow through the core for a brief interval. Concurrently, core power decreases via void reactivity insertion and insertion of the shutdown rods. The release of stored heat from the core diminishes. The cladding temperature peaks (first peak) and begins to decrease.

^aCladding temperatures for each computational rod are searched and the maximum cladding temperature is located each time plotting data is stored. During the transient, different computational rods will have the maximum temperature. Figure 5 is a composite representation of the maximum cladding temperature.

As the primary system pressure continues to decrease, flashing begins in all four cold legs and voiding appears in the pump-suction inlets. Pump performance degrades, and the intact cold-leg mass flows rapidly diminish and approach zero. The interval of lower plenum refilling that began with recovery of the flow in CL 2A is terminated and the lower plenum resumes emptying. Flow enters the top of the core through the guide tubes and holes in the upper core plate (countercurrent flow). Sources of the liquid in the upper plenum include coolant existing from the time of accident initiation, liquid entering the upper plenum from the pressurizer and HL 1, and liquid entering the upper plenum from the upper head. The core liquid volume fraction remains about the same for the remainder of the blowdown period, and the core temperature decrease continues. Top-down cooling is provided by the liquid flow passing from the upper plenum to the top of the core. The fuel assemblies receive different amounts of water depending upon their location. Some of the design factors producing the nonsymmetrical top-down flows are location relative to the control rod guide tubes, location relative to the pressurizer hot leg (HL 1), and the core radial power profile. Thus, some portions of the core experience a top-down quench and others are cooled only a little from the top-down flow of coolant. The TRAC modeling of the guide tubes and core is such that the guide tube flow is distributed to all fuel rods.

Early in the blowdown period, the valves isolating the CMTs from the DVI lines are opened. A small flow is induced by the liquid head in the CMT and flows into the downcomer. However, all the flow from the CMT bypasses the core as it is entrained in the flow rising upward through the downcomer and carried into the broken cold leg and out the break.

System Response

Automatic Depressurization System:

The ADS is not activated. Operation is based upon CMT level. The time at which the CMT level decreases to the trip level occurs well beyond the blowdown period.

Passive Containment Cooling System:

Vapor and two-phase fluid pass through the break and exhaust into the containment. A constant containment back pressure of one atmosphere was specified for the TRAC calculation. In reality, the containment atmosphere pressure and temperature increase and a reactor trip signal is generated when a containment overpressure of 5 psi is reached. The increasing containment back pressure will have no effect on the primary because the break remains choked throughout this interval.

Passive Heat Removal System:

The S signal is generated on one of its initiators (e.g., high containment pressure, radiation leakage, or low pressurizer pressure). The S signal initiates CMT actuation (opens the isolation valve). CMT actuation initiates PRHRS actuation

(opens the isolation valve). Flashing and flow reversal occur in the PRHRS inlet piping immediately following break initiation, and two-phase flow passes into HL 1 and renders the PRHRS ineffective. Draining of the PRHRS inlet piping supplies an indeterminate amount of the liquid to HL 1 and thence the top of the core where it can participate in the top down quench of the core that occurs during this phase. The draining of the PRHRS heat exchanger (PRHRHX) volume and outlet piping inventory into the SG 1 exit plenum provides added liquid inventory to the RCS. The mass flows back into the RCS from the PRHRS at the hot leg and SG 1 exit plenum are shown in Fig. 20.

Passive Safety Injection System:

The primary system pressure remains above the 4.83 MPa (700 psi) accumulator set point (Fig. 12) so there is no accumulator injection during this period (Fig. 15). CMT recirculation begins during this period once the S signal induces CMT actuation (opens the isolation valve). The opening of the CMT isolation valve is followed by a small recirculation flow as shown in Fig. 18. However, the CMT remains filled with liquid (Fig. 19) because the CMT is replenished by liquid delivered through the PBLs (Fig. 21). The IRWST and sump do not drain during this period.

Primary Coolant System:

Break flow. Liquid flows through the break and into the containment during the first few seconds following the break. Figures 22 and 23 show the break mass flows and exit vapor fractions, respectively. For the remainder of the blowdown period, two-phase critical flow with increasing vapor content passes through the break, and by the end of the blowdown period the liquid content in the break flow is small. The break flow peaks early, during the interval when liquid passes out of the break. The vessel-side break flow is significantly larger than the pump-side break flow. Flashing in the core maintains a higher pressure on the vessel side. Also the operating pump actually is a resistance to flow out of the pump side of the break. The vessel-side break flow retains more liquid content longer than the pump side.

RCPs. Figure 24 shows the total mass flow in each loop at the steam generator exit plenum. The break causes an increase in mass flow in each loop but more so in loop 2, the loop with the broken cold leg. The RCPs operate in single-phase mode until void appears in the pump suction shortly after 5 s. However, pump performance degrades rapidly thereafter, and the loop flows also rapidly decrease. The RCPs continue to operate throughout this period.

Cold legs. Because the RCPs continue to operate, the intact-loop cold leg flows (CL 1A and 1B) remain constant until voiding occurs in the pump suction at 5 s. The flows then rapidly decrease. Figures 25 and 26 show the cold-leg mass flows and voiding, respectively. The flow in CL 2A is reduced immediately following accident initiation as the break in CL 2B consumes most of the flow

arriving in the SG 2 plenum that is common to both CL 2A and 2B. The flow in CL 2B is simply the break flow. However, as the pressure in the broken cold leg decreases, the flow through the break flow decreases. Voiding at the break then begins, which increases flow resistance resulting in a further reduction in mass flow. The incoming flow from the steam generator plenum is diverted to the intact pump RCP 2A. Voiding begins in the inlets of all RCPs shortly thereafter and the flows through the intact cold legs (1A, 2A, and 2A) rapidly decrease. Processes/phenomena in the break, cold legs, and vessel are tightly coupled as discussed in the blowdown period overview.

Hot legs. HL 1 (intact loop) and HL 2 (broken loop) display significantly different behavior immediately following accident initiation. Flow in HL 2 continues in the normal flow direction (Fig. 28). However, a brief interval of high flow results from the increased pressure difference induced by the break. The HL 1 flow bifurcates. Part of the flow continues in the normal flow direction through SG 1 (Fig. 27). The remainder of the flow reverses and flows backward into the upper plenum. Pressurizer draining contributes to this flow (Fig. 14). Liquid entering the upper plenum from HL 1 participates in top-down cooling of the core. Voiding begins almost immediately in the hot legs because the temperatures are higher in this portion of the primary coolant system. Figures 29 and 30 show the hot-leg voiding.

Pressurizer. The pressurizer empties a large fraction of its inventory through the surge line and into HL 1 within the first 8 s following the break (Fig. 14). The pressurizer blowdown occurs while its pressure is higher than in the remainder of the primary system (Fig. 12). Once the pressurizer pressure equalizes with the remainder of the primary system, its discharge rate slows. During the blowdown period, the pressurizer discharge is the primary source of the total makeup flow (Fig. 31).

Steam generators. Voiding occurs in the hottest and highest portions of the steam generator primary much as that described for the hot legs. Similarly, the outlet flows track those of the corresponding cold legs.

Reactor System:

Control rods. Upon receipt of the S signal, the control rods insert over a period of ~1 s and are fully inserted by ~1 s following the S signal (i.e., essentially 2 s after the break). The initial shutdown of the reactor results from negative reactivity inserted by core voiding (Fig. 39). However, the inserted control rods maintain the reactor in a shutdown condition once the core is refilled. The control rods will not be discussed further for the remaining periods.

Lower plenum. The coolant inventory in the lower plenum decreases (Fig. 53) for the first 3 s after the accident. During this interval, the break is supplied by both the flows through the intact cold legs (1A, 1B, and 2A) and the vessel inventory. The lower plenum inventory recovers briefly once the intact cold legs

can supply the break (see the cold-leg discussion for this period), but this partial refilling of the lower plenum lasts only until the RCPs void at 5 s and the flows through the intact cold legs decrease and approach zero. At the end of this period, 50% of the liquid inventory of the lower plenum is lost. Figure 54 shows the lower plenum liquid and saturation temperatures. The lower plenum coolant reaches saturation at 5 s; it remains saturated until ~40 s, when the lower plenum is refilled with subcooled accumulator flow.

Core region. Flashing begins shortly after the break occurs as a result of primary system depressurization (Fig. 33). The core liquid flow reverses and flows downward to the lower plenum (Fig. 34) and upward to the broken loop through the downcomer. Vapor flow continues in the normal direction throughout much of the core, resulting in countercurrent flow within the core and at the core exit. During this period, flow passes downward from the upper plenum into the upper portions of the core (Fig. 35). In addition, flow passes downward from the upper head and is delivered to the top of the core through the guide tubes. However, the deliver of coolant from the upper plenum to the core is interrupted for ~2 s beginning at 2 s. This interrupts the top-down quench of the fuel rods (see fuel-rod discussion for this period). More top-down quenching occurs in the outer core region because of more liquid down flow in the outer core region. Figure 37 shows the core-outlet liquid mass flow for the inner ring and outer ring of the modeled core region. Figure 38 shows the corresponding vapor mass flows. The flow in the core has a multidimensional character and this is reflected in different rates of cladding heating and cooling throughout the core. Voiding in the core inserts negative reactivity and is the initial mechanism for core power decrease before the control rods are inserted (Fig. 39). A two-phase mixture continues in the core throughout this period, but the amount of liquid remaining in the core at the end of this period is small (Fig. 11). Core-inlet and core-outlet flows for each core sector cell are given in Apps. A and B, respectively.

Upper plenum. The vessel upper plenum begins to void immediately following break initiation and is almost fully voided by the end of the period (Fig. 56). Fluid exits the upper plenum through the broken-loop hot leg and via top-down draining of liquid through the upper core support plate into the top of the core (Fig. 37). Countercurrent flow exists in the upper plenum. Vapor enters the upper plenum from the core region (Fig. 38) and early in the period, the intact-loop hot leg delivers water to the upper plenum.

Upper head. The vessel upper head communicates with the upper plenum through the guide tubes and drain holes in the upper head support plate. It also communicates with the top of the downcomer annulus. The guidetubes can also deliver coolant directly to the top of the core. After a delay of ~5 s, the upper head begins to void and is almost fully voided by the end of this period (Fig. 55). The largest flow from the upper head is to the upper plenum through the drain holes (Fig. 58), although this flow does not begin for ~3 s following the accident. Some of this upper-head flow is swept across the upper plenum into the broken-

cold-leg hot leg and thus does not reach the upper core plate. Upper head inventory is also delivered directly to the top of the core through the guide tubes^b (Fig. 52). The guide tube flow begins immediately following accident initiation. The upper head to downcomer flow is small (Fig. 59).

Downcomer. The downcomer annulus remains either full or nearly full until ~7 s (Fig. 51). Then the downcomer begins to rapidly empty and ~65% of the liquid inventory is lost by the end of the period. The voiding proceeds from the top of the downcomer annulus downward under the influence of the cold-leg break. When the voiding reaches the level of the broken cold-leg nozzle, voiding contributes to a continuation of the break flow decrease, which to this time has been dominated by the decrease of the primary system pressure. Early in the transient, flow from the intact cold legs passes around the downcomer annulus and out the broken cold leg. In addition, inventory from the other areas of the vessel supply the break until the flow has diminished to a level that can be supplied by flow through the intact cold legs.

Fuel rods. Heat transfer from the fuel rods to the coolant degrades as portions of the core void and the fuel cladding temperatures begin to rapidly increase. Essentially all the stored energy in the fuel rods is redistributed from the center of the fuel rods to the outer periphery of the fuel rods and the cladding (Fig. 40). The cladding temperature increase slows markedly beginning at ~5 s, and the blowdown or first peak cladding temperature is reached at ~7 s (Fig. 13). The blowdown period fuel-rod temperature increase is terminated by a combination of processes/phenomena occurring in the primary system. These processes/phenomena alter the core power to flow ratio. The decreasing core power and removal of core stored energy affect the power component. The flow component is more complex.

Immediately following break initiation, the vessel side flow is larger than can be supplied by coolant entering the downcomer annulus from the intact cold legs. Thus, the required additional flow is supplied from vessel inventory. When core inventory depletion by flow processes is combined with coolant flashing in the core, a large fraction of the core becomes vapor filled. At ~3 s, the vessel-side break flow can be completely supplied by the flows entering the downcomer annulus from the intact cold legs. This is caused by the combination of flow recovery in CL 2A (Fig. 24) and the decrease in break flow (see blowdown period overview and cold-leg discussions for this period). The coolant delivered to the downcomer annulus in excess of that needed to supply the break is delivered to the lower plenum and core. The liquid inventories of both the lower plenum and the core increase (Fig. 11). The coolant entering the core boils and the resultant

^b In the TRAC model, the guidetube flow is delivered directly to the top of the core and is distributed uniformly over all assemblies modeled in the cell. In the actual AP600 reactor design, the guidetube flow is delivered to a select number of assemblies in the core and not to all the assemblies. Furthermore, the guidetubes have slots that communicate between the inner portion of the guidetube and the upper plenum. These guidetube details are not included in the TRAC model.

steam flow cools the core. The cladding temperatures are decreasing at the end of the blowdown period.

The TRAC calculation showed considerable variation in top-down quenching and rewetting with radial and azimuthal location and relative location to the break. To illustrate, Figs. 41 and 42 show average rod cladding temperatures at two vessel cell locations, cells 1 and 4. Cell 1 is in the inner core ring of azimuthal sector 1, the same azimuthal sector of hot-leg 1; it is also the cell that the maximum hot-rod peak clad temperature occurs in. Cell 4 is in the inner core ring of cold leg 2A azimuthal sector, two sectors away from the broken cold leg sector. Figures 43 and 44 show the hot rod cladding temperatures at the same two cells. Figures 45 and 46 show the average rod cladding temperatures for cells 9 and 13, which correspond to the outer core ring at the same azimuthal sectors. As can be seen, cell 1 receive more top-down quenching and cooling than cell 4. In general, those cells away from the break receive more top-down flow than those near the break. Also, the outer ring cells receive more top-down quenching and cooling than the inner ring cells, a consequence of CCFL that limits the liquid downflow in the inner core ring because of a higher vapor upflow. Average-rod and hot-rod temperatures for each core sector cell are presented in Apps. C and D, respectively.

Fuel-rod cladding temperatures as a function of core elevation at selected transient times are in Figs. 47 through 50. A detailed view of the progression of rod heatup, cooling, and reflood can be obtained through careful study of such data. Figures 47 and 48 are for an average-power rod and Figs. 49 and 50 are for a maximum-power fuel rod, both rods in core sector cell 4. For example, much of the upper portion of the core (approximately the upper 1-1/2 m, 5 ft) is quenched during the blowdown period (Figs. 47 and 49). This quenching arises from liquid flows entering the top of the core through the upper core support plate (Fig. 36). Fuel-rod cladding temperatures as a function of core elevation at selected transient times are presented in Apps. E and F for each core sector cell, App. E for average-power fuel rods and App. F for maximum-power fuel rods.

Guide tubes. The vessel guide tubes provide a flow path whereby fluid from the upper head proceeds directly to the top of the core (Fig. 52). Although some of the holes in the upper core plate are covered by the guide tubes, others are not. This distinction is lost in the TRAC input model which divides the vessel into 16 sectors, each of which represent in some average way fuel elements that are both directly under guide tubes and fuel elements that are removed from guide tube locations. Significant guide tube flow delivery to the top of the core occurs only during the blowdown period. This flow begins immediately as the pressure in the upper plenum and core decrease under the influence of the break. The steady-state fluid temperature in the upper head is between the hot- and cold-leg temperatures, but closer to the cold-leg temperature. Thus, flashing in the upper head is delayed for several seconds after the start of the accident but sustains guide tube flows as the primary pressure decreases. The guide tubes play no

significant role during either blowdown or the remainder of the transient and will not be discussed further.

Vessel structures. The vessel structures include the core support plates, core barrel, downcomer walls, etc. These structures also contain stored heat that interacts with the coolant. Vessel structures appear to play an insignificant role in this or the remaining periods of the LBLOCA and they will not be discussed further.

Bypass flows. There are several small flows that bypass the core and are unavailable for core cooling. These include rod thimble flow, core bypass flow, reflector cooling flow, and reflector cavity flow. During steady state, these flows are ~7.5% of the total loop flow. The fluid in these regions flash during the depressurization transient. The bypass flows play no significant role during either blowdown or the remainder of the transient and will not be discussed further.

Steam Generator System (Secondary Side):

The S signal initiates feedwater valve closure, and closure is completed during this period. In addition, the containment overpressure signal leads to closure of the main steam isolation valve (MSIV) during this period. Thus, the steam generator is isolated during this period and both feedwater and steam flows decrease to zero (Fig. 57). The SG-pressure is slightly higher than the primary pressure at the end of this period but secondary-to-primary heat transfer is insignificant because the tubes on the primary side of the SG are highly voided.

5.2. Refill Period (12.3 to 43 s)

Overview

The refill period begins at the time accumulator injection flow is initiated, and ends when sufficient water from the PSIS has entered the lower plenum to nearly or fully refill the lower plenum. The end of the refill period also corresponds to the start of the reflood period. Identification of the transition from the refill period to the reflood period is somewhat uncertain, as the lower plenum is not completely refilled and the collapsed liquid level is fluctuating when the sustained core inventory increase begins. Refill begins at ~12.3 s and ends at ~43 s (Fig. 11).

Early in the refill period, the CMTs supply water to the DVI line. However, as the primary system pressure continues to decrease, ECC flows from the accumulators increase and eventually terminate the CMT flows. Accumulator injection is initiated at the start of the refill period when the primary pressure decreases to 4.83 MPa (700 psi) (Fig. 12). The coolant flows to the reactor vessel downcomer through the DVI lines. Early in the period the injected liquid does not enter the lower plenum. Rather, ECC entering the downcomer through the DVI lines is entrained by core-generated steam passing upward through the downcomer, carried into the broken cold leg, and exhausted into the containment through the break. Thus, the liquid inventories of the

core, lower plenum, and downcomer continue to decrease during the early part of the refill period. In this steam-filled environment, the core begins to reheat (Fig. 13).

ECC bypass continues only as long as core-generated steam passes through the downcomer and exhausts to the containment through the break. Steam can be generated only so long as coolant is entering the core. No coolant enters the core from the lower plenum during the early part of the refill period (Fig. 34). More important is the cessation of coolant flow from the upper plenum into the top of the core at ~20 s (Fig. 35). Shortly thereafter, all remaining liquid in the core turns to steam and by 23 s the core is steam filled (Fig. 11).

Concurrent with the termination of top-down liquid flow at 20 s, core-generated steam production decreases. The downcomer begins to refill at 20 s and a second later the lower plenum begins to refill. At 43 s, the lower plenum first fills to the lower core support plate (Fig. 11). There is a small accumulation of water in the core beginning at 37 s but the core is still heating at the end of the period (Fig. 13).

System Response

Automatic Depressurization System:

The ADS is not activated during this period (See Blowdown Period System Description).

Passive Containment Cooling System:

The containment atmosphere pressure and temperature continue to increase during this period. The pressure peaks at ~50 psia (Ref. 8) and remains between 45 and 50 psia for an extended period. The system pressure appears to remain high enough to keep the break choked throughout period. We again note that a constant containment back pressure of one atmosphere was specified for the TRAC calculation. Precise statements regarding the time at which the break planes unchoke are not possible because the calculation was not performed with a coupled model of the primary system and the containment.

Passive Heat Removal System:

The flow entering the PRHRS piping from the hot leg is highly voided at the start of the refill period and fully voided by the end of the period. Vapor entering the PRHRSHX condenses, but the energy transferred to the IRWST heat sink is minor. The flow at the PRHRS outlet is liquid and contributes to the liquid inventory in SG 1. Figure 20 shows the PRHRS inlet and outlet mass flows. The PRHRS is not designed to operate during accidents in which highly-voided conditions exist in the primary system.

Passive Safety Injection System:

Accumulator flow injection begins at ~12.3 s (Fig. 15) when the system pressure drops below the 4.83 MPa (700 psi) accumulator set point (Fig. 12). The accumulator flow rapidly terminates the CMT flow that began during the blowdown period. Choking in the DVI nozzle venturi occurred at 22 s, limiting the accumulator flow thereafter. Neither the IRWST nor the sump drain during this period.

Primary Coolant System:

Break flow. The pump-side break flow is essentially all vapor, and critical flow conditions persist during this period (Fig. 23). The vessel-side break flow entrains some liquid flow from the downcomer but it too is highly voided. The decrease of the primary pressure (Fig. 12) and the highly voided nature of the flows from each side of the break contribute to a diminishing break mass flow (Fig. 22). At the start of the refill period, the total break flow is ~5700 kg/s. At the end of the refill period, the break flow is near zero.

RCPs. The reactor coolant pumps trip at ~16 s. This has very little effect on the mass flow because the flow through the pumps is highly voided at the start of the refill period, and pump performance is highly degraded.

Cold legs. The cold legs progress from a highly voided to a near fully voided condition during this period (Fig. 25). The connection to the cold-leg PBL voids, and a vapor path is opened to the top of the CMT, which initiates CMT draining as previously discussed.

Hot legs. The broken-loop HL 2 is essentially fully voided from the beginning of the refill period (Fig. 29). The intact-loop HL 1 is highly but not fully voided at the beginning of the period (Fig. 28). There is a flow from this hot leg back into the upper plenum between 10 and 20 s. This flow is from the pressurizer and backflow from the loop steam generator. Both hot legs are fully voided by the end of the refill period.

Pressurizer. After the pressurizer pressure equalizes with the primary pressure near the end of the blowdown period, the rate at which the pressurizer inventory is discharged into the loop-1 hot leg slows. The pressurizer discharges the remainder of its inventory into the loop-1 hot leg by the end of the refill period.

Steam generators. The steam generator tube bundles void at ~16 s and remain voided. As the primary system pressure decreases, secondary-to-primary reverse heat is possible. However, because the primary-side tube bundles are vapor filled, the secondary-to-primary heat transfer is insignificant. Some mass flows back into HL 1 from the steam generator between 10 and 20 s.

Reactor System:

Lower Plenum. The key process during this period is refilling of the lower plenum to set the stage for core reflood. At the start of the refill period, the lower plenum inventory decreases (Fig. 11), and it continues to decrease until ~22 s. During the interval between 12.3 and 22 s, the break flow rapidly decreases as discussed previously. Steam generation in the core has diminished because the core approaches a fully voided condition and there is little flow of either liquid or vapor at the bottom of the core, which can pass into the downcomer and retard the flows (Fig. 34). Consequently, the ECC flows injected through the DVI lines begin to refill the downcomer and lower plenum at ~22 s. The liquid level in the lower plenum first reaches the bottom of the core at ~43 s and this time is declared as the end of the refill period and the beginning of the reflood period. Flow oscillations occur during the lower plenum refilling process.

Core Region. The core is at decay power levels and is maintained in a shutdown condition by the control rod reactivity (Fig. 39). The core is ~90% voided at the start of the refill period and fully voided by 20 s. Between 12.3 and 20 s, the downward flow of liquid into the top of the core from the upper plenum is decreasing and approaches zero (Fig. 35). After 20 s, the vapor in the core is heated and moves upward but the vapor mass flow is very small and produces little cooling of the core.

Upper Plenum. The upper plenum is ~90% voided at the start of this period, becomes fully voided by 25 s, and remains fully voided throughout the remainder of the refill period (Fig. 56). The upper plenum supplies essentially all the liquid flow into the core between 12.3 and 20 s. The coolant flow from the upper plenum into the core supplies the liquid that sustains steam generation in the core and ECC bypass.

Upper Head. The upper head is ~90% voided at the start of this period, becomes fully voided shortly thereafter, and remains fully voided throughout the remainder of the refill period (Fig. 55). The liquid in the upper head at the beginning of the period enters the upper plenum through the upper support plate drain holes (Fig. 58) and the downcomer through the downcomer-upper head flow path (Fig. 59). There is no flow into the upper plenum through the guide tubes after the upper head liquid level drops below the top of the guide tubes near the end of the blowdown period.

Downcomer. See the description of lower-plenum processes and phenomena for the refill period.

Fuel Rods. At the start of the refill period, the fuel rods cool as a result of liquid introduced into the core late in the blowdown period. The temporary restoration of liquid flow into the core during the blowdown period occurred when the intact-loop cold leg flows were sufficient to supply the rapidly decreasing vessel-

side break flow. However, subsequent voiding in the cold legs at the end of the blowdown period terminates the core flow recovery and the core becomes vapor filled during the refill period as previously discussed. In this vapor filled environment, the cladding-to-coolant heat transfer degrades and the fuel rods begin to reheat (Fig. 13). As previously discussed, the flows refilling the lower plenum are oscillatory. Thus, some liquid begins to appear at the core inlet before the end of the refill period (Fig. 34). The core heats up (Fig. 13) and continues to heat to the end of the period. The flow of liquid downward from the upper plenum into the core between 12.3 and 20 s removes some of the core decay heat, especially at the top of the core as shown in Fig. 48.

Steam Generator System (Secondary Side):

Secondary-to-primary heat transfer is initiated during this period, but the steam-generator primary is vapor filled and the reverse heat transfer is limited.

5.3. Reflood Period (43 to 240 s)

Overview

Reflood begins after the lower plenum refills and the core begins to refill (Fig. 11). Reflood is completed when the entire core is quenched. Initially, core reflood is quite rapid because (1) the downcomer head is initially resisted by only a steam-filled core, and (2) core-generated steam flows through the core, coolant loops, and break are small so the pressure resisting the downcomer head is small. For this analysis, the reflood period begins ~43 s after accident initiation.

Because of the high fuel rod temperatures at the beginning of reflood, the entire spectrum of thermal regimes, starting with single-phase liquid and progressing upward through the core with nucleate boiling; transition boiling; film boiling; churn two-phase flow; dispersed droplet flow; and single-phase steam flow, are encountered. However, by the end of this period, fuel temperatures have peaked and the entire core is quenched (Fig. 13).

Because of droplet carryover from the core and subsequent deentrainment at the upper core plate and grid spacers, top quenching and local quenching occur in addition to bottom quenching. Higher vapor velocities and liquid entrainment occur in the central region of the core where higher-powered fuel rods are located. The entrained liquid has a cooling effect on the fuel rod regions above. The upper portions of the core remain cooler because significant cooling occurred during the previous period as liquid from the upper plenum entered and cooled the upper portions of the core (Figs. 47 and 48).

Some of the entrained liquid is deentrained at the upper core plate. The remainder is carried into the upper plenum, where it is deentrained, forming a two-phase pool. Liquid from the pool can reenter the low-power regions of the core through the upper support plate because of the lower vapor velocities in those regions. A three-dimensional flow pattern results: in the core, flow is from the low- to high-power regions, while in the upper plenum the flow passes from the high- to low-power regions. Liquid from the upper plenum two-phase pool may be further entrained and

carried over into the hot legs. In traversing the upper plenum, this liquid may be further deentrained on upper plenum internal structures.

As the bottom quench progresses upward through the core, more liquid is carried over to the upper plenum pool. Conditions exist (steam passing through the upper plenum pool) by which liquid can be entrained and carried into the hot legs. If the liquid carried through the hot legs reaches the steam generators, it will be boiled by reverse steam generator heat transfer, causing a pressure increase in the steam generator bundle. In the current generation Westinghouse PWRs, the loop seals are liquid full so any vapor generated in the steam generators increases the hot-leg pressure and can retard the core reflood process. This phenomenon is called "steam binding." The AP600 does not have loop seals, and a vapor path is open to the vessel from both sides of the steam generator, making it unlikely that steam binding will be significant in the AP600. There is some liquid accumulation in the steam-generator inlet late in this period, which will alter the loop pressure losses somewhat.

For much of the reflood period, manometer oscillations between liquid in the downcomer and the core lead to an oscillatory reflood rate. The downcomer liquid level (head) is the driving potential for liquid to enter the core. Liquid passing through the downcomer and entering the core from the lower plenum boils; the increased pressure in the core alters the core-downcomer force balance and reduces the flow from the downcomer. With reduced core flow, there is less steam generation, the core-side pressure decreases and again alters the core-downcomer force balance causing an increased downcomer to core flow in this part of the cycle. Associated with the oscillations is increased liquid entrainment and carryover that accelerate core quenching.

Quenching of the maximum-power fuel rods occurred at the same time that the accumulator emptied.

System Response

Automatic Depressurization System:

The ADS is not activated during this period (See Blowdown Period System Description).

Passive Containment Cooling System

The cooling processes of the PCCS become more important as the transient proceeds. The primary functions of the containment are several. First, the containment is to provide a barrier to fission product release. To do so, the integrity of the containment structures must be preserved. Thus, the containment pressure increase must be limited. Second, the decay heat of the core must be transferred to the ultimate heat sink, the atmosphere. If systems were not provided to cool the containment, the pressure would rise and possibly fail the containment which is an essential system during the long-term cooling period.

The break planes unchoke during the refill period. Precise statements regarding the time at which the break planes unchoke are not possible because the calculation was not performed with a coupled model of the primary system and the containment. The containment and primary coolant system are coupled during this period but the coupling does not appear to have a strong impact on core cooling processes. The PCCS is not modeled in the TRAC calculation. The following qualitative description of PCCS operation is provided for completeness.

Early in the transient, energy transfer to the atmosphere through the steel containment structure is enhanced by evaporation of liquid deposited on the outside of the steel containment structure near the top of the structure. Buoyancy induced air flow through the air gap between the steel concrete structure and the concrete shield building also cools the structure. By the time the PCCS water supply is depleted during the long-term cooling period, the decay heat had decreased sufficiently so that the buoyancy induced air flow through the air gap between the steel containment structure and the concrete shield building can remove the decay heat of the core.

Passive Heat Removal System:

The PRHRS mass inventory is depleted either from flashing or from draining, and this system does not contribute to energy removal from the primary.

Passive Safety Injection System:

The sole source of emergency coolant injection during this period is via accumulator injection (Fig. 15); this circumstance continues until the accumulator empties, which occurred in this transient at about the same time that the last of the maximum-power fuel rods were quenched. Figures 16 and 17 respectively show the accumulator liquid levels and the fraction of initial liquid volume. Noncondensable gas from the accumulators is discharged into the DVI lines at ~190 s, which rapidly decreases the mass flow of the remaining accumulator liquid. The discharge of gases into the DVI lines increases the pressure in the DVI lines such that CMT flow injection is delayed for a short time after the accumulators have discharged their liquid inventory. Typically, analyses of the LBLOCA transient are terminated before CMT injection resumes because the key safety acceptance parameter, the peak cladding temperature, has been reached and the core is cooling.

Primary Coolant System:

Break flow. The impact of the break on primary system behavior, major during the blowdown and early refill periods, becomes less important throughout the refill period and is of little importance during the reflood period. Neither the pump-side nor vessel-side break flows are critical, and flows are near zero (Fig. 22). The pump-side flow is vapor until the refill process is well advanced

(Fig. 23). The vessel-side break flow is nearly so, but significant amounts of liquid appear at the vessel-side break plane after 60 s, as the oscillating downcomer liquid level approaches the cold-leg nozzle connections to the vessel. The liquid entrainment out the break increases the net system mass flow loss (Fig. 32) and slows the vessel refill rate as can be seen in the integrated net mass flow loss, Fig. 33.

RCPs. The reactor coolant pumps still are rotating at a fairly high rate (Fig. 60), even though they were tripped at 16 s. The average mass flow through the loop-1 pumps during the reflood period is 17 kg/s. The average mass flow through the loop-2 intact cold leg pump is 10 kg/s, whereas the mass flow through the broken cold-leg pump is 24 kg/s. The flow consists mostly of vapor during this period; therefore, even though the mass flows are low, the volumetric flows are relatively high. The volumetric flows of the loop-1 pumps are $\sim 13.7 \text{ m}^3/\text{s}$. The volumetric flow of the loop-2 intact cold-leg pump is $12 \text{ m}^3/\text{s}$, and the volumetric flow of the broken cold-leg pump is $26 \text{ m}^3/\text{s}$. For comparison, the pump volumetric flow at steady-state full power is $3.2 \text{ m}^3/\text{s}$.

Cold legs. The intact cold legs are essentially voided, and the flow consists mostly of vapor (Figs. 26 and 25, respectively). After 60 s, the oscillating downcomer liquid level reaches the cold-leg-nozzle connections to the vessel and significant amounts of liquid begin to move through the broken-loop cold leg to the break.

Hot legs. The hot legs are vapor filled during the early part of the reflood period (Figs. 28 and 29). As the upper plenum begins to accumulate liquid later in the transient (Fig. 11), small amounts of liquid are entrained and carried into the hot legs. If carried into the steam generators, reverse heat transfer from the secondary side of the steam generators vaporizes the liquid. In current Westinghouse commercial plants, the vapor generation in the steam generators participates in a process/phenomena called "steam binding." Steam binding occurs when liquid vaporizes in the steam generator and the pressure increases propagate toward the core. The increased core pressure offsets some of the downcomer liquid head and the core reflood rate decreases. In plants with a loop seal, such pressure increases are possible because the liquid in the loop seal blocks pressure equalization. AP600 does not have loop seals and we believe that steam binding will not occur because vapor generated in the steam generators can flow unobstructed to both sides of the core.

Pressurizer. The pressurizer is voided.

Steam generators. See the previous discussion of reflood phenomena in the hot legs. During the latter phases of the reflood period, liquid is carried to the steam generator inlets (Figs. 28 and 29). Some of the liquid is deentrained there, and that which is carried into the steam generator tubes is vaporized.

Reactor System:

Lower Plenum. The reflood period begins when lower plenum refilling is completed. Because of the oscillatory filling process, the actual time assigned to the start of this period is somewhat uncertain. However, by 45 s, the lower plenum is essentially full (Fig. 53) and lower plenum liquid is subcooled (Fig. 54).

Core Region. The core-outlet flow is highly oscillatory from a time shortly before the end of the refill period and continuing until the core is completely reflooded (Fig. 34). The flow oscillations are considerably damped in the confined flow passages of the core [compare the core-outlet mass flows (Fig. 35) to the core-outlet mass flow (Fig. 34)]. The liquid fraction, although oscillatory, steadily increases (Fig. 11) and then decreases at 200 s because of the decrease in accumulator flow (Fig. 15). For much of the reflood period, manometer oscillations between liquid in the downcomer and the core lead to an oscillatory reflood rate. Liquid entering the core from the lower plenum boils and the increased pressure in the core reduces the flow from the downcomer. The downcomer flow is set by balance of the liquid level (head) in the downcomer and the pressure in the core.

Upper Plenum. The upper plenum begins the reflood period in a fully voided condition (Fig. 56). However, as the reflood period continues, the core liquid level increases, accompanied by significant steam generation (Fig. 35) that carries liquid into the upper plenum (Fig. 36). A small amount of liquid accumulates in the upper plenum (Fig. 56), but there are several competing processes that prevent a large accumulation of liquid. These processes include entrainment and transport of liquid into the hot legs, as previously discussed, and the flow of liquid to regions of the upper core support plate above the lower powered regions of the core. As the steam generation in these regions is small, some of the upper plenum liquid flows downward into the top of the core.

Upper Head. The upper head remains fully voided during this period (Fig. 55).

Downcomer. The downcomer continues to refill from accumulator flow injection through the DVI line (Fig. 11). Large flow oscillations continue to occur. The downcomer does not fully refill because once the liquid reaches the level of the cold-leg nozzle connections to the vessel, downcomer liquid flows into the broken cold leg and out the break.

Fuel Rods. At the start of the reflood period, fuel rod temperatures in much of the core are increasing (Figs. 41-46). However, as the core begins to refill, the heat transfer environment of the fuel rods change. The primary direction of the quench is from the bottom up, as shown in Figs. 48 and 50, for the average-power and maximum-power rods respectively. The upper 1-1/2 m (~5 ft) of the core were quenched during the refill period. There is a minor reheat of the upper core during the early part of the reflood period, but the cladding temperatures remain well below the peak cladding temperatures lower in the core. Coolant advancing

upward from the bottom of the core is the primary mechanism for core cooling during reflood. The lower sections of the fuel rods are cooled by liquid convection and nucleate boiling, higher elevations of the fuel rods by film boiling, and even higher elevations of the fuel rods by nucleate boiling. The quench front advances upward in the core and eventually the entire core is quenched as the core refills.

Steam Generator System (Secondary Side):

See the discussion of hot-leg phenomena during the reflood period.

5.4. Long-Term Cooling Period (240 s and Beyond)

Overview

Long-term cooling starts when the fuel rods have been quenched completely. At that point, system pressures have decreased enough that the gravity-driven core makeup tanks and IRWST can start draining into the reactor vessel. There is sufficient water from the IRWST alone to flood the containment to a level at which the broken cold-leg sections are completely submerged, thus forming a liquid natural-circulation cooling path between the core and containment. This mode of cooling is designed to remove the reactor core heat indefinitely.

System Response

Automatic Depressurization System:

The ADS will be activated on a core makeup tank liquid level trip signal but will not have any effect because the primary system pressure already has decreased to containment pressure levels.

Passive Containment Cooling System:

The cooling processes of the PCCS is the dominant mode of cooling for the long-term cooling period. The heat removed by the natural-circulation cooling loop eventually will be transferred to the containment wall and to the external atmosphere. The PCCS is not modeled in the TRAC calculation. By the time the PCCS water supply is depleted during the long-term cooling period, the decay heat has decreased sufficiently so that the buoyancy-induced air flow through the air gap between the steel containment structure and the concrete shield building can remove the decay heat of the core.

Passive Heat Removal System:

The PRHRS mass inventory is depleted either from flashing or from draining; this system does not contribute to energy removal from the primary system.

Passive Safety Injection System:

The core makeup tanks will start to drain early in the long-term cooling period. They are orificed so that at their designed flow, the CMTs will drain for several hours.

Primary Coolant System:

Break flow. The break eventually will be submerged with water from the IRWST.

RCPs. The pumps will cease rotating as they become submerged with water from the IRWST.

Cold legs. The cold legs eventually will be submerged with water from the IRWST.

Hot legs. The horizontal sections of the hot legs eventually will be submerged with water from the IRWST.

Pressurizer. The pressurizer is voided.

Steam generators. The voided primary side of the steam generator will have no effect.

Reactor System:

Lower Plenum. The lower plenum will be completely full.

Core Region. The core eventually will be filled with water from the IRWST.

Upper Plenum. The upper plenum eventually will be filled to above the hot-leg connections.

Upper Head. The upper head will remain voided during this period.

Downcomer. The downcomer eventually will be filled to above the cold-leg connections.

Fuel Rods. The fuel-rod heat transfer eventually will change from saturated nucleate boiling to single-phase liquid convective heat transfer.

Steam Generator System (Secondary Side):

The secondary side will have no effect because there is no primary flow circulation.

6.0. COMPARISON WITH WCOBRA/TRAC

The TRAC calculation results were compared with the Westinghouse WCOBRA/TRAC results presented in the AP600 Standard Safety Analysis Report.¹⁰ Table II presents a summary comparison of the TRAC and WCOBRA/TRAC results for transient event times and selected calculated parameters. WCOBRA/TRAC transient calculation plots were also scanned, digitized, and overlaid on TRAC calculation results for a graphical comparison. It should be noted that the WCOBRA/TRAC results do not reflect the latest AP600 design. We have requested the latest Westinghouse 80% DEGB LBLOCA calculation but have not yet received it. A 100% DEGB LBLOCA WCOBRA/TRAC calculation, recently received from Westinghouse, also provided some insight in the general differences between TRAC and WCOBRA/TRAC.

Figure 60 compares the upper plenum pressures for the first 40 s of the transient, which shows very good agreement between the two calculations. Figure 61 compares the accumulator flow rates. The TRAC accumulator flow is ~60 kg/s higher than the WCOBRA/TRAC flow. As indicated in the previous TRAC LBLOCA report, we believe the WCOBRA/TRAC accumulators to be calibrated to a different design flow rate. Figure 62 compares the lower plenum liquid levels. TRAC shows a momentary refill during blowdown whereas WCOBRA/TRAC did not. TRAC shows the lower plenum being emptied more than WCOBRA/TRAC but then refilling at a faster rate. Figure 63 compares the downcomer liquid level. TRAC shows the downcomer level not emptying as much, a slightly faster refill, and considerably stronger flow oscillations between the lower plenum and downcomer.

The next set of figures compare fuel rod cladding temperatures. The method of modeling the core in WCOBRA/TRAC is different from TRAC, which makes the comparison somewhat difficult. In WCOBRA/TRAC, the core is modeled with vertical one-dimensional fluid channels that are subdivided into a number of cells. Crossflow paths can be specified between these fluid channels. Five types of fuel assembly channels (referred to as rods by Westinghouse) are modeled:

- Rod 1 models a hot rod at the maximum allowed linear heat rate^c;
- Rod 2 models an average rod in the hot assembly containing the hot rod;
- Rod 3 models an average rod in an assembly covered by an open hole or support column;
- Rod 4 models an average rod in an assembly covered by a guide tube; and
- Rod 5 models the low power peripheral assembly next to the reflector blocks.

The fluid channels are connected together with crossflow connections. Aside from the peripheral assembly representation, there appears to be no radial or azimuthal dimensionality to the WCOBRA/TRAC core model. By contrast, the TRAC core model is divided into two radial rings and eight azimuthal sectors for a total of 16 fluid

^c The number of actual fuel rods modeled in each type of fuel assembly channels is Westinghouse proprietary information.

channels, each modeling the same number of average-power fuel rods. Each TRAC fluid channel also models a supplemental maximum-power fuel rod.

Figure 64 compares the hot rod peak cladding temperatures. For the WCOBRA/TRAC pct, this represents the maximum cladding temperature at all rod elevations for Rod 1. For TRAC, the hot rod modeled in core sector cell 4 is the fuel rod that has the maximum peak cladding temperature throughout the transient. The comparison shows that TRAC has a lower blowdown PCT and a higher reflood PCT than WCOBRA/TRAC (the temperature values are given in Table II). Also, TRAC reflood PCT occurs much earlier than WCOBRA/TRAC, and after the reflood PCT, TRAC shows a slightly more rapid cooldown rate than WCOBRA/TRAC.

Next, rod cladding temperatures are compared at specific rod elevations, 6 ft, 8.5 ft, and 10 ft. For each comparison, two TRAC rod temperatures are shown to the one WCOBRA/TRAC rod temperature. The two TRAC temperatures on each plot provide an indication of the radial and azimuthal variation in rod temperatures calculated by TRAC. Figures 65 through 67 compare hot rod cladding temperatures at 6 ft, 8.5 ft, and 10 ft, respectively. Figures 68 through 70 compare average rod temperatures at the same respective rod elevations. Finally, Figures 71 through 73 compare the TRAC average rod temperatures in radial ring 2 to the WCOBRA/TRAC peripheral assembly Rod 5.

At the 6 ft. rod elevation, TRAC blowdown PCTs are lower than WCOBRA/TRAC, but TRAC reflood PCTs are significantly higher than WCOBRA/TRAC. WCOBRA/TRAC show higher cooling and quenching after blowdown PCT, and quenching after 80 s. At the 8.5 ft. rod elevation, TRAC blowdown PCTs are lower than WCOBRA/TRAC. WCOBRA/TRAC rod heatup period after blowdown is much longer than TRAC and cooling turnaround does not occur until after 100 s. At the 10 ft. rod elevations, TRAC blowdown and reflood PCTs are significantly lower than WCOBRA/TRAC. WCOBRA/TRAC quenches longer after blowdown peak but heatup period after quench is longer than TRAC.

Core vapor and liquid mass flow plots were also presented in the WCOBRA/TRAC analysis, but these are not compared with TRAC results because the number of fuel assemblies represented in the WCOBRA/TRAC mass flow plots are not known.

In general, there is reasonable agreement between the two calculations. A significant similarity is in the calculation of the hot-rod PCT. Both the TRAC and WCOBRA/TRAC calculations show the reflood PCT to be higher than the blowdown PCT. A major difference in calculation results is in the cooling of average-powered rods during the late-blowdown phase. The WCOBRA/TRAC calculation showed a complete rewetting and quenching of average-powered rods during the late-blowdown phase, with average-rod cladding temperatures being cooled down to saturation-temperature levels. The TRAC calculation shows a considerable variation, with those rods furthest away from the break showing more quenching and rewetting than those rods nearer the break.

Westinghouse calculations predict more extensive core cooling following the first peak than predicted in the TRAC-PF1/MOD2 calculation. As described in the previous paragraph, TRAC predicts that the increased delivery of coolant to the downcomer and core following recovery of flow through CL 2A. This coolant entering the core boils and the steam that is generated passes upward through the upper core support plate. The steam flow inhibits the downward flow of coolant from the upper plenum and guidetubes. As a consequence, top-down cooling of the core is limited. The Westinghouse calculations show an increase in the lower plenum liquid content at about the same time predicted by TRAC but this liquid does not enter the core. Thus, there is no steam generation and related retardation of downward flow of liquid from the upper plenum into the core. It is not possible to declare which representation of blowdown phenomena is more correct at the present time.

However, we do note that changes made to core heat transfer models as TRAC evolved from MOD1 to MOD2 result in diminished heat transfer following the first peak in several LBLOCA calculations. Thus, changes to the TRAC heat transfer models may play a substantial role in creating the phenomenological differences observed in the TRAC and Westinghouse calculations.

The two-phase flow representation in the vessel component of WCOBRA/TRAC also may be the reason for the difference in quenching behavior. The TRAC reflood model does not account for quenching due to a falling liquid film. WCOBRA/TRAC uses a two-fluid, three-field representation of two-phase flow in the vessel component. The three fields are a continuous vapor field, a continuous liquid field, and an entrained liquid droplet field. TRAC has just a two-field representation.

7.0. CONCLUSIONS AND RECOMMENDATIONS

An updated 80% DEGB cold-leg LBLOCA has been calculated for the Westinghouse AP600 advanced reactor design. The calculation reflects AP600 design changes and corrections to the TRAC code and plant model. Hot-rod PCT of 1021 K (1378°F) and 1197 K (1695°F) were calculated for the blowdown and reflood phases, respectively. These temperatures are below the App. K limit of 2200°F but near the cladding oxidation temperature of 1700°F. The TRAC calculation results were compared to the Westinghouse SSAR WCOBRA/TRAC LBLOCA results for the same size break. Transient event times and peak clad temperatures were in reasonable agreement but there were significant differences in the detailed phenomena calculated by the two codes. The reasons for these differences are still being investigated. Further study of the differences in plant modeling, transient calculation assumptions, code computational method, and code models and correlations are recommended. The calculation was performed with a plant model that had undergone an independent quality assurance check. Additional break sizes and break locations need to be analyzed to confirm the most severe break postulated by Westinghouse.

REFERENCES

1. J. F. Lime and B. E. Boyack, "TRAC Analysis of an 80% Double-Ended Cold-Leg Break for the AP600 Design," Los Alamos National Laboratory document LA-UR-94-2503 (July 1994).
2. J. C. Lin, et. al., "TRAC-PF1/MOD2 Code Manual," Volumes 1-4, Los Alamos National Laboratory report LA-12031-M, NUREG/CR-5673 (in press).
3. R. J. Beelman, S. M. Sloan, and J. E. Fisher, "AP600 Quality Assured RELAP5 Input Model Description," Idaho National Engineering Laboratory report EGG-NRE-10824 (rough draft and proprietary) (Last revised: June 28, 1993).
4. P. R. Shire and J. W. Spore, "TRAC-PF1/MOD1 Analysis of a Minimum-Safeguards Large-Break LOCA in a US/Japanese PWR with Four Loops and 15x15 Fuel," Los Alamos National Laboratory report LA-2D/3D-TN-86-18 (December 1986).
5. B. E. Boyack to F. Odar, "Minutes of May 26-27, 1994, AP600 Working Group Meeting," Los Alamos National Laboratory letter TSA-12-94-220 (June 13, 1994).
6. G. Dejarlais and M. Ishii, "Inverted Annular Flow Experimental Study," Argonne National Laboratory report ANL-85-30 (NUREG/CR-4277) (1985).
7. R. A. Nelson and C. Unal, "A Phenomenological Model of the Thermal Hydraulics of Convective Boiling During the Quenching of Hot Rod Bundles. Part I: Thermal Hydraulic Model," *Nuclear Engineering and Design* **136**, 277-298 (1992).
8. C. Unal and R. A. Nelson, "A Phenomenological Model of the Thermal Hydraulics of Convective Boiling During the Quenching of Hot Rod Bundles. Part II: Assessment of the Model with Steady-State and Transient Post-CHF Data," *Nuclear Engineering and Design* **136**, 299-318 (1992).
9. C. Unal, E. Haytcher, and R. A. Nelson, "A Phenomenological Model of the Thermal Hydraulics of Convective Boiling During the Quenching of Hot Rod Bundles. Part III: Model Assessment Using Winfrith Steady-State, Post-CHF, Void-Fraction and Heat-Transfer Measurements and Berkeley Transient-Reflood Test Data," *Nuclear Engineering and Design* **140**, 211-227 (1993).
10. Westinghouse Electric Corporation, "AP600 Standard Safety Analysis Report," prepared for the US Department of Energy, Document No. DE-AC03-90SF18495, Revision 0 (June 26, 1992).
11. Boyack, B., Duffey, R., Giffith, P., Lellouche, G., Levy, S., Rohatgi, U., Wilson, G., Wulff, W. and Zuber, N., "Quantifying Reactor Safety Margins: Application of Code Scaling, Applicability, and Uncertainty Evaluation Methodology to a Large-Break Loss-of-Coolant Accident," EG&G Idaho, Inc. report NUREG/CR-5249, also EGG-2552 (October 1989).

TABLE I
EXTENDED LBLOCA SEQUENCE OF EVENTS

Time (s)	Event
0	Break occurs.
0.35	"S" signal occurs from containment 5-psi overpressure signal.
0.86	Reactor trip from "S" signal, steam generators isolated.
2.1	CMT and PRHRS isolation valves start to open. A very small amount of CMT mass flow occurs but ceases once accumulator flow starts.
7	Maximum hot-rod peak cladding temperature during blowdown: 1021 K (1378°F).
8	Pressurizer empties.
12	Accumulators start to inject.
17.1	RC pumps tripped.
22	Peak accumulator flow of 408 kg/s (900 lb/s) occurs; flow limited by choking at the DVI nozzle venturi.
30	Lower plenum starts to refill.
43	Core reflood begins.
58	Maximum hot-rod peak cladding temperature during reflood: 1197 K (1695°F).
165	All average-power rods are quenched to saturation temperature levels.
190	Accumulator noncondensable gas enter DVI lines.
240	All maximum hot rods are quenched to saturation temperature levels. Accumulators completely empty of liquid.
265	Core makeup tank A start to drain.
275	DVI line pressure sufficient low enough that IRWST drain line check valve can open allowing IWRST injection.
280	Calculation terminated. Decay power remaining to be removed: 52.5 MW _t .

TABLE II
COMPARISON TO WCOBRA/TRAC 80% DEGB LOCA

	TRAC	<u>W</u> COBRA/TRAC
Reactor trip	0.86 s	<1 s
CMT isolation valves start to open	2.1 s	2.2 s
Pressurizer empties	8 s	7 s
Accumulators start to inject	12 s	12 s
RCP trip	17.1 s	17.2 s
Maximum accumulator flow	408 kg/s (900 lb/s)	331 kg/s (730 lb/s)
Lower plenum starts to refill	30 s	34 s
Average-rod PCT during blowdown	808 K (995°F)	847 K (1064°F)
Hot-rod PCT during blowdown	1021 K (1378°F)	1073 K (1472°F)
Core reflood begins	43 s	50 s
Average-rod PCT during reflood	864 K (1095°F)	738 K (868°F)
Hot-rod PCT during reflood	1197 K (1695°F)	1125 K (1565°F) ^a
Time that hot-rod PCT occurs	58 s	102 s

^aWith code uncertainty included, the WCOBRA/TRAC PCT was cited to be 1254 K (1798°F)

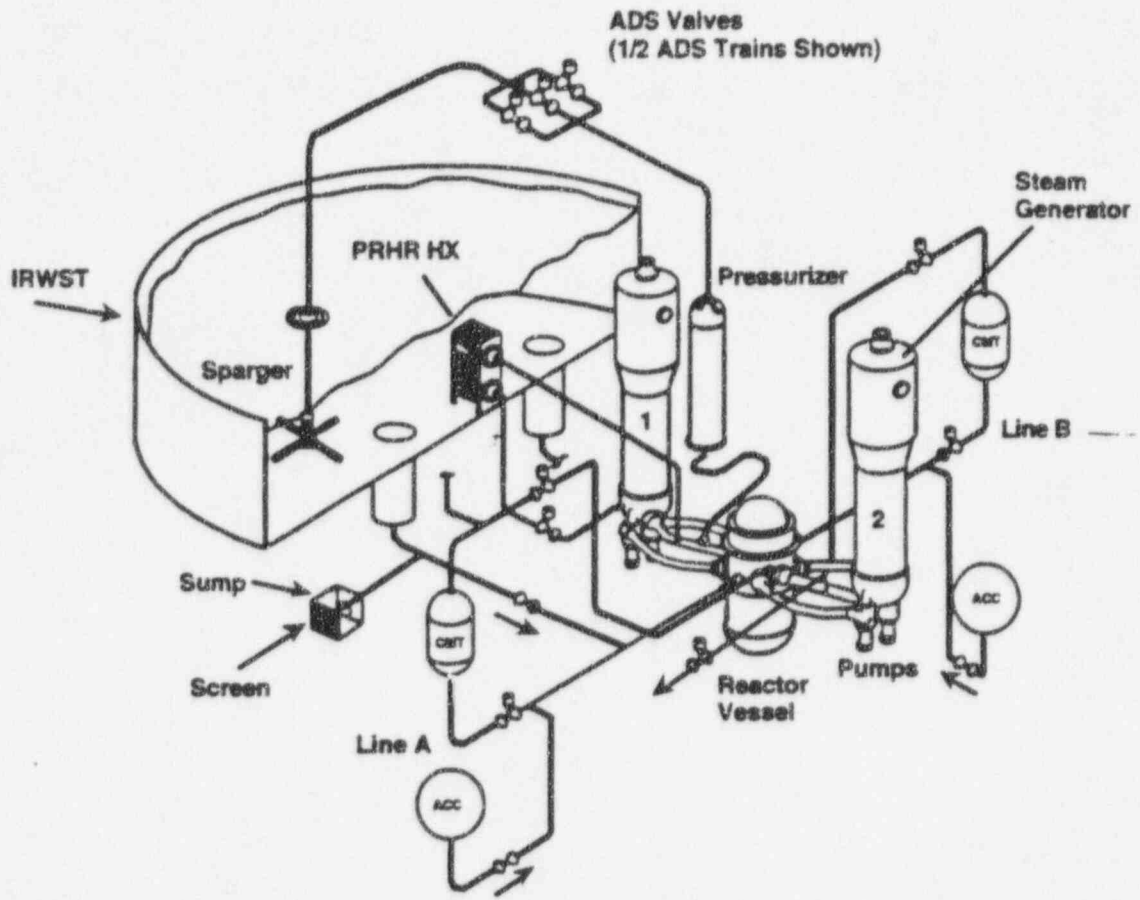


Fig. 1. AP600 plant isometric.

A - Internal condensation and natural circulation transfers heat from the core to the steel containment.

B - The containment is continuously cooled by natural circulation of air between the containment vessel and surrounding shield building.

C - Initially, containment cooling is enhanced by gravity-fed water from tanks above the containment.

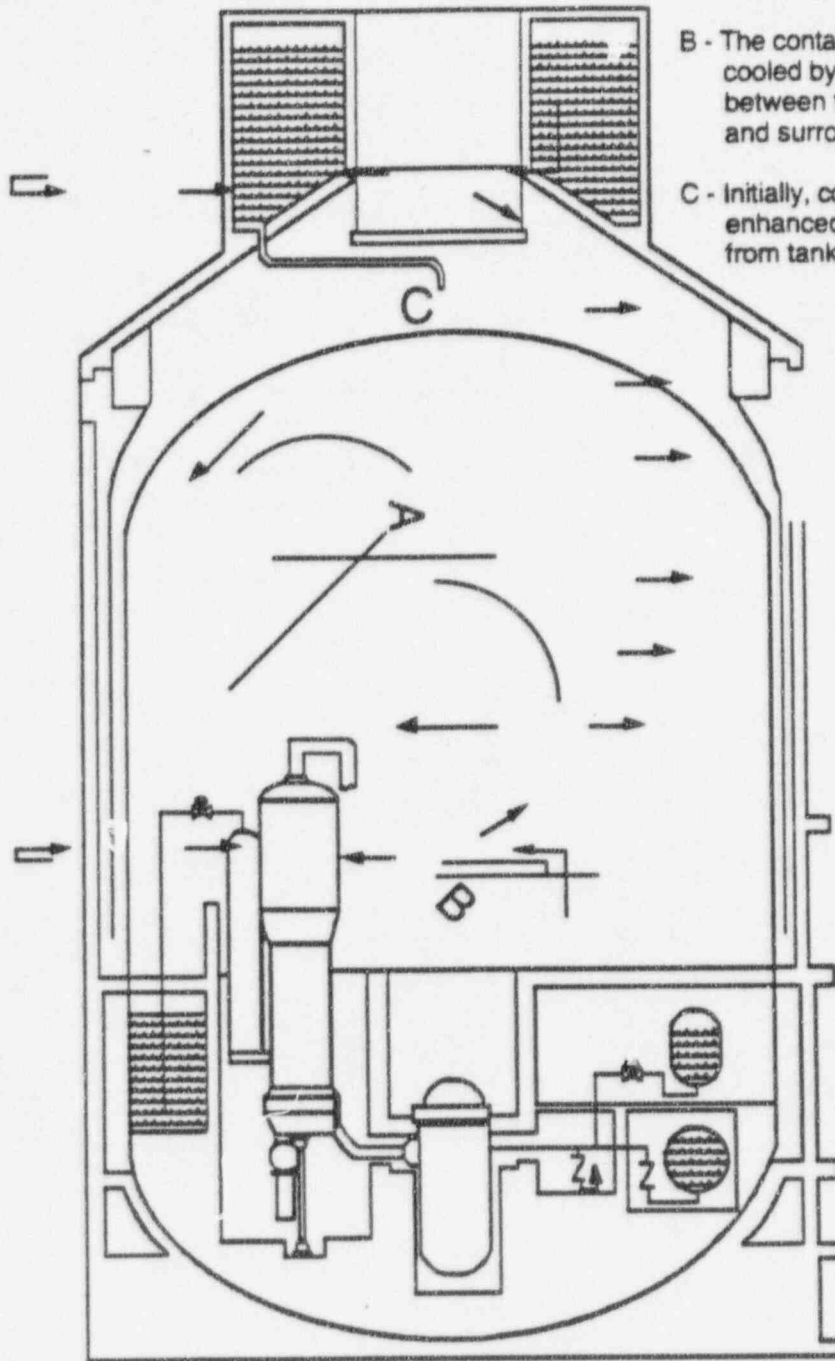


Fig. 2. AP600 containment cutaway view.

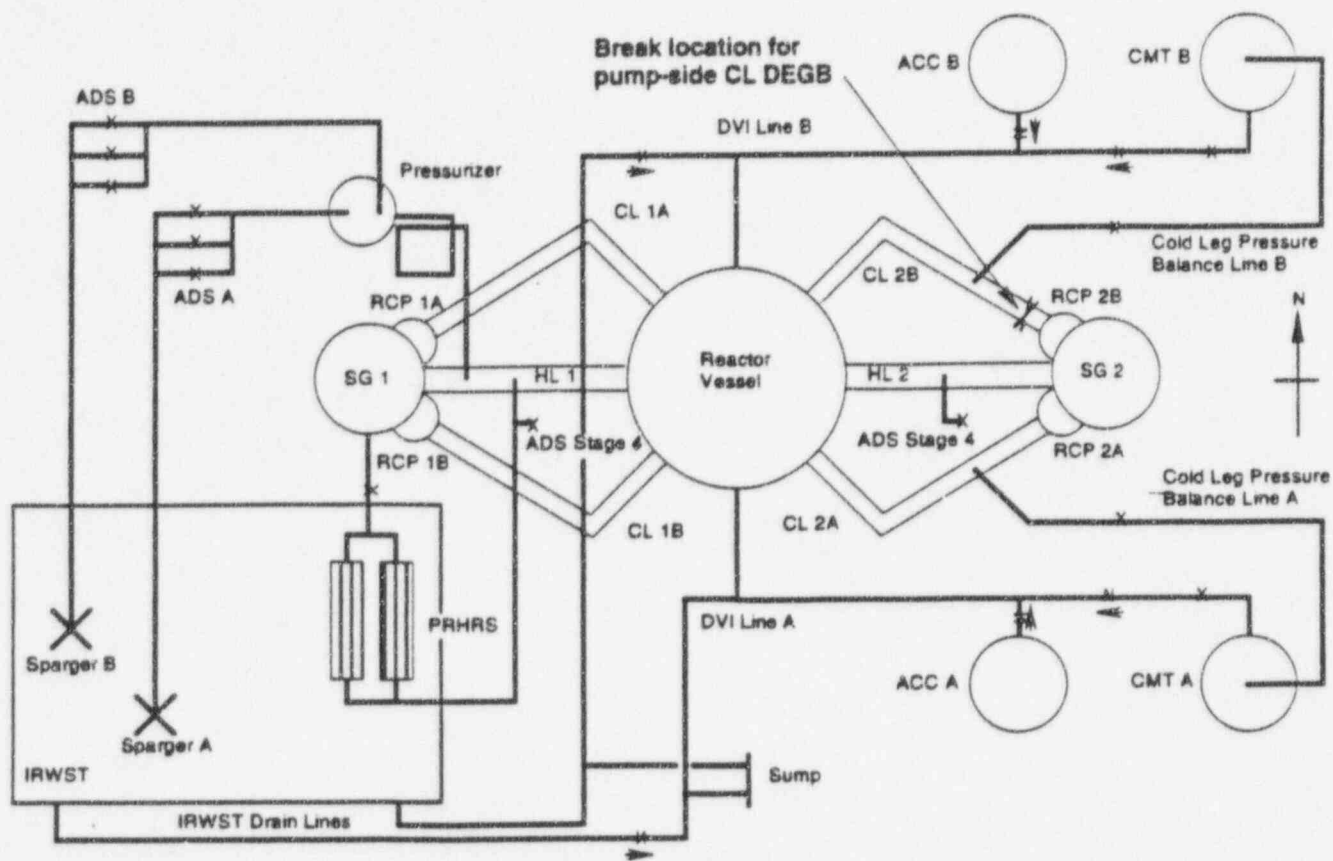


Fig. 3. Schematic of AP600 reactor coolant system and passive safety systems.

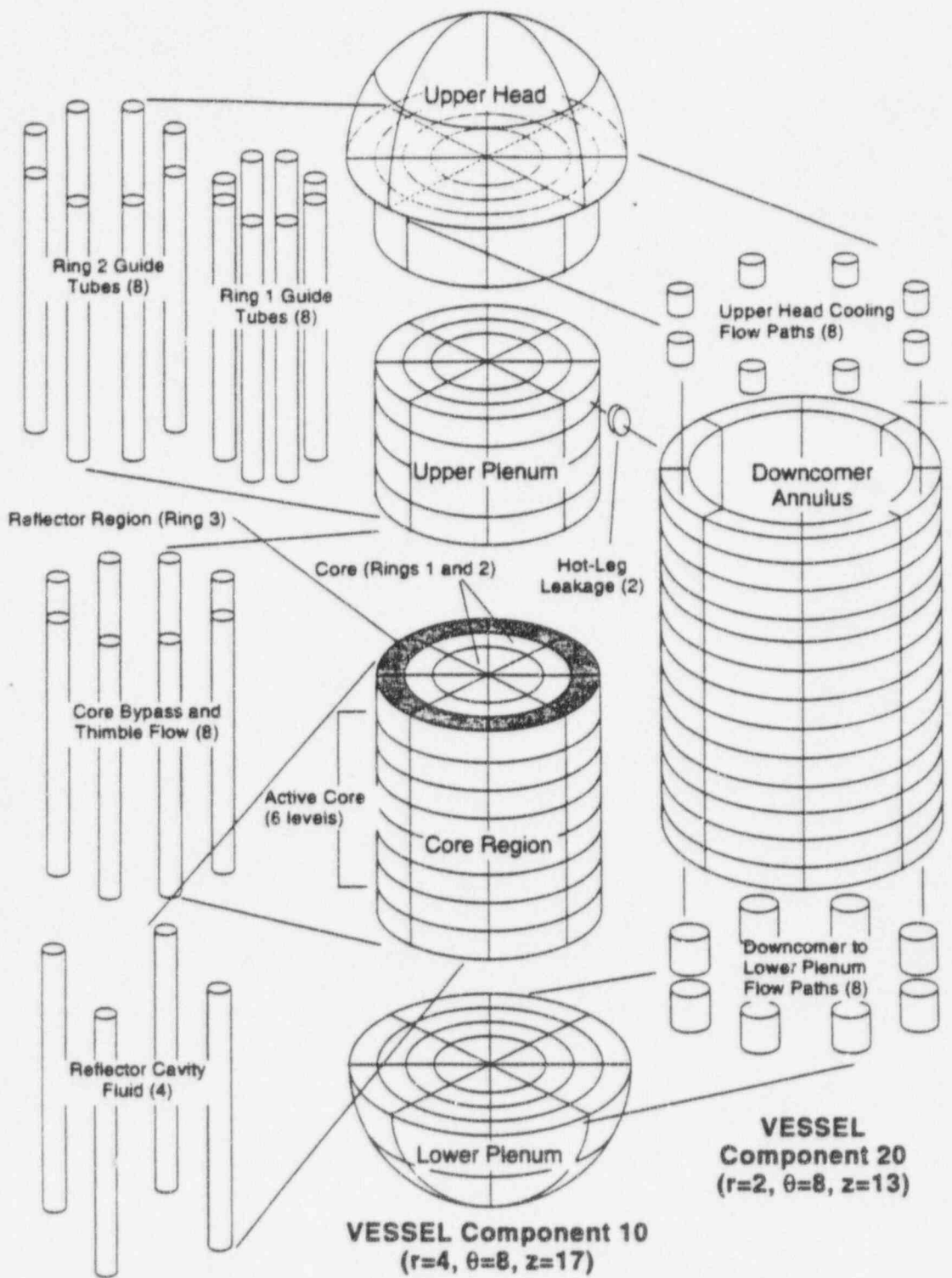


Fig. 4. Isometric view of reactor vessel model.

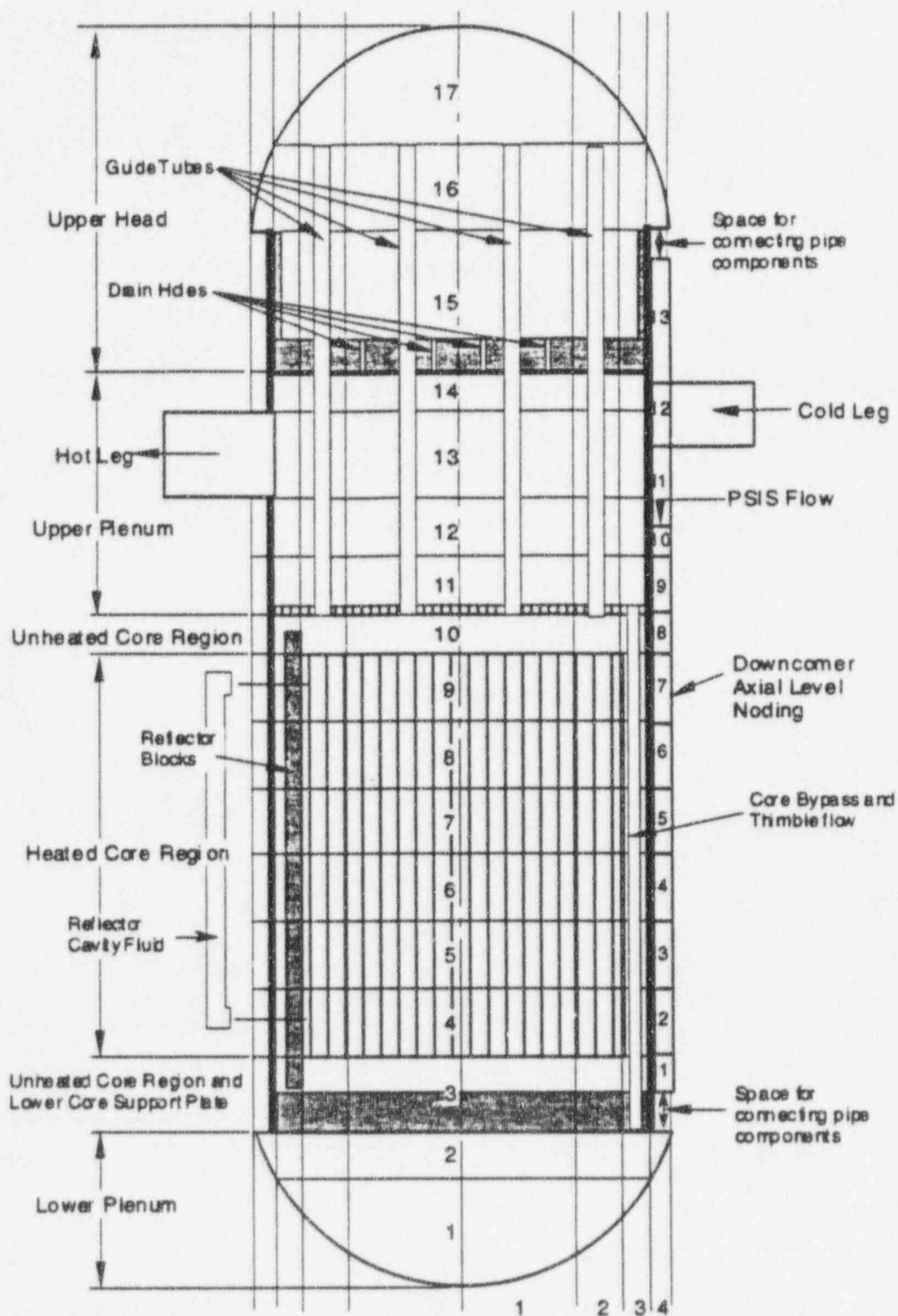


Fig. 5. Elevation view of reactor vessel model, including downcomer noding.

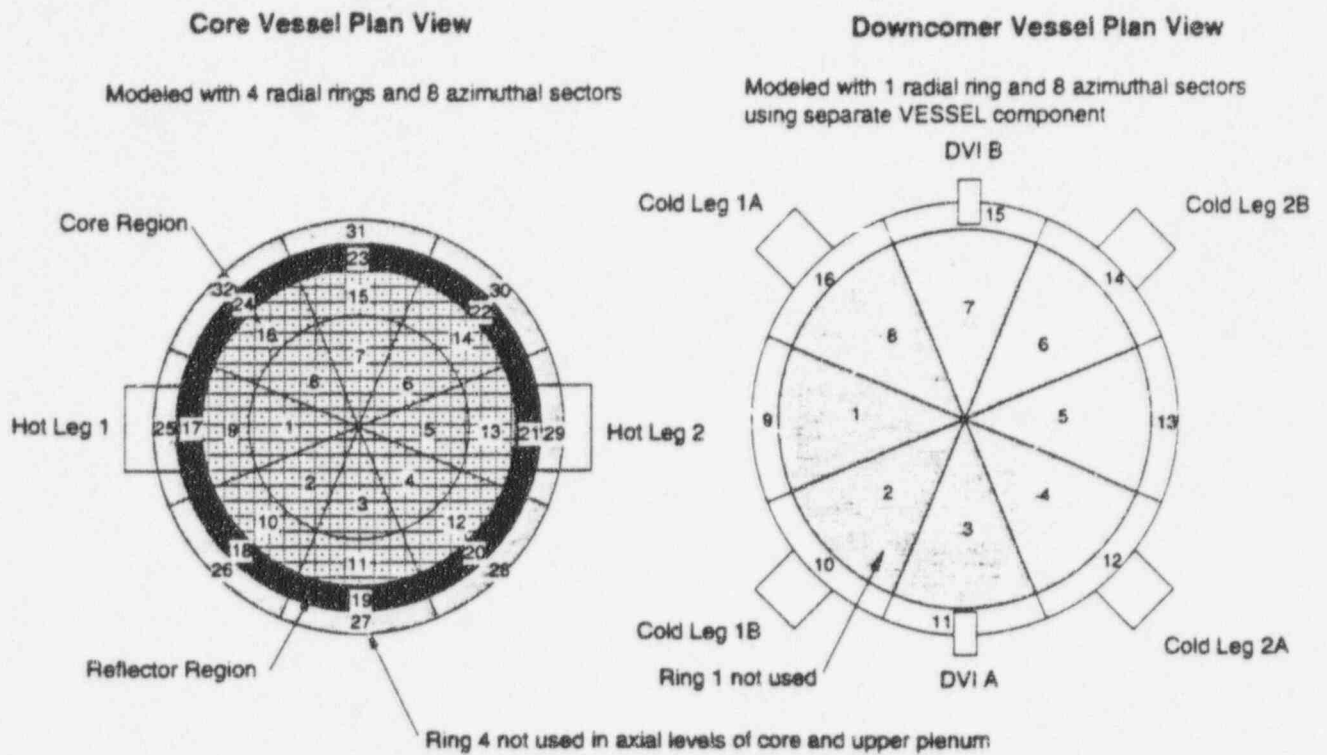


Fig. 6. Plan views of reactor vessel model.

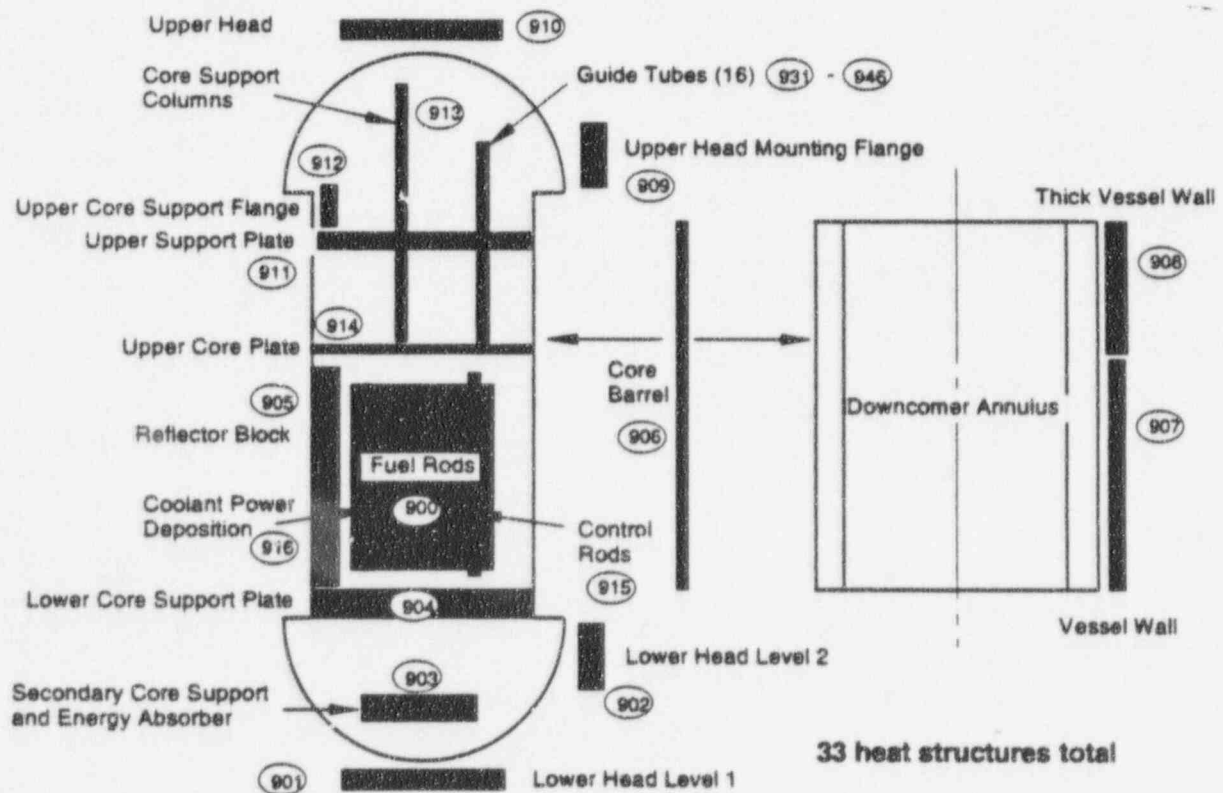


Fig. 7. Reactor vessel heat structures.

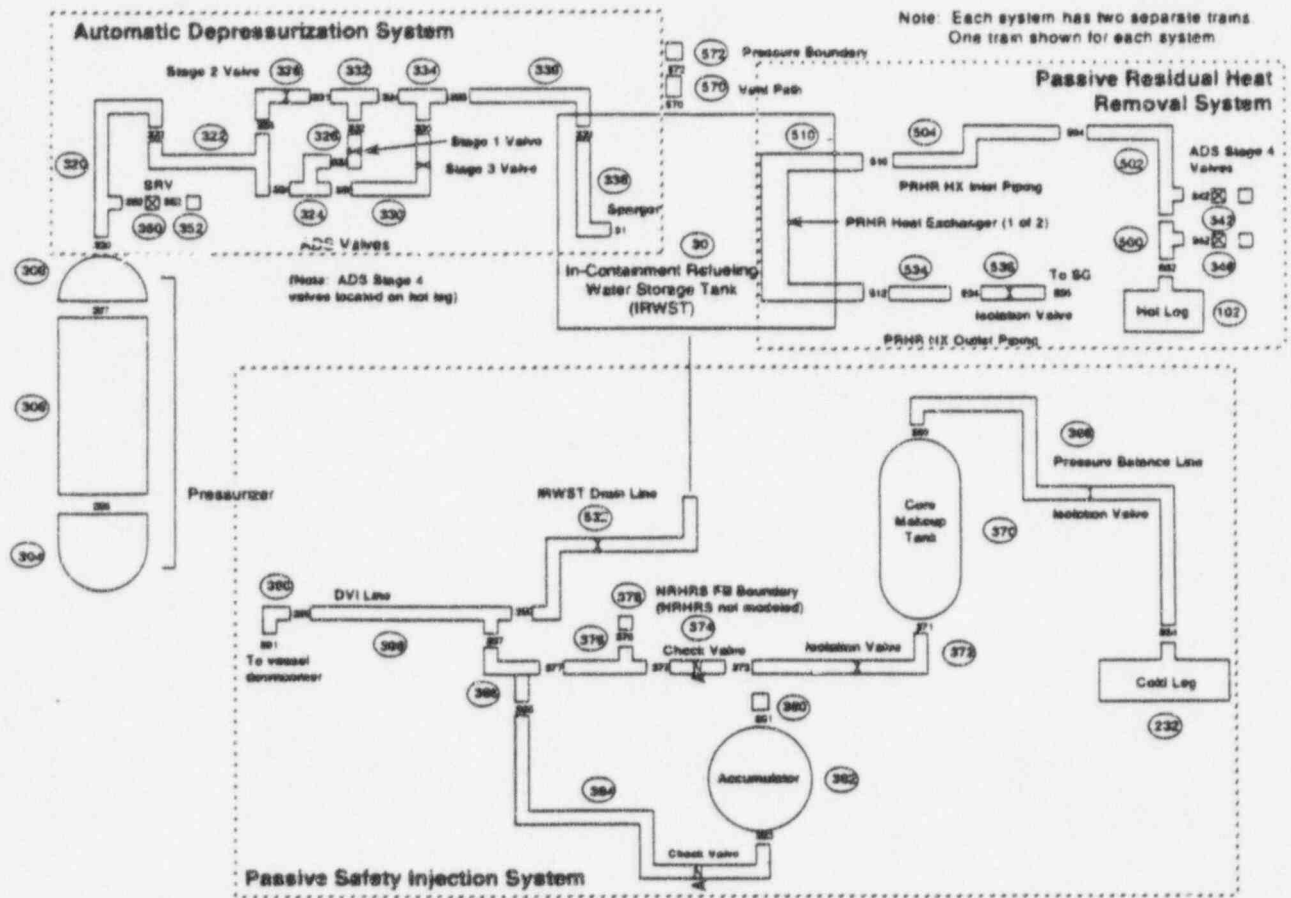


Fig. 10. Passive Safety Systems model overview.

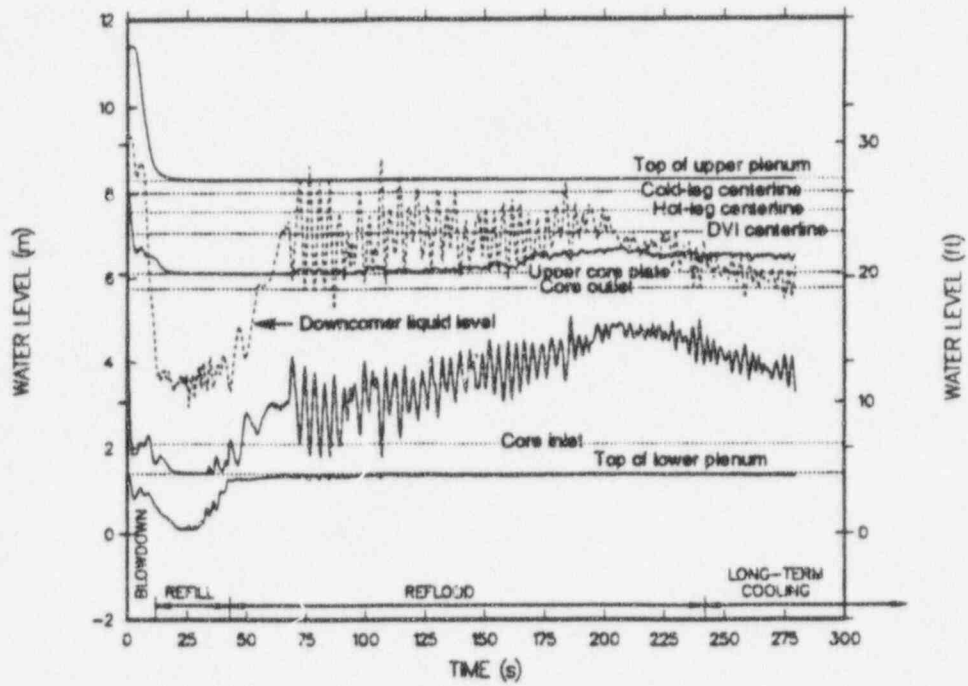


Fig. 11. Vessel-collapsed liquid levels.

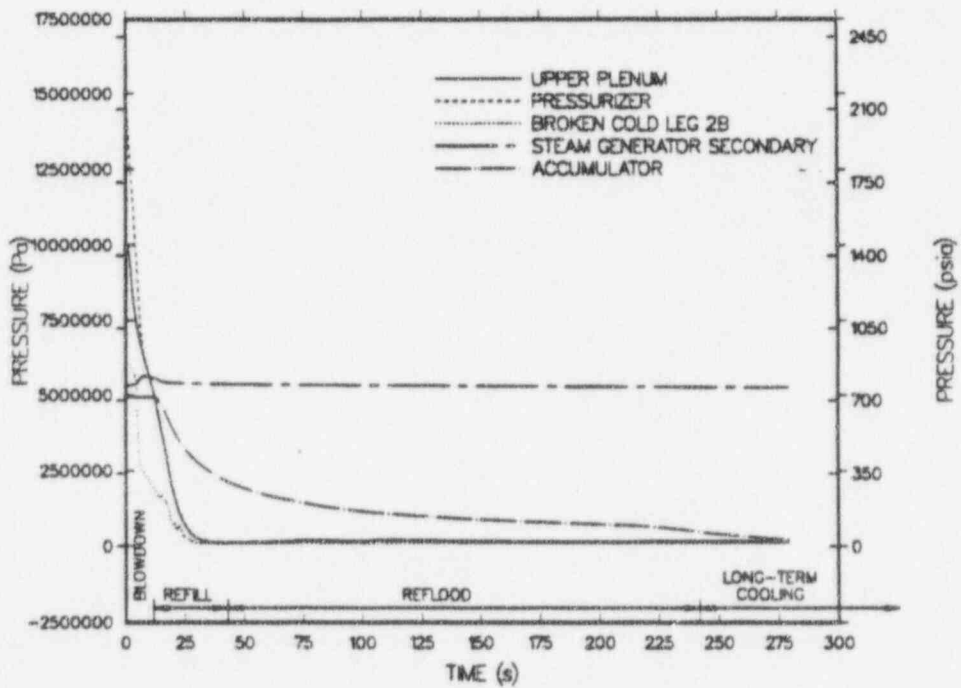


Fig. 12. System pressures.

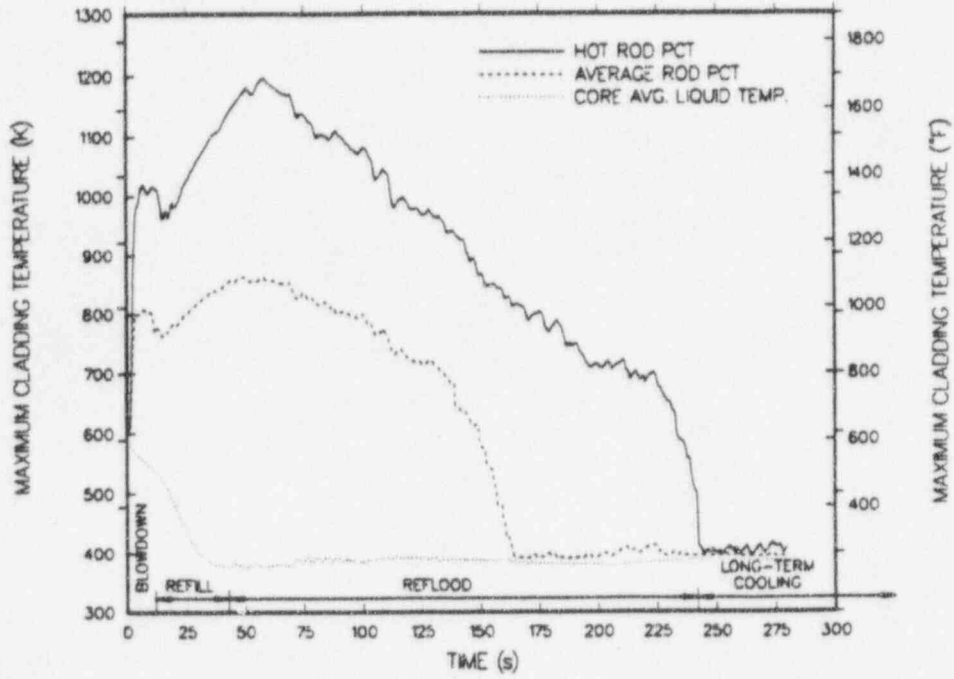


Fig. 13. Fuel-rod maximum cladding temperatures.

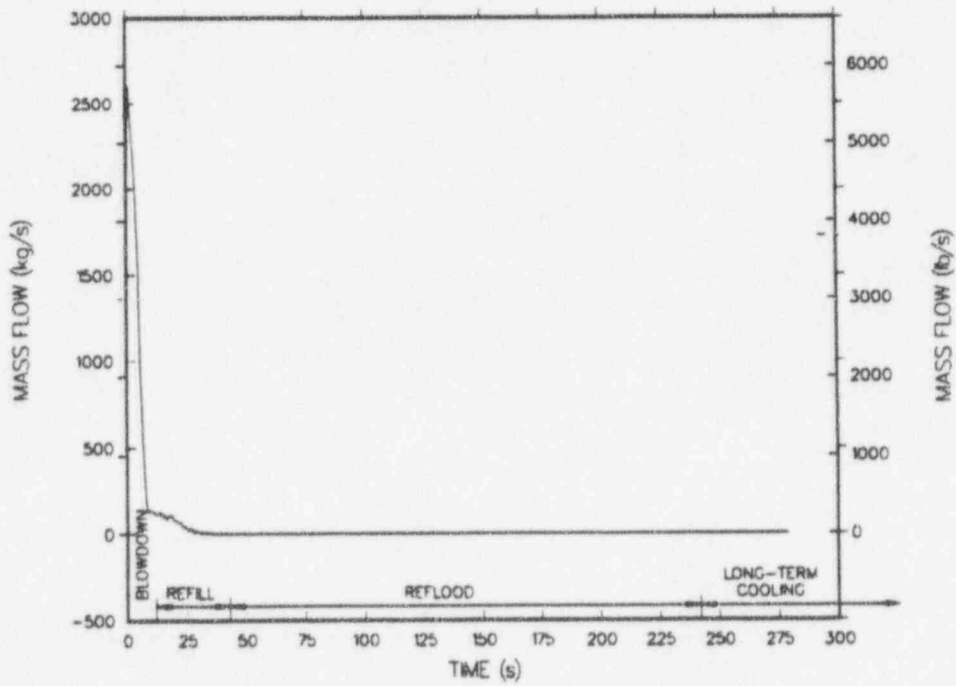


Fig. 14. Pressurizer mass flow.

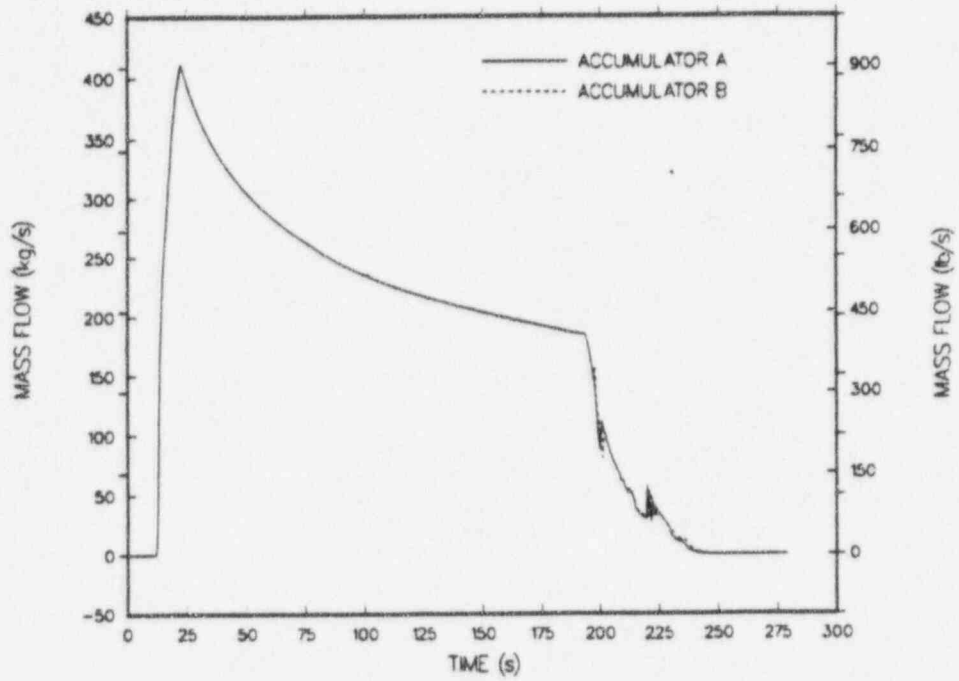


Fig. 15. Accumulator mass flows.

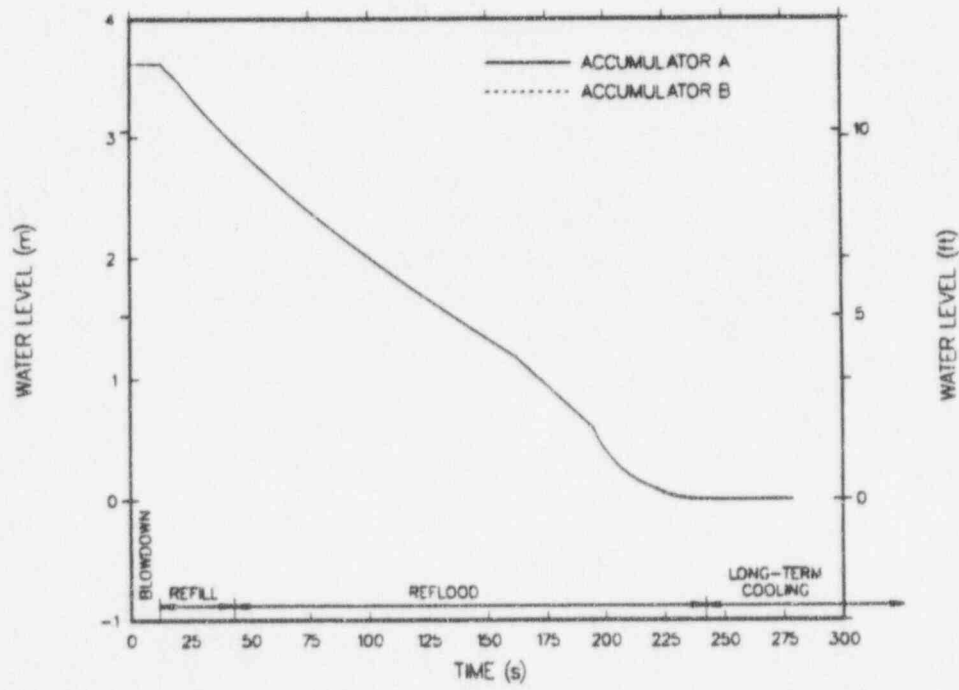


Fig. 16. Accumulator liquid level.

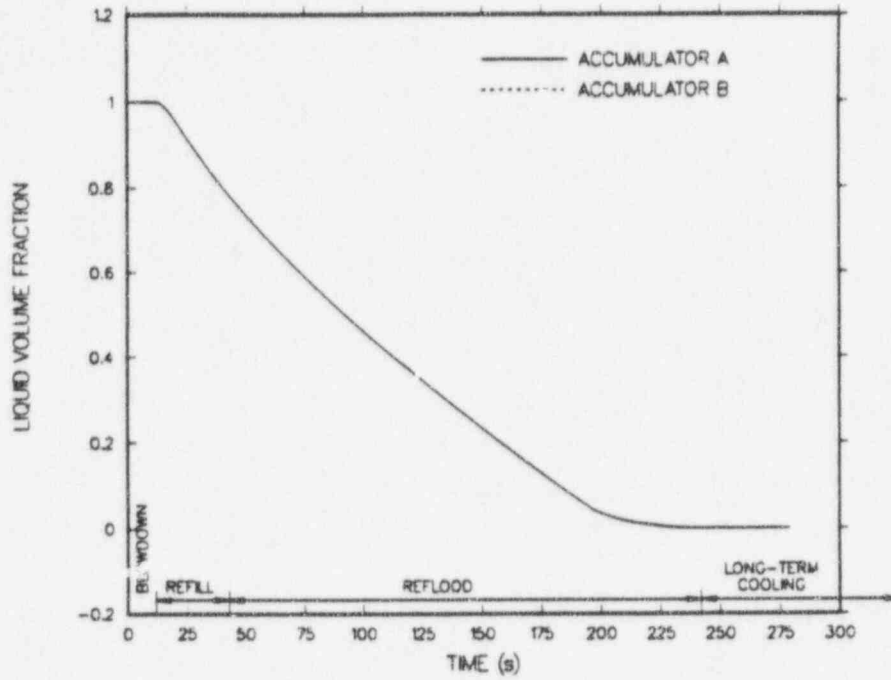


Fig. 17. Accumulator liquid volume fraction.

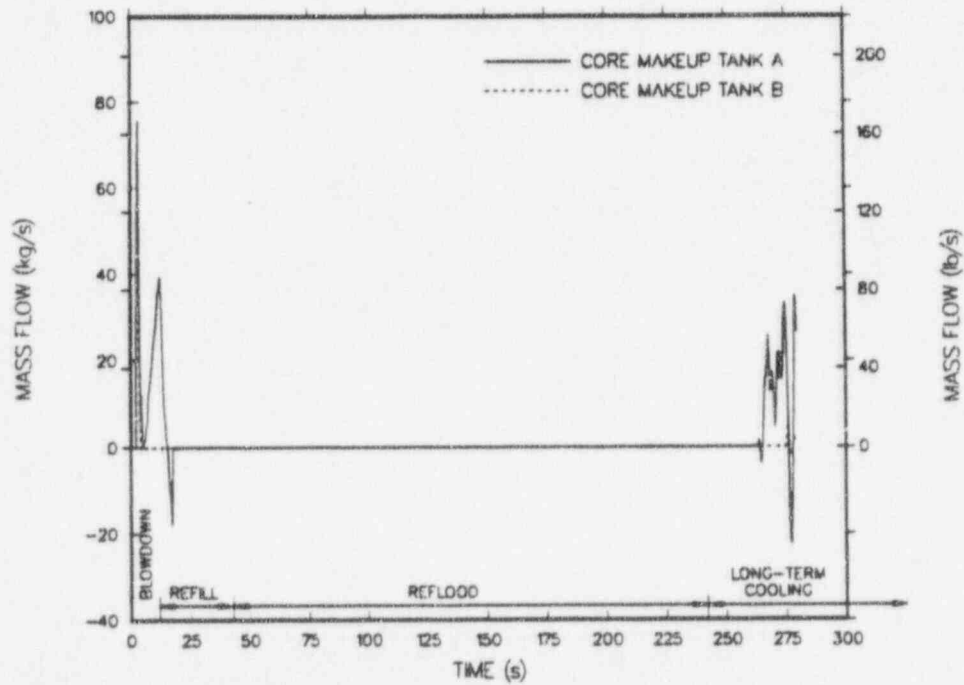


Fig. 18. Core makeup tank mass flows.

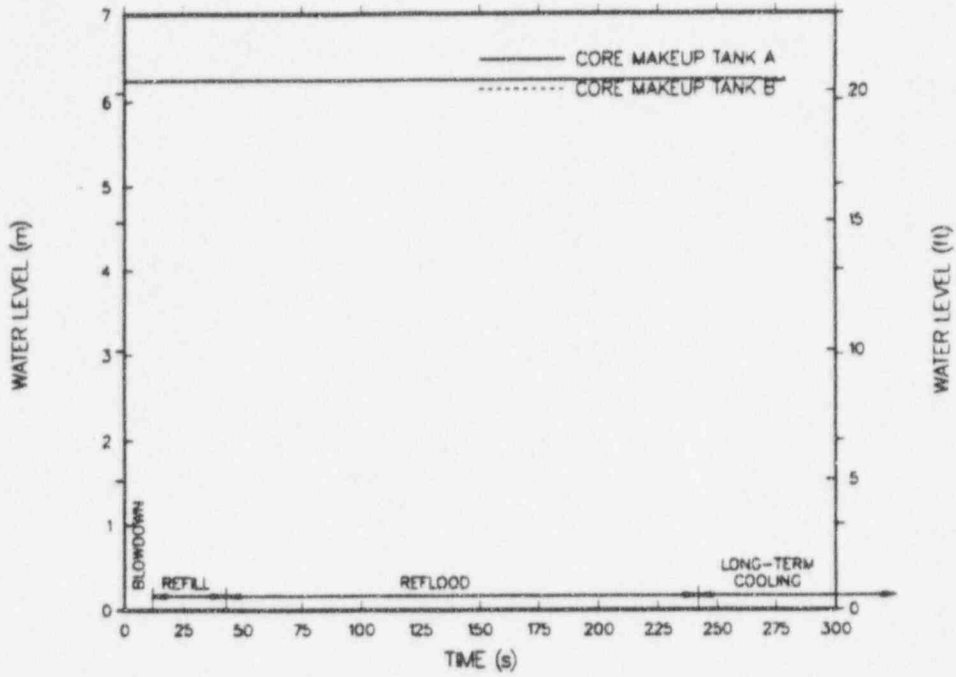


Fig. 19. Core makeup tank liquid level.

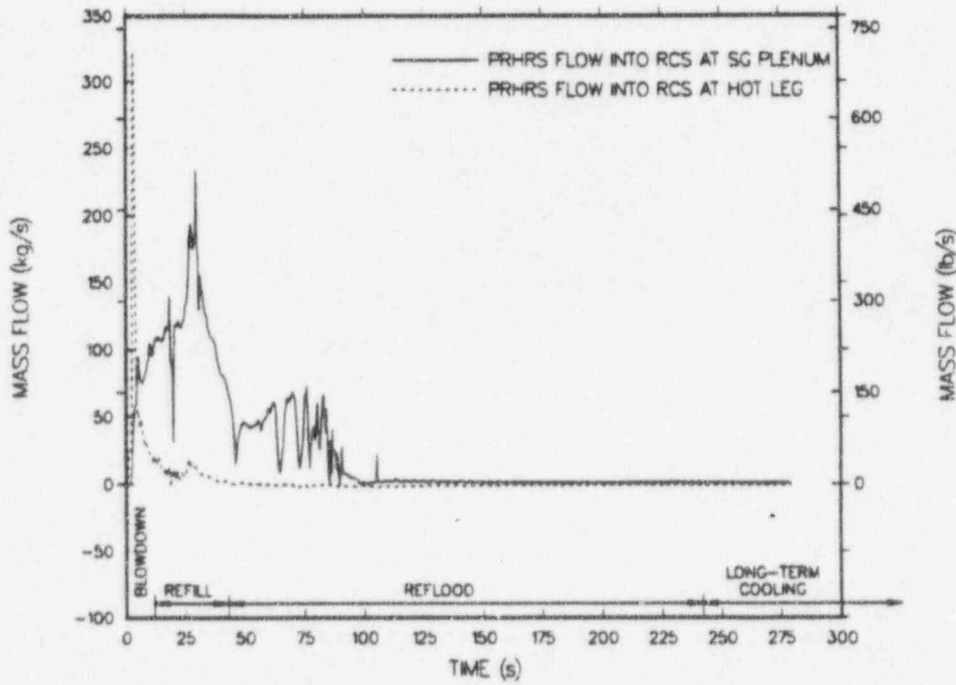


Fig. 20. PRHRS mass flows.

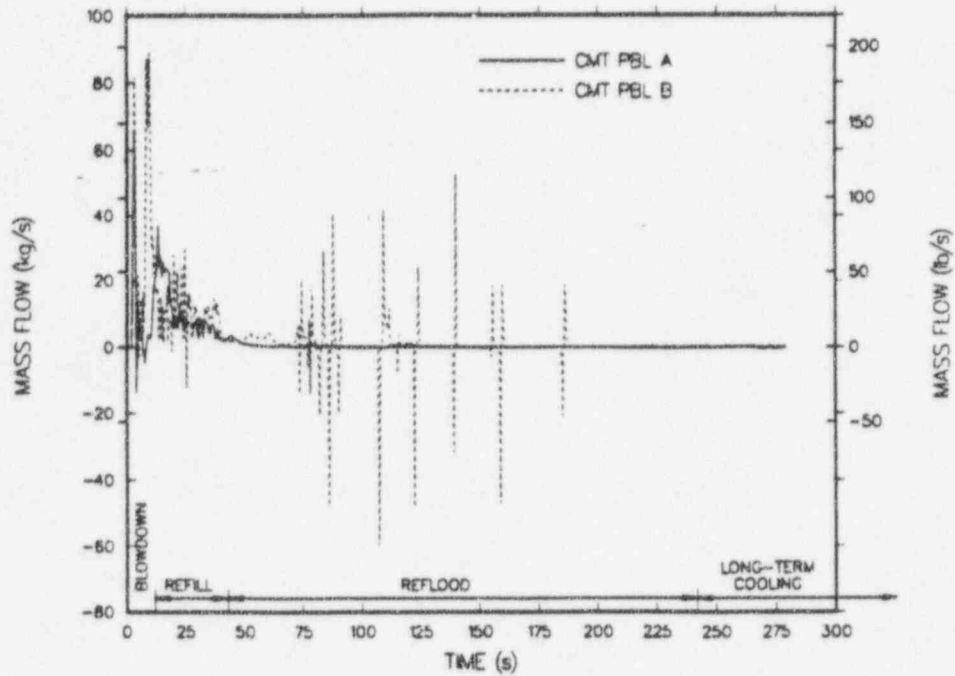


Fig. 21. Core makeup tank-pressure balance-line mass flows.

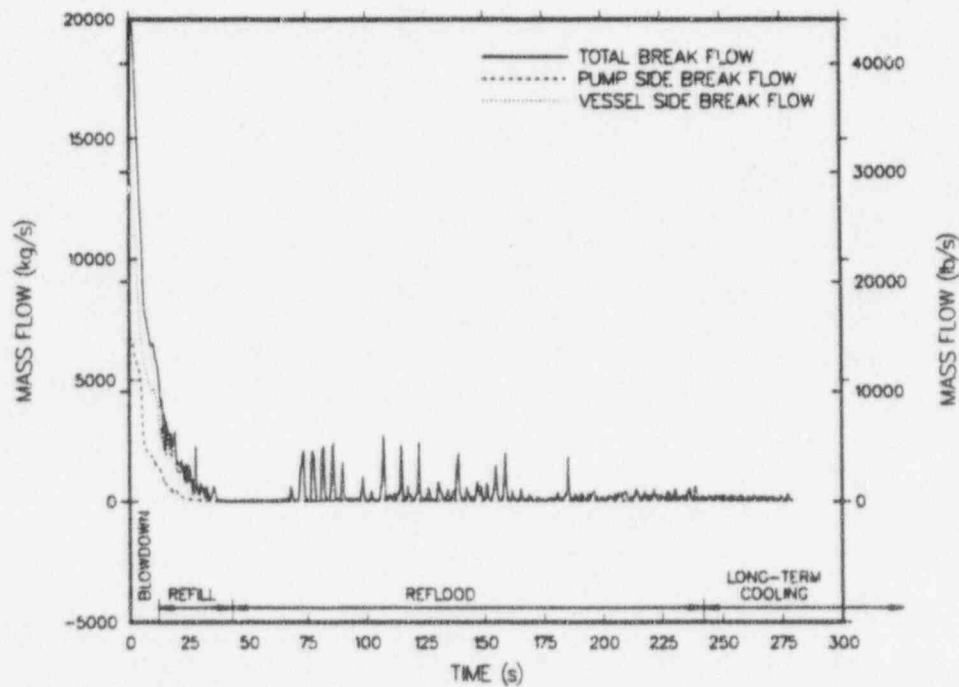


Fig. 22. Break mass flows.

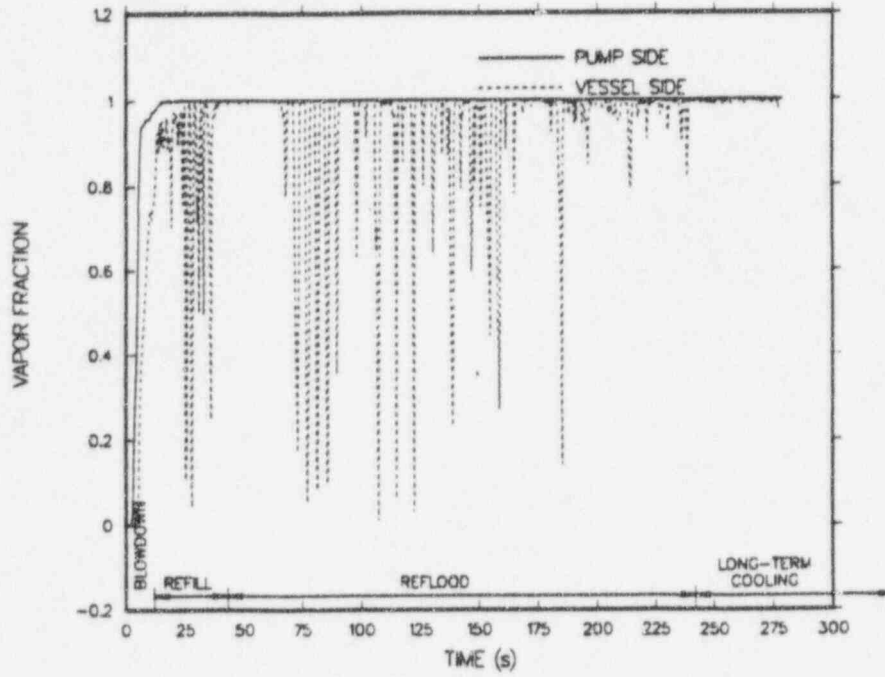


Fig. 23. Break exit voiding.

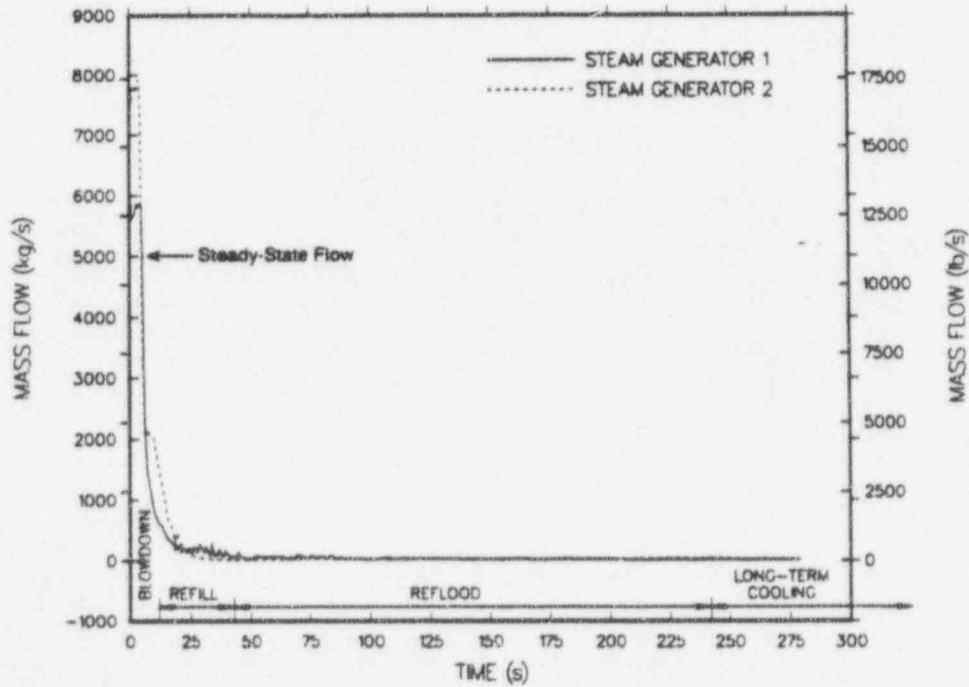


Fig. 24. Steam-generator primary-outlet mass flows.

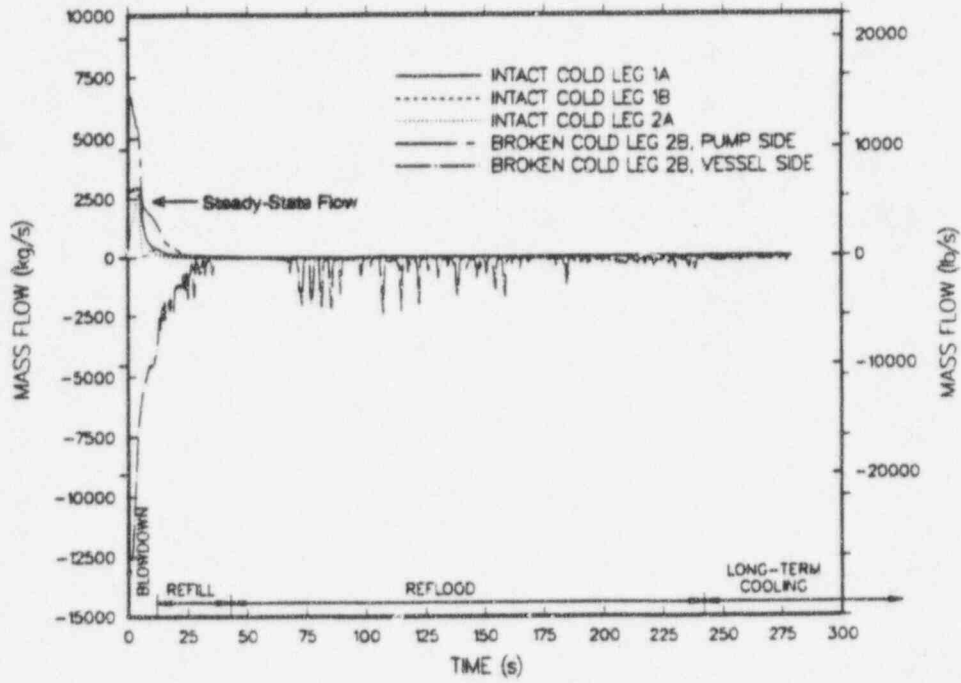


Fig. 25. Cold-leg mass flows.

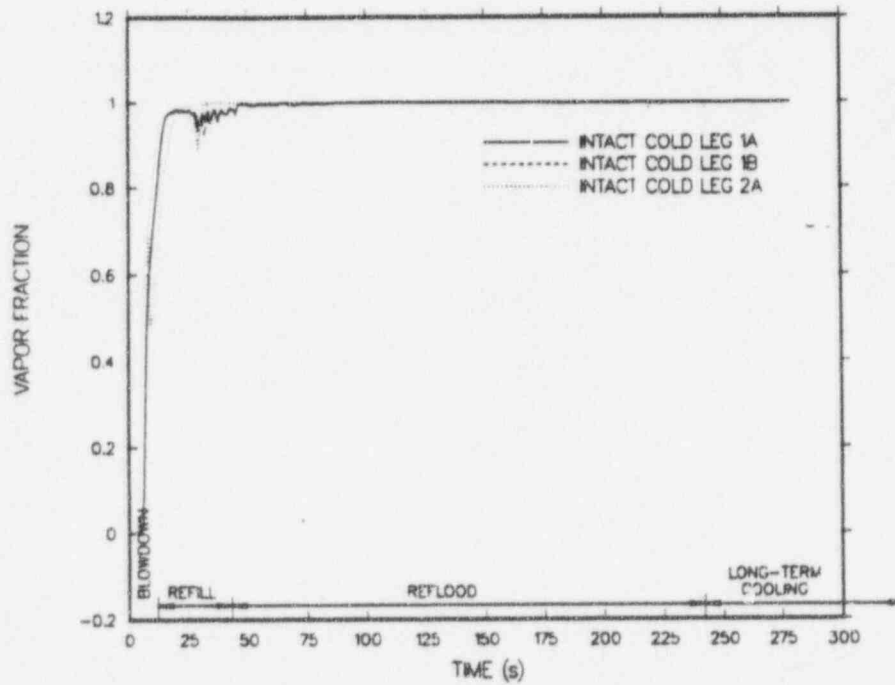


Fig. 26. Intact cold-leg voiding.

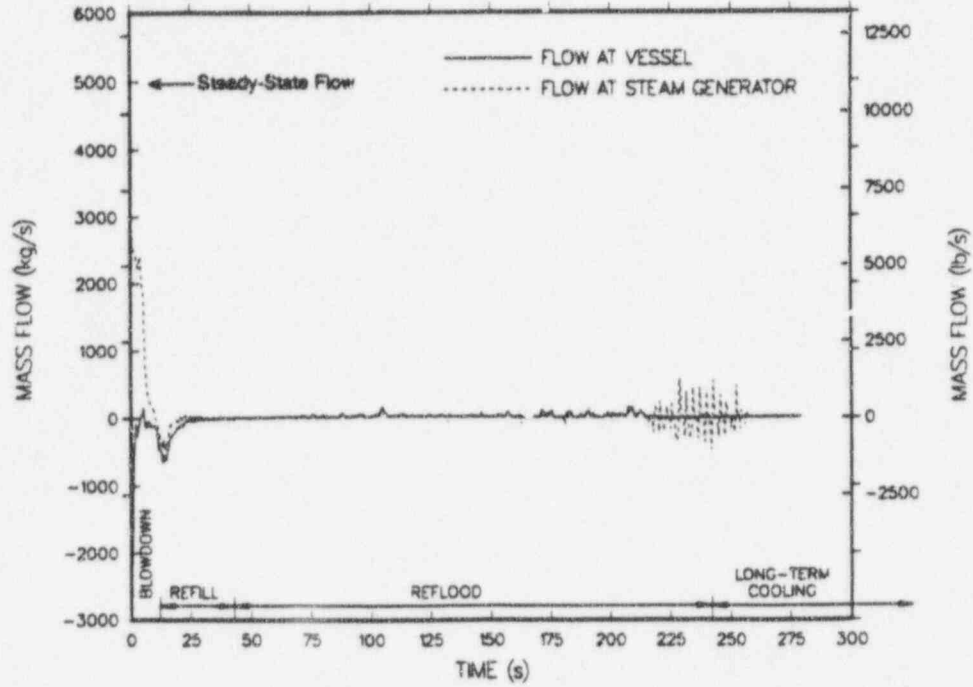


Fig. 27. Hot-leg 1 mass flows.

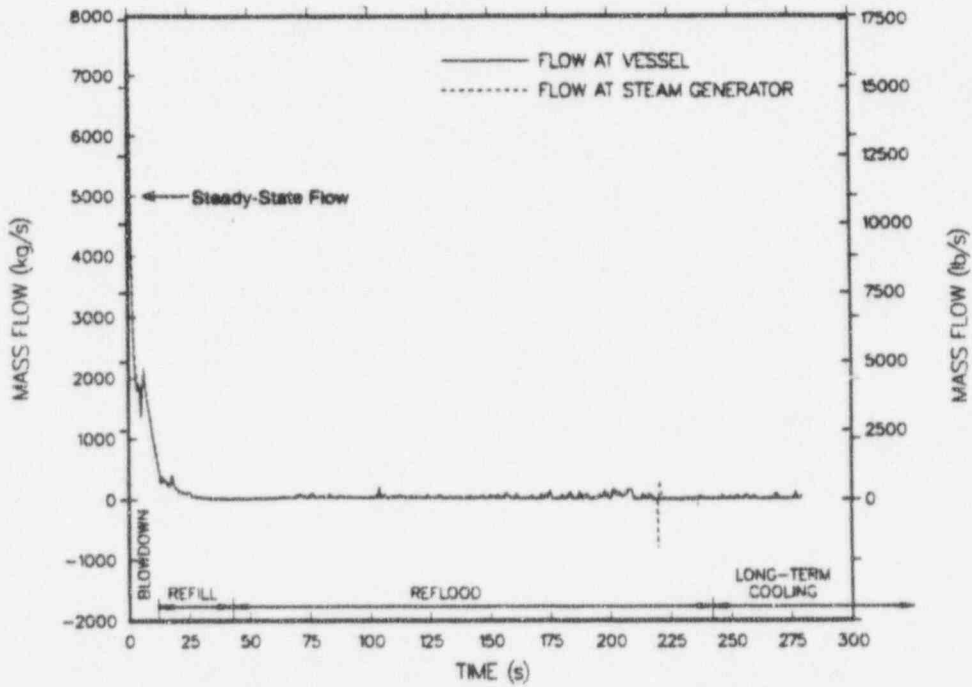


Fig. 28. Hot-leg 2 mass flows.

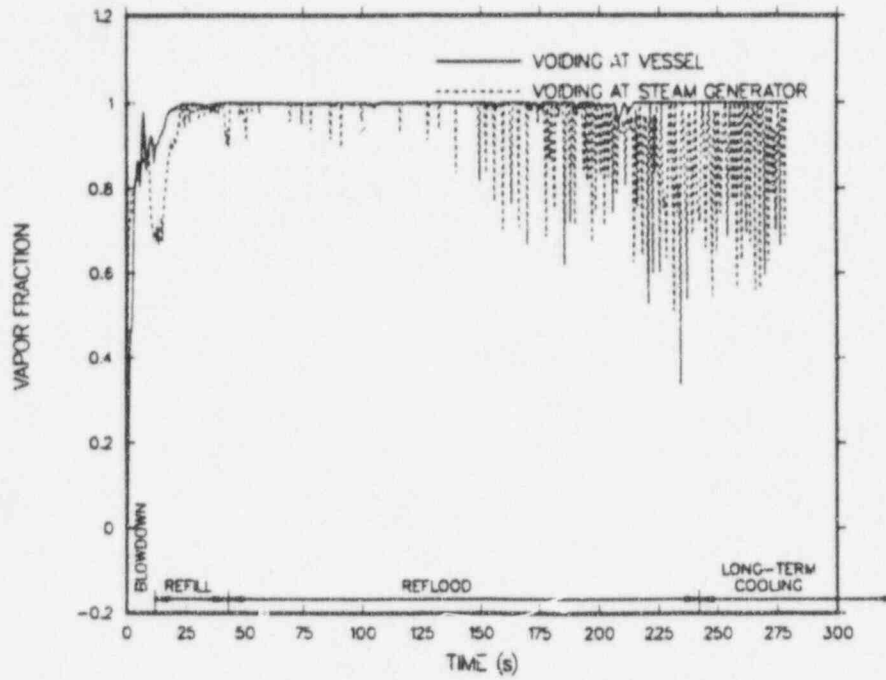


Fig. 29. Hot-leg 1 voiding.

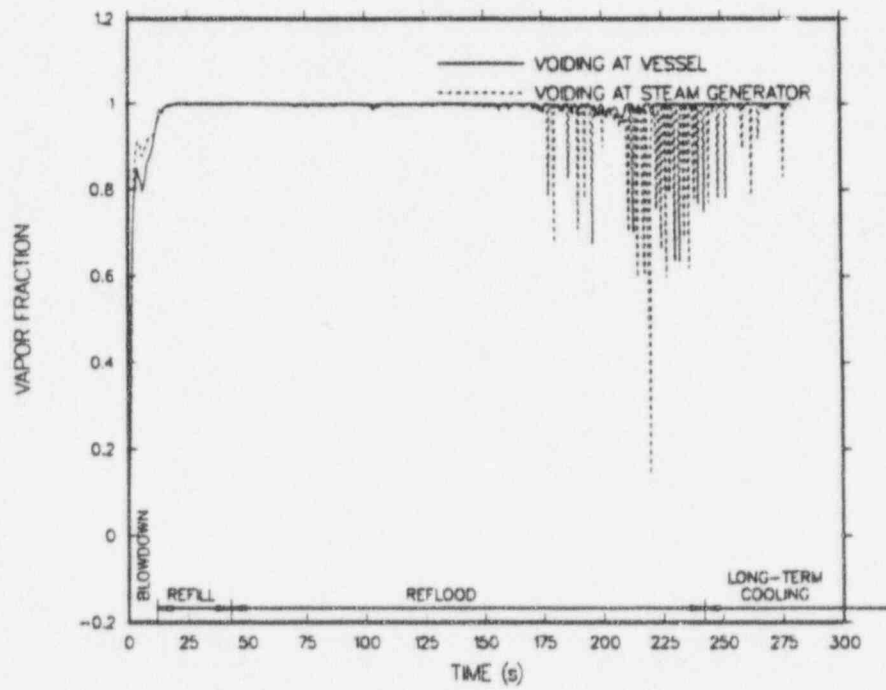


Fig. 30. Hot-leg 2 voiding.

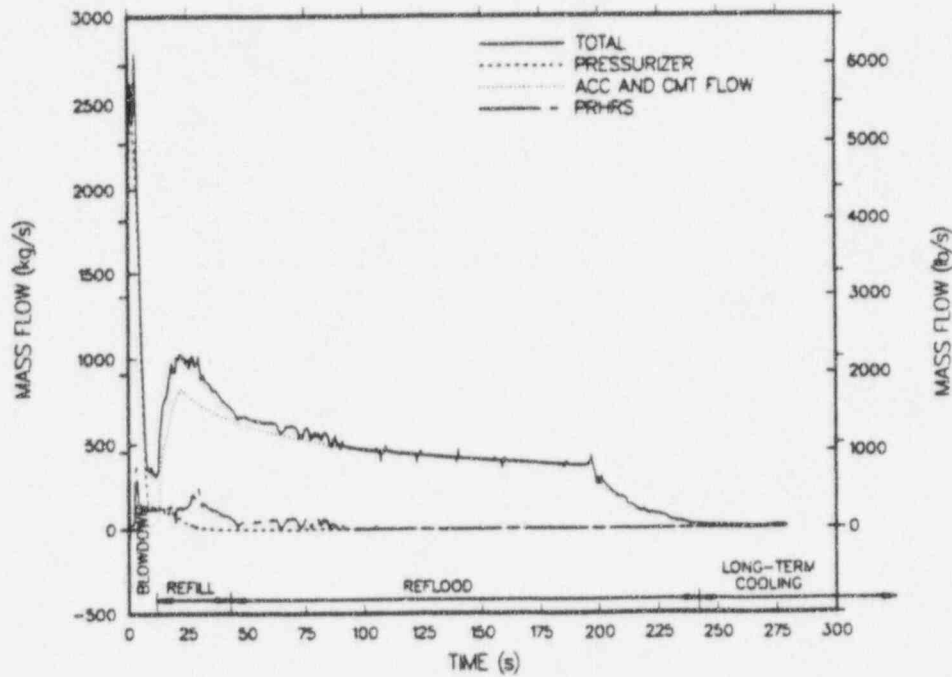


Fig. 31. Total makeup flow.

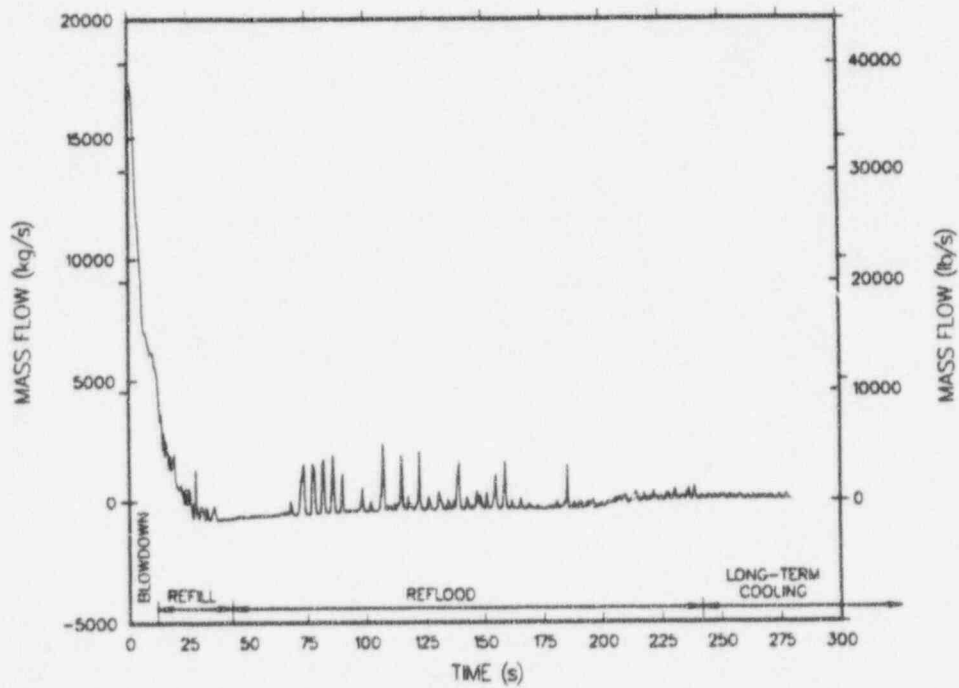


Fig. 32. Net-system mass-flow loss.

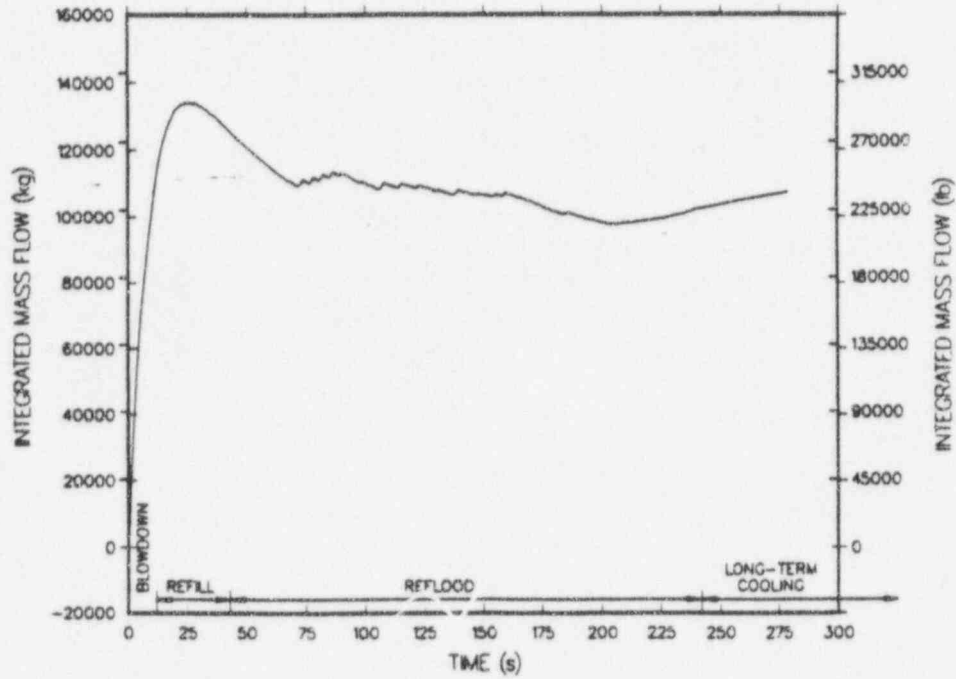


Fig. 33. Integrated net-system mass-flow loss.

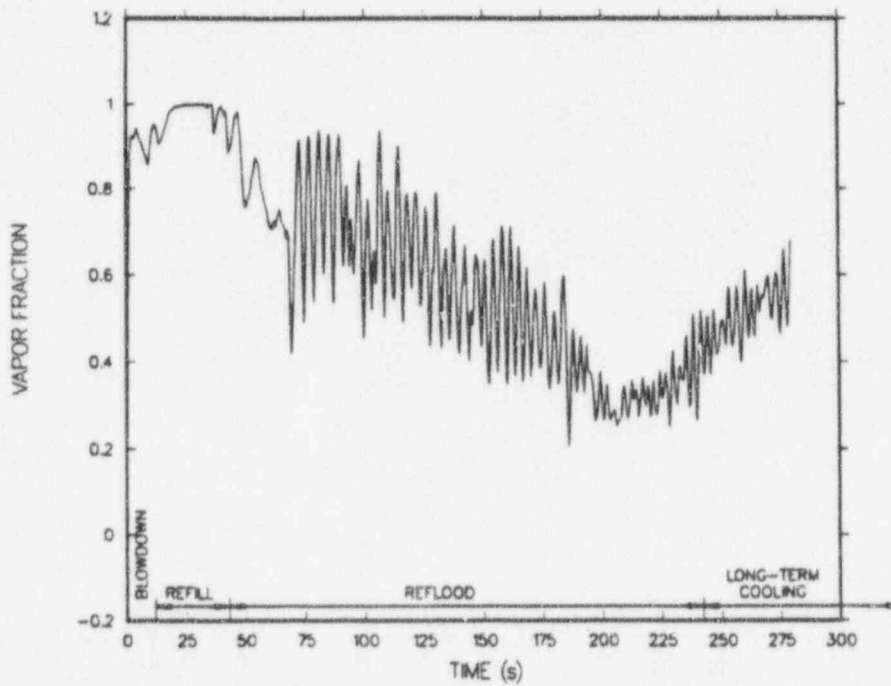


Fig. 34. Heated core-average vapor fraction.

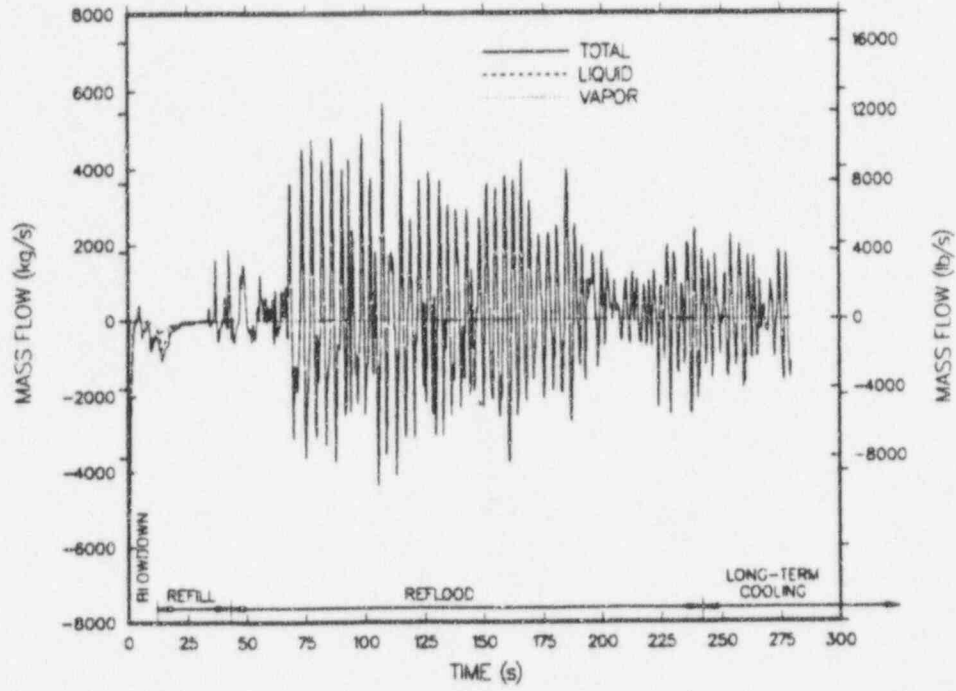


Fig. 35. Core-inlet mass flows.

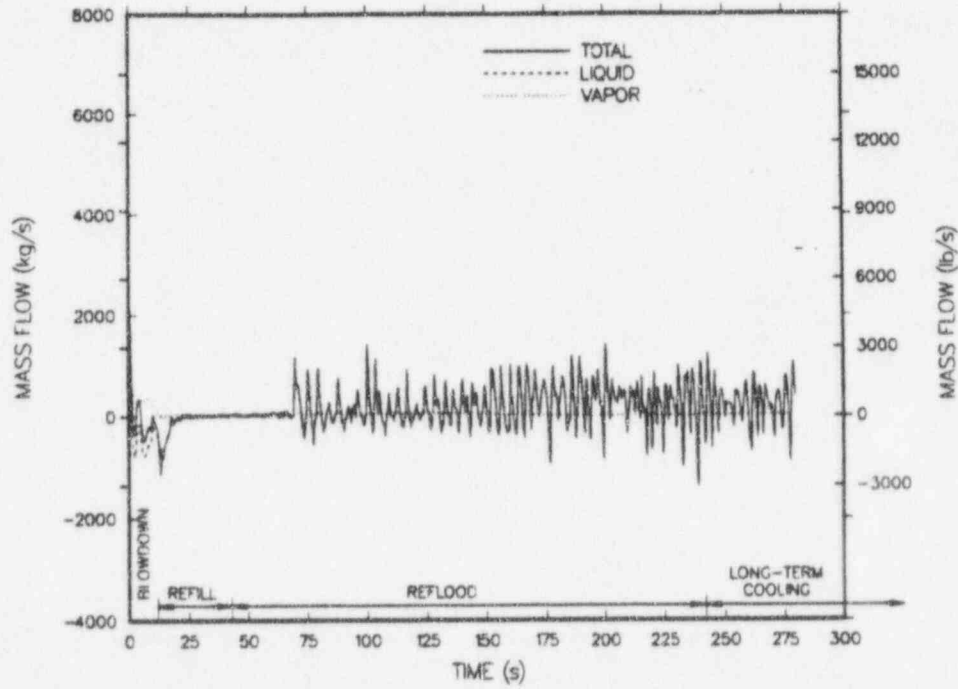


Fig. 36. Core-outlet mass flows.

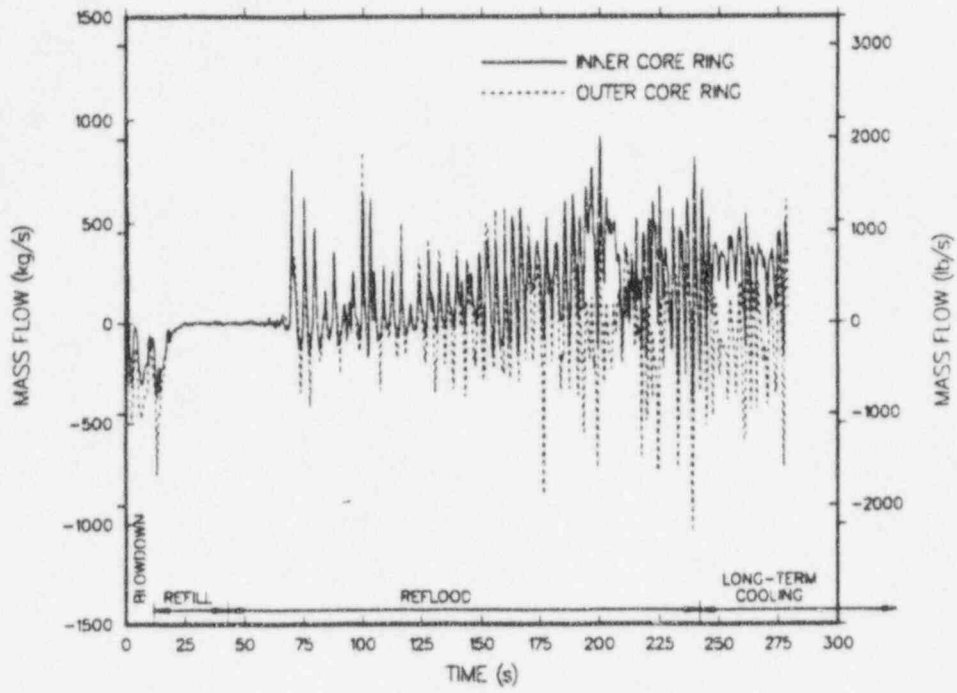


Fig. 37. Core-outlet liquid-mass flows.

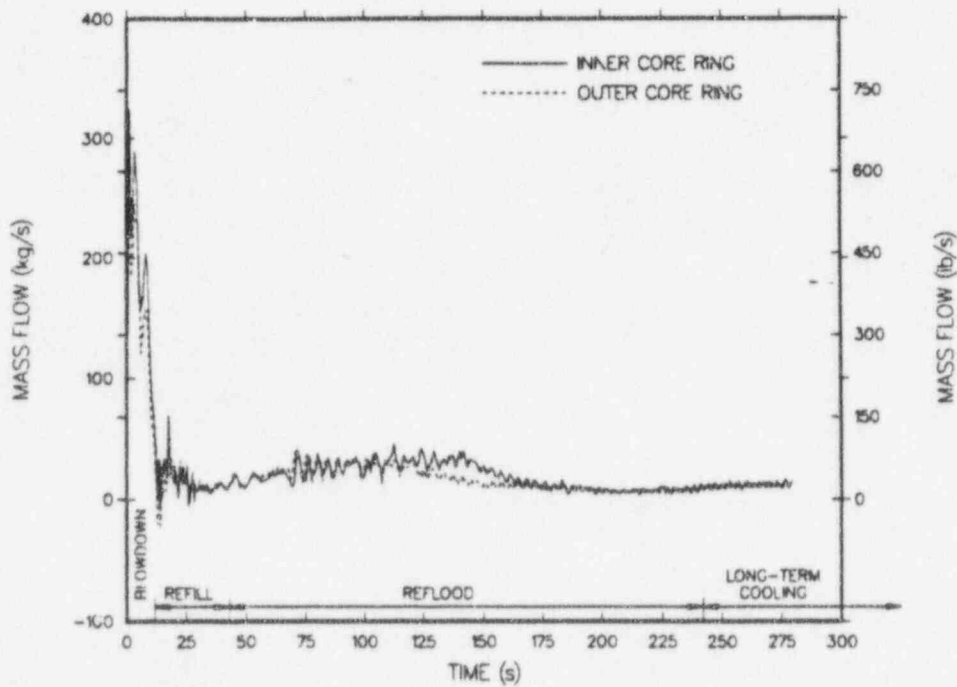


Fig. 38. Core-outlet vapor-mass flows.

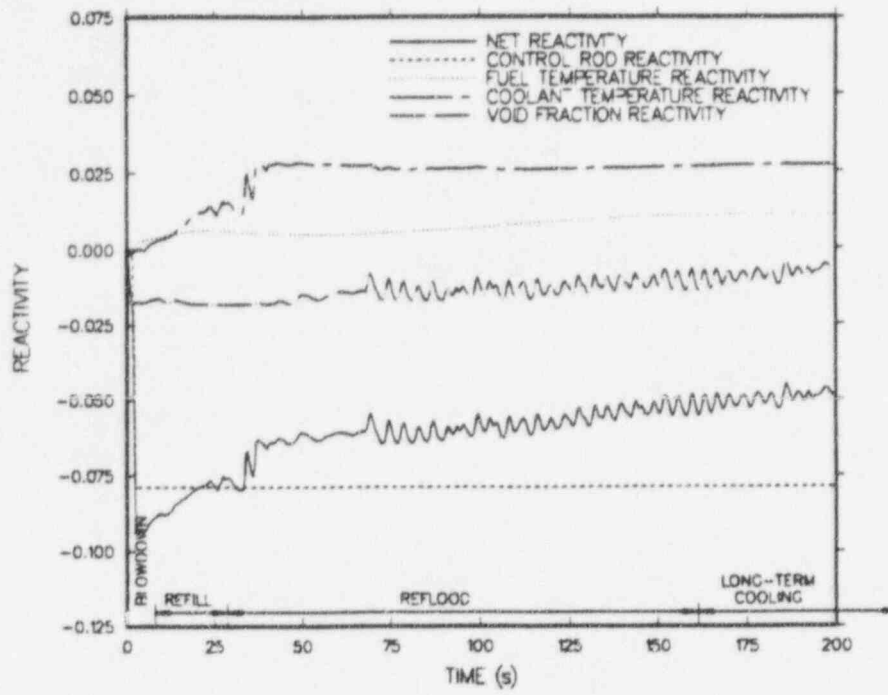


Fig. 39. Fuel-rod reactivities.

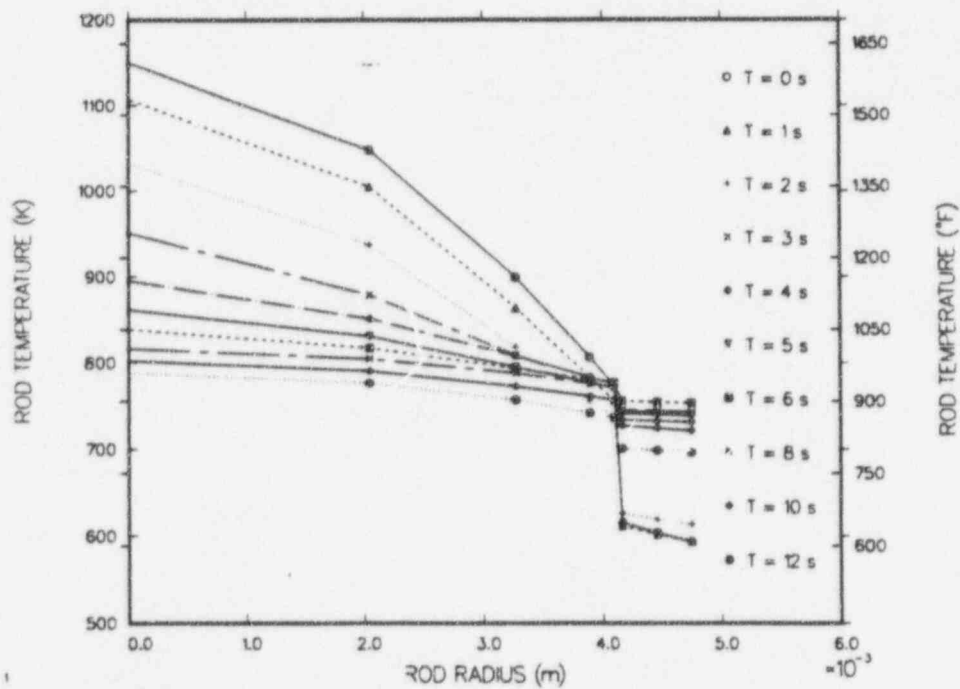


Fig. 40. Stored-energy distribution in fuel rod with time.

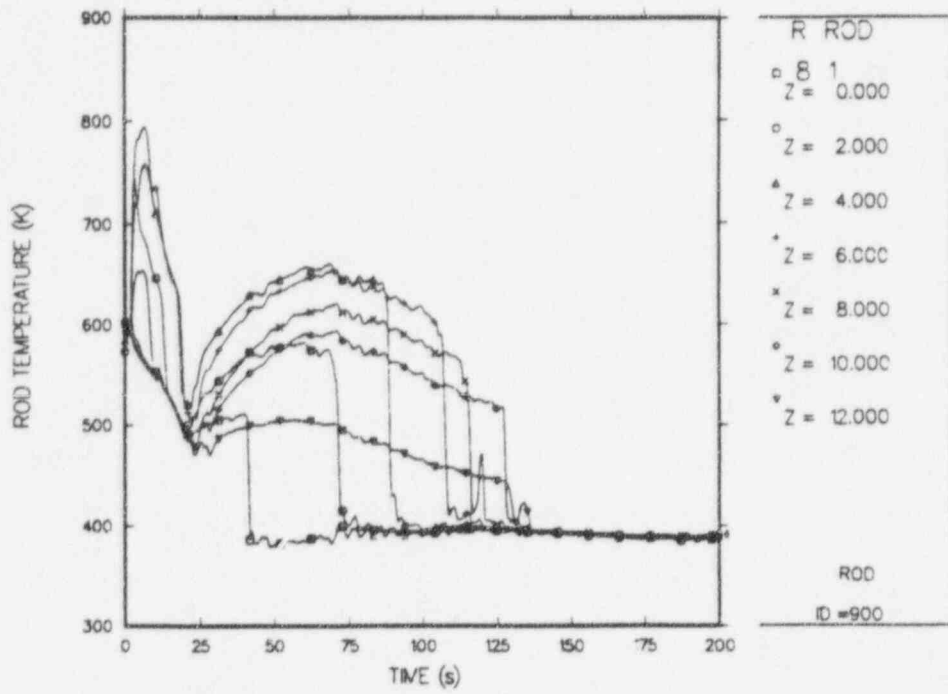


Fig. 41. Average-rod temperatures in cell 1 ($r = 1, \theta = 1$).

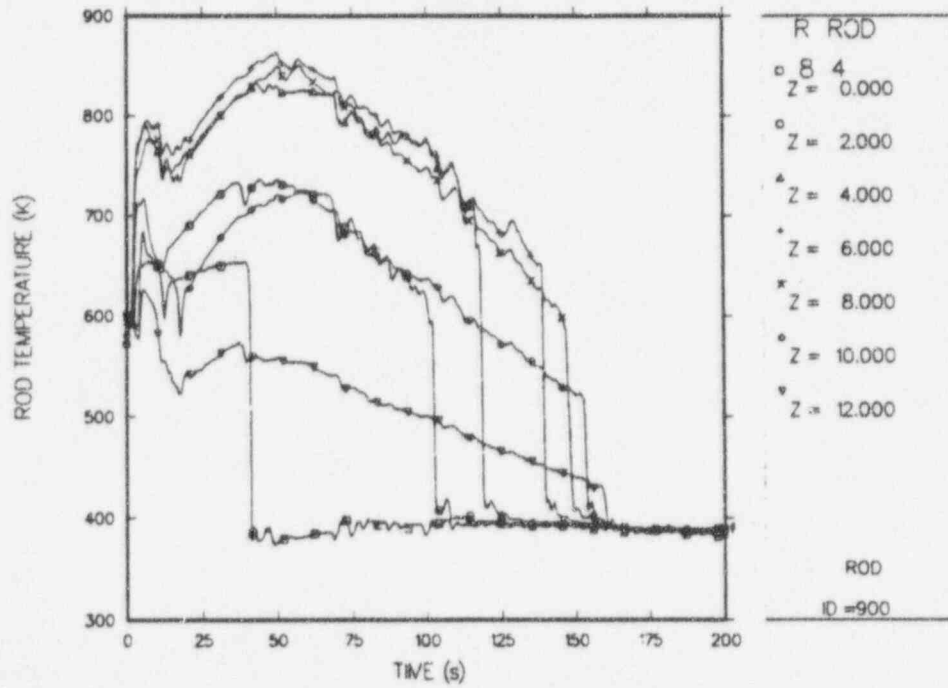


Fig. 42. Average-rod temperatures in cell 4 ($r = 1, \theta = 4$).

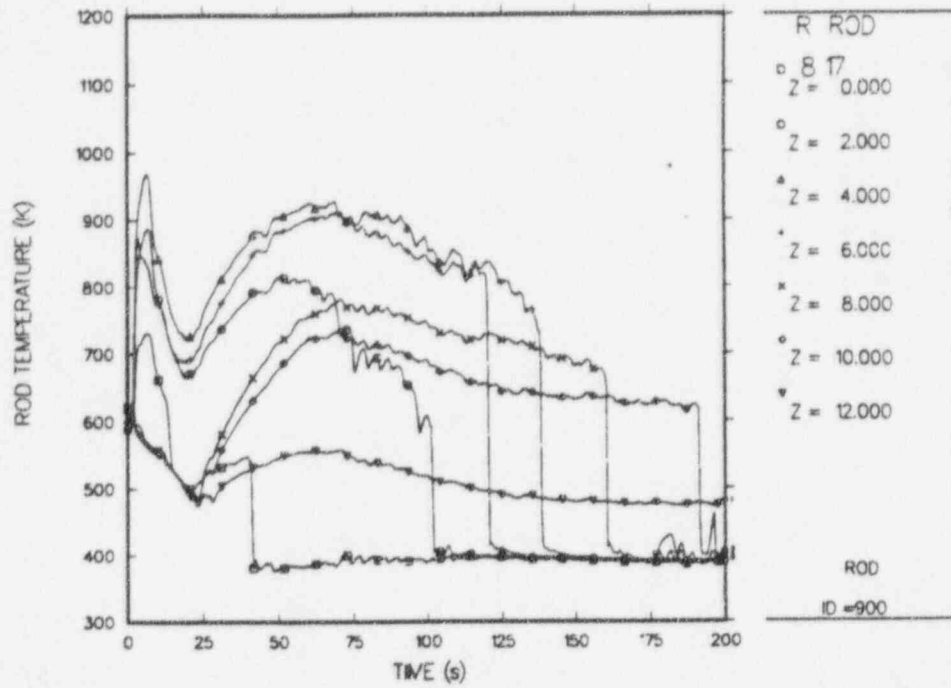


Fig. 43. Hot-rod temperatures in cell 1 ($r = 1, \theta = 1$).

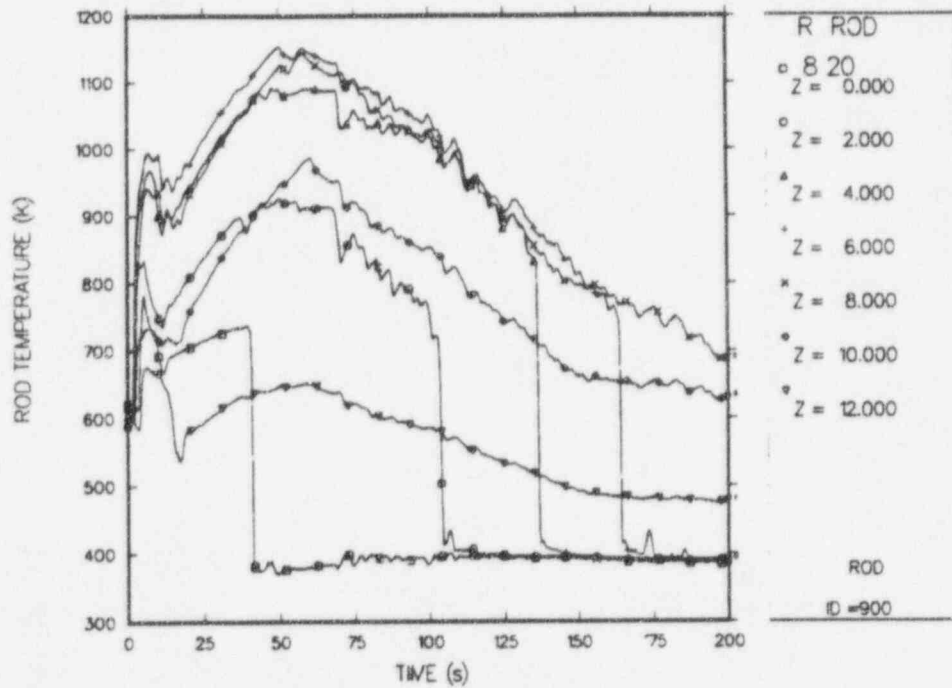


Fig. 44. Hot-rod temperatures in cell 4 ($r = 1, \theta = 4$).

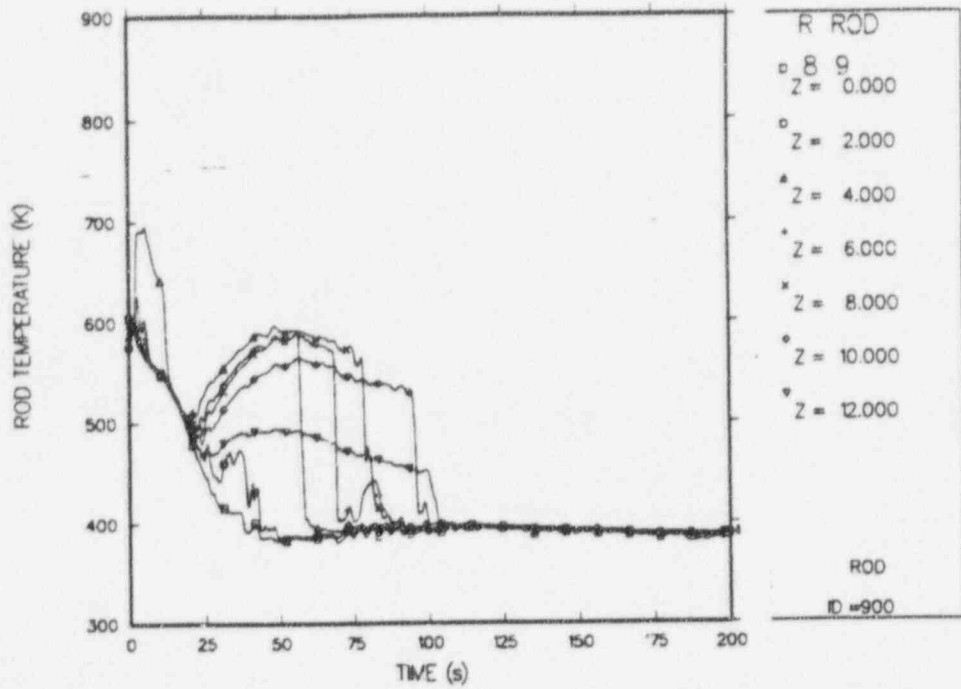


Fig. 45. Average-rod temperatures in cell 9 ($r = 2, \theta = 1$).

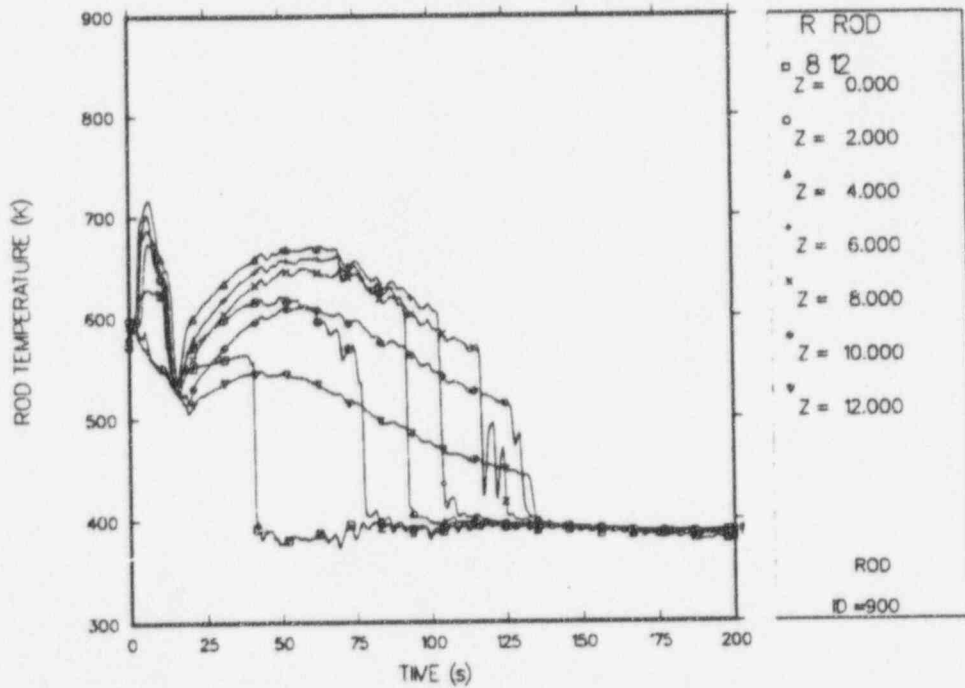


Fig. 46. Average-rod temperatures in cell 12 ($r = 2, \theta = 4$).

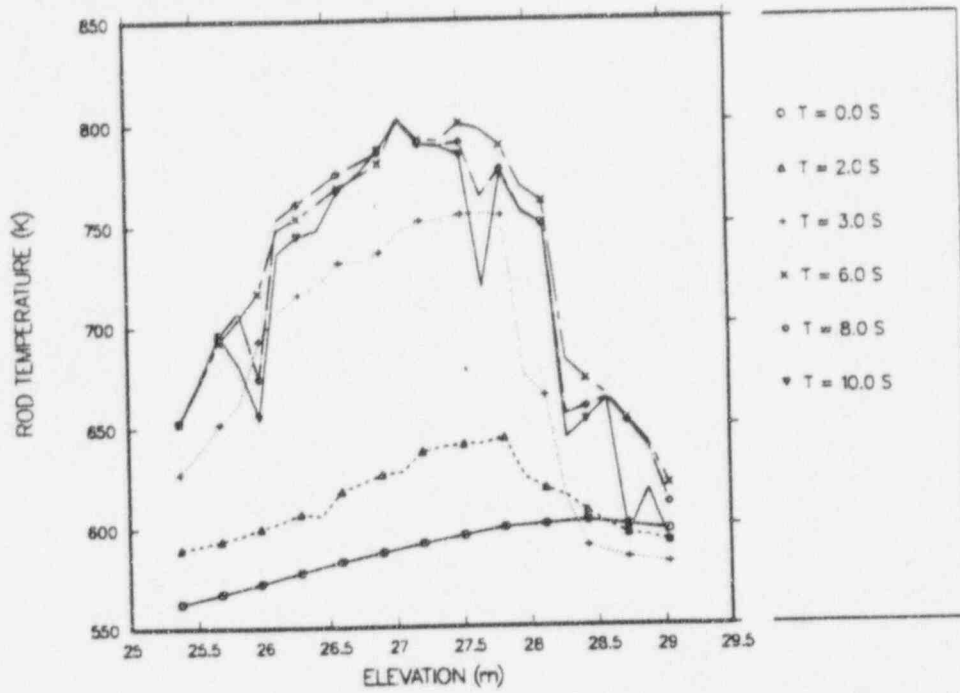


Fig. 47. Cell 4 average-rod temperatures vs rod elevation, 0 to 10 s.

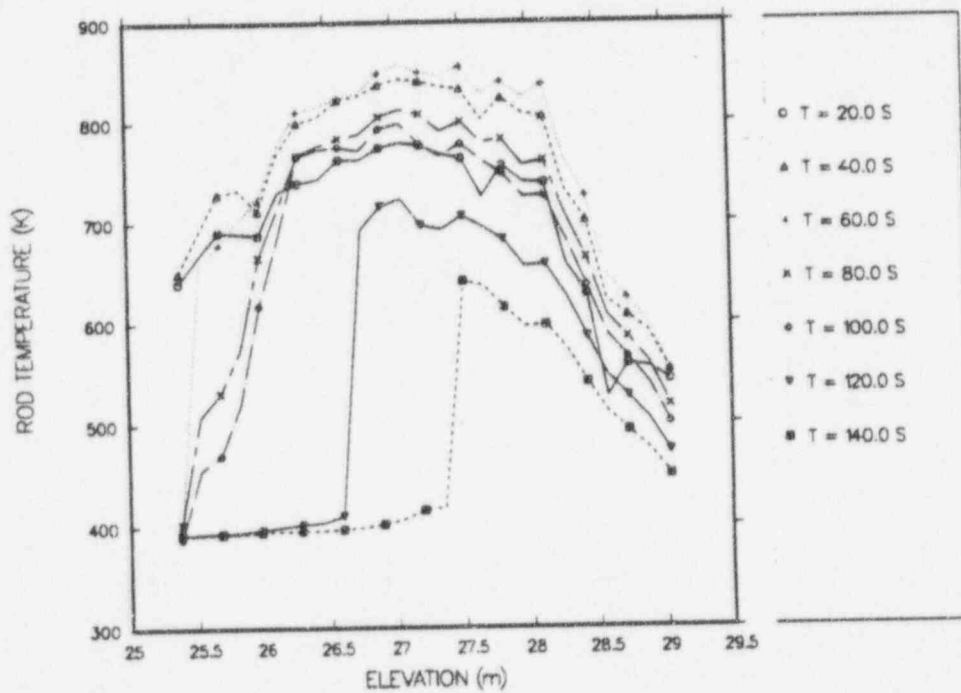


Fig. 48. Cell 4 average-rod temperatures vs rod elevation, 20 to 140 s.

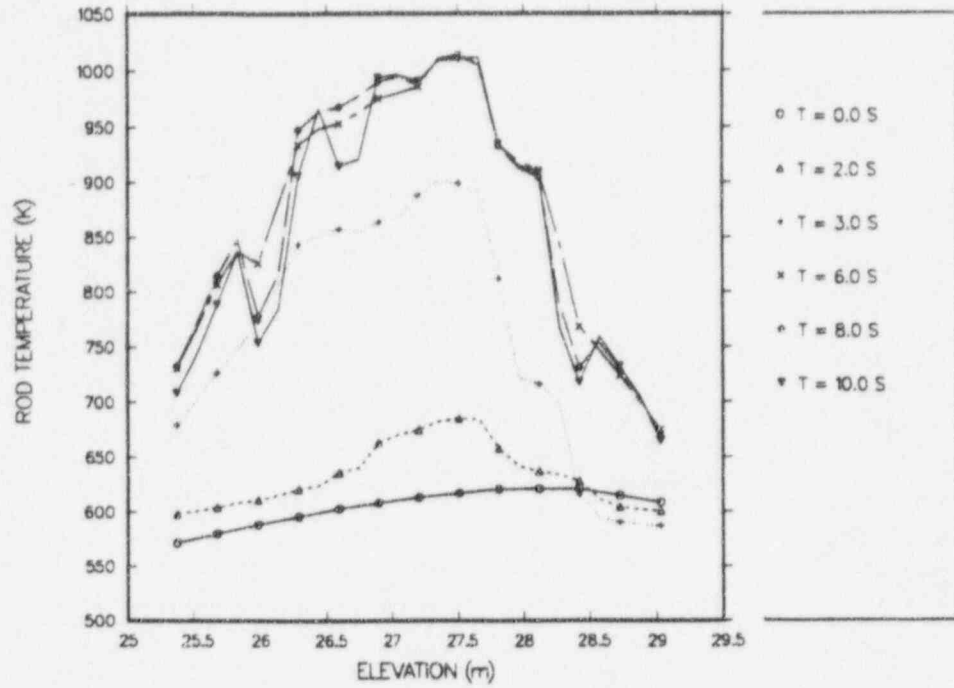


Fig. 49. Cell 4 hot-rod temperatures vs rod elevation, 0 to 10 s.

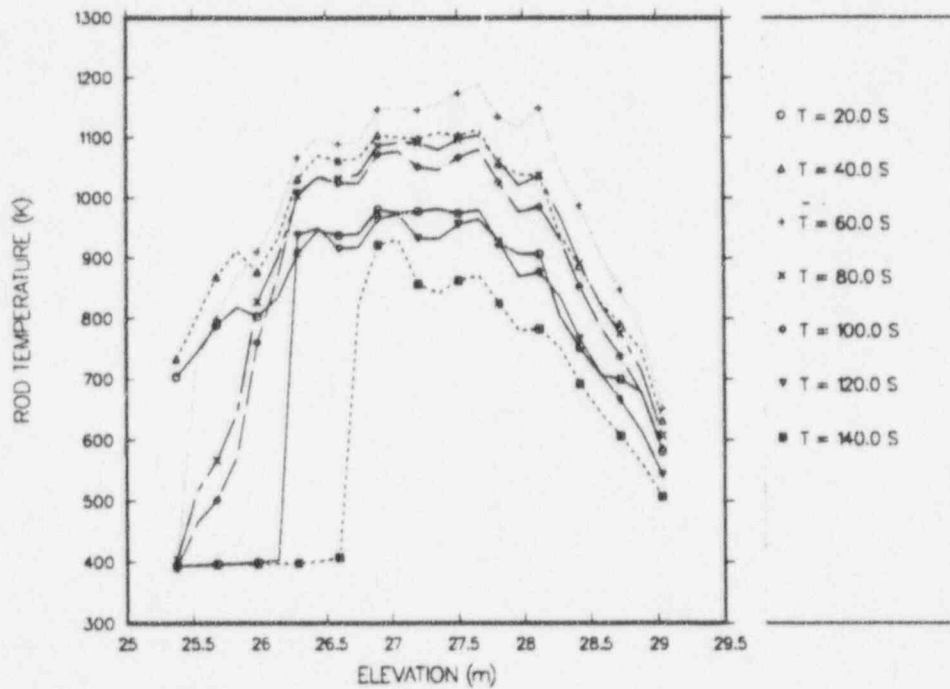


Fig. 50. Cell 4 hot-rod temperatures vs rod elevation, 20 to 140 s.

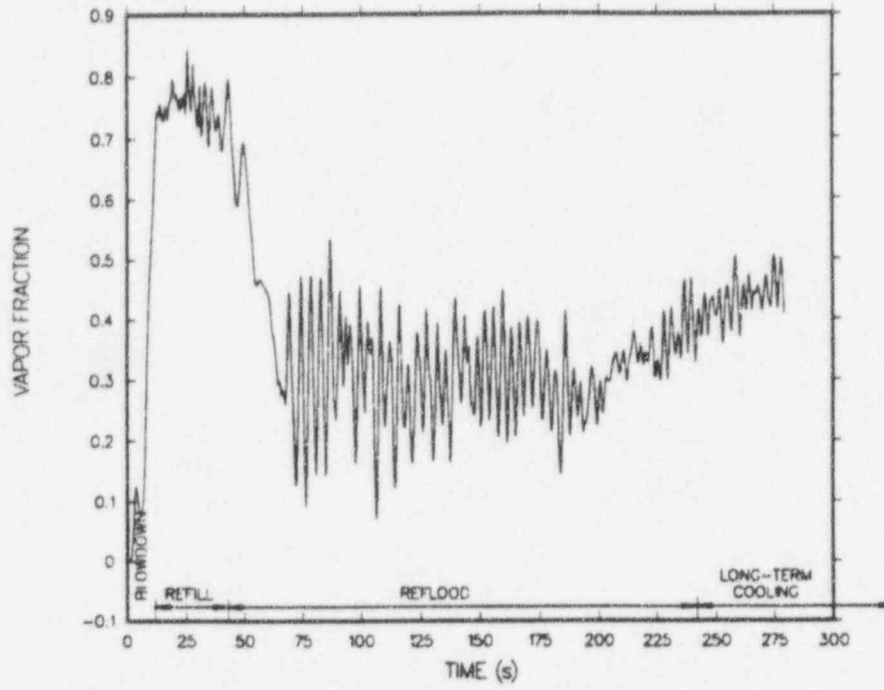


Fig. 51. Downcomer average vapor fraction.

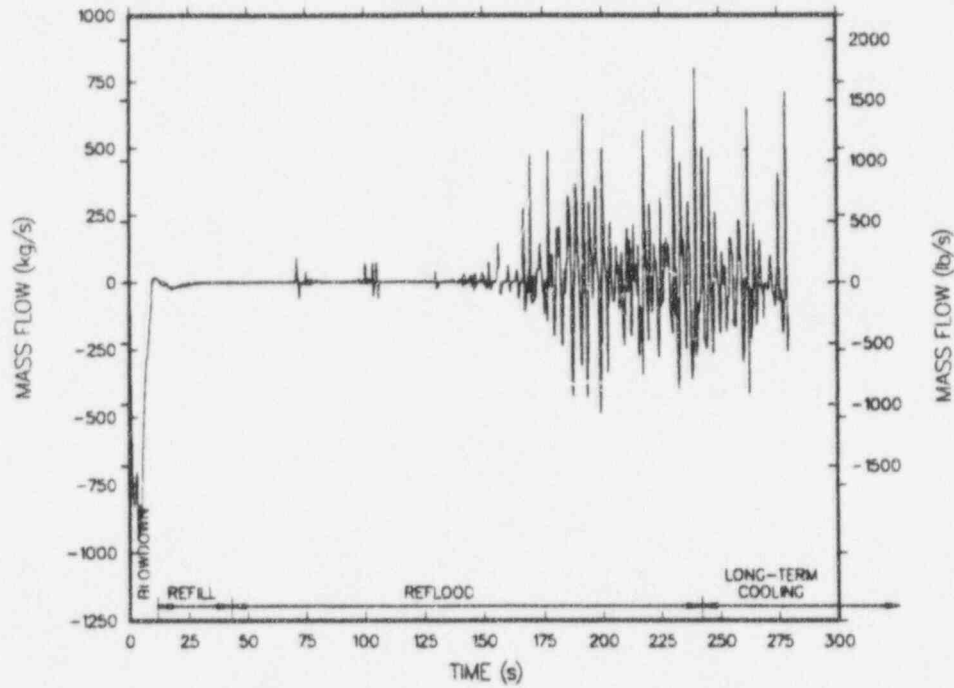


Fig. 52. Total guide tube flow.

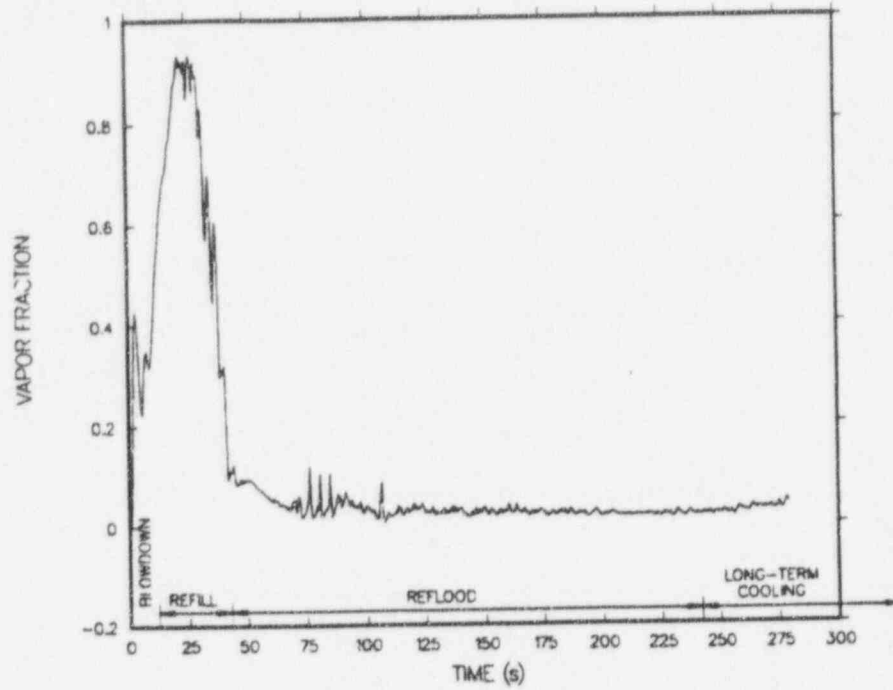


Fig. 53. Lower-plenum average vapor fraction.

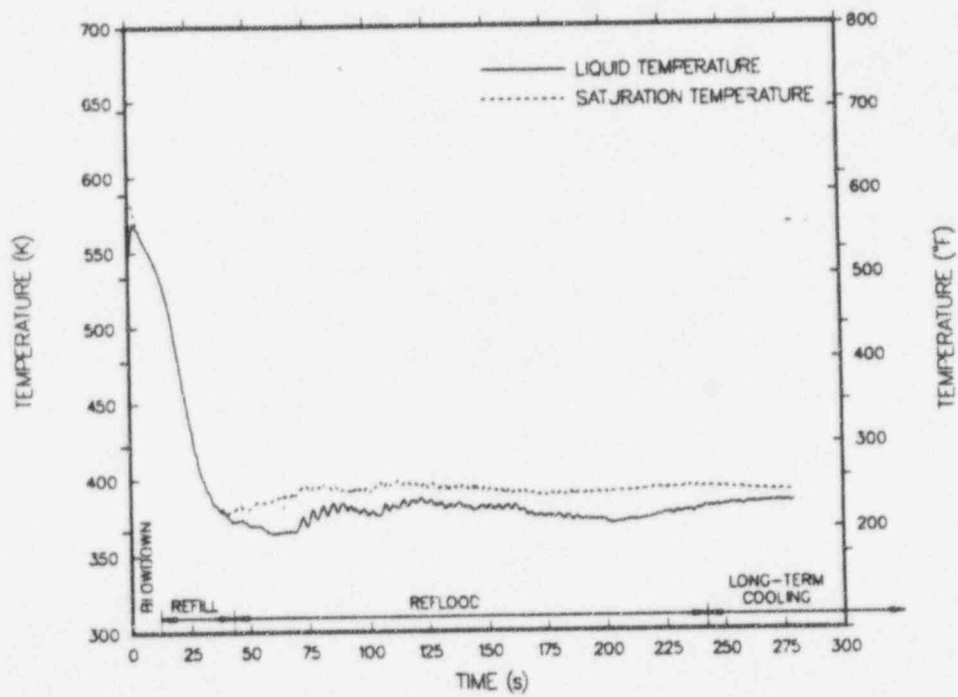


Fig. 54. Lower-plenum coolant temperatures.

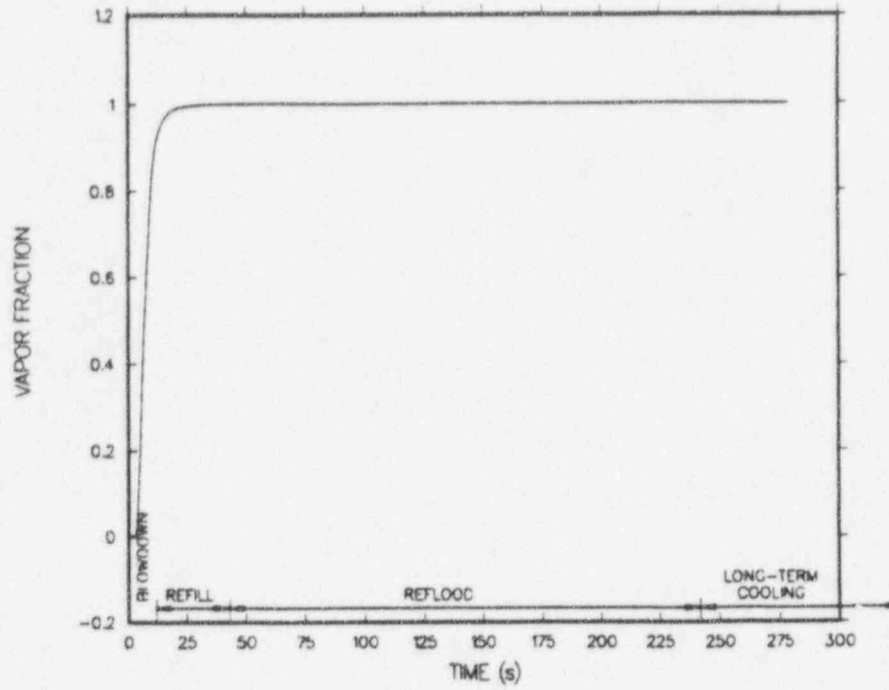


Fig. 55. Upper-head average vapor fraction.

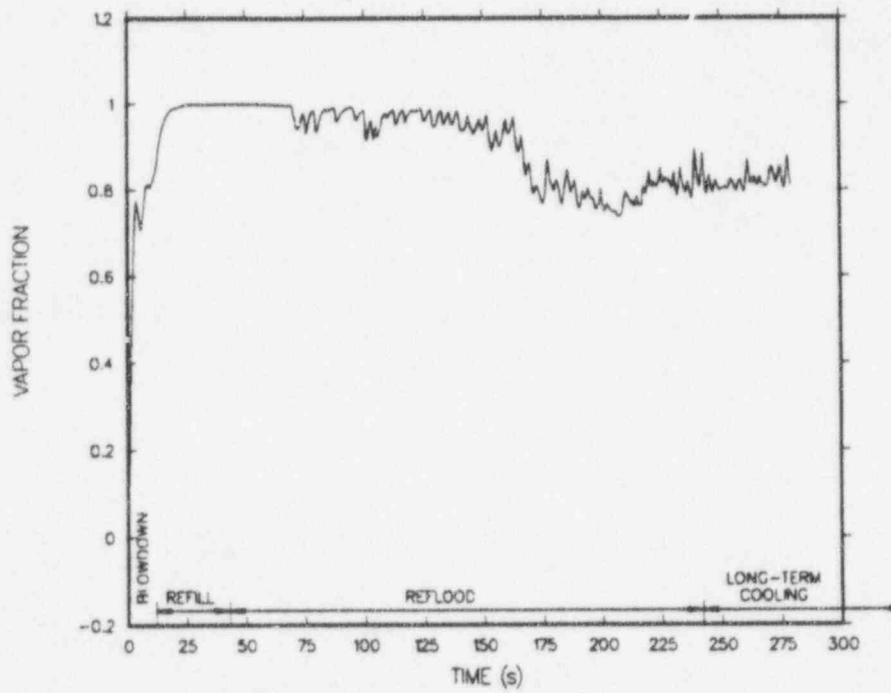


Fig. 56. Upper-plenum average vapor fraction.

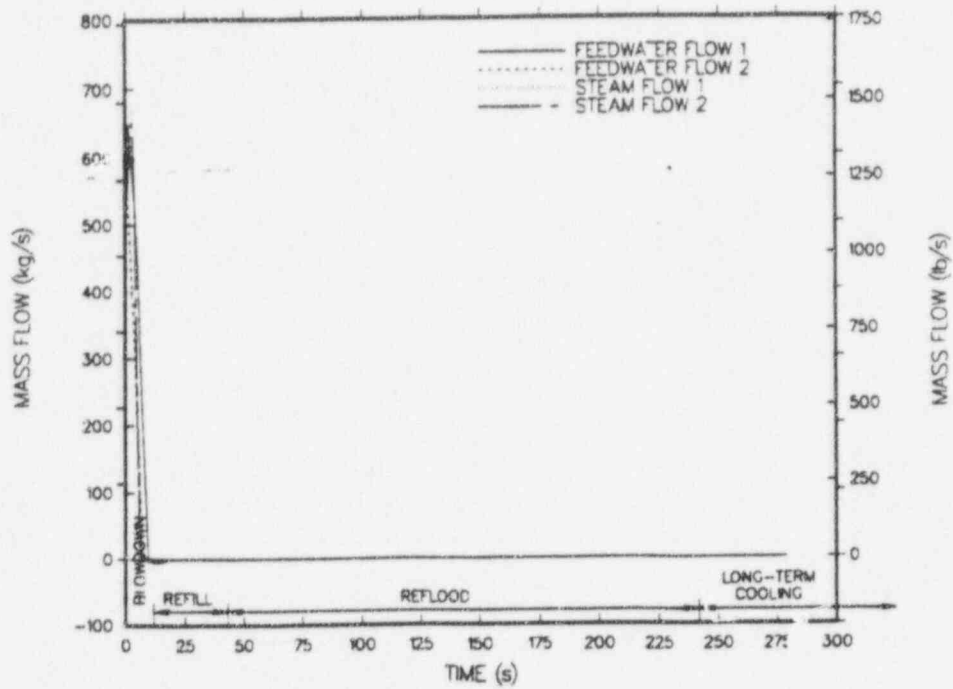


Fig. 57. Steam and feedwater mass flows.

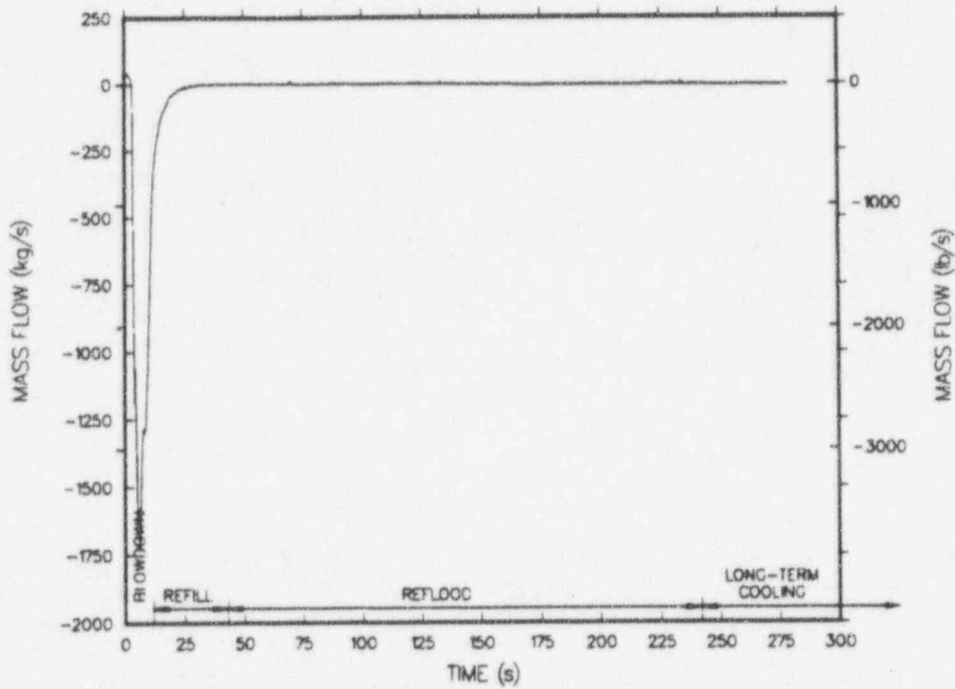


Fig. 58. Total upper-head support-plate drain-hole mass flow.

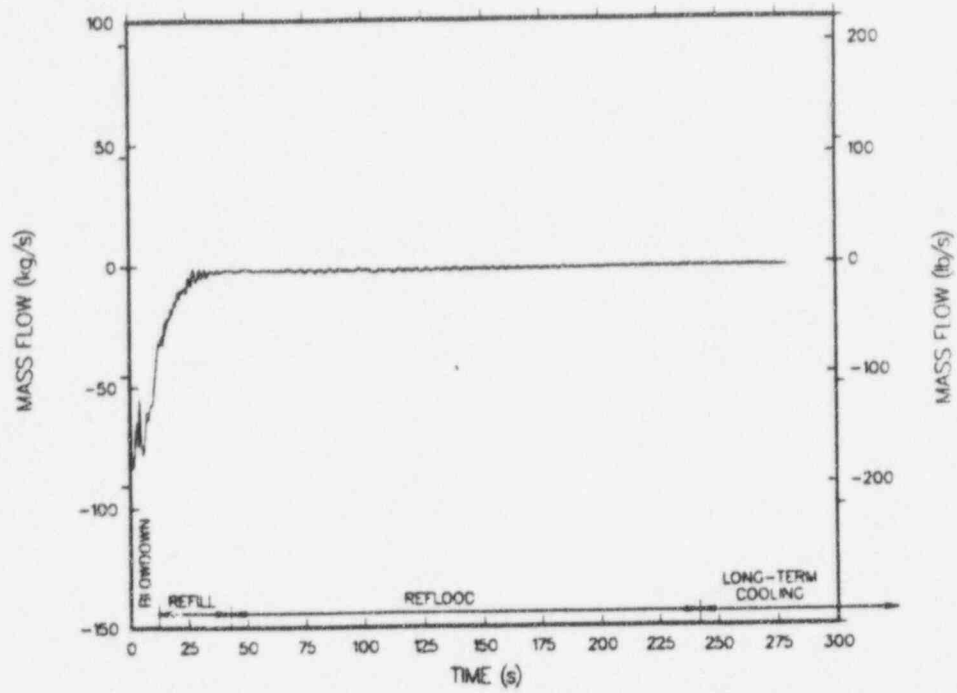


Fig. 59. Downcomer-to-upper-head mass flow.

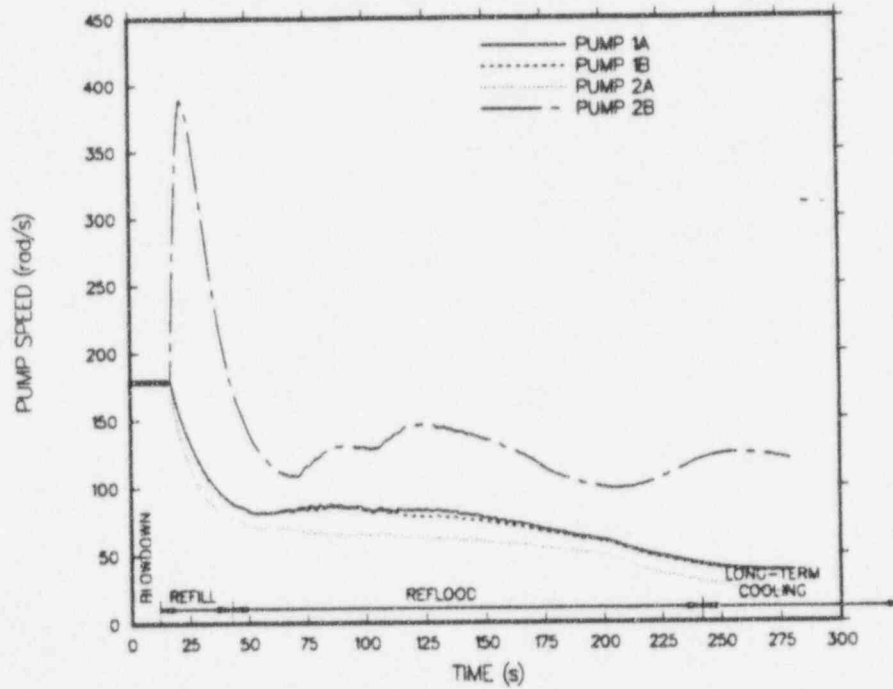


Fig. 60. Reactor-coolant pump-rotor speeds.

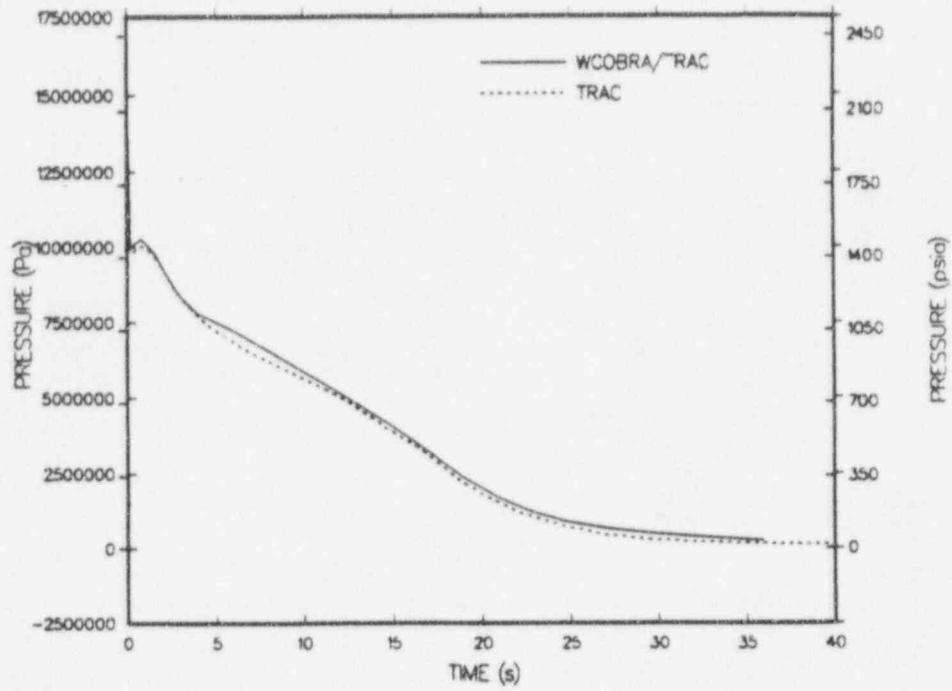


Fig. 61. Comparison of WCOBRA/TRAC and TRAC upper-plenum pressure.

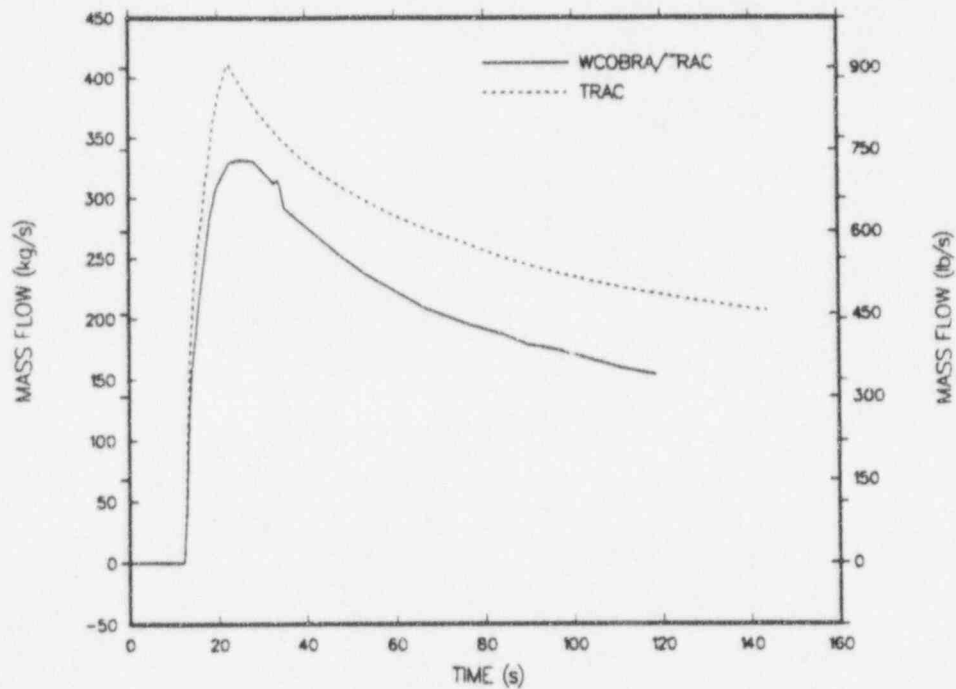


Fig. 62. Comparison of WCOBRA/TRAC and TRAC accumulator mass flow.

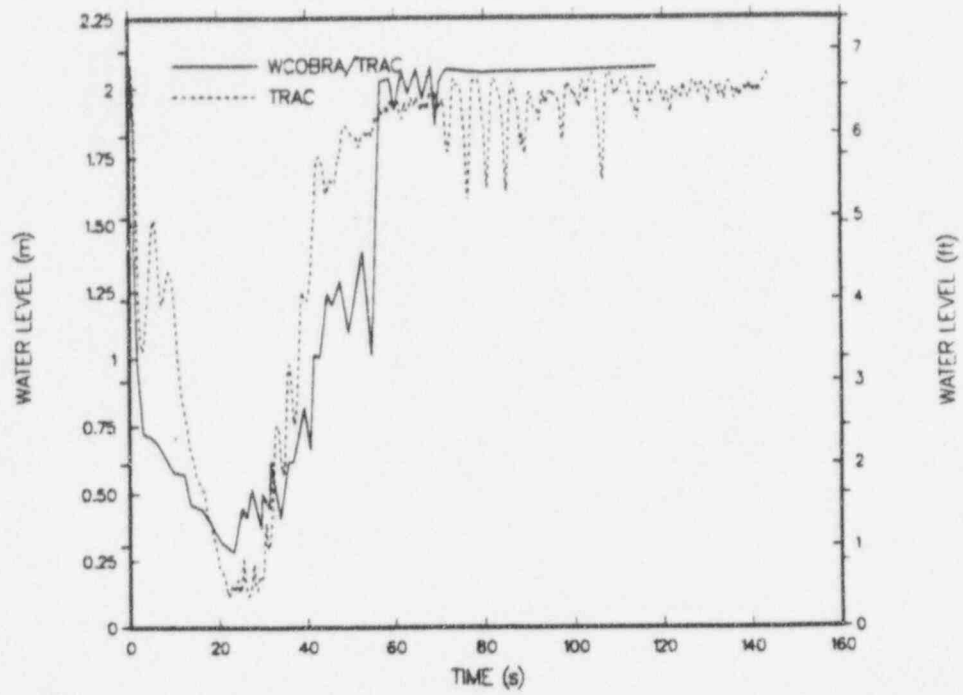


Fig. 63. Comparison of WCOBRA/TRAC and TRAC lower-plenum liquid level.

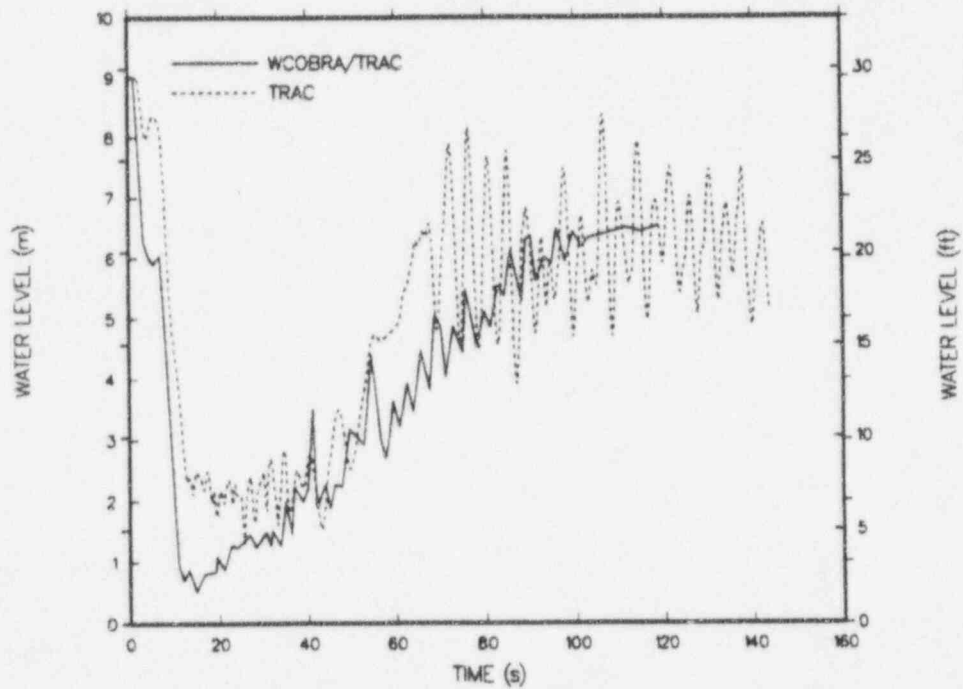


Fig. 64. Comparison of WCOBRA/TRAC and TRAC downcomer liquid level.

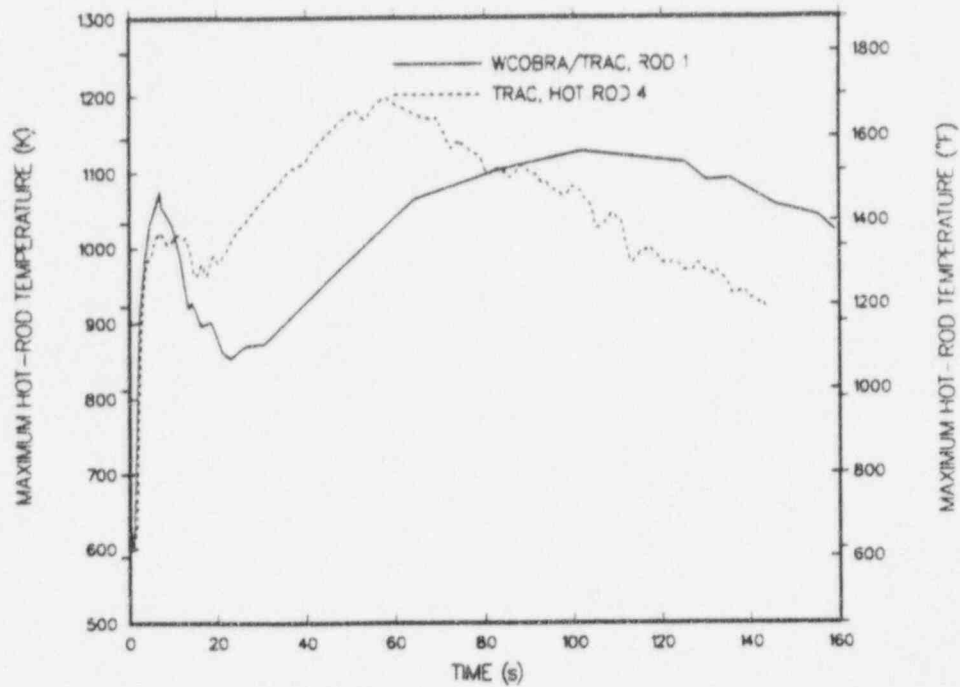


Fig. 65. Comparison of WCOBRA/TRAC and TRAC hot-rod peak cladding temperatures.

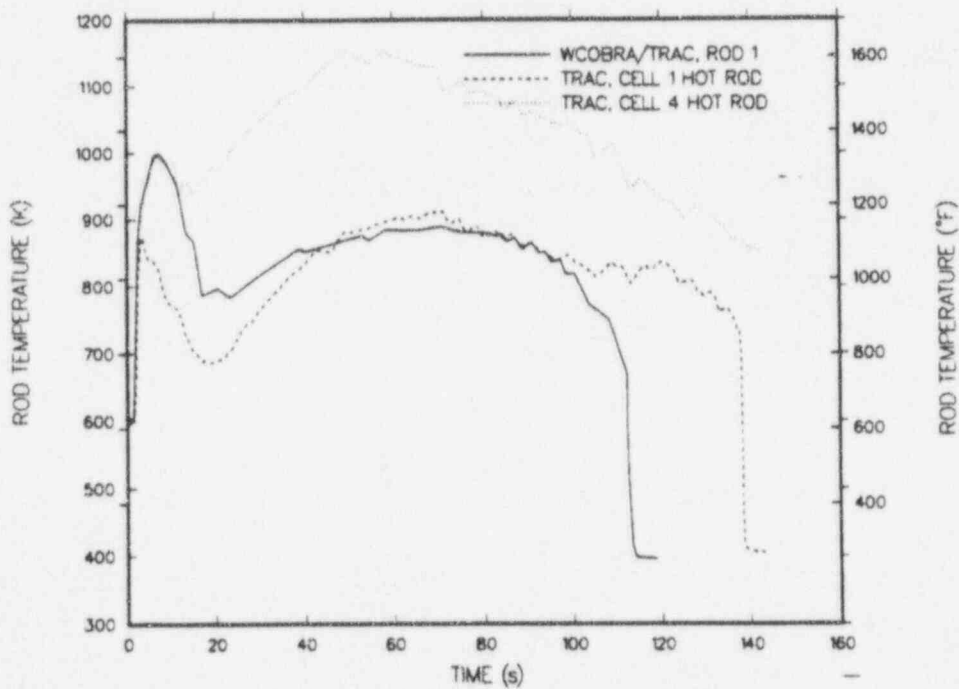


Fig. 66. Comparison of WCOBRA/TRAC and TRAC hot-rod cladding temperatures at 6-ft rod elevation.

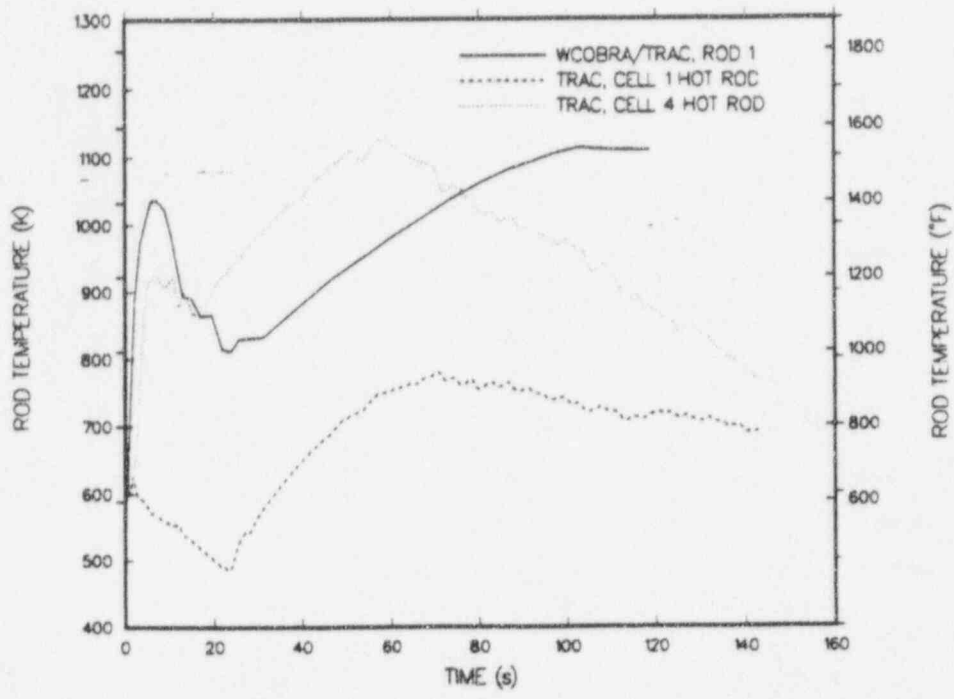


Fig. 67. Comparison of WCOBRA/TRAC and TRAC hot-rod cladding temperatures at 8.5-ft rod elevation.

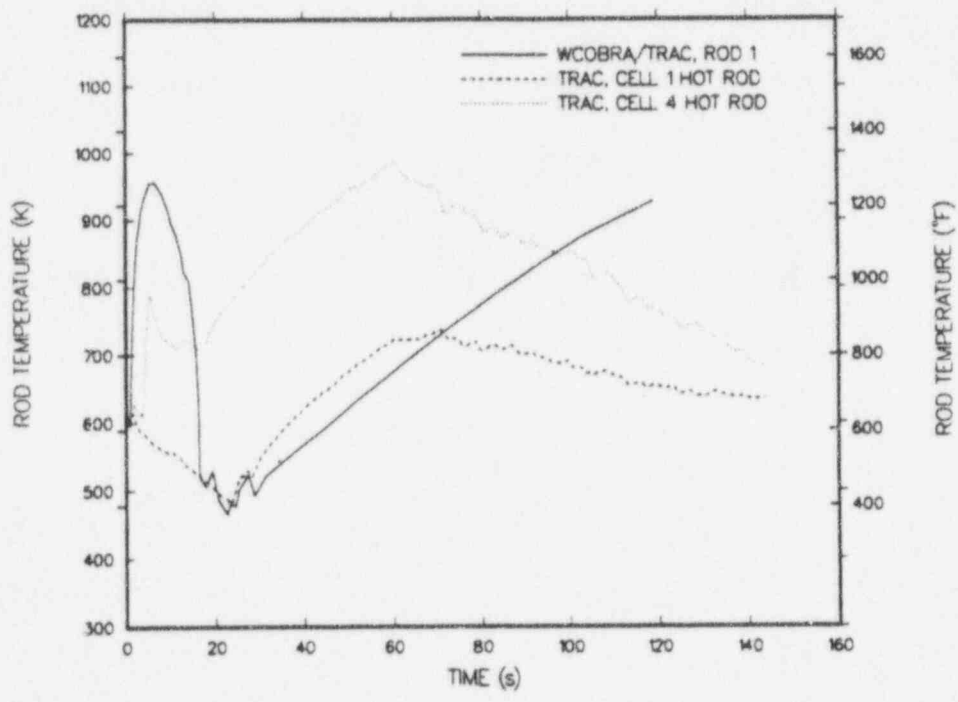


Fig. 68. Comparison of WCOBRA/TRAC and TRAC hot-rod cladding temperatures at 10-ft rod elevation.

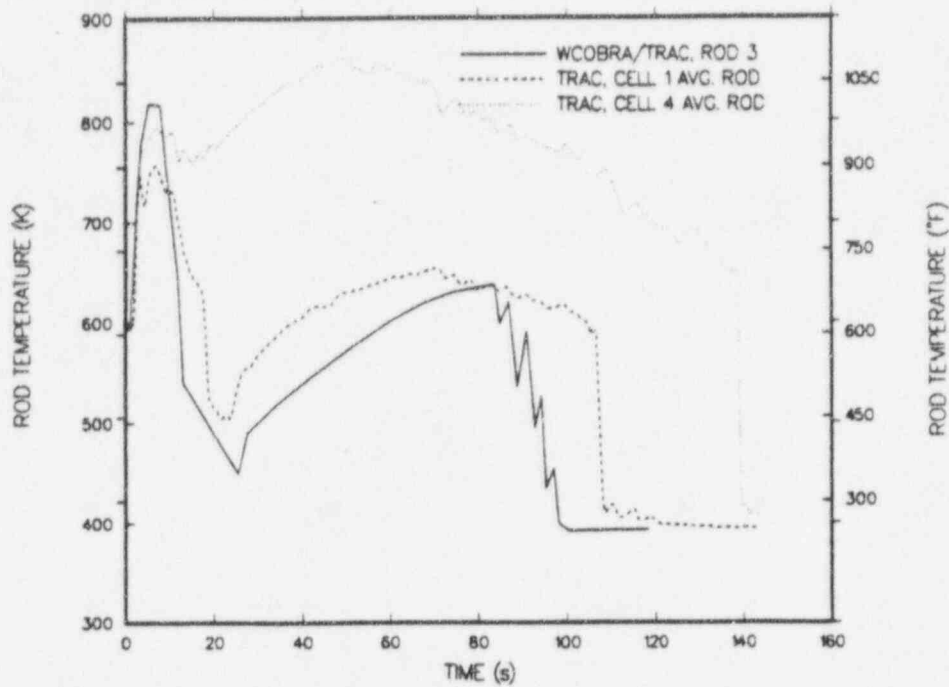


Fig. 69. Comparison of WCOBRA/TRAC and TRAC average-rod cladding temperatures at 6-ft rod elevation.

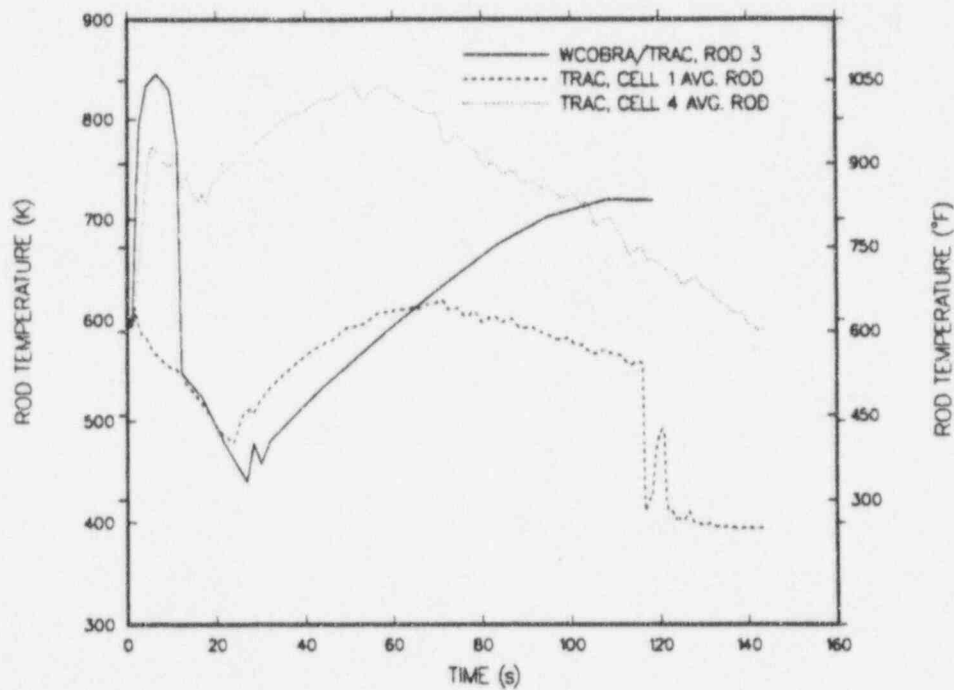


Fig. 70. Comparison of WCOBRA/TRAC and TRAC average-rod cladding temperatures at 8.5-ft rod elevation.

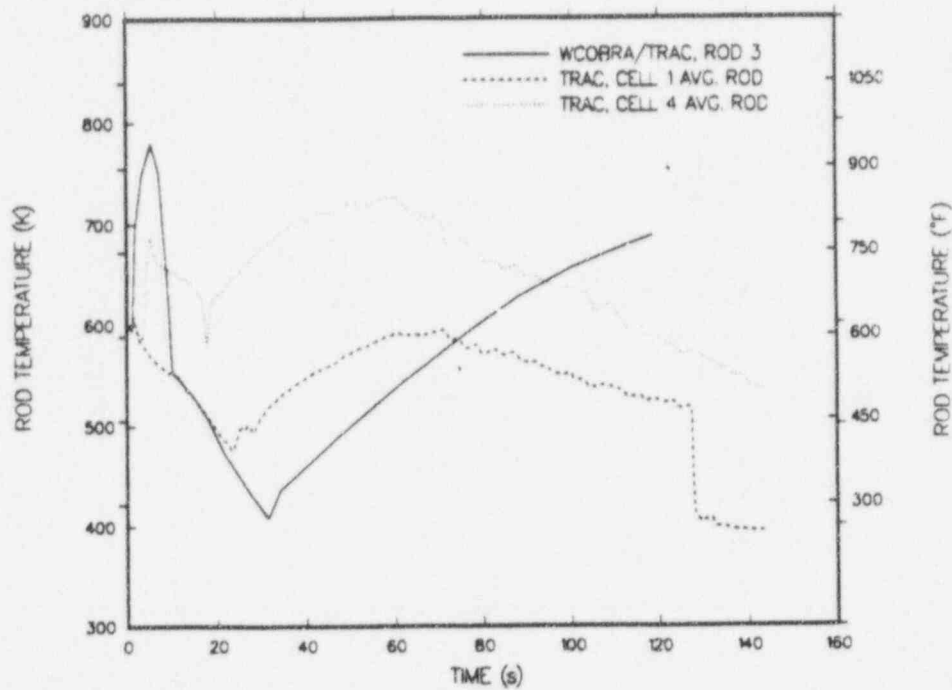


Fig. 71. Comparison of WCOBRA/TRAC and TRAC average-rod cladding temperatures at 10-ft rod elevation.

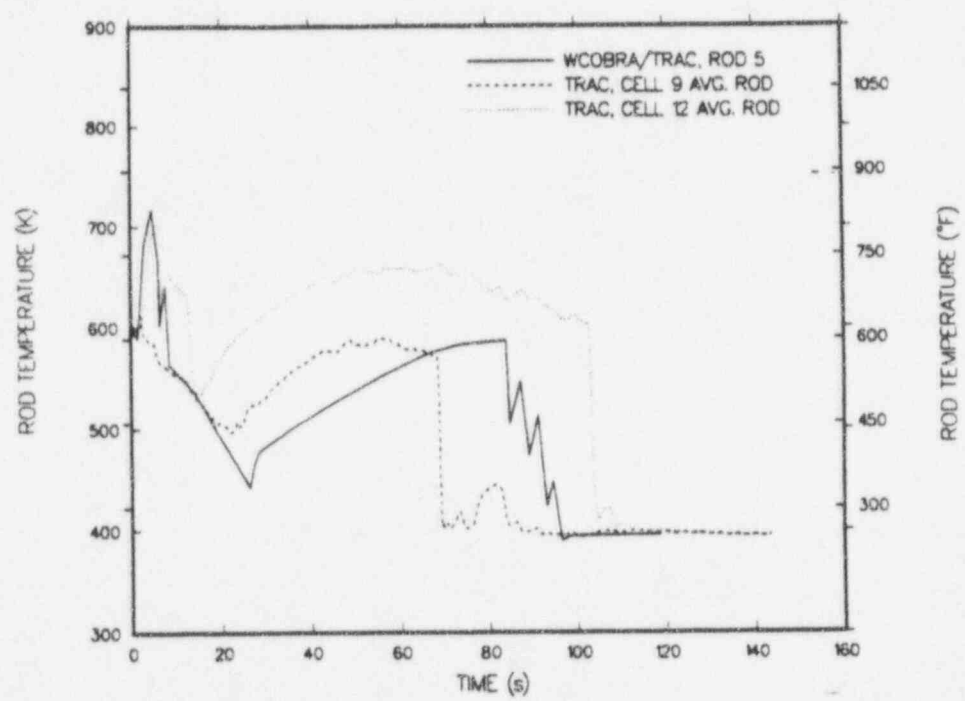


Fig. 72. Comparison of WCOBRA/TRAC peripheral-rod cladding temperatures to TRAC outer-ring average-rod cladding temperatures at 6-ft rod elevation.

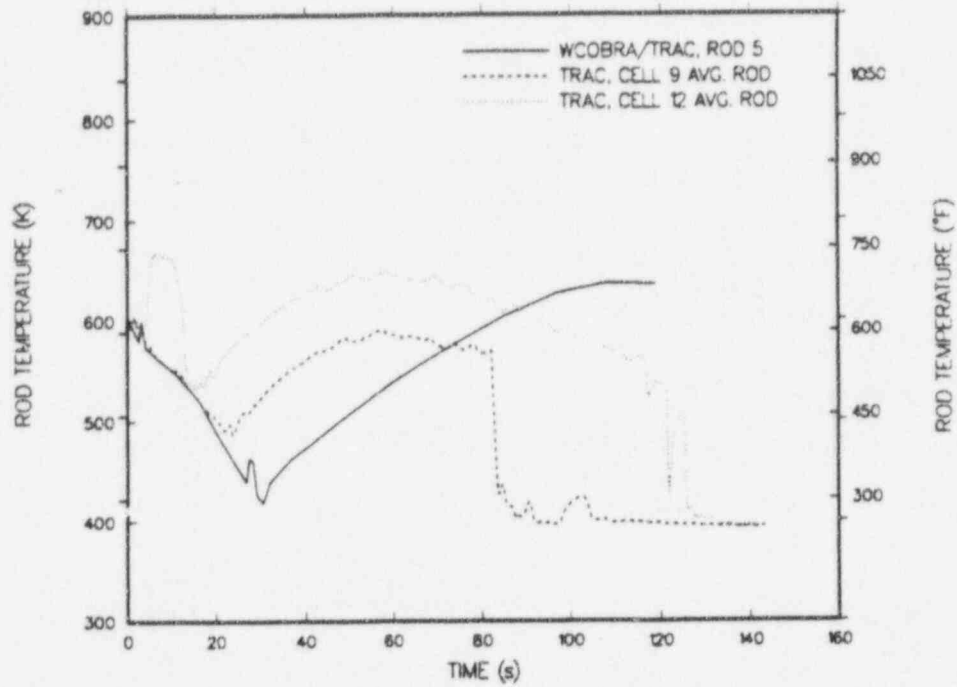


Fig. 73. Comparison of WCOBRA/TRAC peripheral-rod cladding temperatures to TRAC outer-ring average-rod cladding temperatures at 8.5-ft rod elevation.

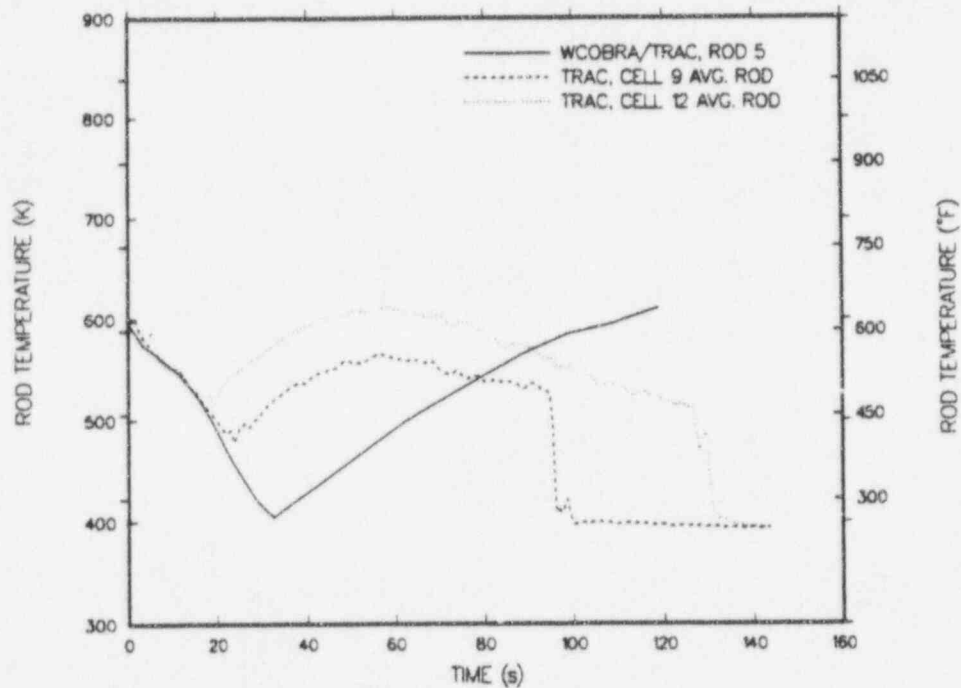


Fig. 74. Comparison of WCOBRA/TRAC peripheral-rod cladding temperatures to TRAC outer-ring average-rod cladding temperatures at 10-ft rod elevation.

APPENDIX A

CORE-INLET MASS FLOWS

Figures A-1 through A-16 depict core-inlet mass flows at each core sector cell. A noding diagram is provided in Fig. 6 of the main text.

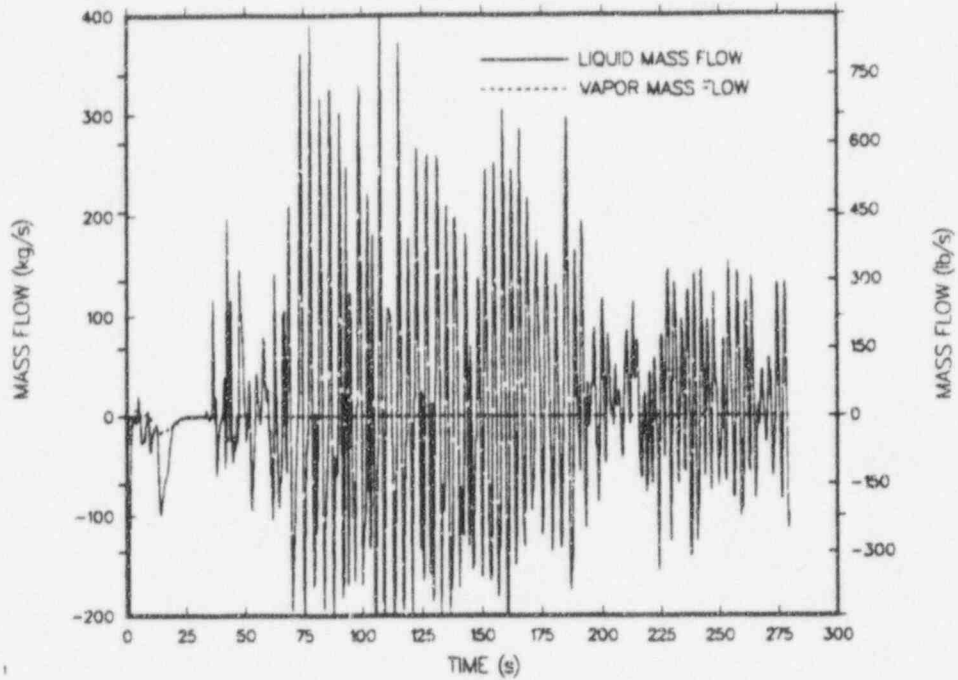


Fig. A-1. Core-inlet mass flow, core sector cell 1 ($r = 1$, $\theta = 1$).

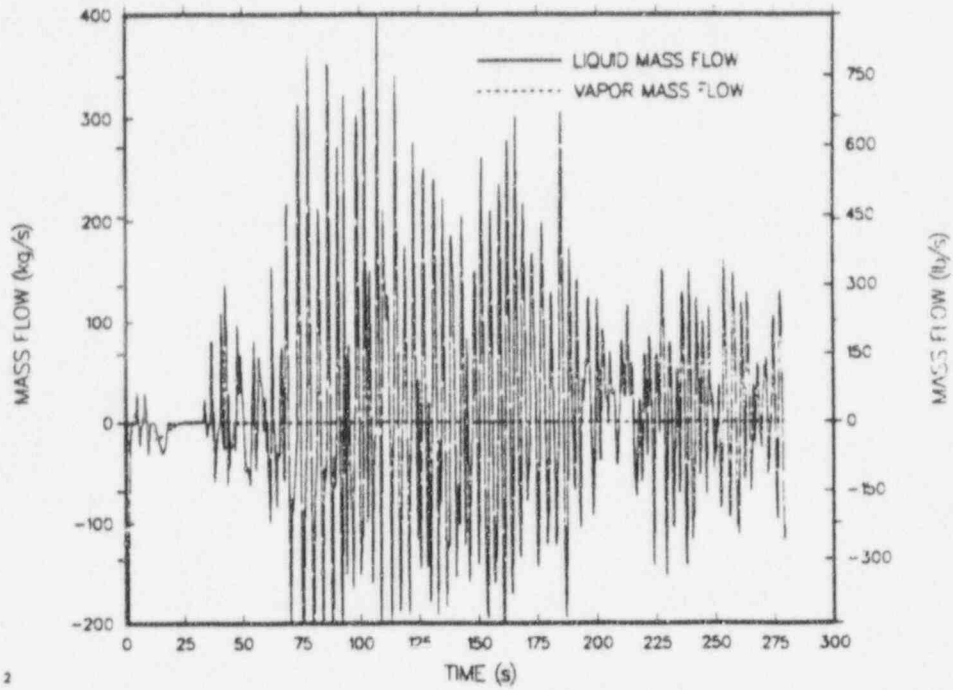


Fig. A-2. Core-inlet mass flow, core sector cell 2 ($r = 1, \theta = 2$).

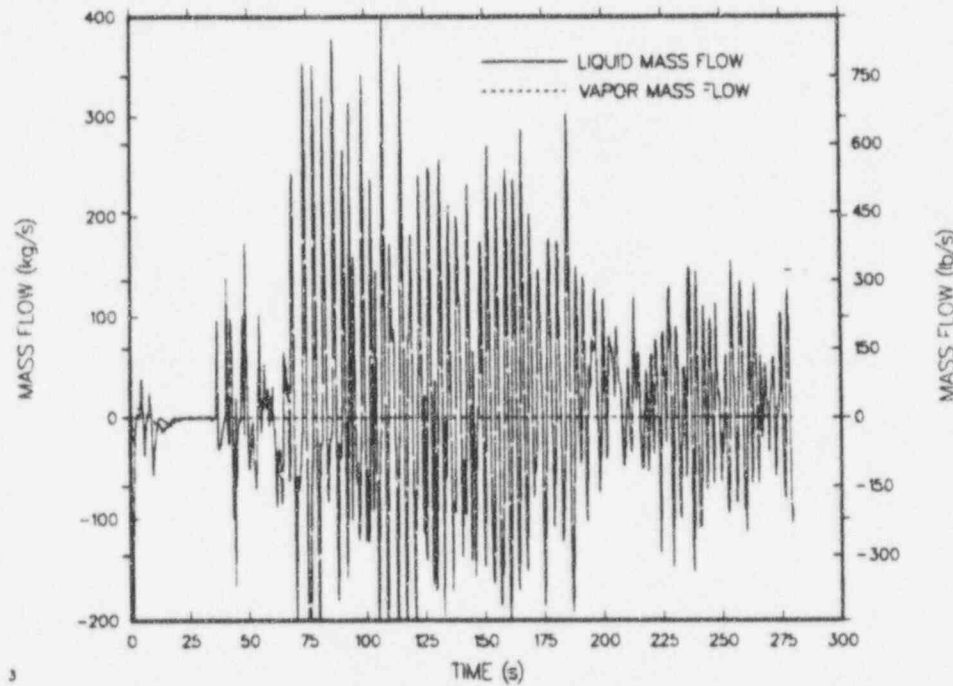


Fig. A-3. Core-inlet mass flow, core sector cell 3 ($r = 1, \theta = 3$).

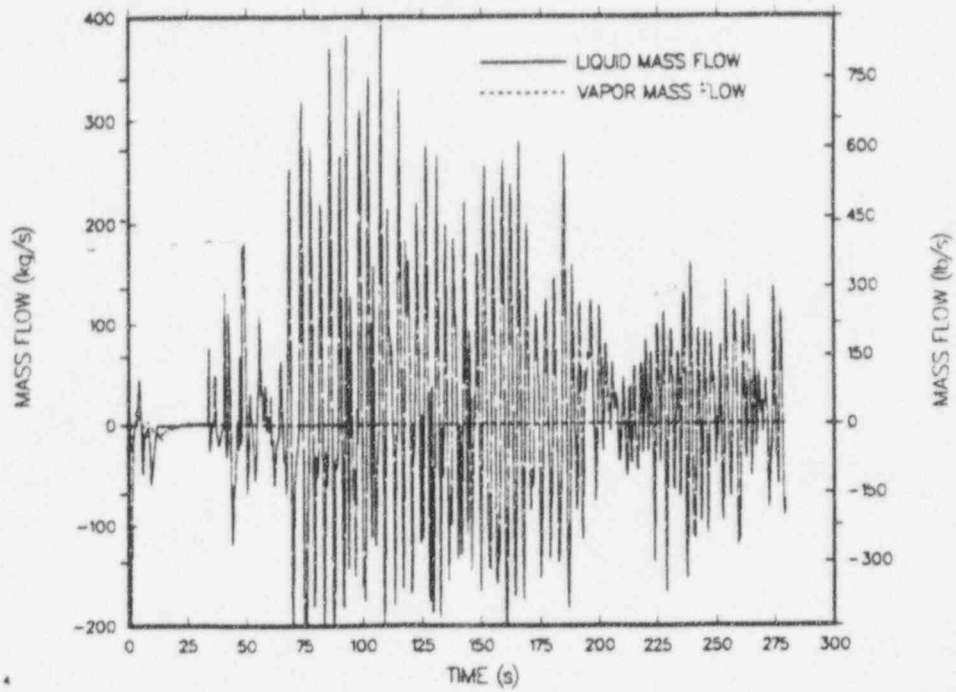


Fig. A-4. Core-inlet mass flow, core sector cell 4 ($r = 1, \theta = 4$).

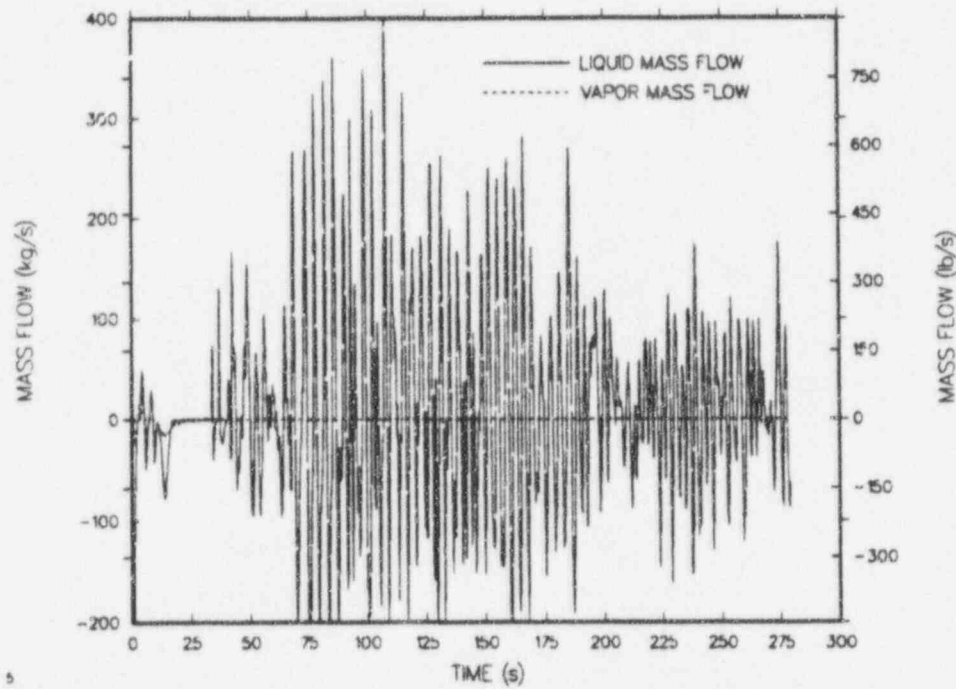


Fig. A-5. Core-inlet mass flow, core sector cell 5 ($r = 1, \theta = 5$).

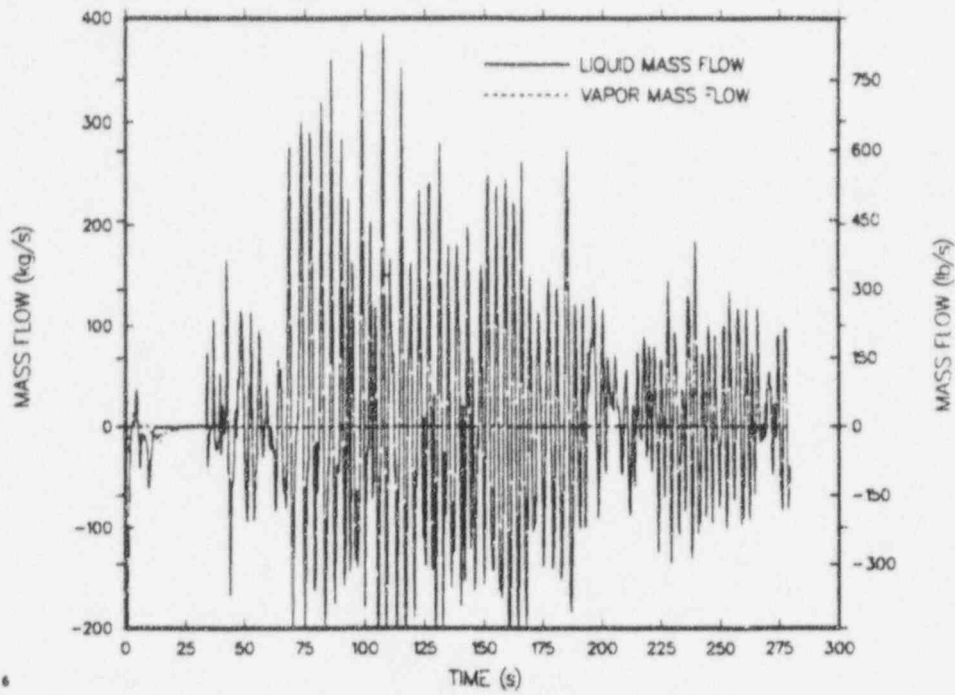


Fig. A-6. Core-inlet mass flow, core sector cell 6 ($r = 1, \theta = 6$).

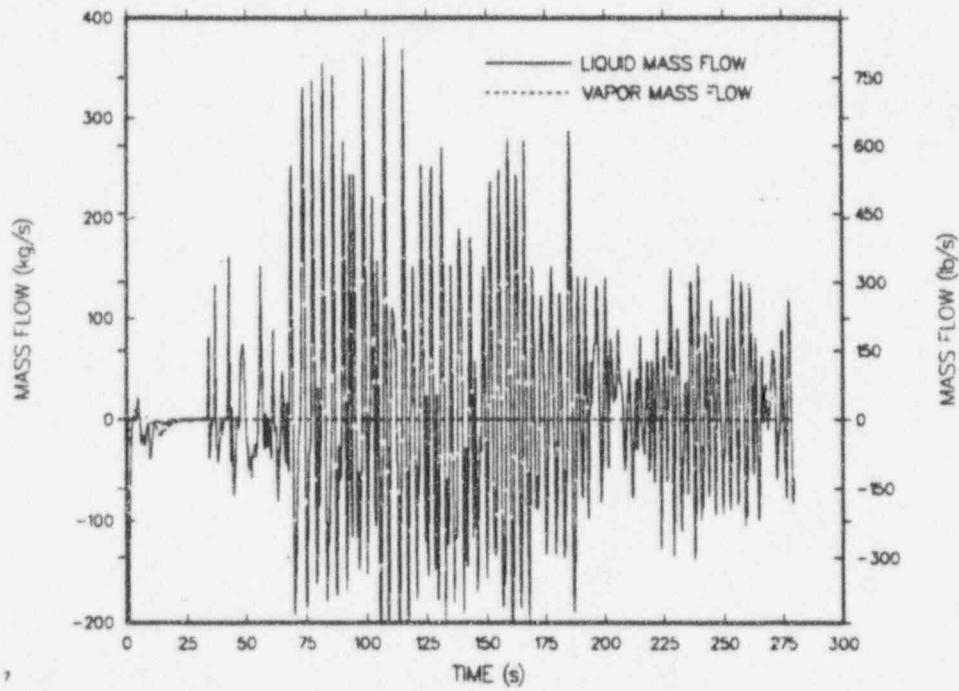


Fig. A-7. Core-inlet mass flow, core sector cell 7 ($r = 1, \theta = 7$).

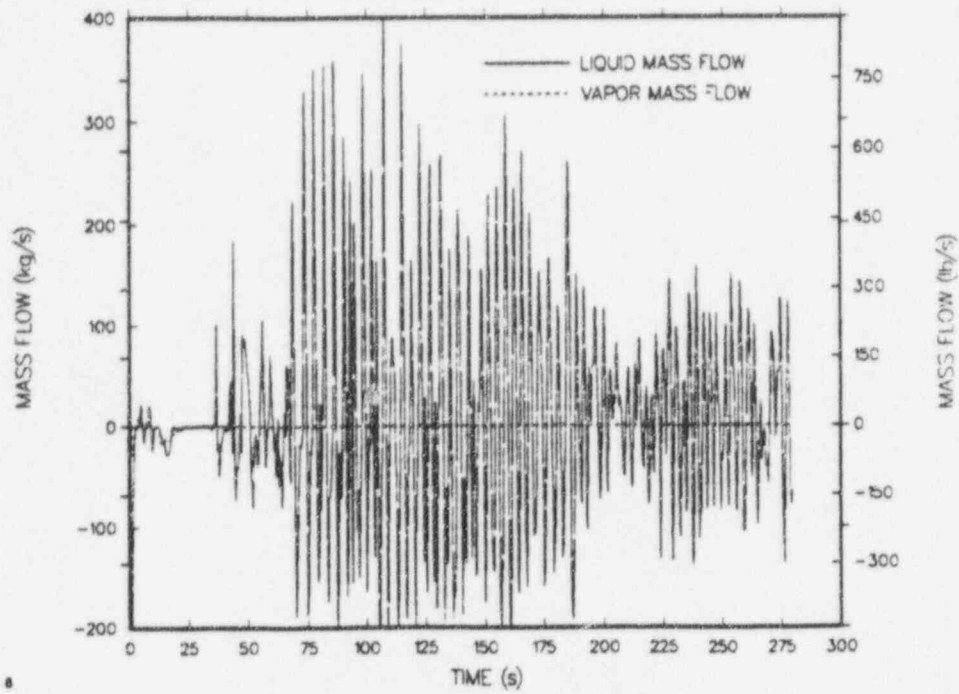


Fig. A-8. Core-inlet mass flow, core sector cell 8 ($r = 1, \theta = 8$).

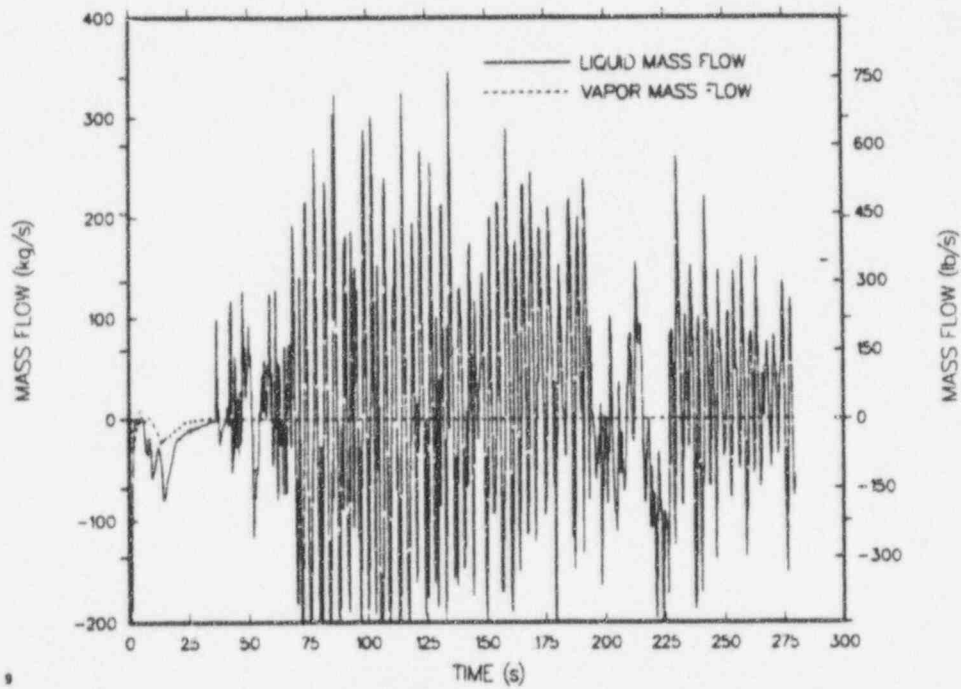


Fig. A-9. Core-inlet mass flow, core sector cell 9 ($r = 2, \theta = 1$).

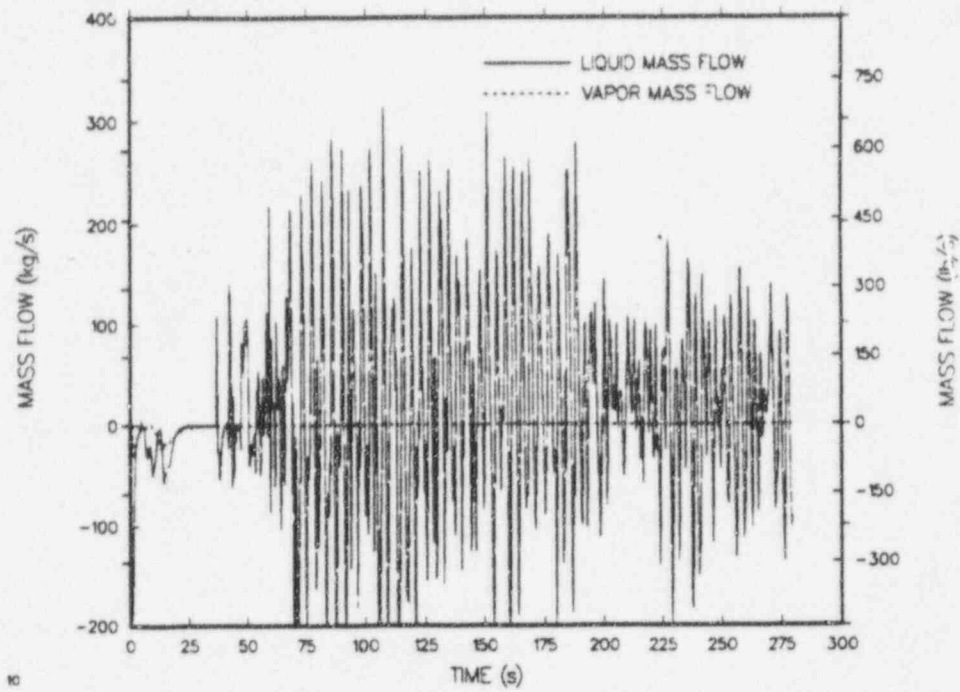


Fig. A-10. Core-inlet mass flow, core sector cell 10 ($r = 2, \theta = 2$).

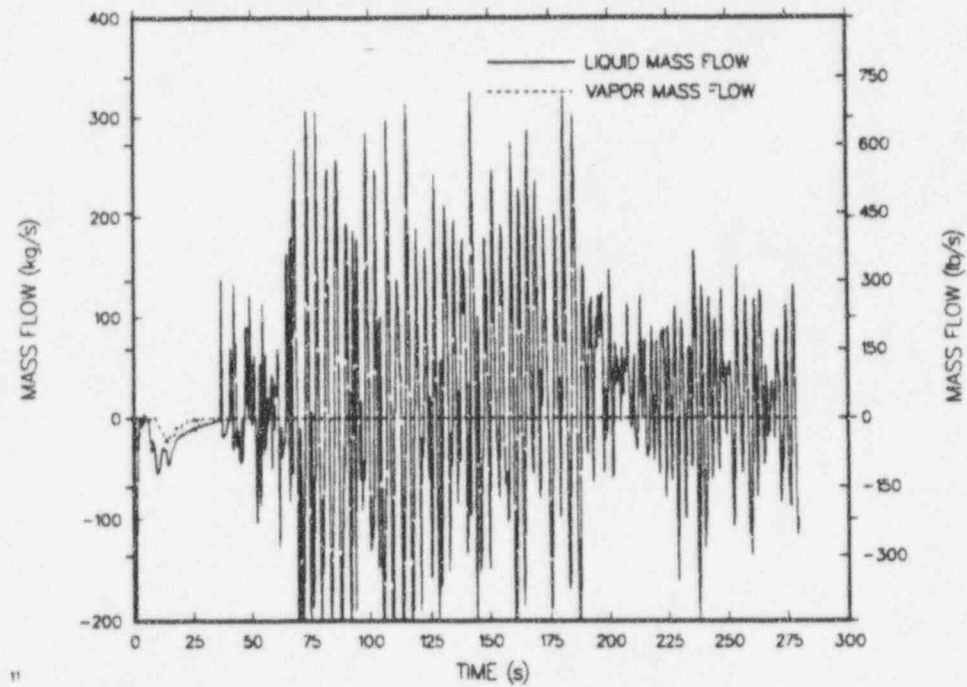


Fig. A-11. Core-inlet mass flow, core sector cell 11 ($r = 2, \theta = 3$).

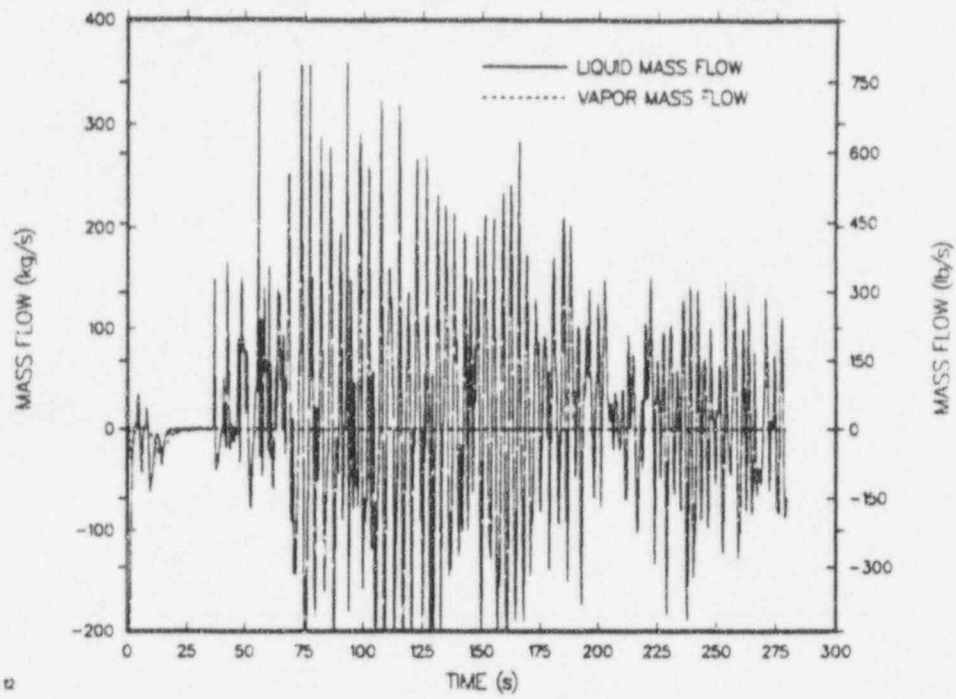


Fig. A-12. Core-inlet mass flow, core sector cell 12 ($r = 2, \theta = 4$).

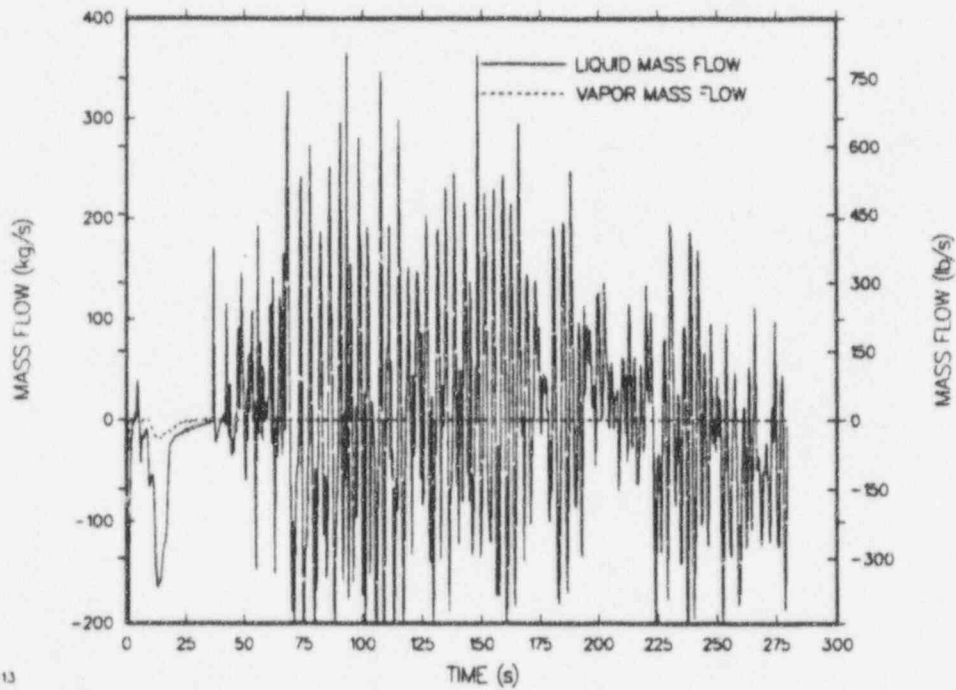


Fig. A-13. Core-inlet mass flow, core sector cell 13 ($r = 2, \theta = 5$).

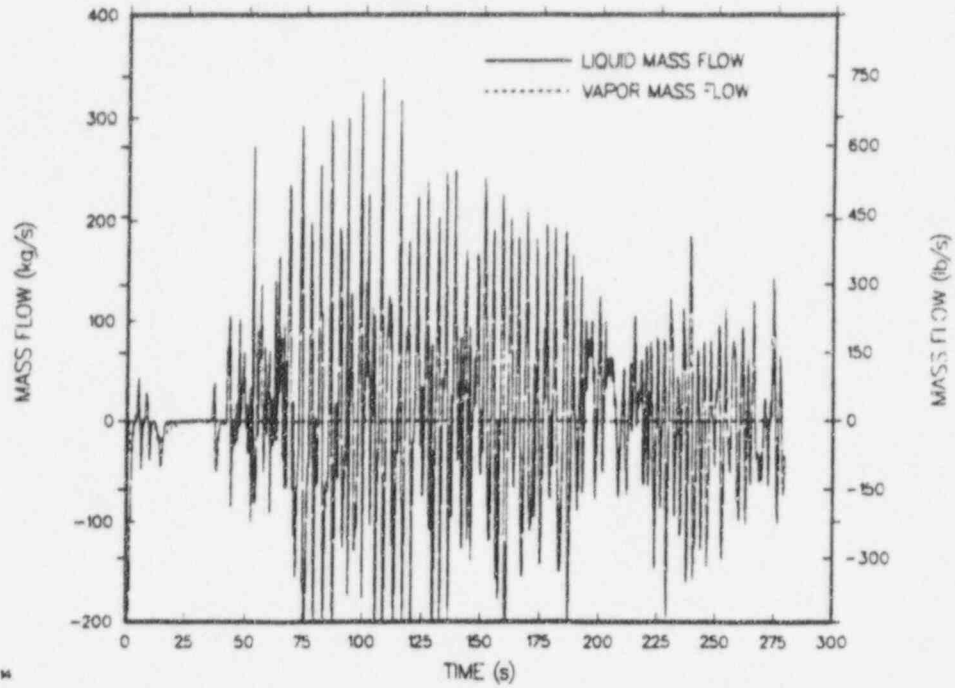


Fig. A-14. Core-inlet mass flow, core sector cell 14 ($r = 2, \theta = 6$).

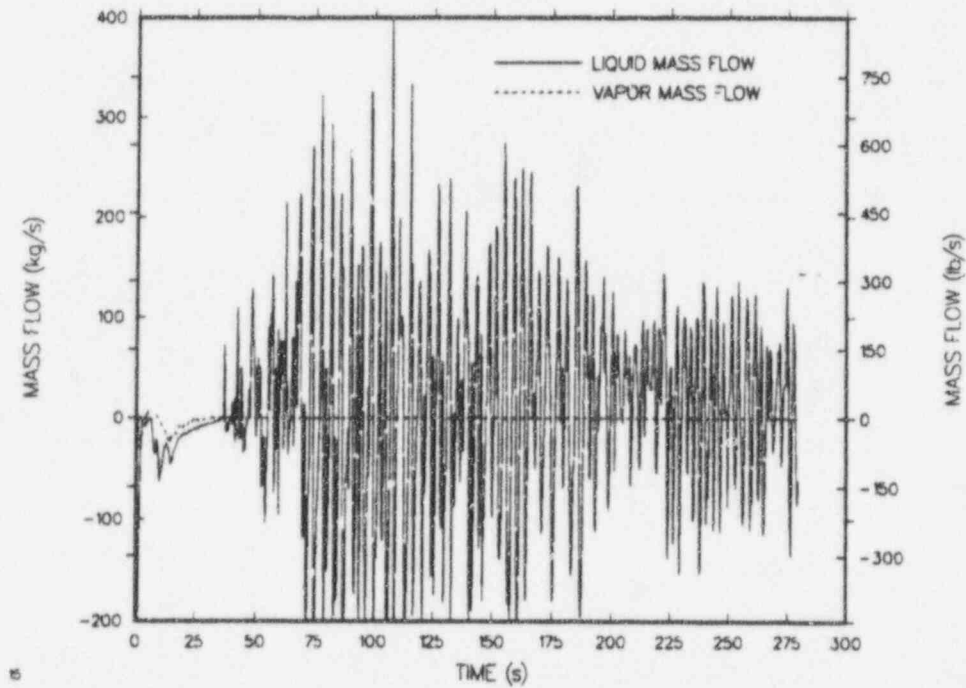


Fig. A-15. Core-inlet mass flow, core sector cell 15 ($r = 2, \theta = 7$).

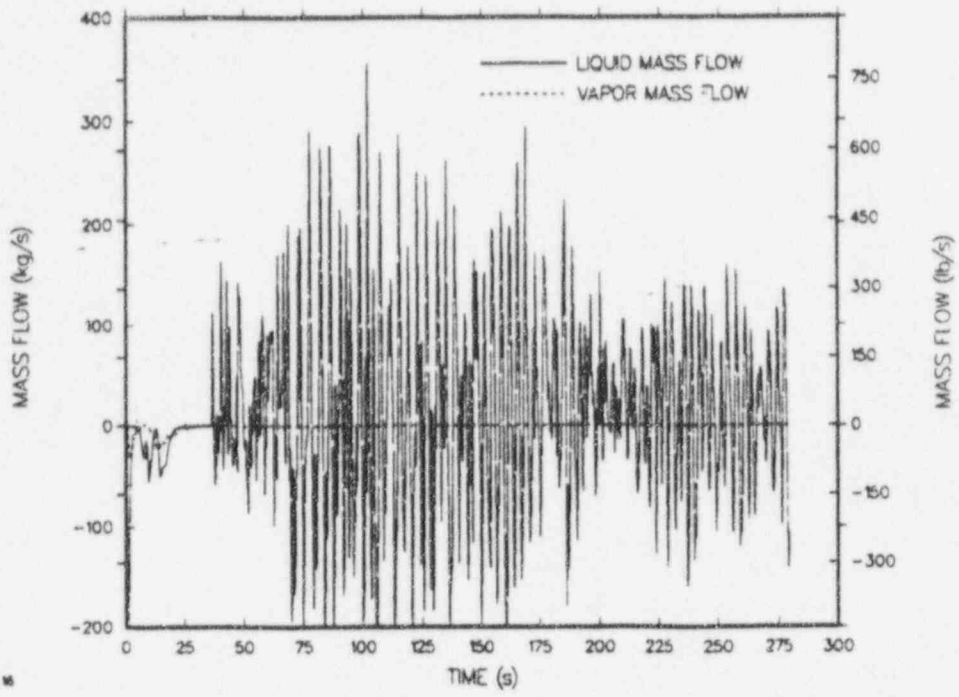


Fig. A-16. Core-inlet mass flow, core sector cell 16 ($r = 2$, $\theta = 8$).

APPENDIX B

CORE-OUTLET MASS FLOWS

Figures B-1 through B-16 depict core-outlet mass flows at each core sector cell. A noding diagram is provided in Fig. 6 of the main text.

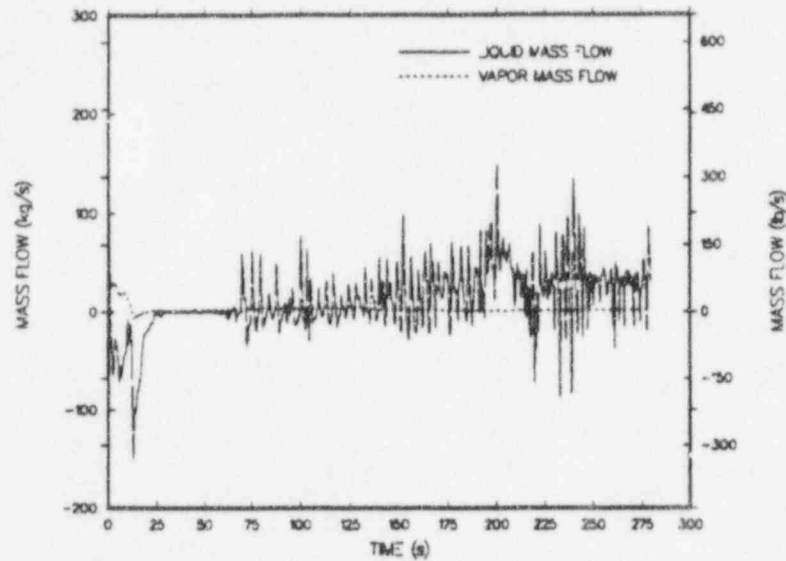


Fig. B-1. Core-outlet mass flow, core sector cell 1 ($r = 1, \theta = 1$).

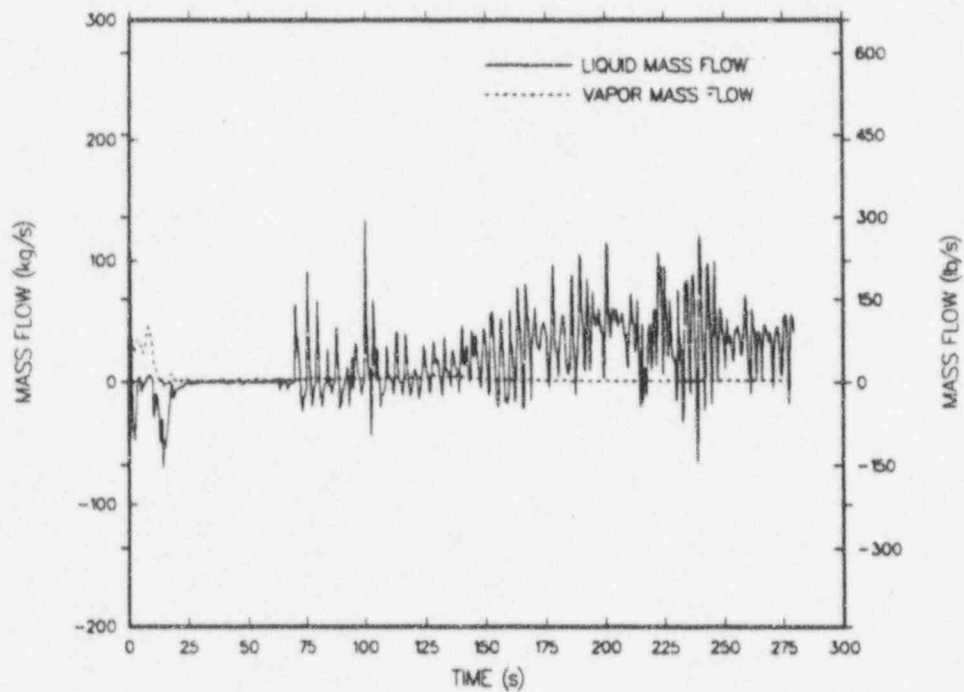


Fig. B-2. Core-outlet mass flow, core sector cell 2 ($r = 1, \theta = 2$).

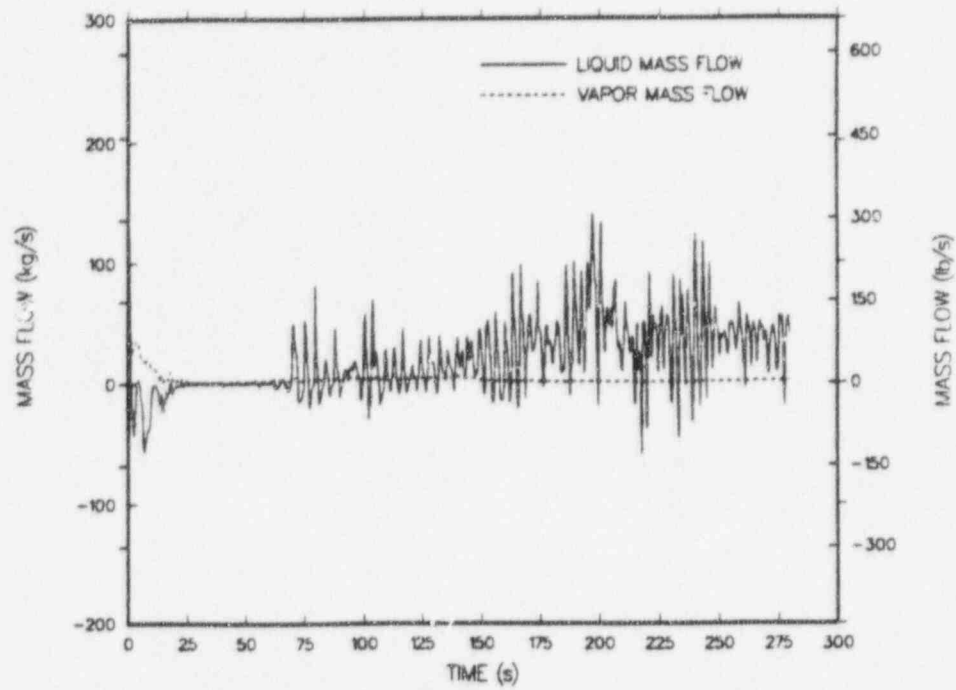


Fig. B-3. Core-outlet mass flow, core sector cell 3 ($r = 1, \theta = 3$).

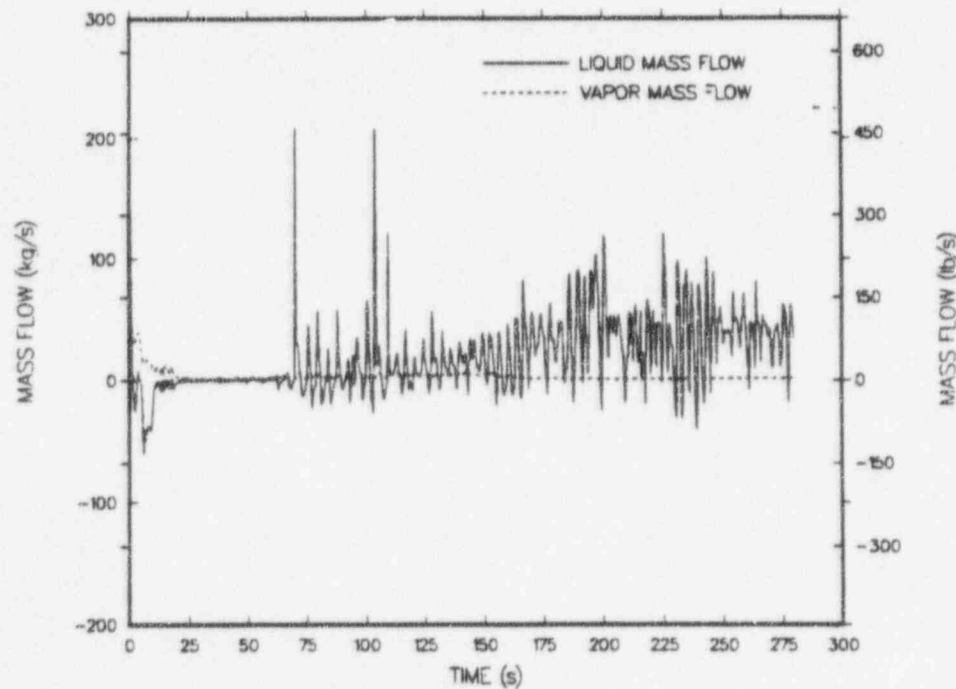


Fig. B-4. Core-outlet mass flow, core sector cell 4 ($r = 1, \theta = 4$).

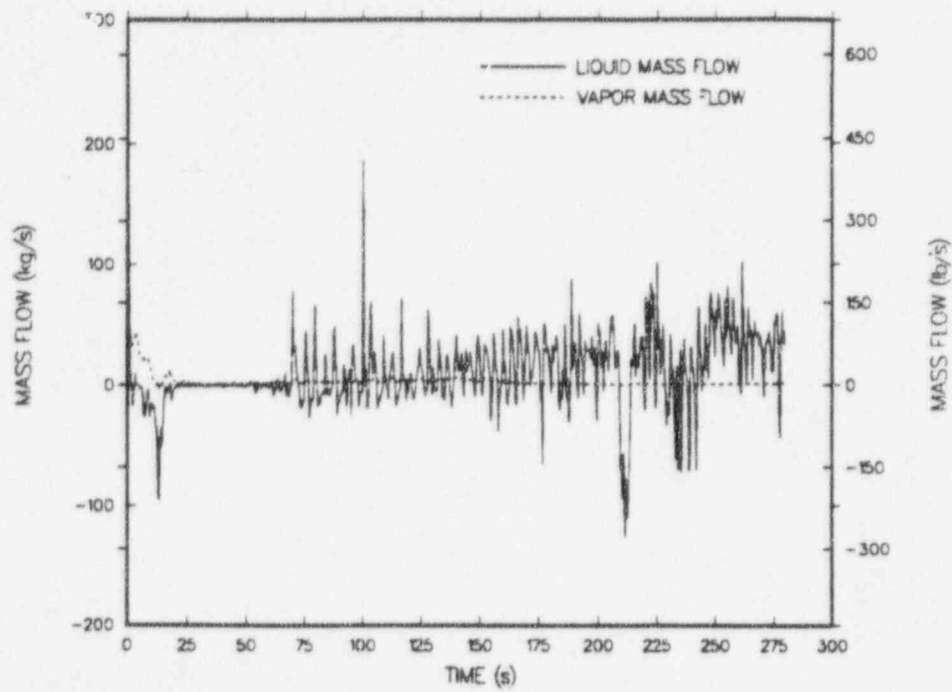


Fig. B-5. Core-outlet mass flow, core sector cell 5 ($r = 1, \theta = 5$).

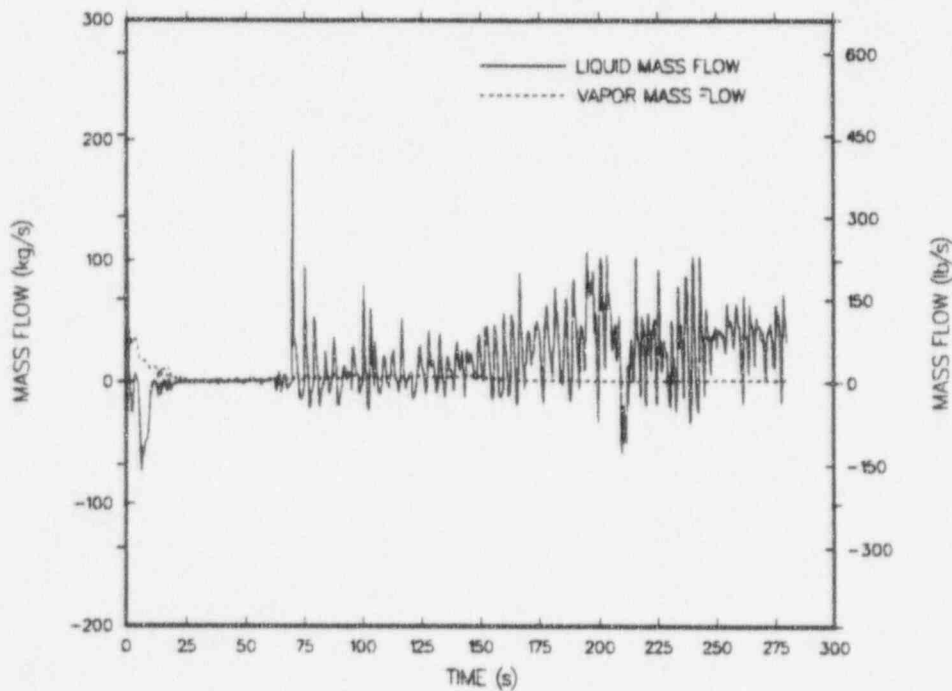


Fig. B-6. Core-outlet mass flow, core sector cell 6 ($r = 1, \theta = 6$).

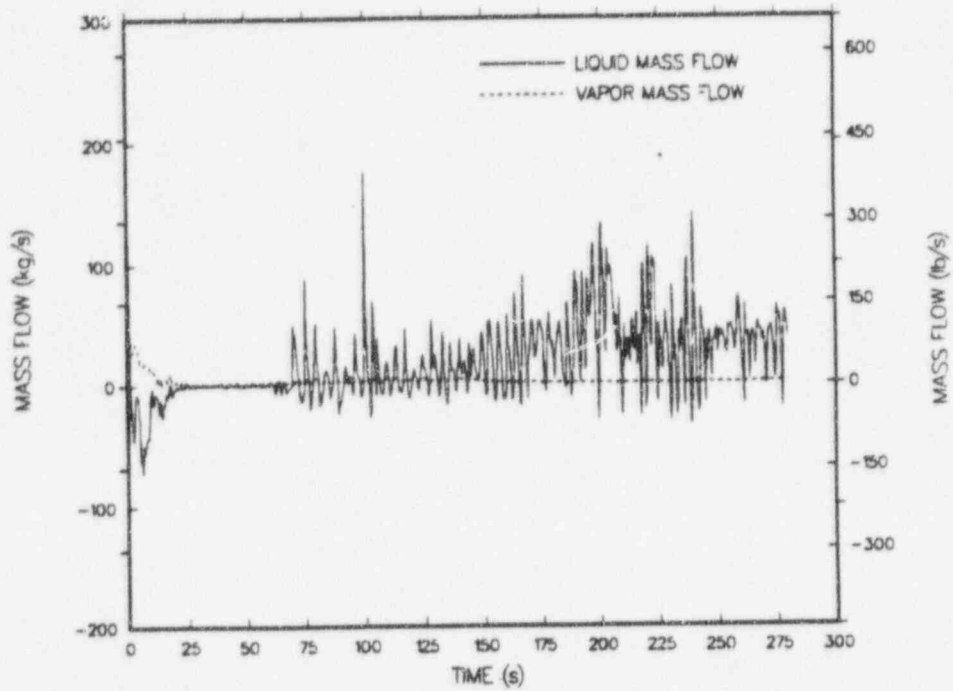


Fig. B-7. Core-outlet mass flow, core sector cell 7 ($r = 1, \theta = 7$).

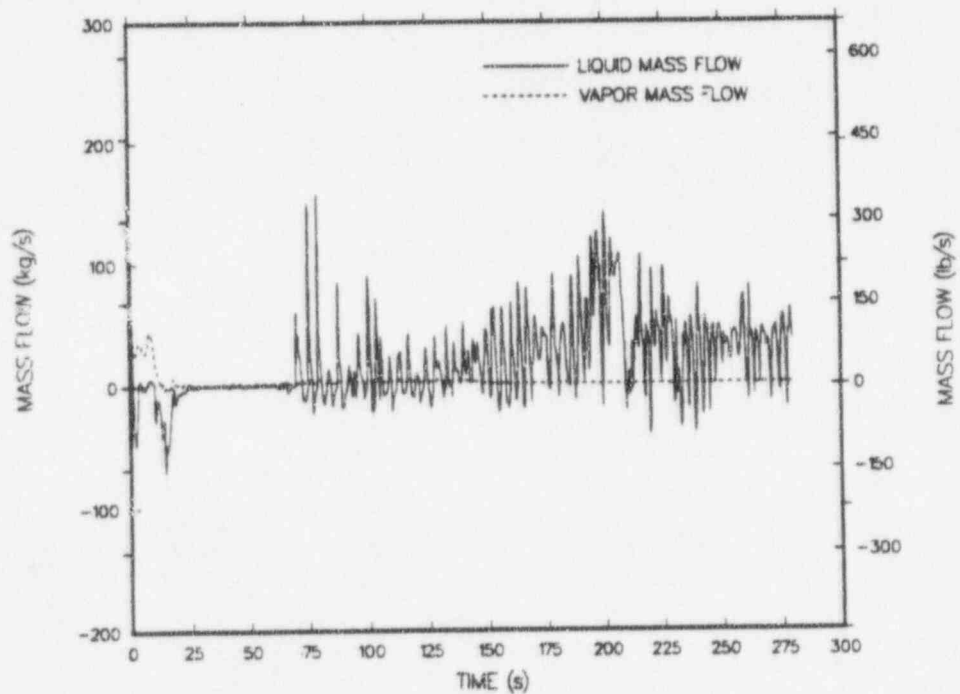


Fig. B-8. Core-outlet mass flow, core sector cell 8 ($r = 1, \theta = 8$).

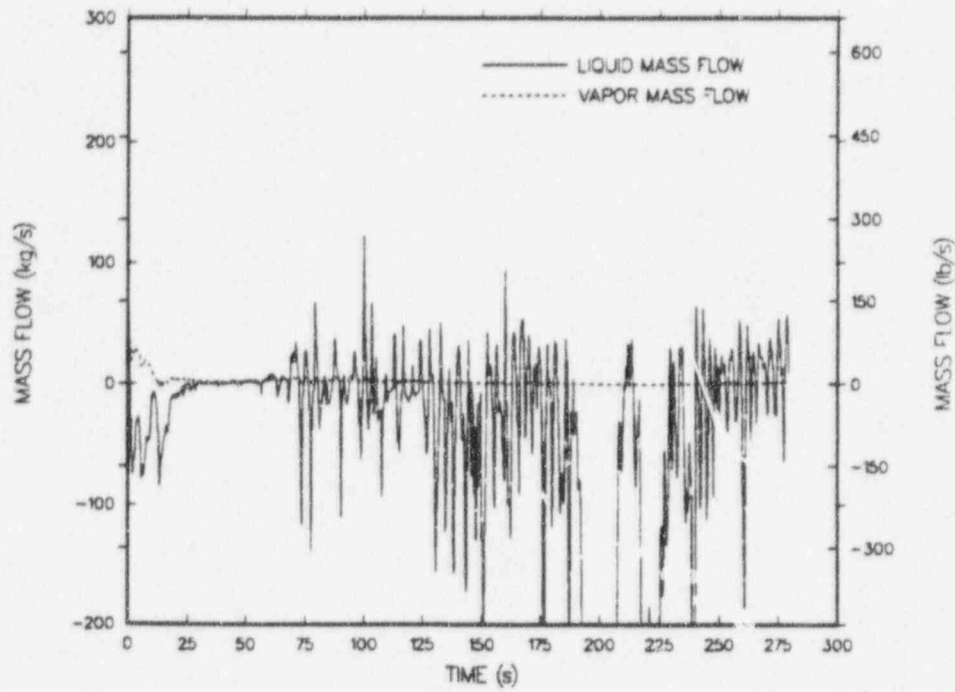


Fig. B-9. Core-outlet mass flow, core sector cell 9 ($r = 2, \theta = 1$).

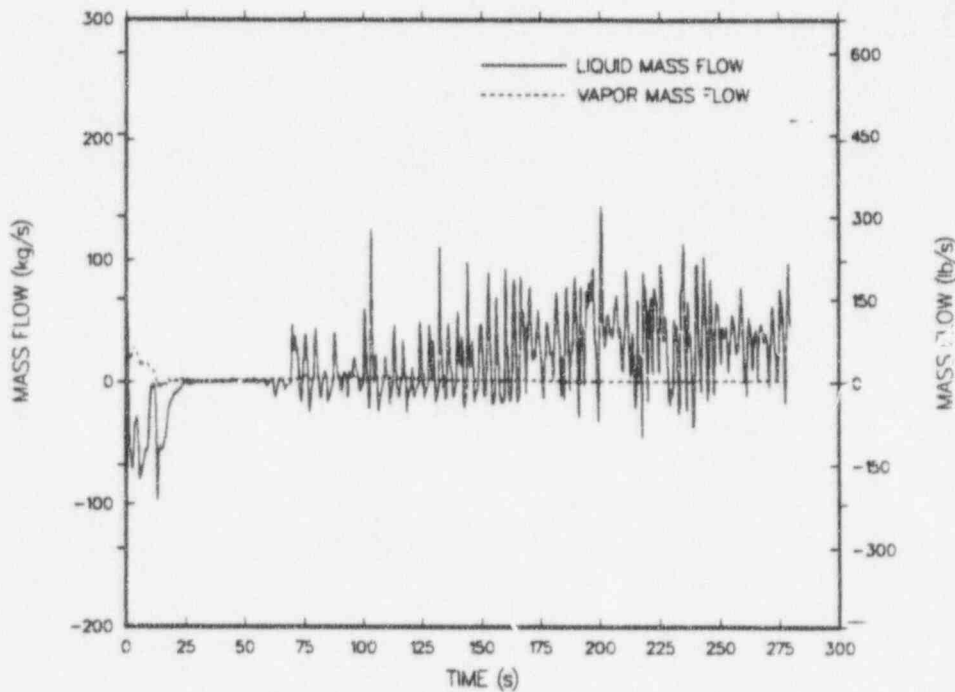


Fig. B-10. Core-outlet mass flow, core sector cell 10 ($r = 2, \theta = 2$).

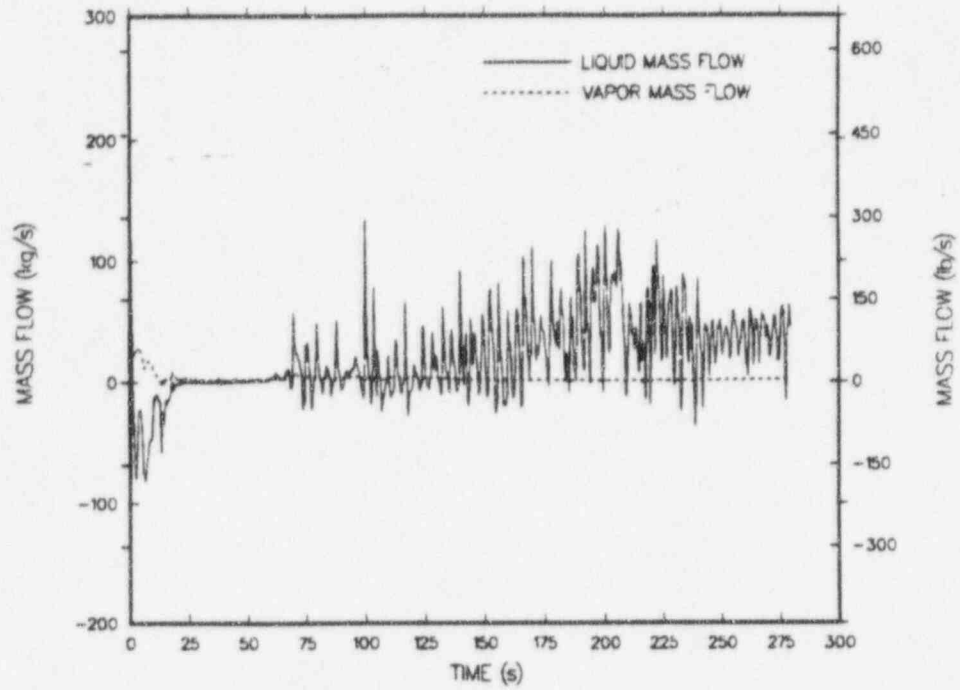


Fig. B-11. Core-outlet mass flow, core sector cell 11 ($r = 2, \theta = 3$).

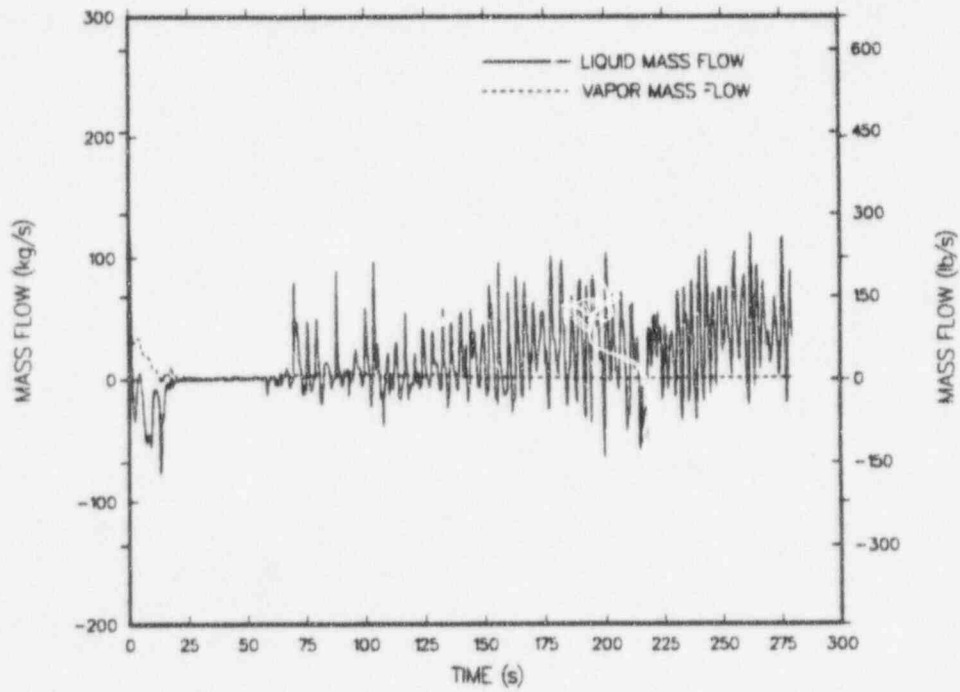


Fig. B-12. Core-outlet mass flow, core sector cell 12 ($r = 2, \theta = 4$).

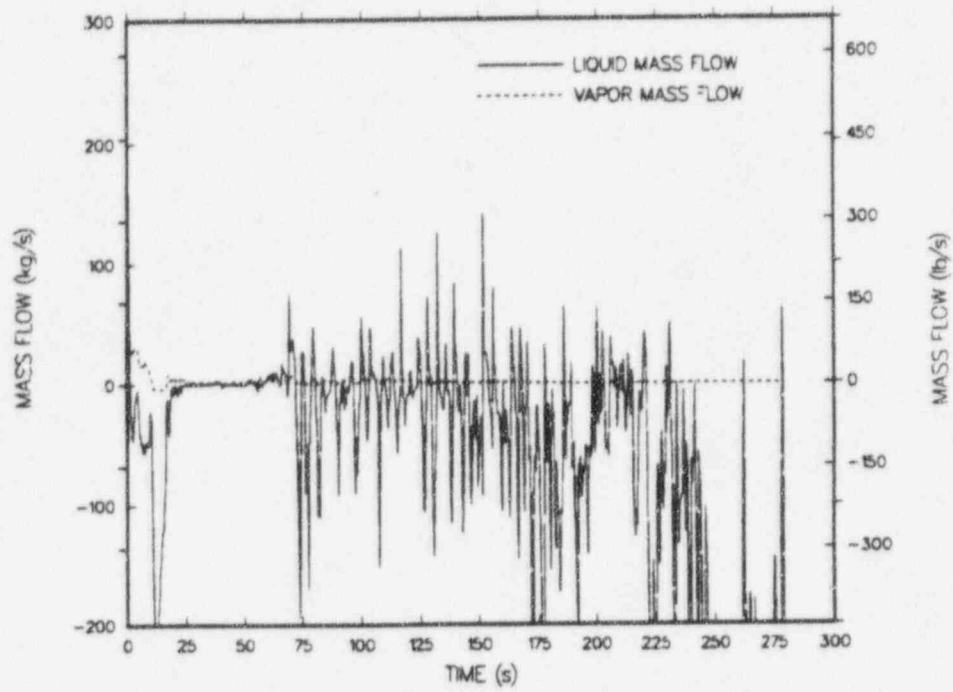


Fig. B-13. Core-outlet mass flow, core sector cell 13 ($r = 2, \theta = 5$).

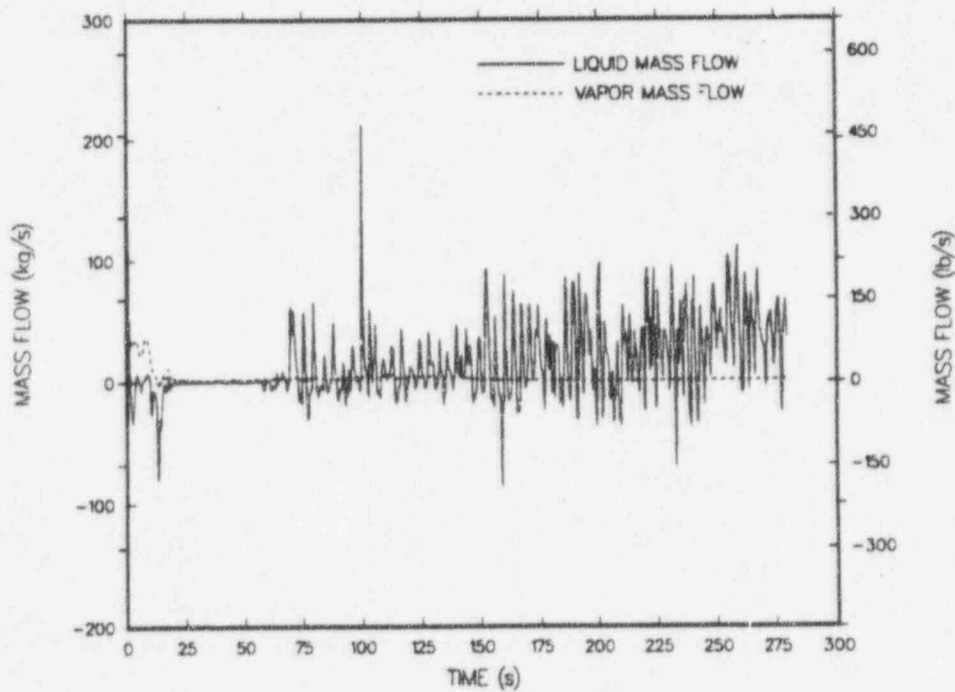


Fig. B-14. Core-outlet mass flow, core sector cell 14 ($r = 2, \theta = 6$).

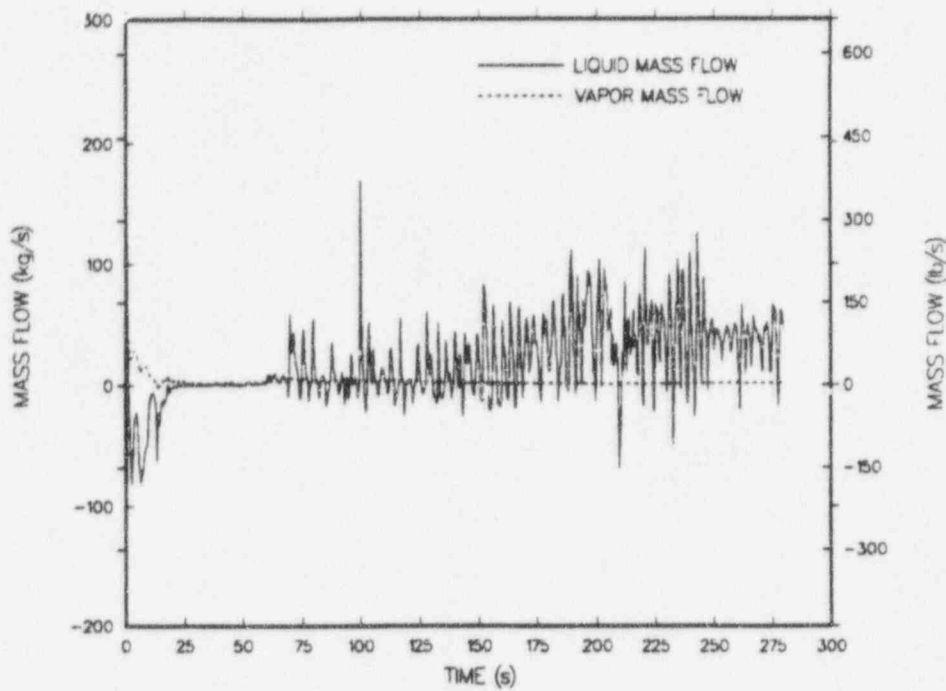


Fig. B-15. Core-outlet mass flow, core sector cell 15 ($r = 2, \theta = 7$).

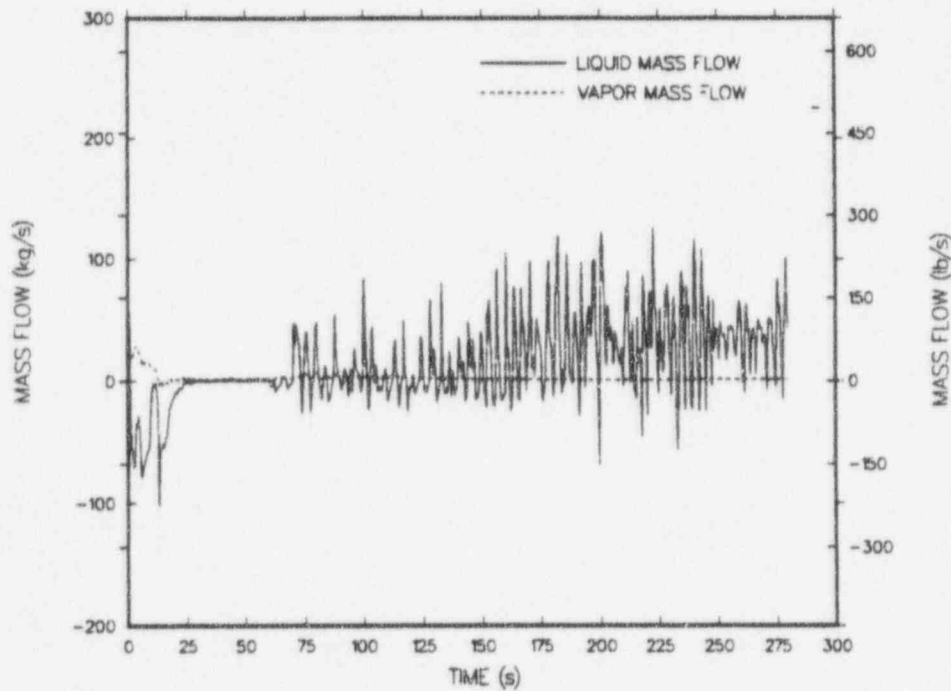


Fig. B-16. Core-outlet mass flow, core sector cell 16 ($r = 2, \theta = 8$).

APPENDIX C

AVERAGE-ROD CLADDING TEMPERATURES

Figures C-1 through C-16 depict average-rod cladding temperatures at selected rod elevations for each core sector cell. A noding diagram is provided in Fig. 6 of the main text.

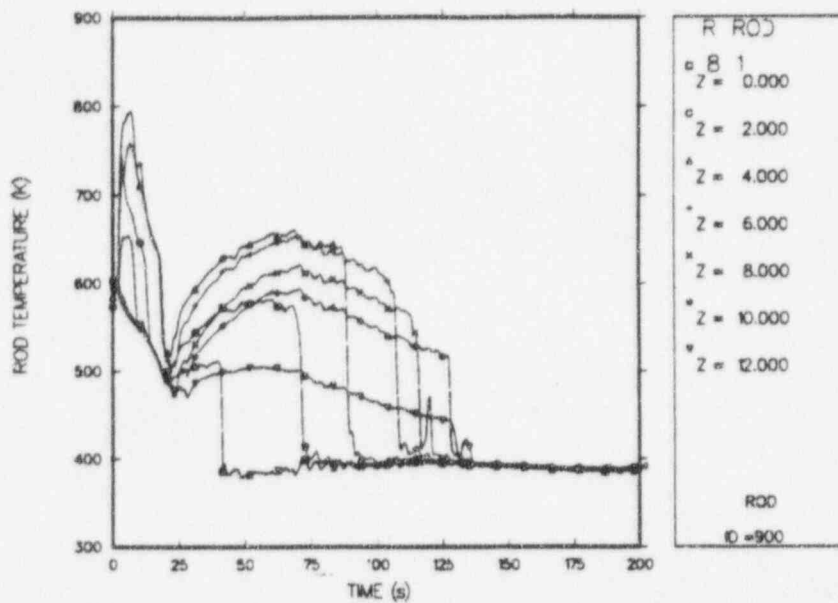


Fig. C-1. Average-rod cladding temperatures, core sector cell 1 ($r = 1$, $\theta = 1$).

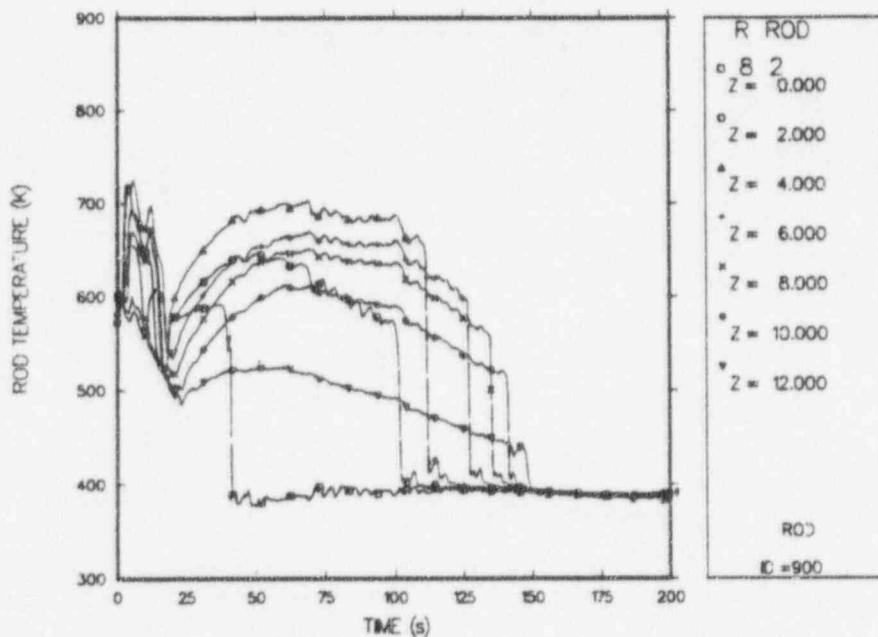


Fig. C-2. Average-rod cladding temperatures, core sector cell 2 ($r = 1$, $\theta = 2$).

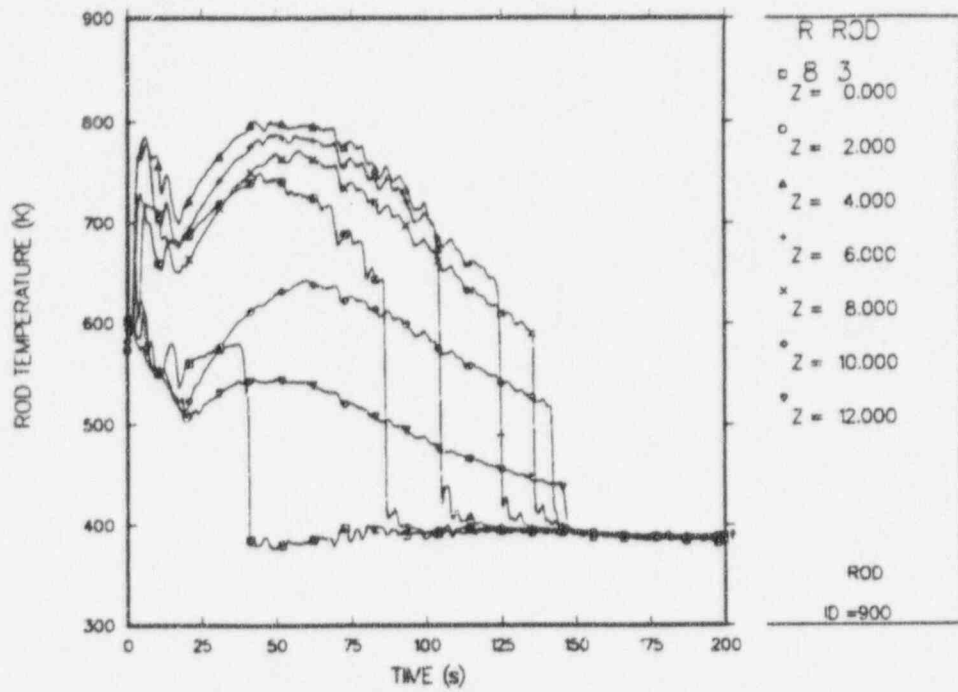


Fig. C-3. Average-rod cladding temperatures, core sector cell 3 ($r = 1, \theta = 3$).

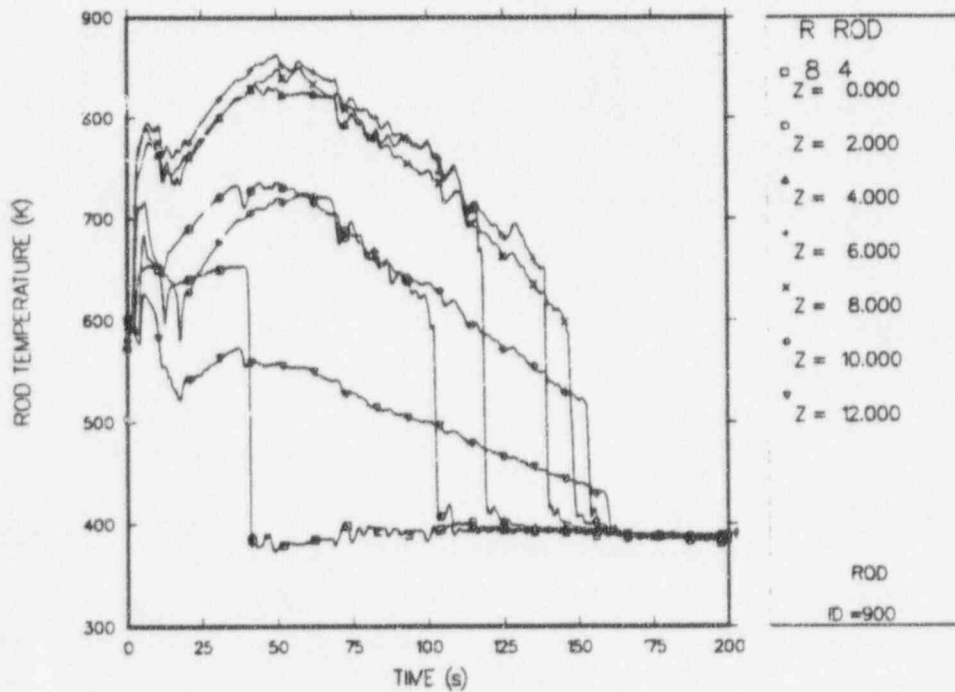


Fig. C-4. Average-rod cladding temperatures, core sector cell 4 ($r = 1, \theta = 4$).

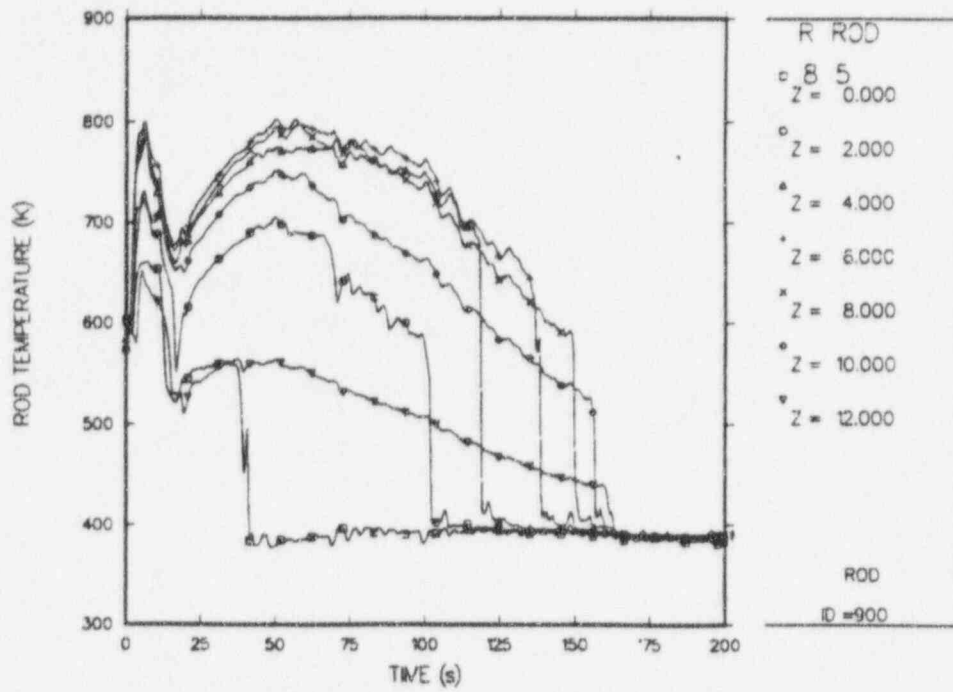


Fig. C-5. Average-rod cladding temperatures, core sector cell 5 ($r = 1, \theta = 5$).

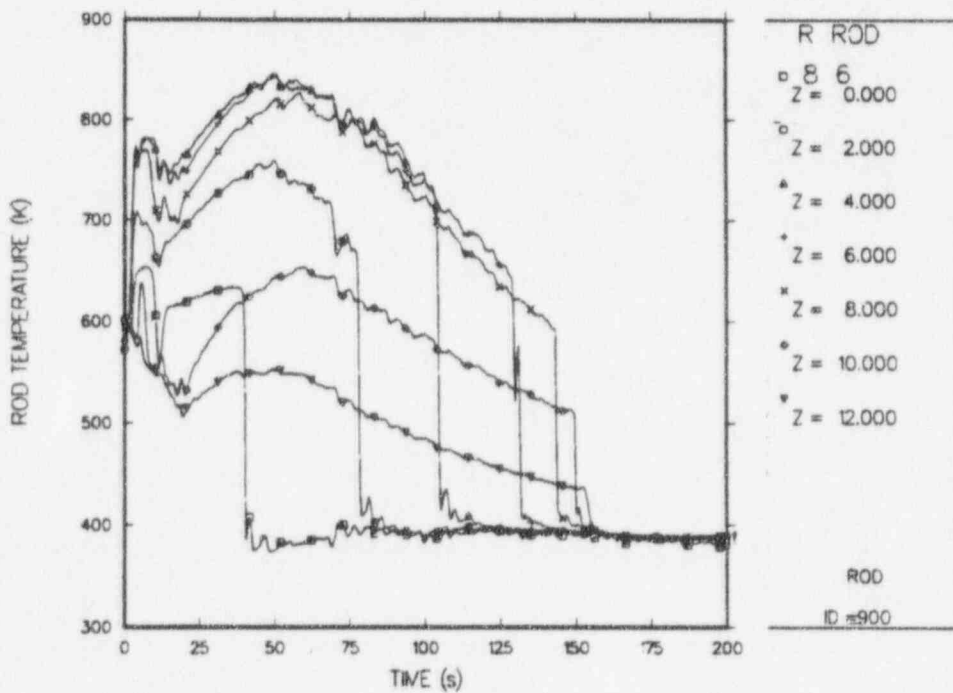


Fig. C-6. Average-rod cladding temperatures, core sector cell 6 ($r = 1, \theta = 6$).

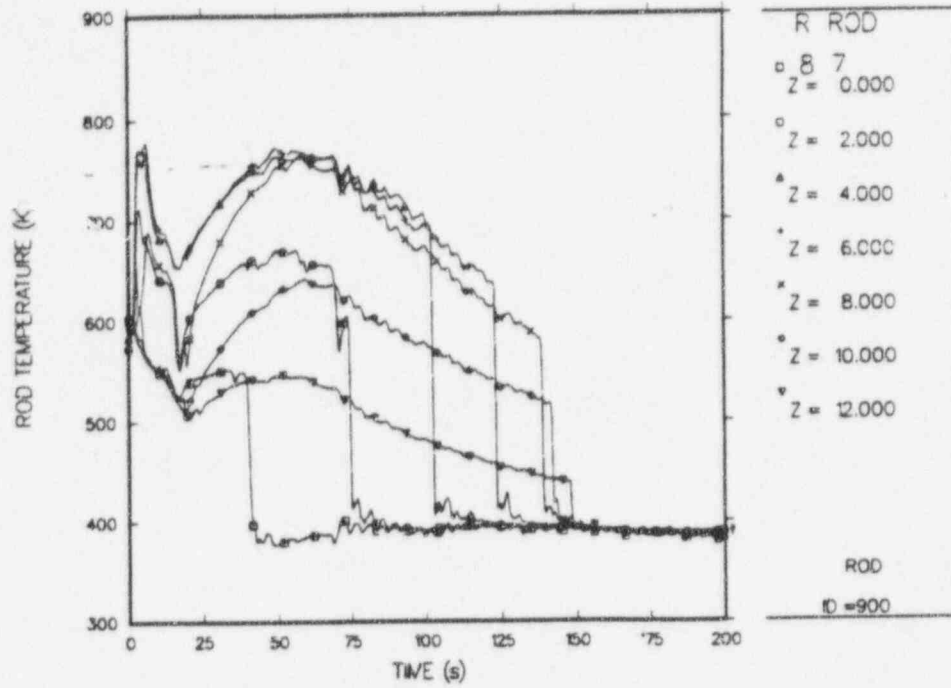


Fig. C-7. Average-rod cladding temperatures, core sector cell 7 ($r = 1, \theta = 7$).

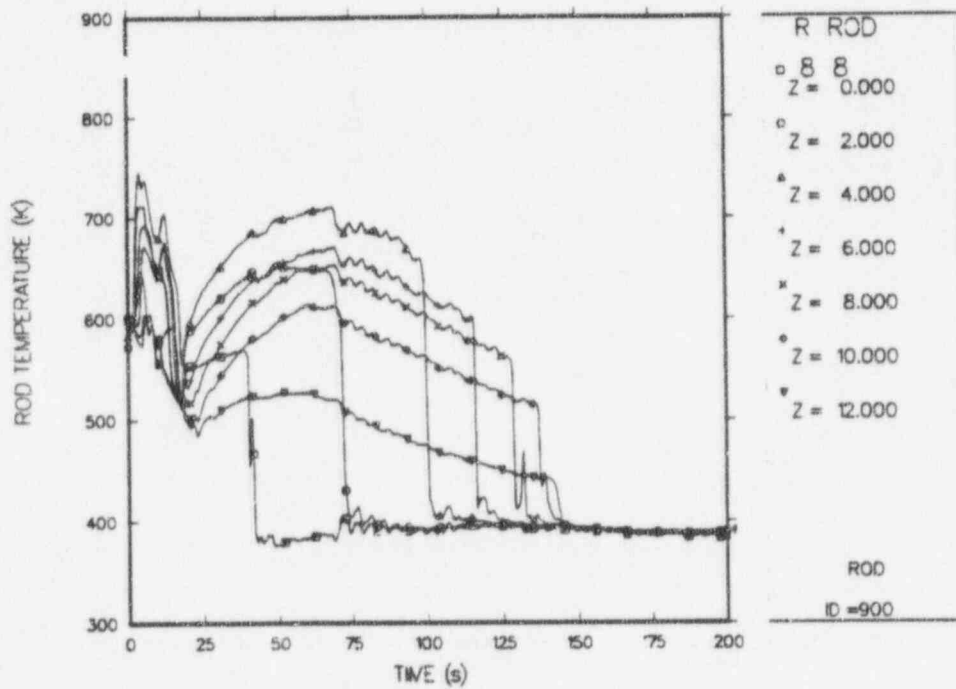


Fig. C-8. Average-rod cladding temperatures, core sector cell 8 ($r = 1, \theta = 8$).

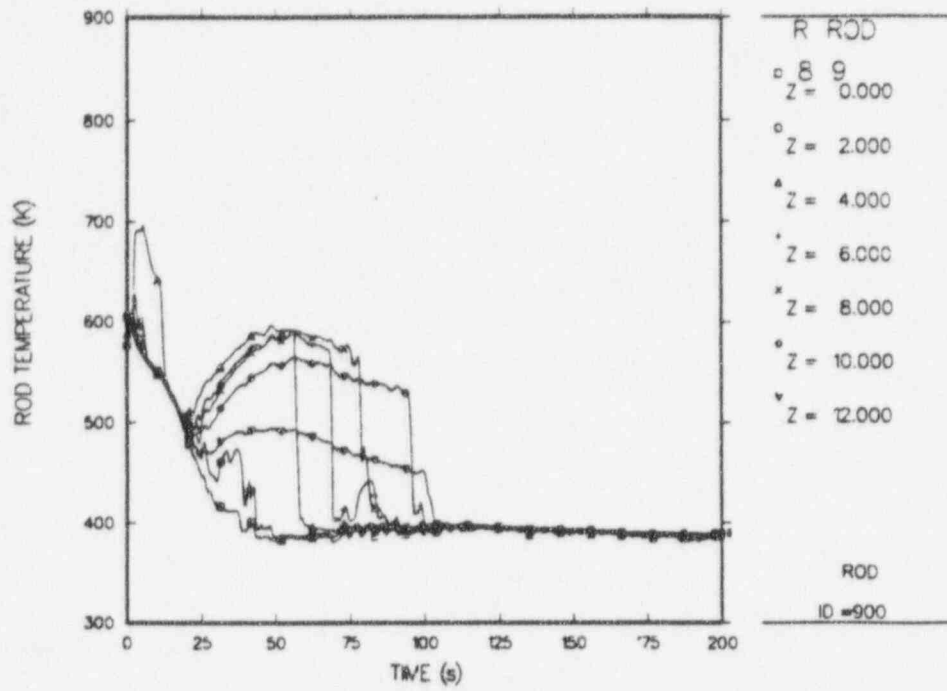


Fig. C-9. Average-rod cladding temperatures, core sector cell 9 ($r = 2, \theta = 1$).

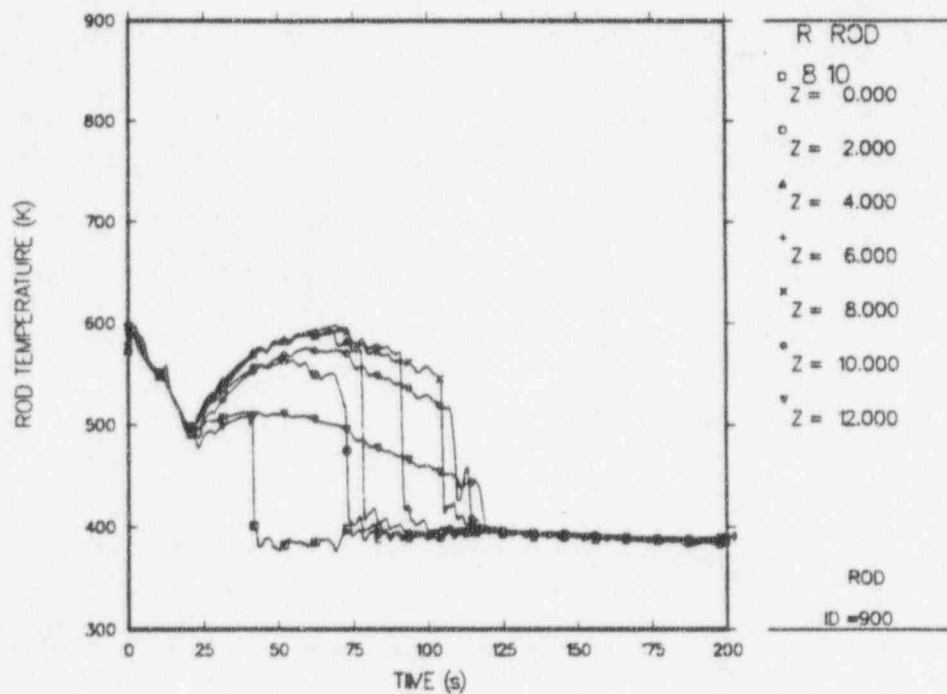


Fig. C-10. Average-rod cladding temperatures, core sector cell 10 ($r = 2, \theta = 2$).

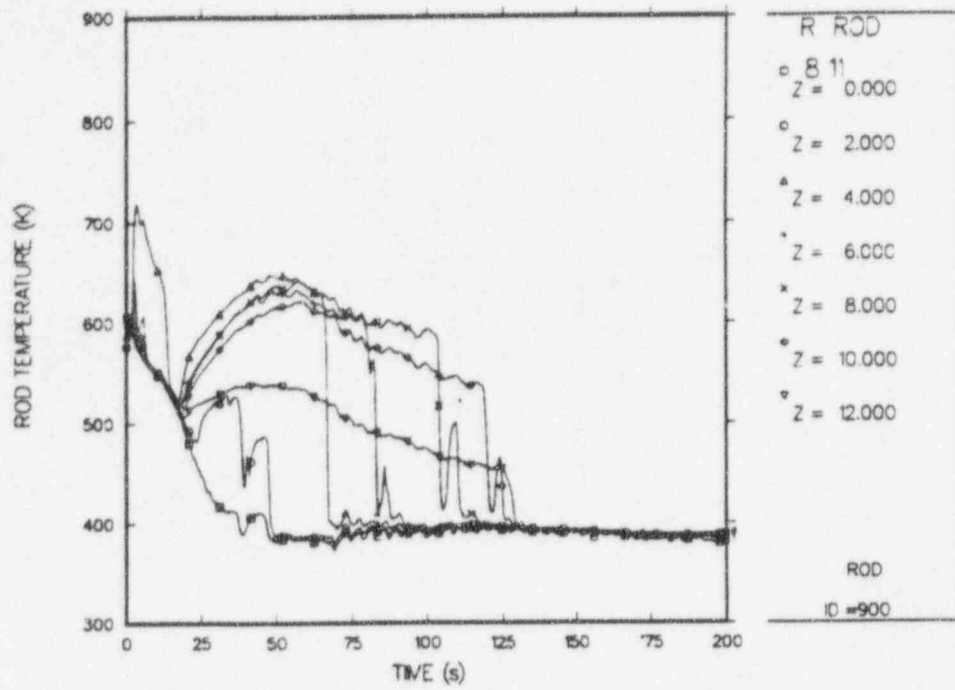


Fig. C-11. Average-rod cladding temperatures, core sector cell 11 ($r = 2$, $\theta = 3$).

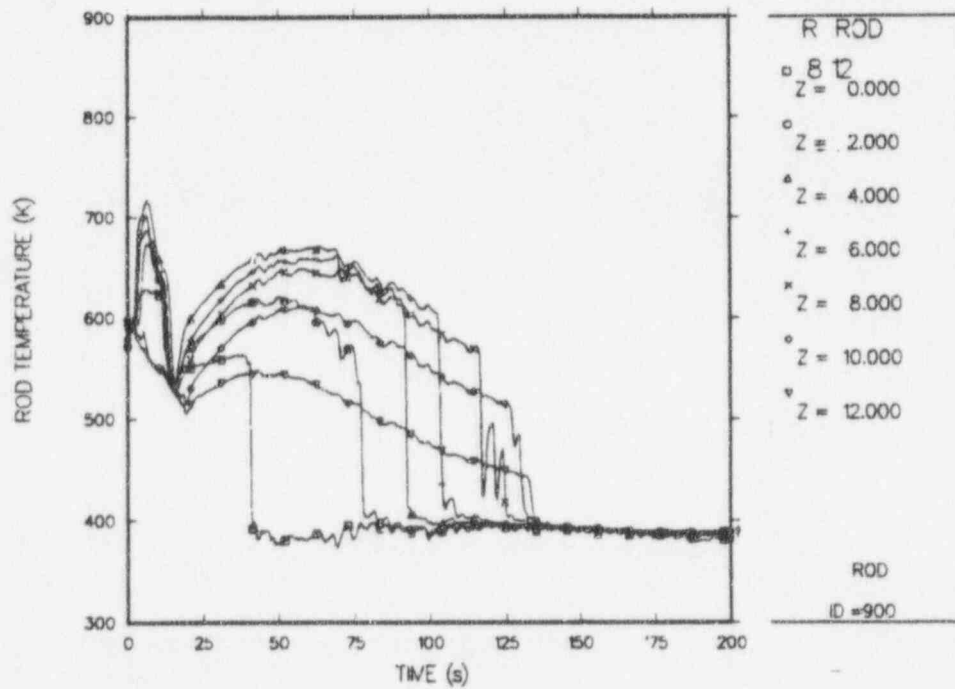


Fig. C-12. Average-rod cladding temperatures, core sector cell 12 ($r = 2$, $\theta = 4$).

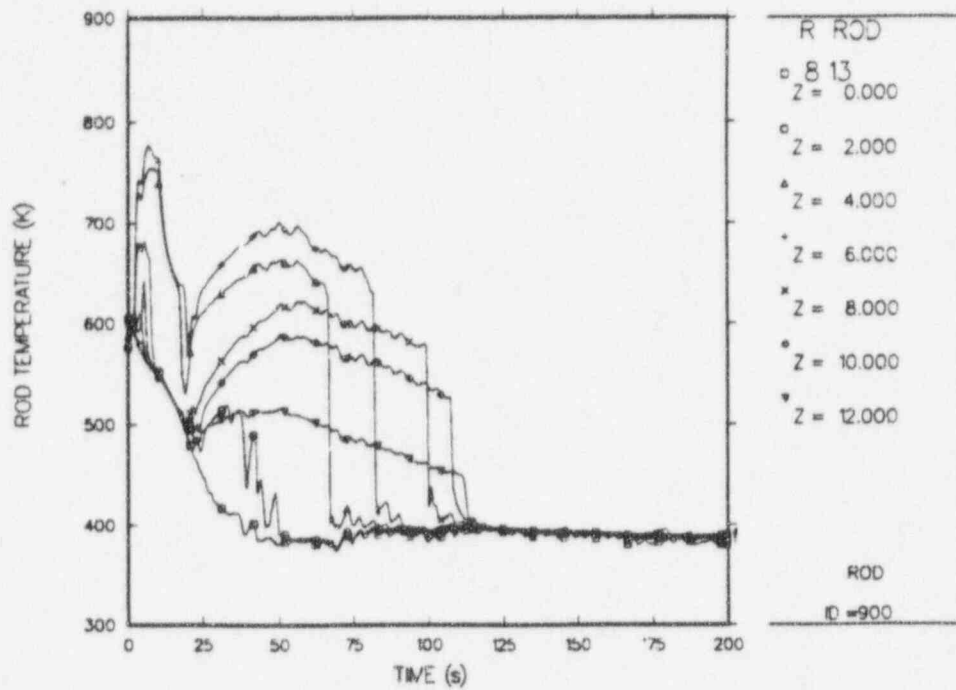


Fig. C-13. Average-rod cladding temperatures, core sector cell 13 ($r = 2, \theta = 5$).

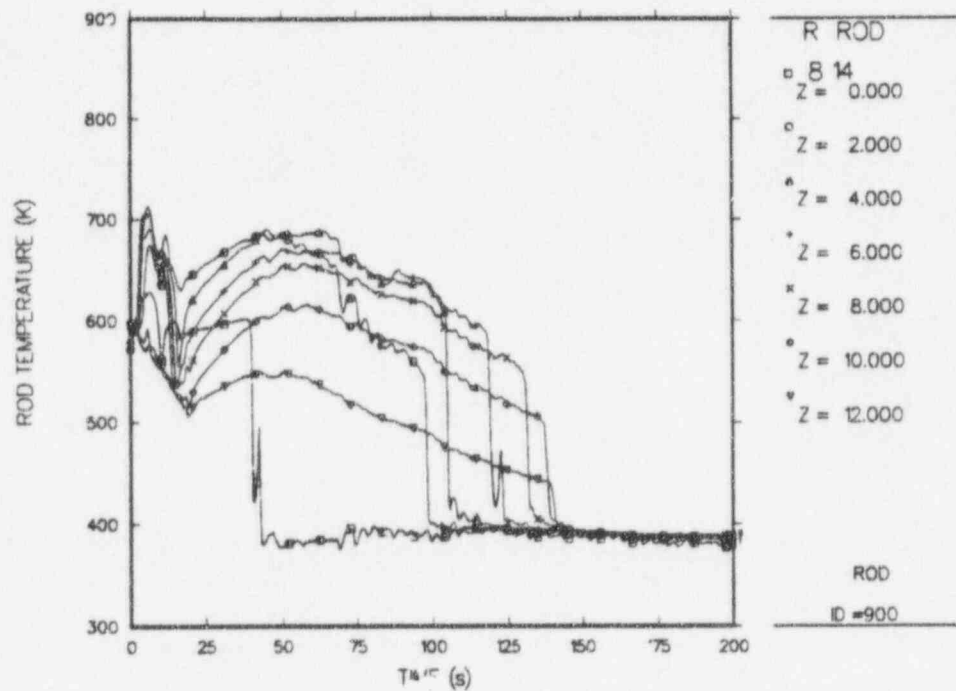


Fig. C-14. Average-rod cladding temperatures, core sector cell 14 ($r = 2, \theta = 6$).

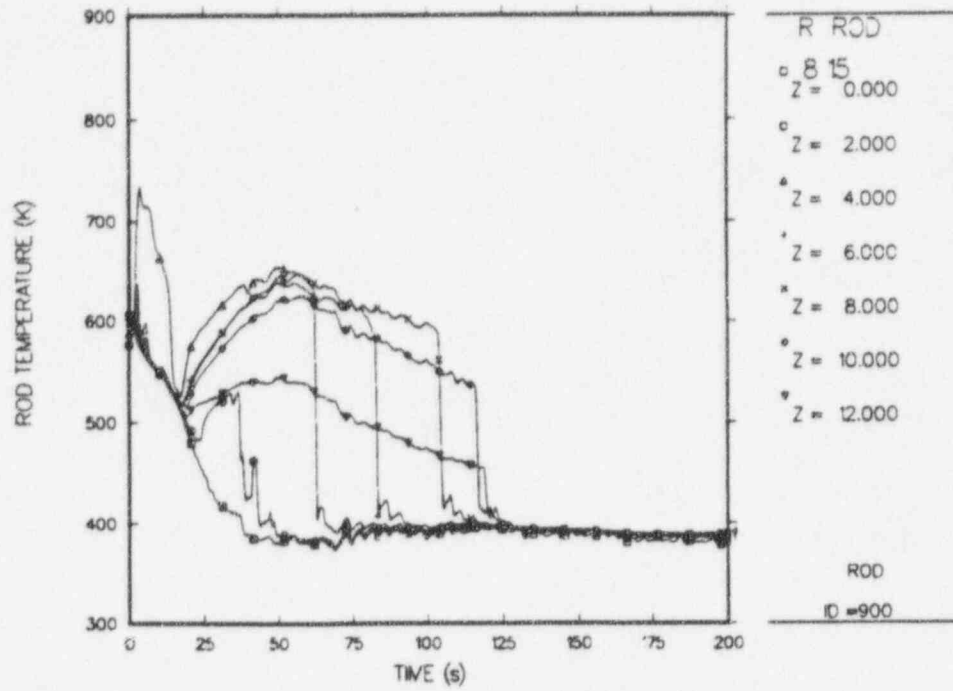


Fig. C-15. Average-rod cladding temperatures, core sector cell 15 ($r = 2$, $\theta = 7$).

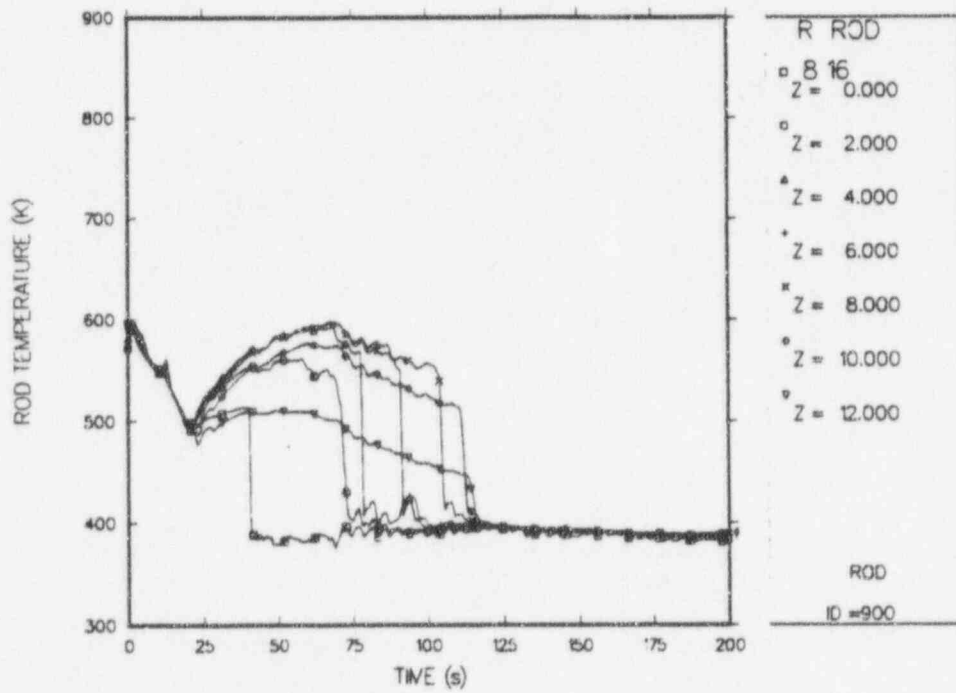


Fig. C-16. Average-rod cladding temperatures, core sector cell 16 ($r = 2$, $\theta = 8$).

APPENDIX D

HOT-ROD CLADDING TEMPERATURES

Figures D-1 through D-16 depict hot-rod cladding temperatures at selected rod elevations for each core sector cell. A noding diagram is provided in Fig. 6 of the main text.

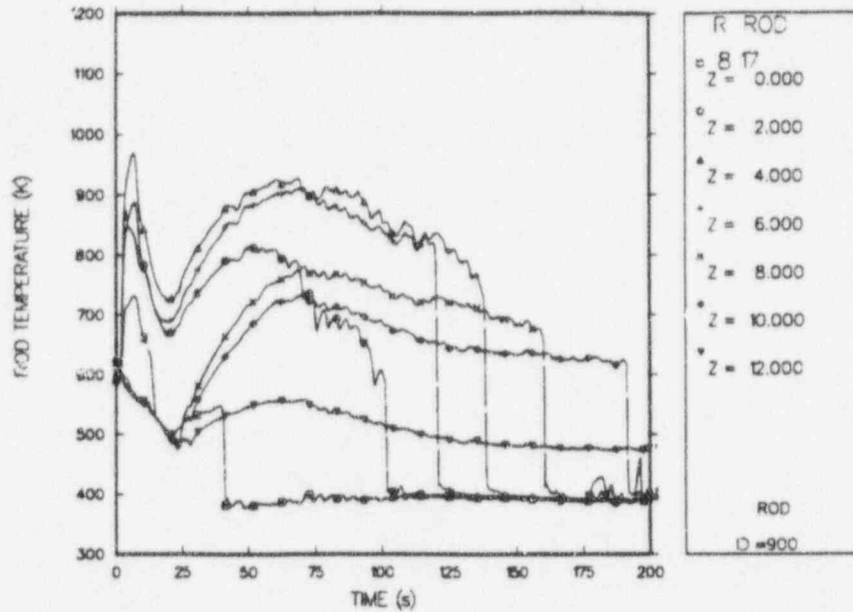


Fig. D-1. Hot-rod cladding temperatures, core sector cell 1 ($r = 1, \theta = 1$).

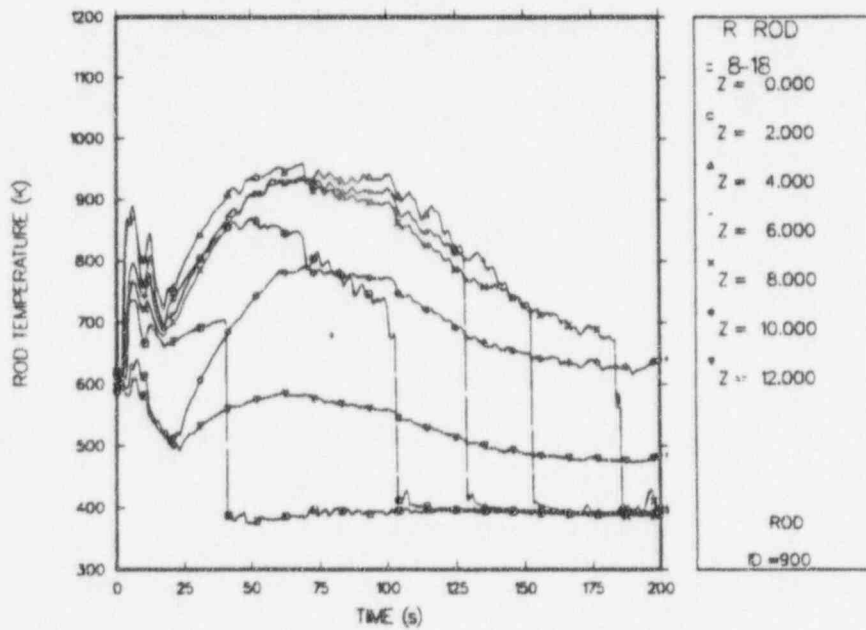


Fig. D-2. Hot-rod cladding temperatures, core sector cell 2 ($r = 1, \theta = 2$).

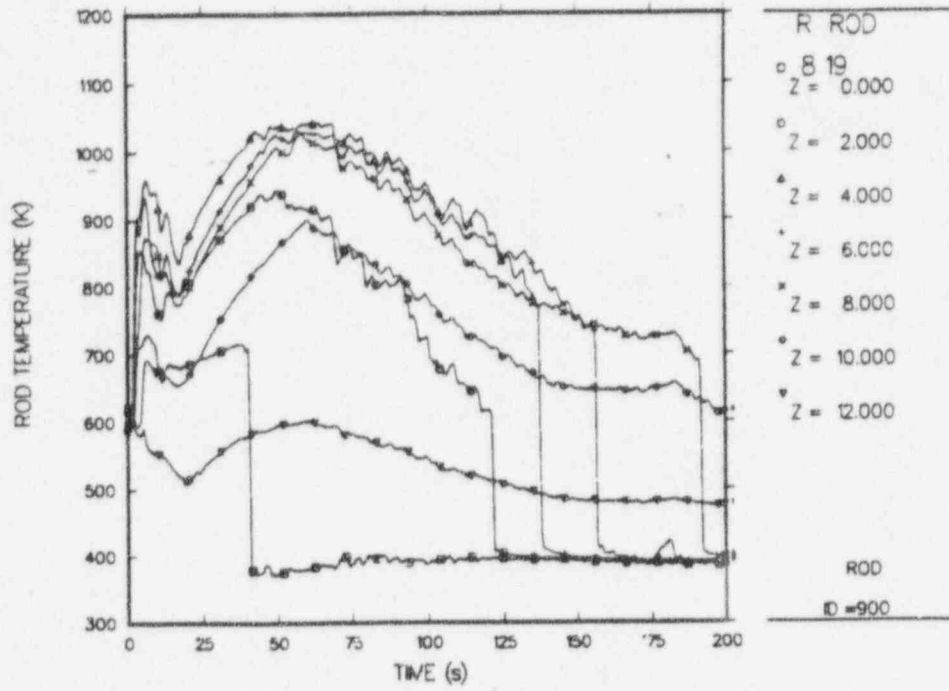


Fig. D-3. Hot-rod cladding temperatures, core sector cell 3 ($r = 1, \theta = 3$).

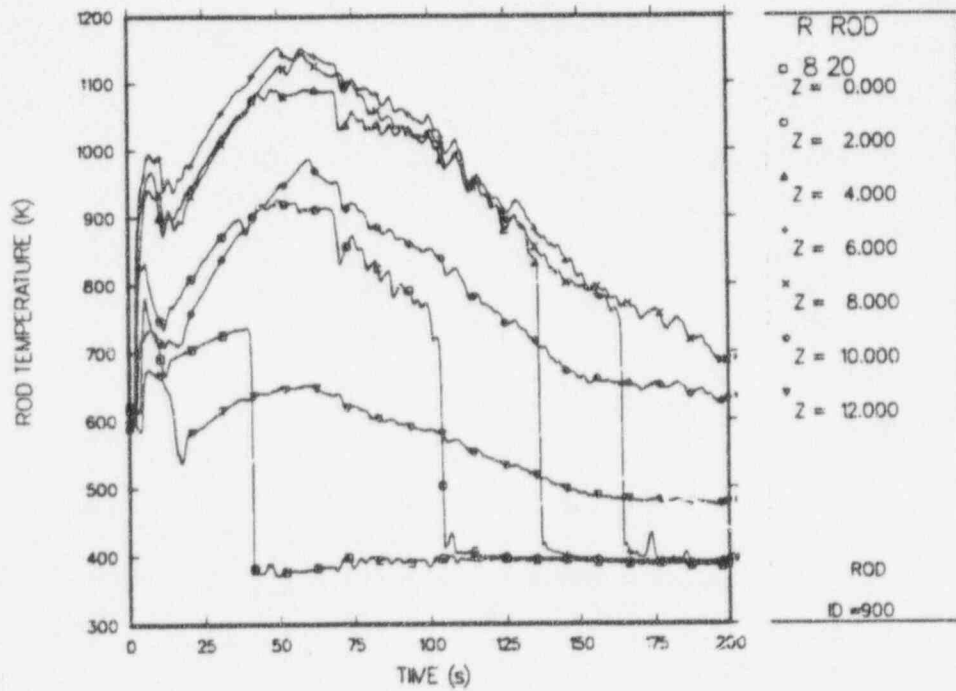


Fig. D-4. Hot-rod cladding temperatures, core sector cell 4 ($r = 1, \theta = 4$).

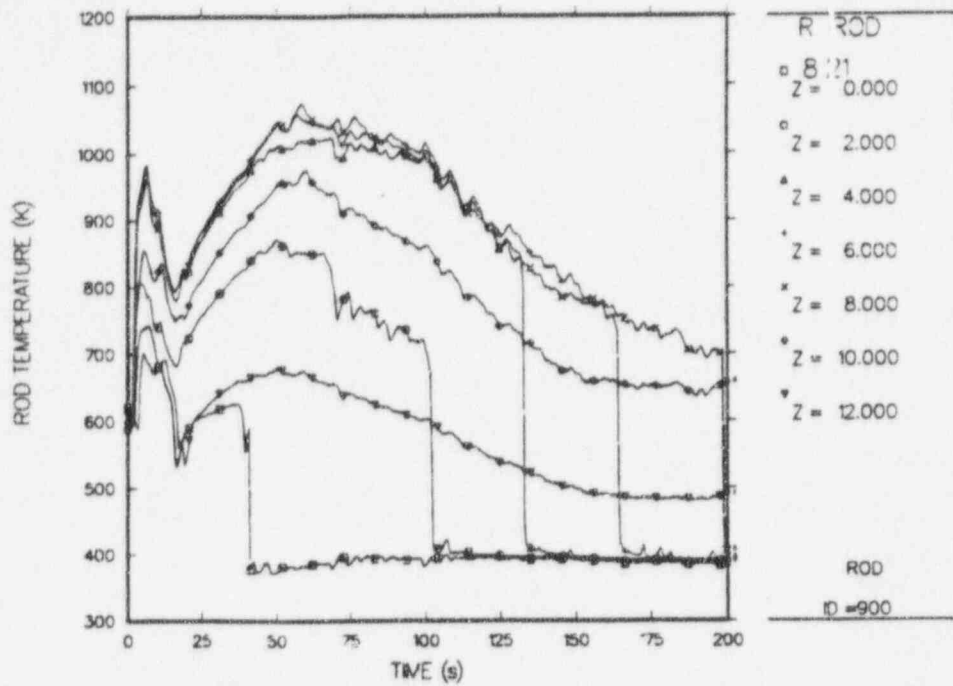


Fig. D-5. Hot-rod cladding temperatures, core sector cell 5 ($r = 1, \theta = 5$).

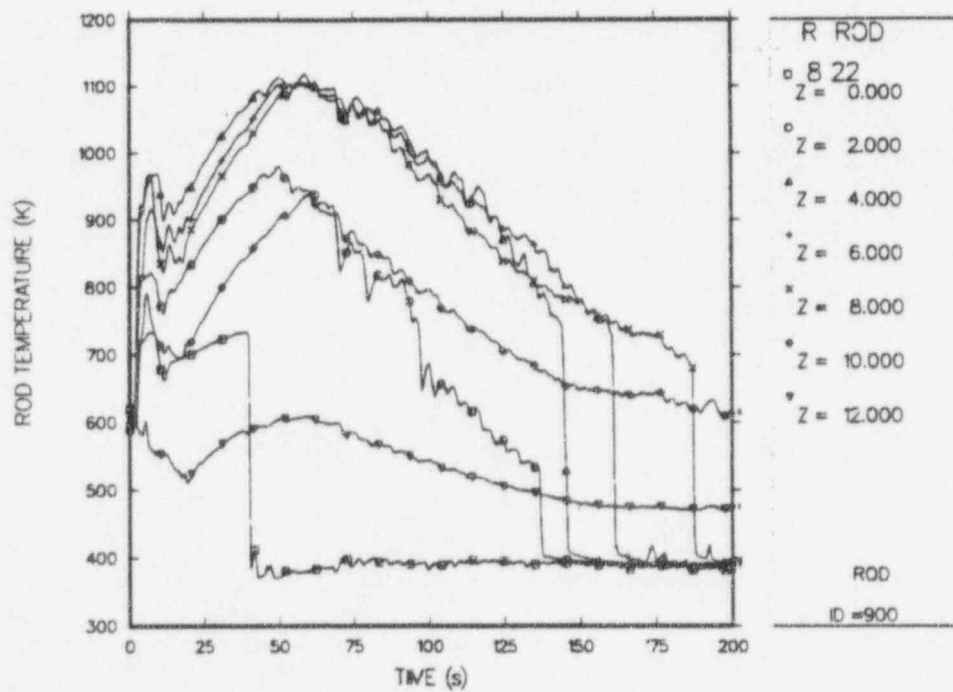


Fig. D-6. Hot-rod cladding temperatures, core sector cell 6 ($r = 1, \theta = 6$).

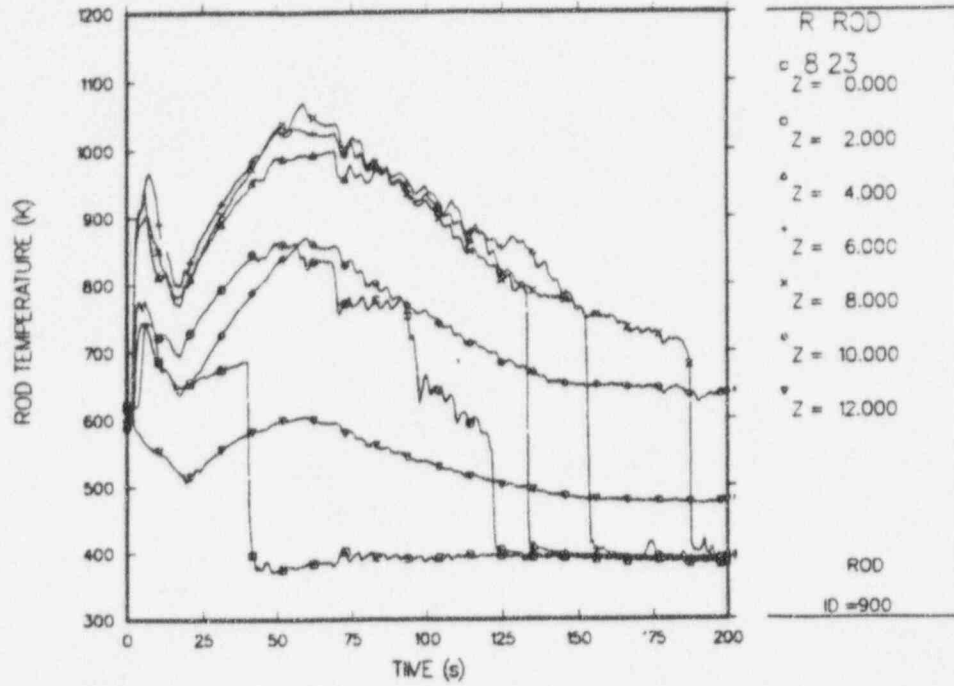


Fig. D-7. Hot-rod cladding temperatures, core sector cell 7 ($r = 1, \theta = 7$).

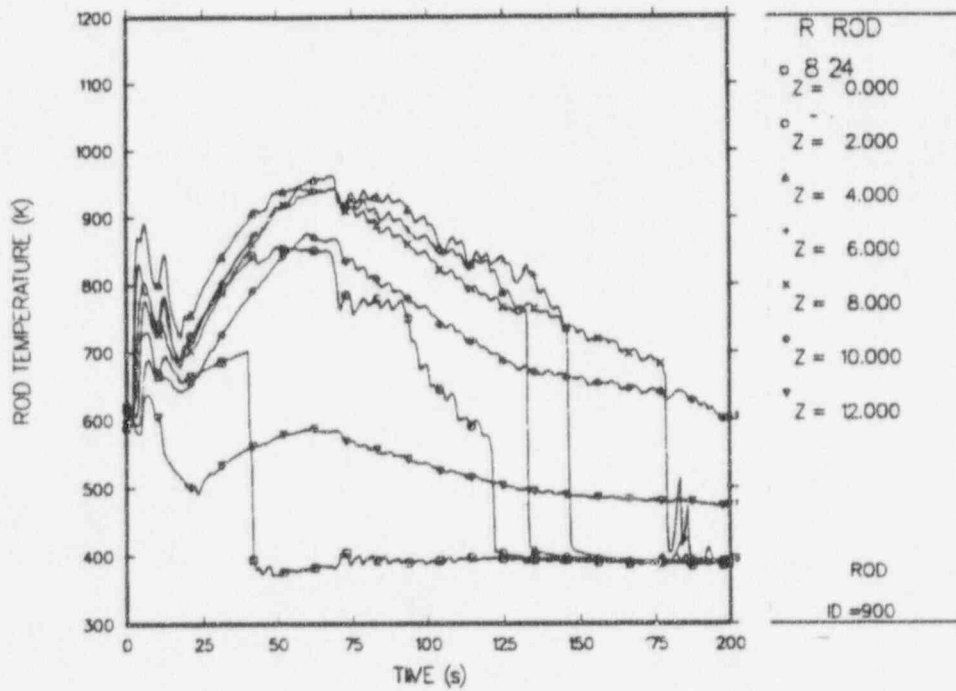


Fig. D-8. Hot-rod cladding temperatures, core sector cell 8 ($r = 1, \theta = 8$).

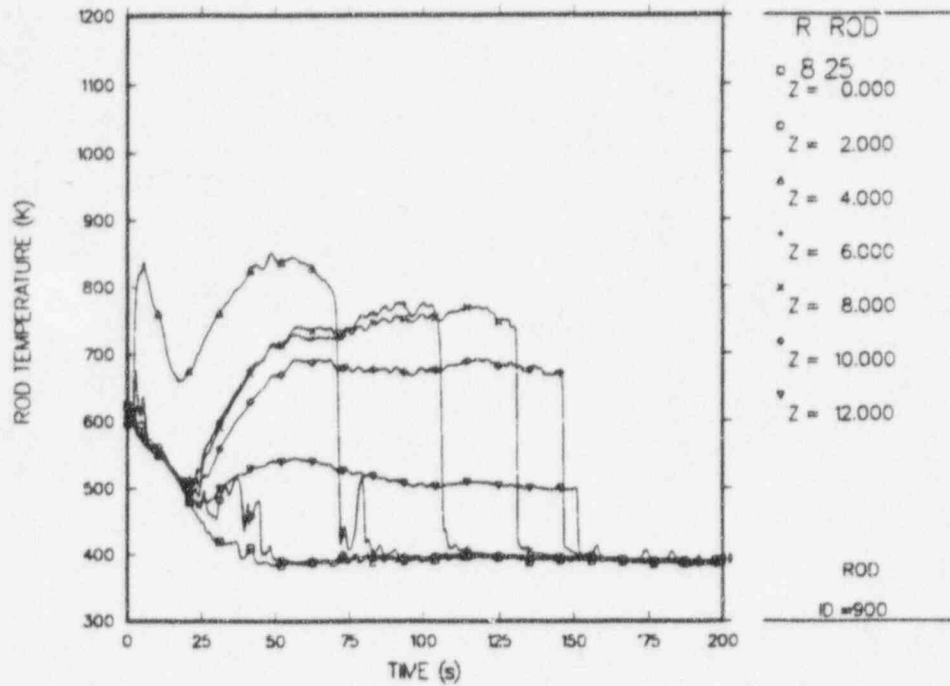


Fig. D-9. Hot-rod cladding temperatures, core sector cell 9 ($r = 2, \theta = 1$).

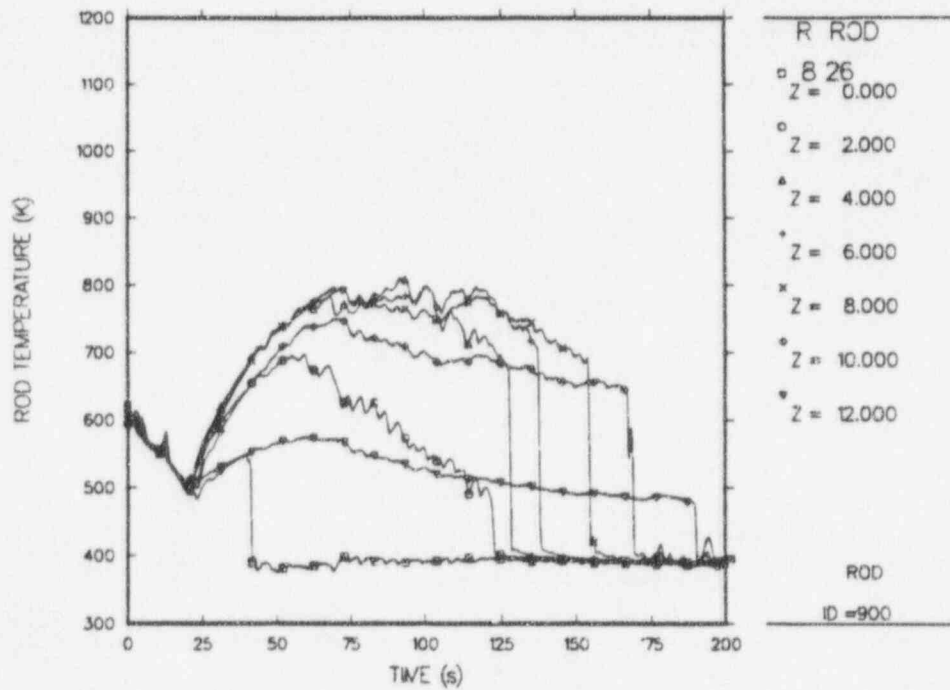


Fig. D-10. Hot-rod cladding temperatures, core sector cell 10 ($r = 2, \theta = 2$).

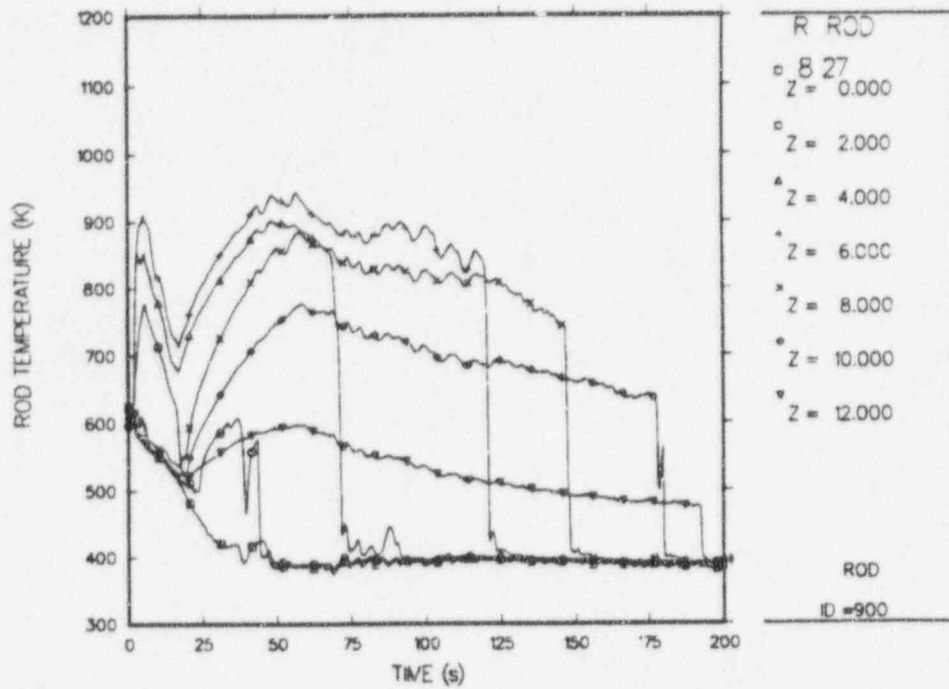


Fig. D-11. Hot-rod cladding temperatures, core sector cell 11 ($r = 2, \theta = 3$).

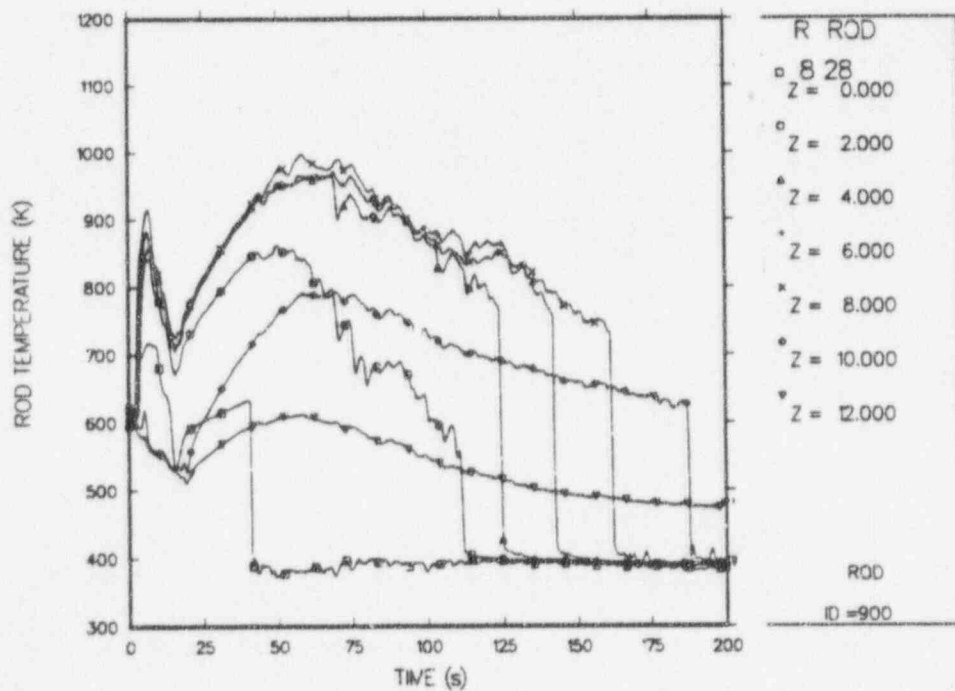


Fig. D-12. Hot-rod cladding temperatures, core sector cell 12 ($r = 2, \theta = 4$).

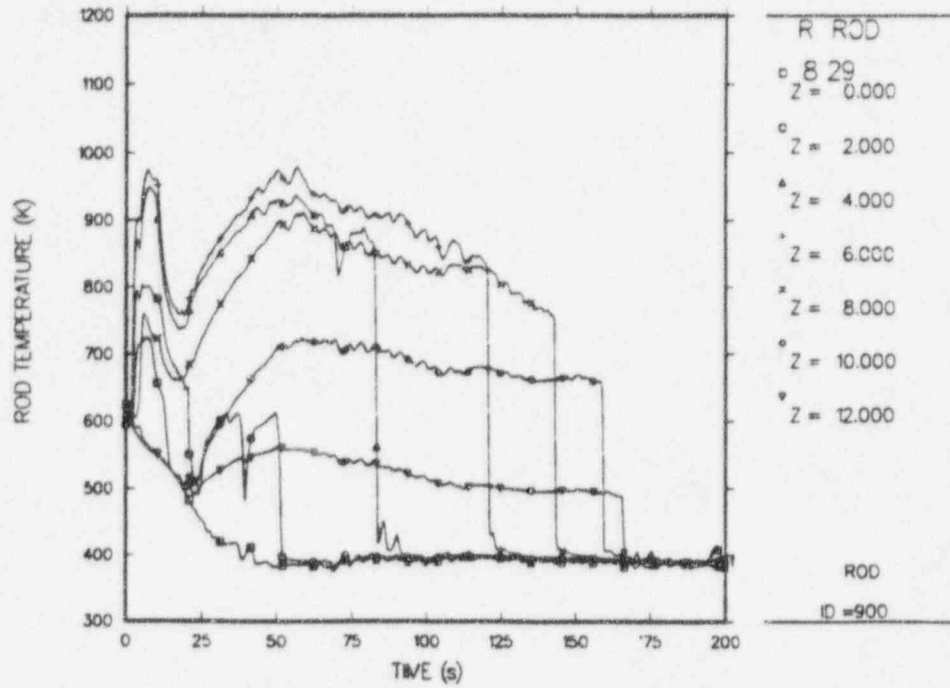


Fig. D-13. Hot-rod cladding temperatures, core sector cell 13 ($r = 2, \theta = 5$).

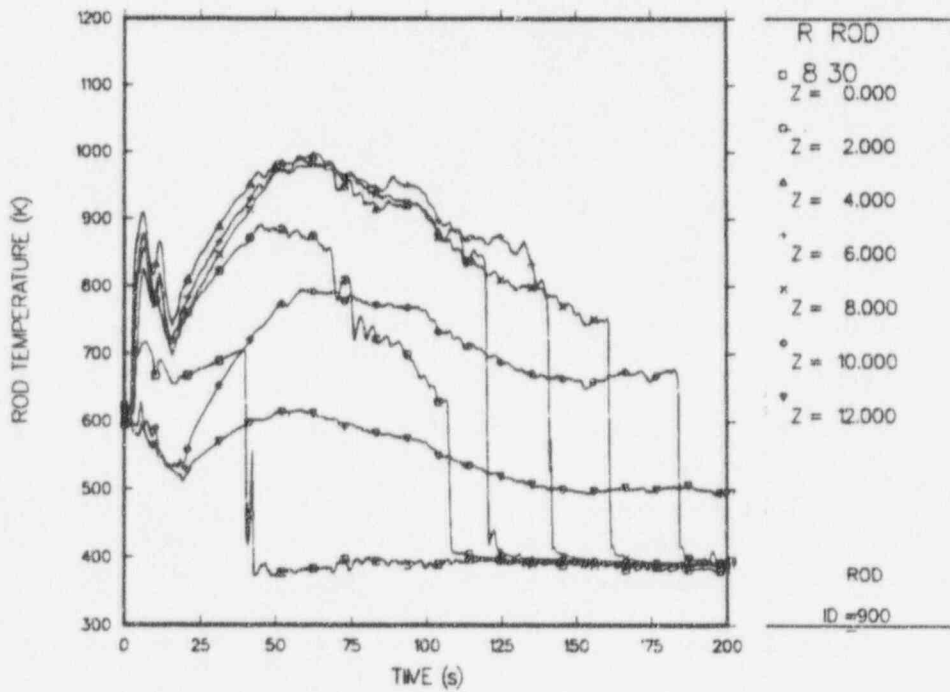


Fig. D-14. Hot-rod cladding temperatures, core sector cell 14 ($r = 2, \theta = 6$).

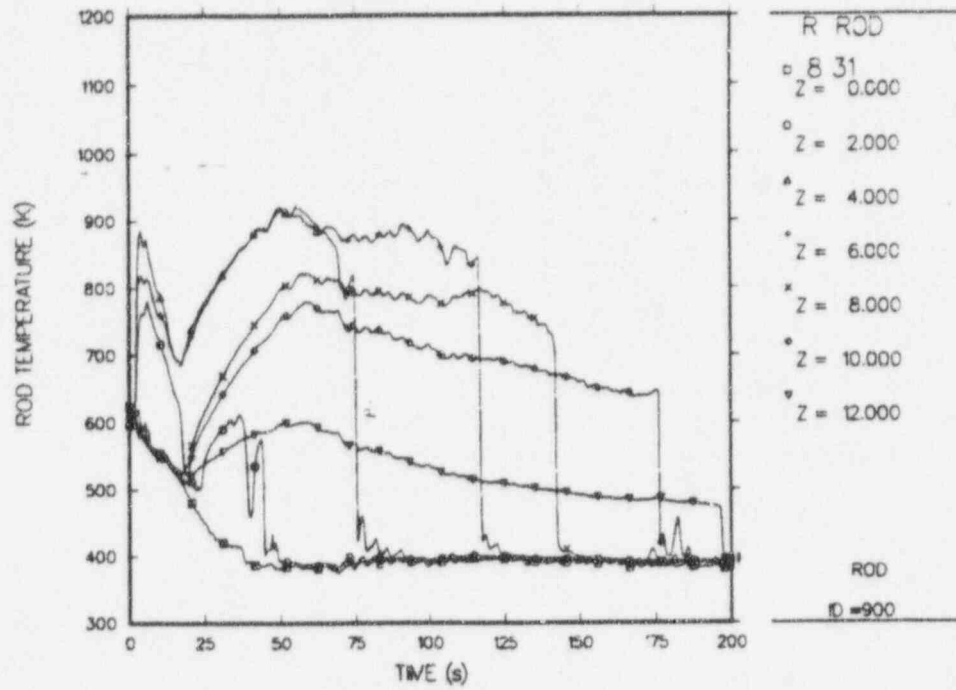


Fig. D-15. Hot-rod cladding temperatures, core sector cell 15 ($r = 2, \theta = 7$).

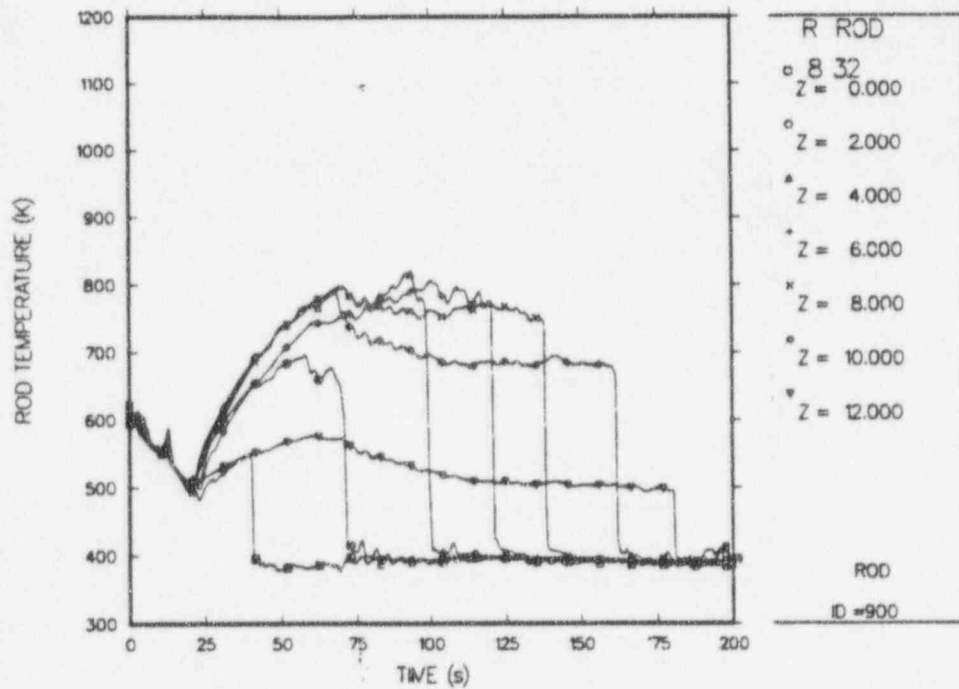


Fig. D-16. Hot-rod cladding temperatures, core sector cell 16 ($r = 2, \theta = 8$).

APPENDIX E

AVERAGE-ROD CLADDING TEMPERATURES VS ROD ELEVATION AT SELECTED TRANSIENT TIMES

Figures E-1 through E-16 depict average-rod cladding temperatures vs rod elevation at selected transient times for each core sector cell. Two plots are presented for each core sector cell. The first plot is for transient times of 0, 2.0, 3.0, 6.0, 8.0, and 10 s. The second plot is for transient times of 20, 40, 60, 80, 100, 120, and 140 s. A noding diagram is provided in Fig. 6 of the main text.

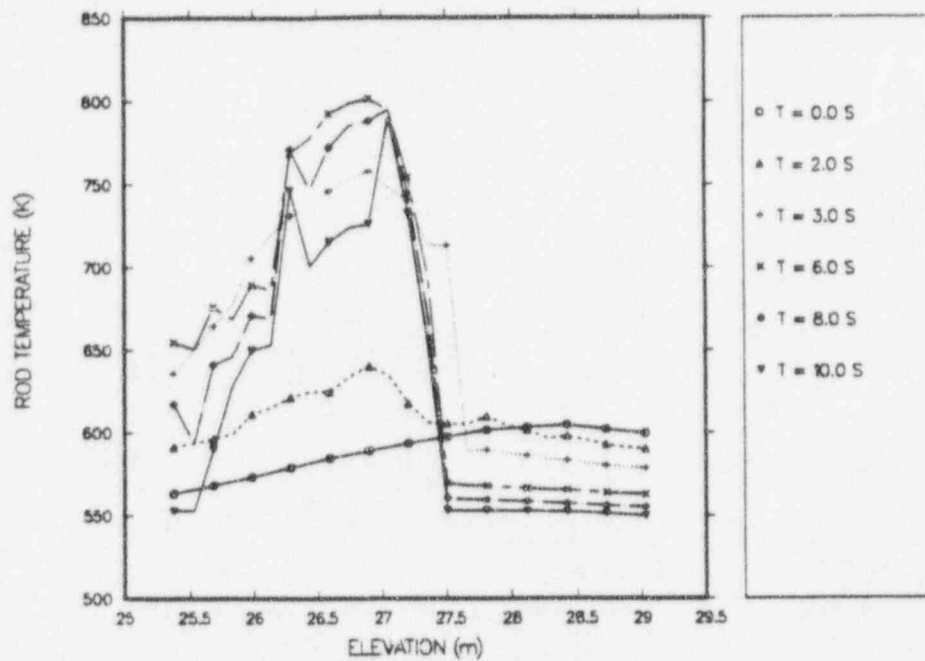


Fig. E-1a. Average-rod cladding temperatures vs core elevation at selected transient times from 0 to 10 s for core cell 1.

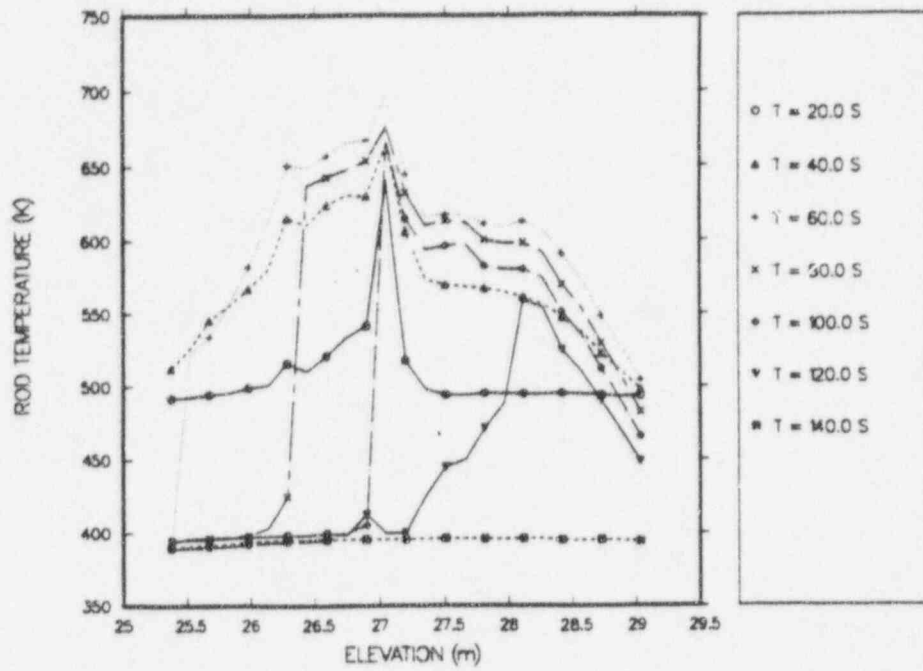


Fig. E-1b. Average-rod cladding temperatures vs core elevation at selected transient times from 20 to 140 s for core cell 1.

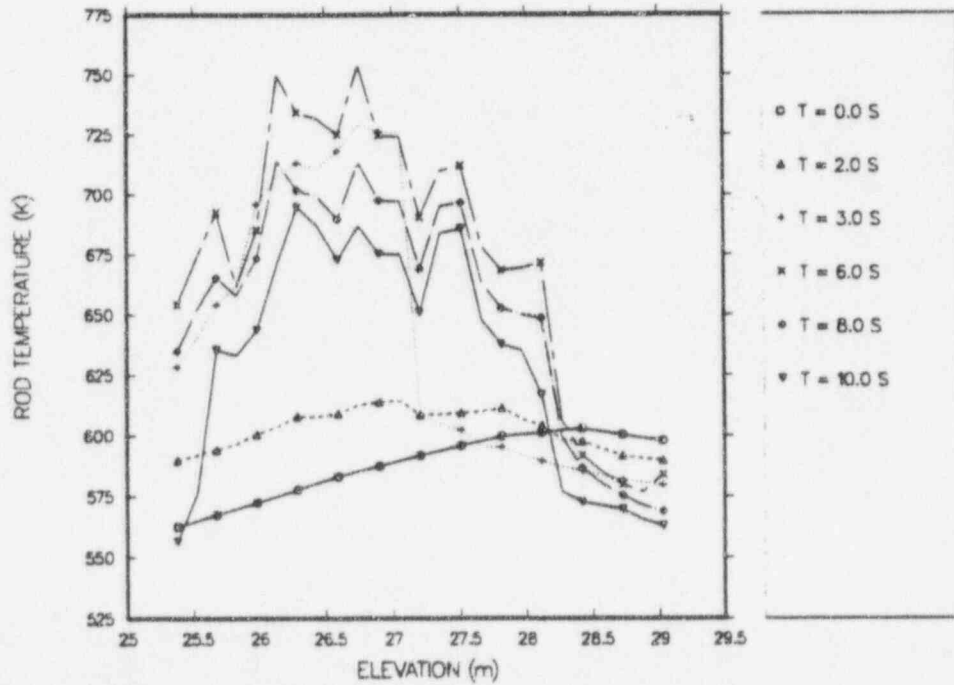


Fig. E-2a. Average-rod cladding temperatures vs core elevation at selected transient times from 0 to 10 s for core cell 2.

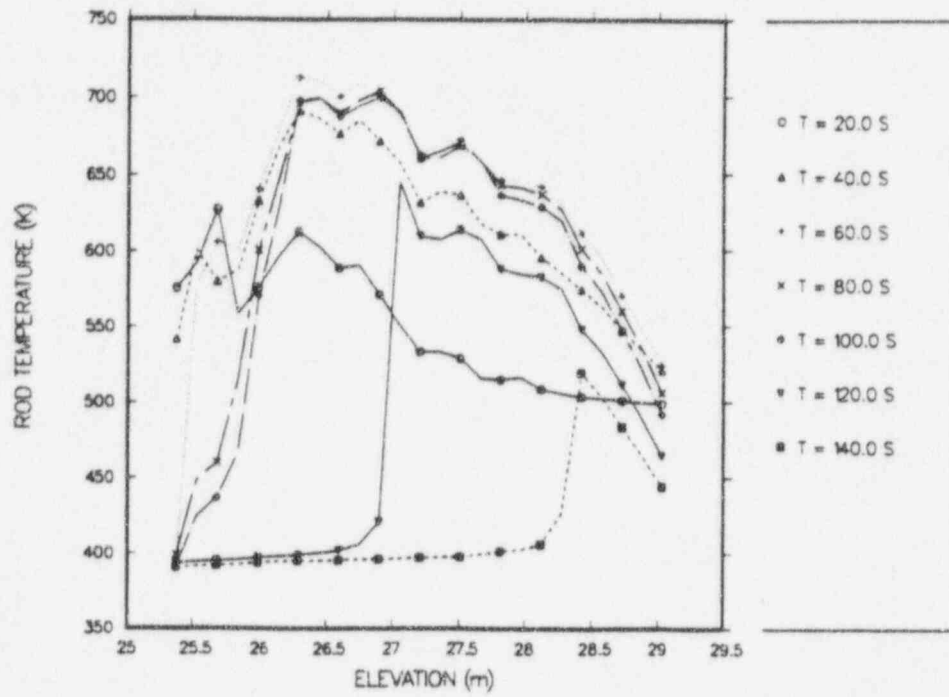


Fig. E-2b. Average-rod cladding temperatures vs core elevation at selected transient times from 20 to 140 s for core cell 2.

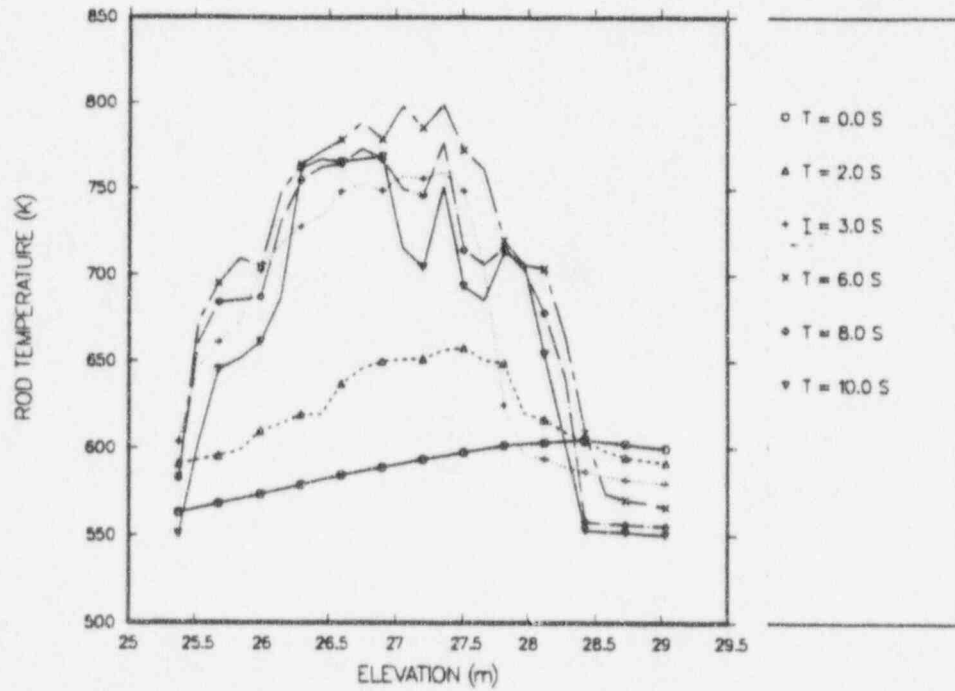


Fig. E-3a. Average-rod cladding temperatures vs core elevation at selected transient times from 0 to 10 s for core cell 3.

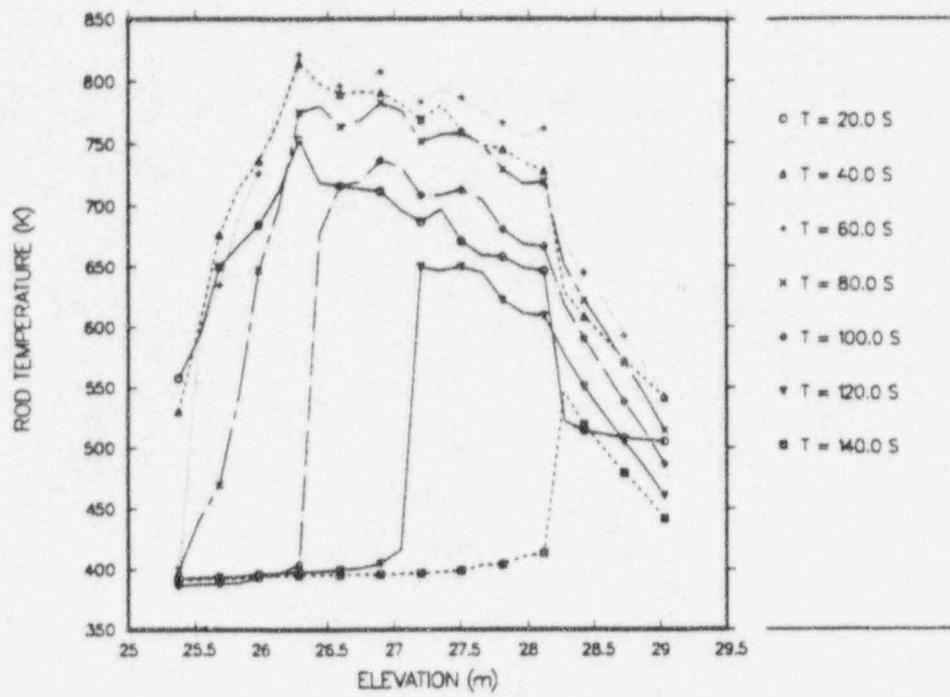


Fig. E-3b. Average-rod cladding temperatures vs core elevation at selected transient times from 20 to 140 s for core cell 3.

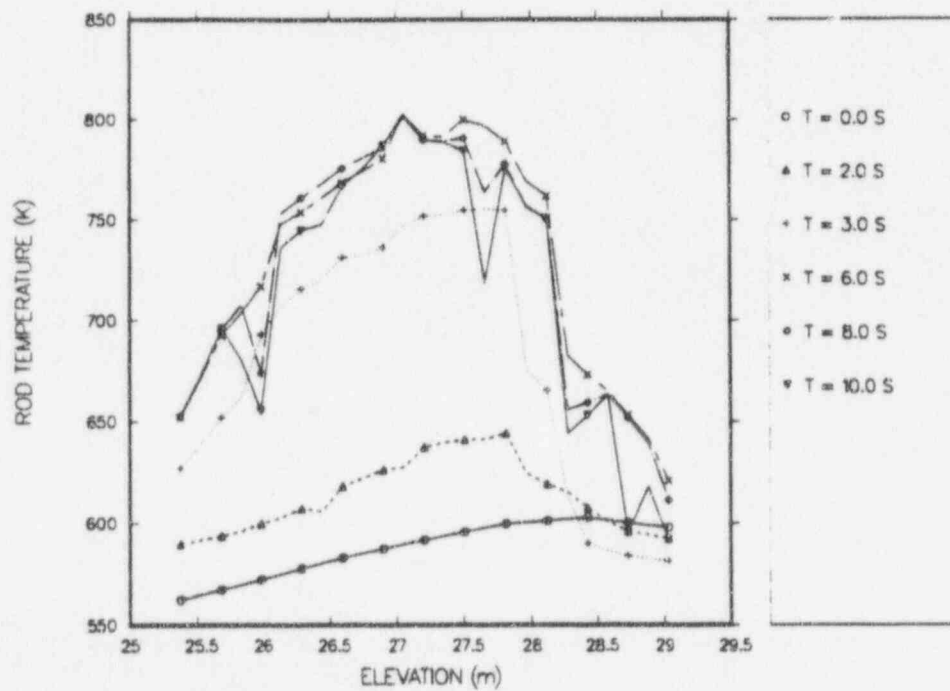


Fig. E-4a. Average-rod cladding temperatures vs core elevation at selected transient times from 0 to 10 s for core cell 4.

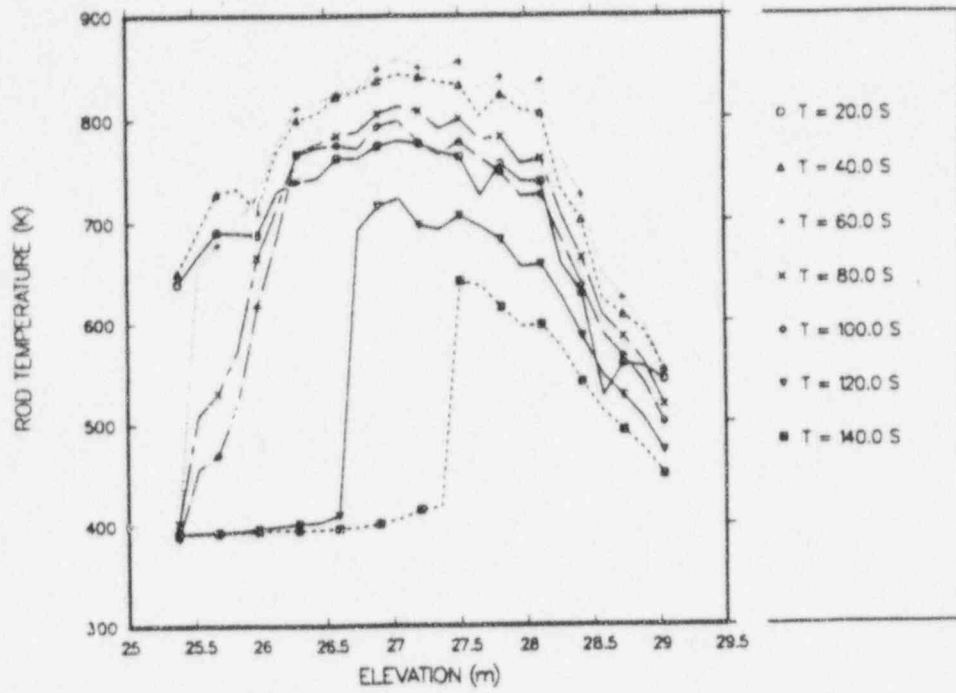


Fig. E-4b. Average-rod cladding temperatures vs core elevation at selected transient times from 20 to 140 s for core cell 4.

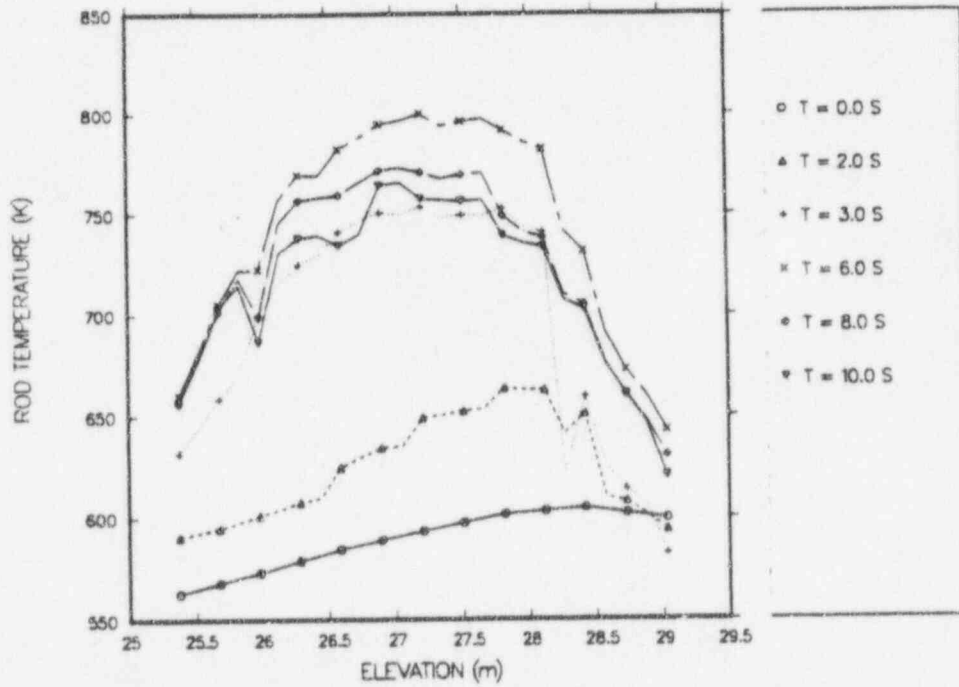


Fig. E-5a. Average-rod cladding temperatures vs core elevation at selected transient times from 0 to 10 s for core cell 5.

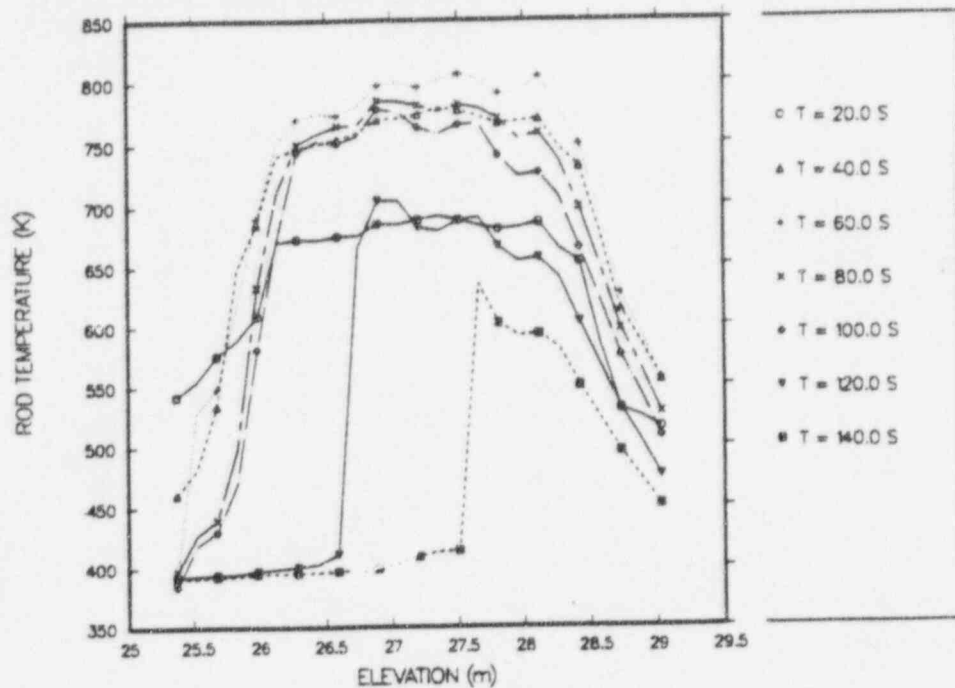


Fig. E-5b. Average-rod cladding temperatures vs core elevation at selected transient times from 20 to 140 s for core cell 5.

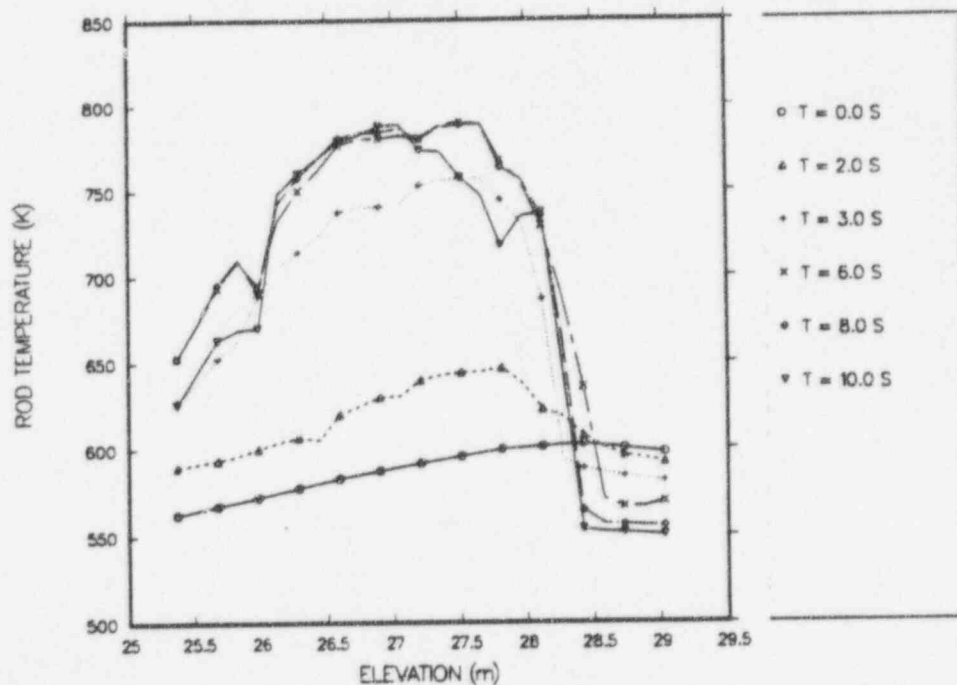


Fig. E-6a. Average-rod cladding temperatures vs core elevation at selected transient times from 0 to 10 s for core cell 6.

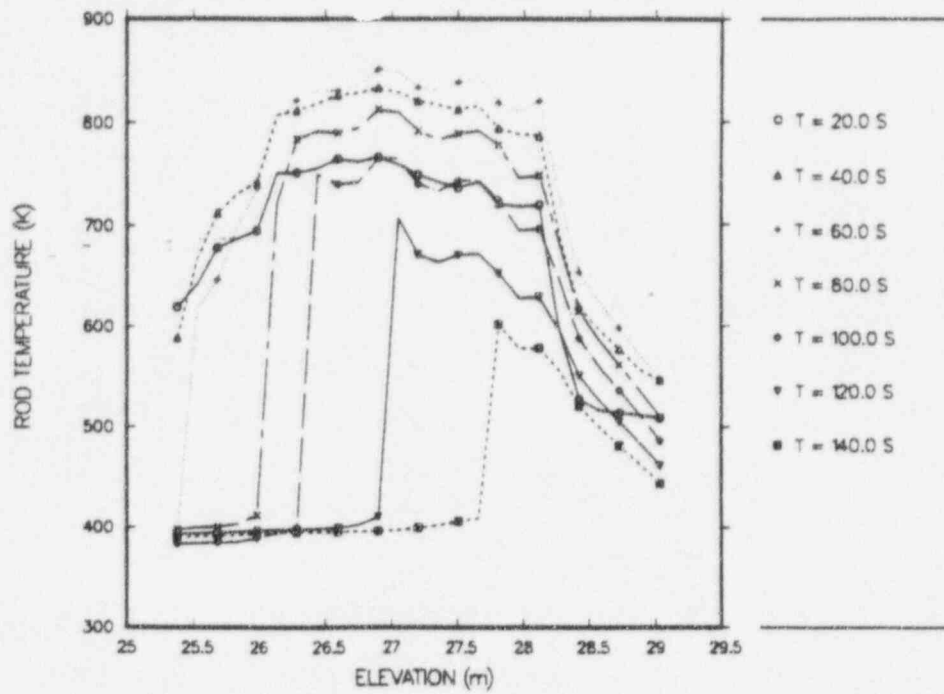


Fig. E-6b. Average-rod cladding temperatures vs core elevation at selected transient times from 20 to 140 s for core cell 6.

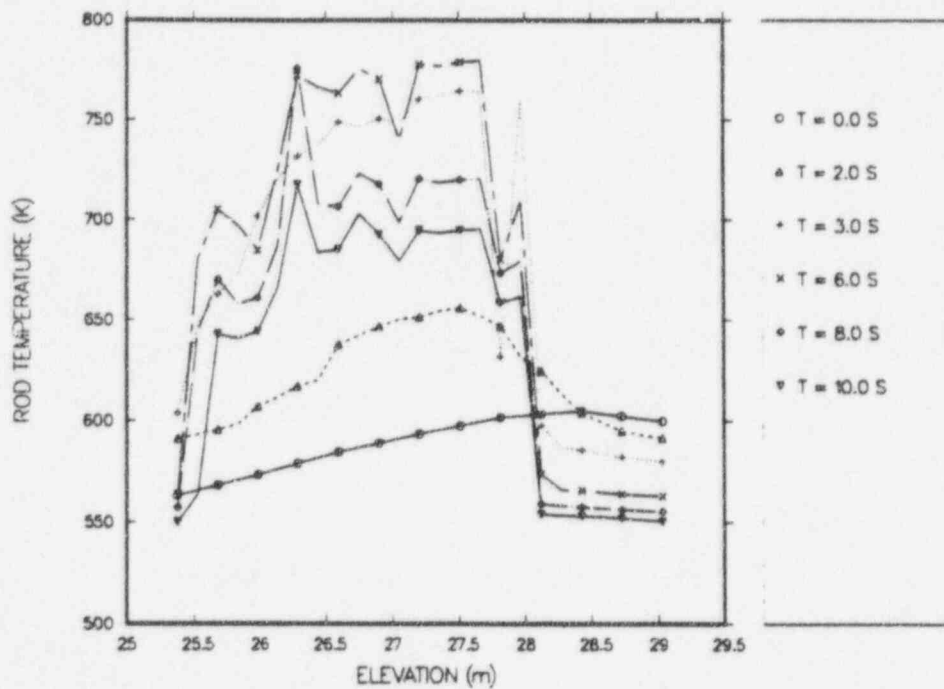


Fig. E-7a. Average-rod cladding temperatures vs core elevation at selected transient times from 0 to 10 s for core cell 7.

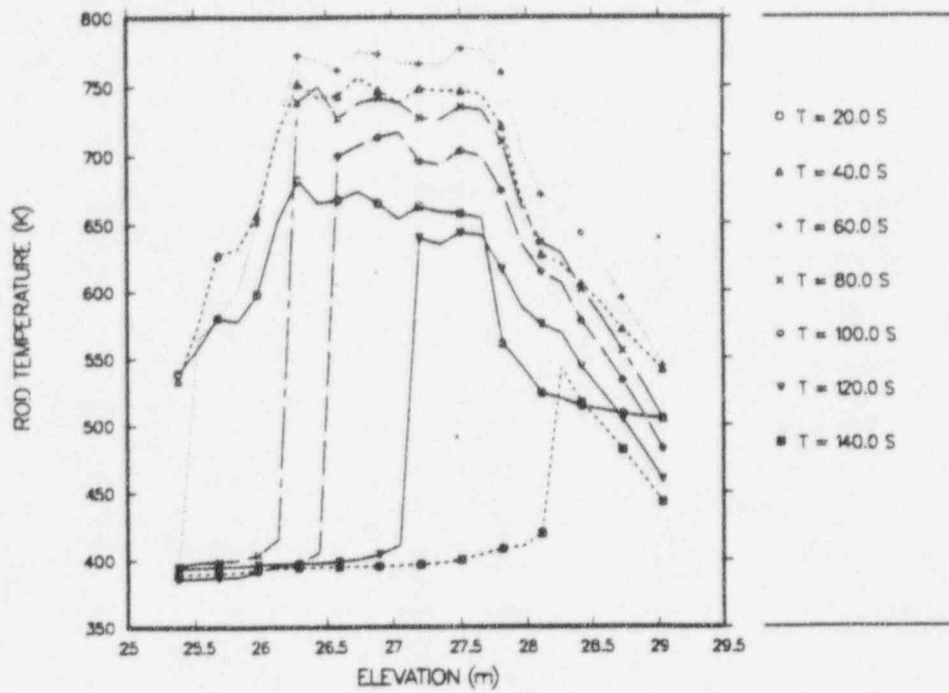


Fig. E-7b. Average-rod cladding temperatures vs core elevation at selected transient times from 20 to 140 s for core cell 7.

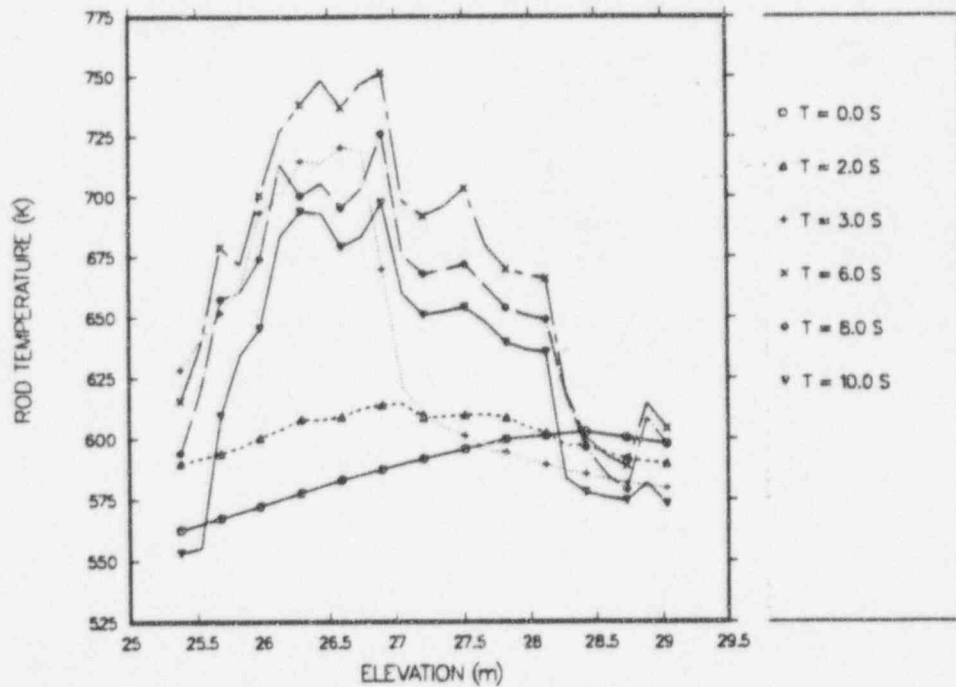


Fig. E-8a. Average-rod cladding temperatures vs core elevation at selected transient times from 0 to 10 s for core cell 8.

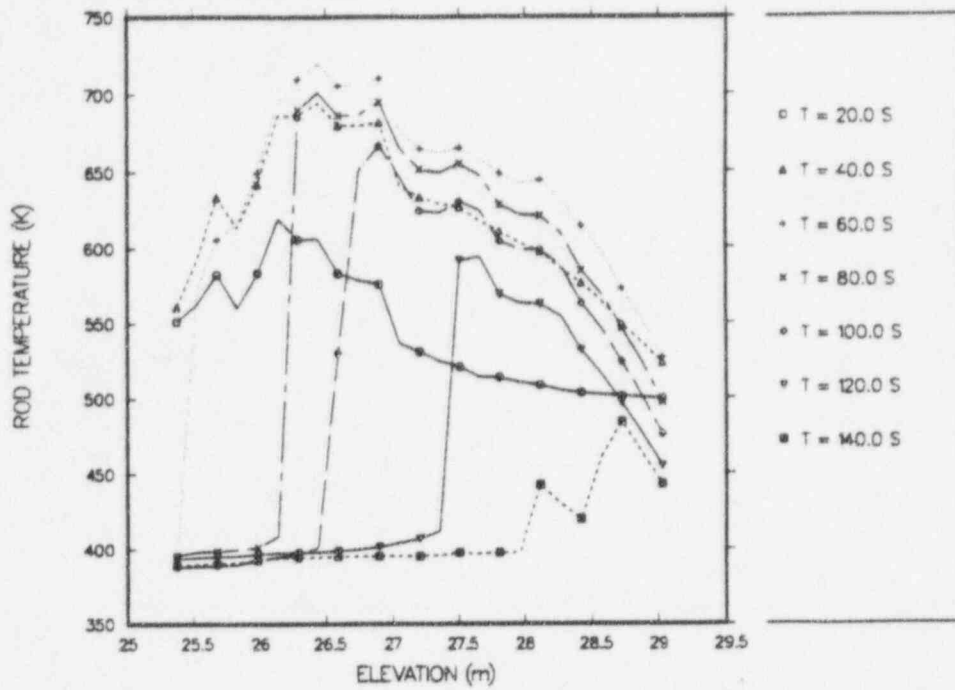


Fig. E-8b. Average-rod cladding temperatures vs core elevation at selected transient times from 20 to 140 s for core cell 8.

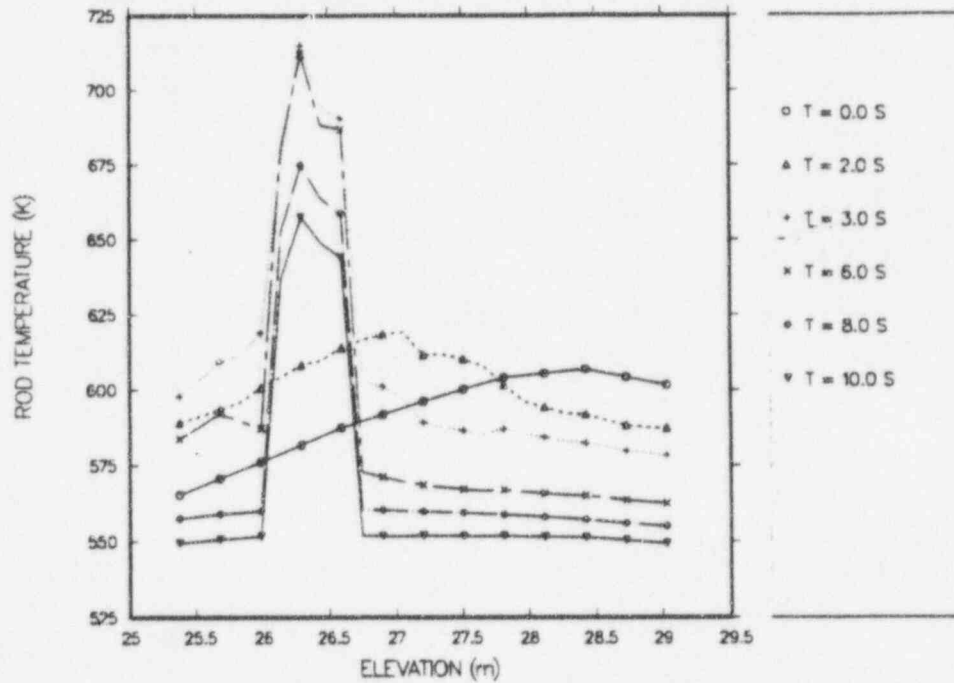


Fig. E-9a. Average-rod cladding temperatures vs core elevation at selected transient times from 0 to 10 s for core cell 9.

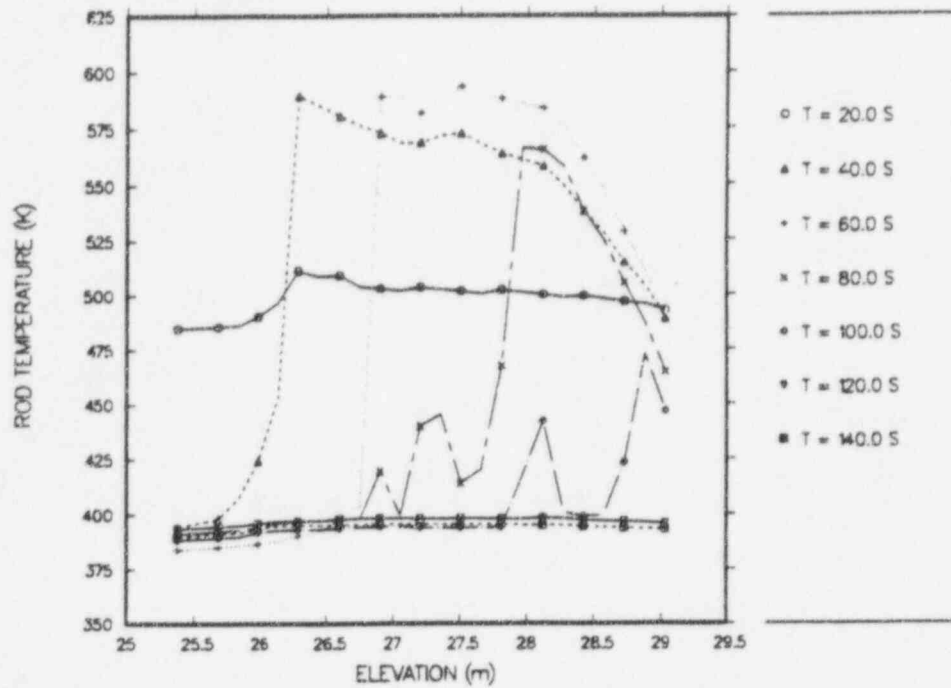


Fig. E-9b. Average-rod cladding temperatures vs core elevation at selected transient times from 20 to 140 s for core cell 9.

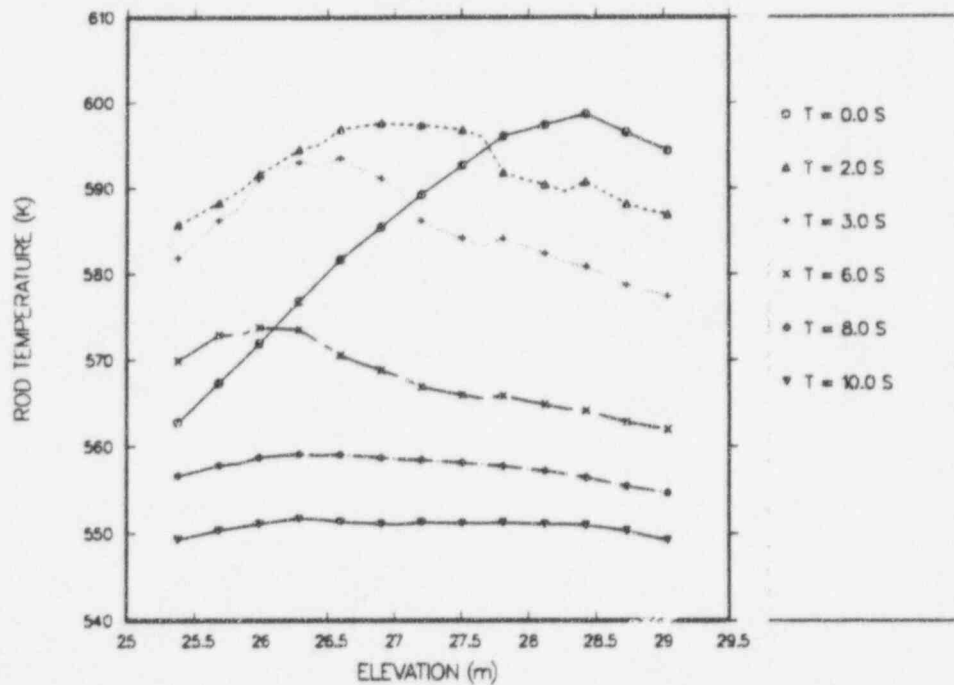


Fig. E-10a. Average-rod cladding temperatures vs core elevation at selected transient times from 0 to 10 s for core cell 10.

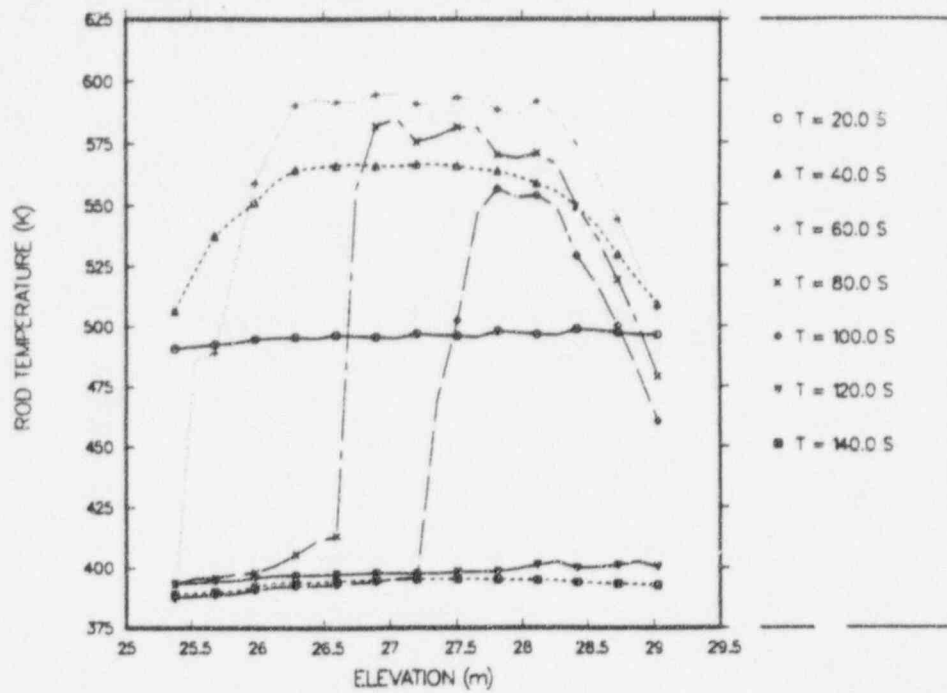


Fig. E-10b. Average-rod cladding temperatures vs core elevation at selected transient times from 20 to 140 s for core cell 10.

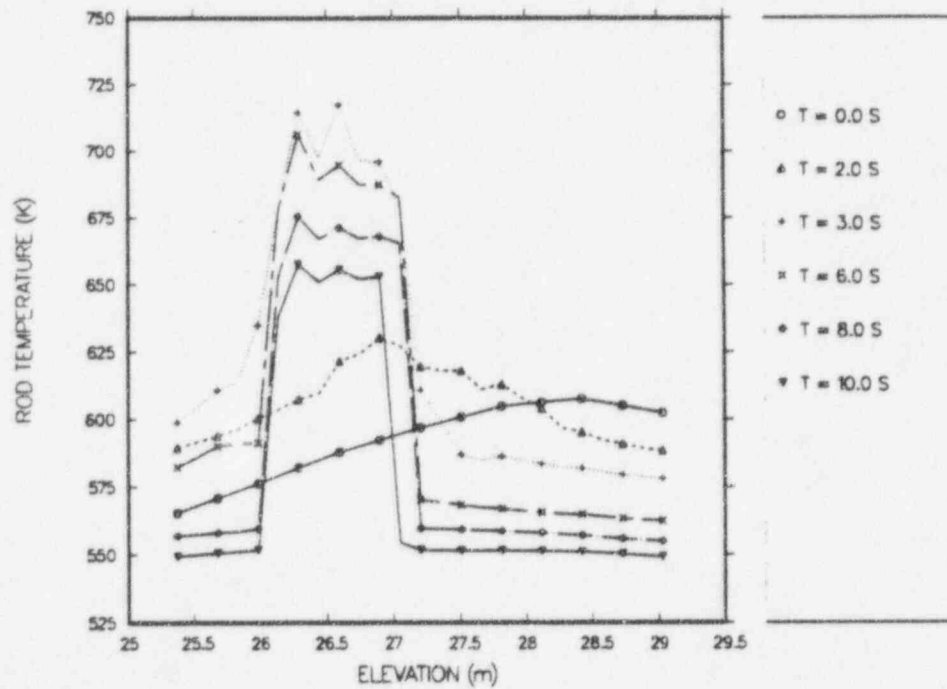


Fig. E-11a. Average-rod cladding temperatures vs core elevation at selected transient times from 0 to 10 s for core cell 11.

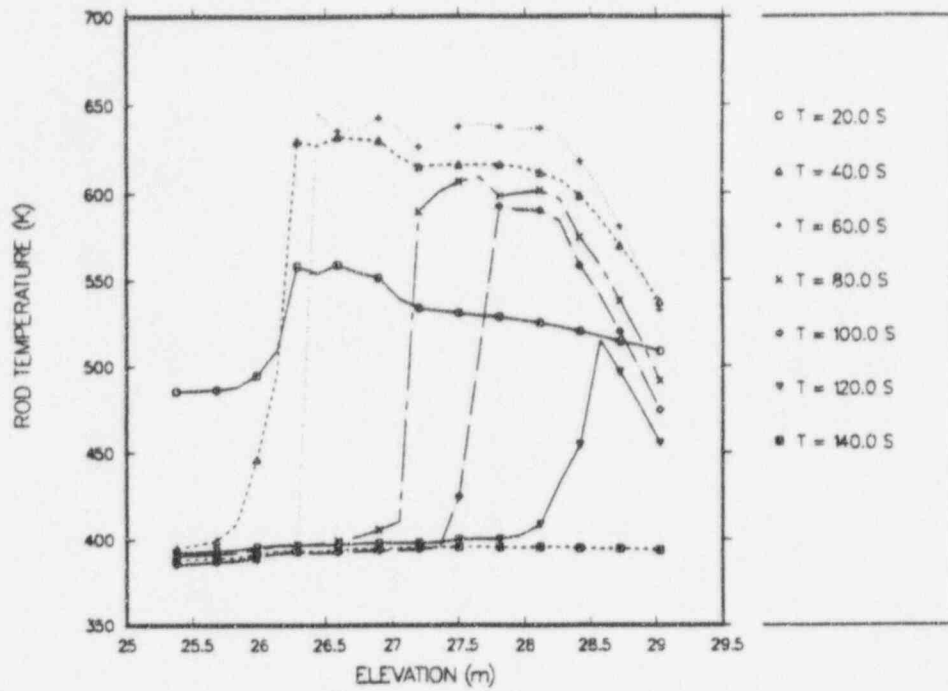


Fig. E-11b. Average-rod cladding temperatures vs core elevation at selected transient times from 20 to 140 s for core cell 11.

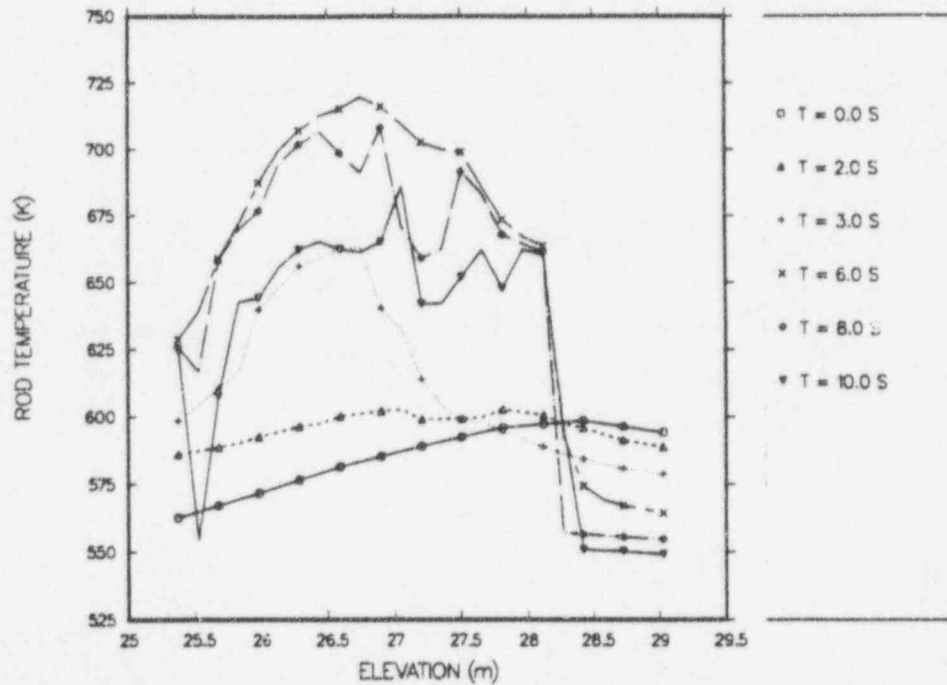


Fig. E-12a. Average-rod cladding temperatures vs core elevation at selected transient times from 0 to 10 s for core cell 12.

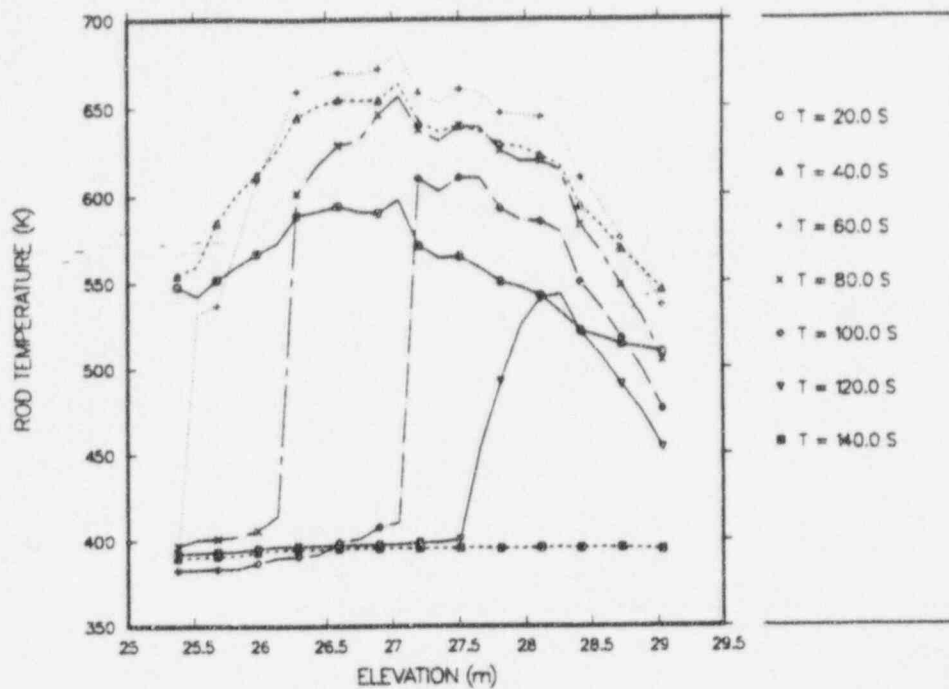


Fig. E-12b. Average-rod cladding temperatures vs core elevation at selected transient times from 20 to 140 s for core cell 12.

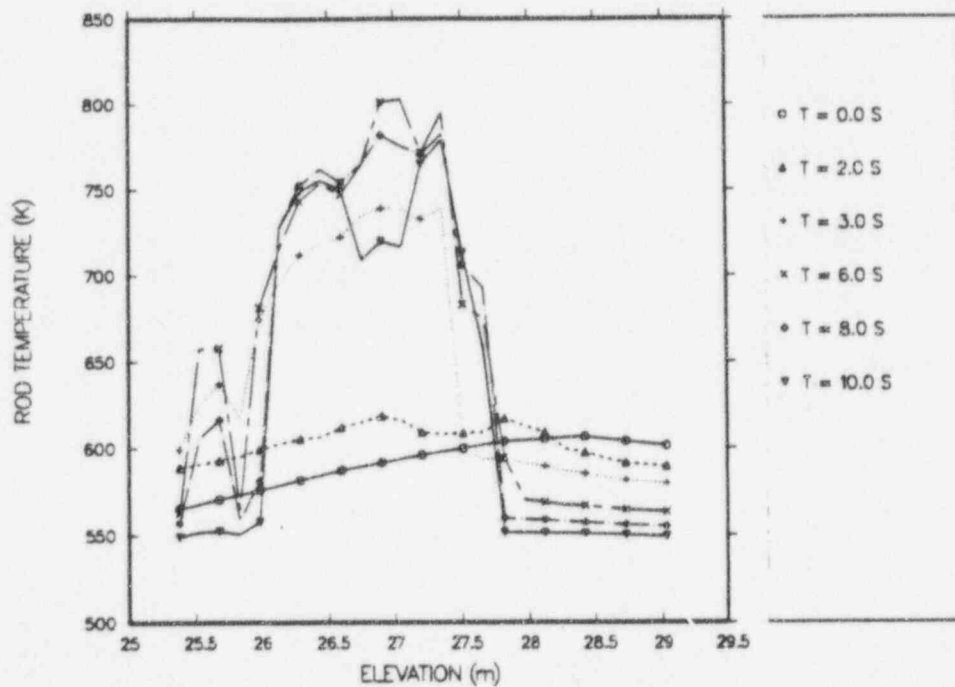


Fig. E-13a. Average-rod cladding temperatures vs core elevation at selected transient times from 0 to 10 s for core cell 13.

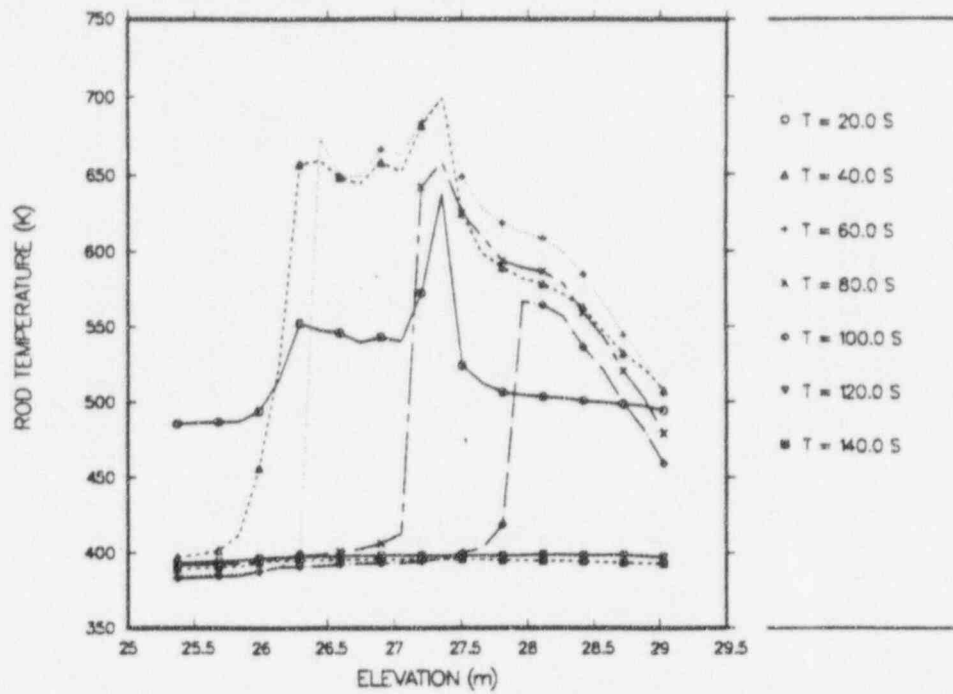


Fig. E-13b. Average-rod cladding temperatures vs core elevation at selected transient times from 20 to 140 s for core cell 13.

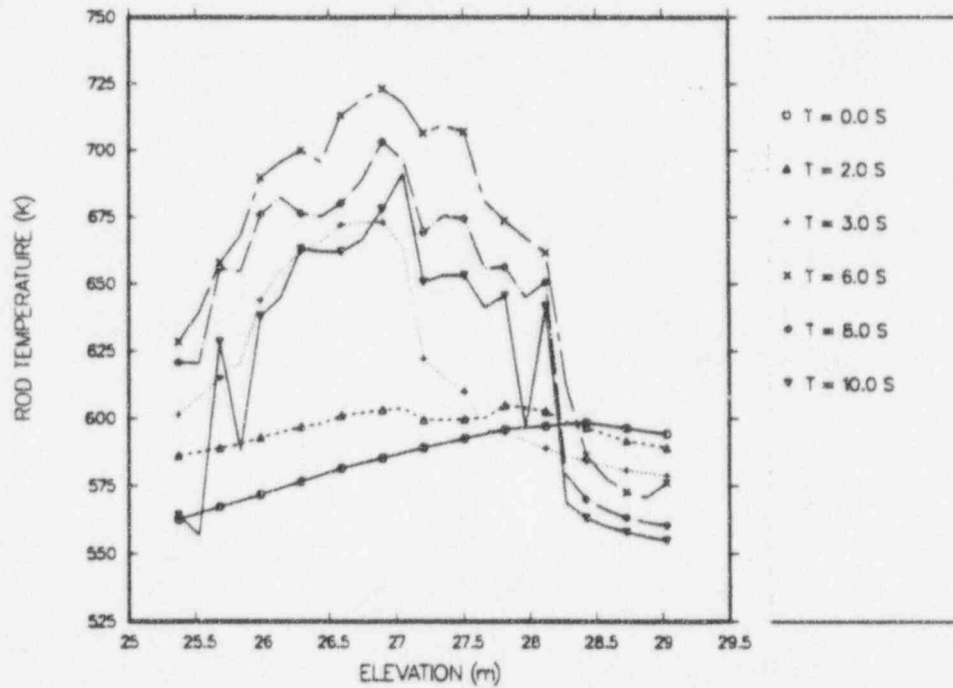


Fig. E-14a. Average-rod cladding temperatures vs core elevation at selected transient times from 0 to 10 s for core cell 14.

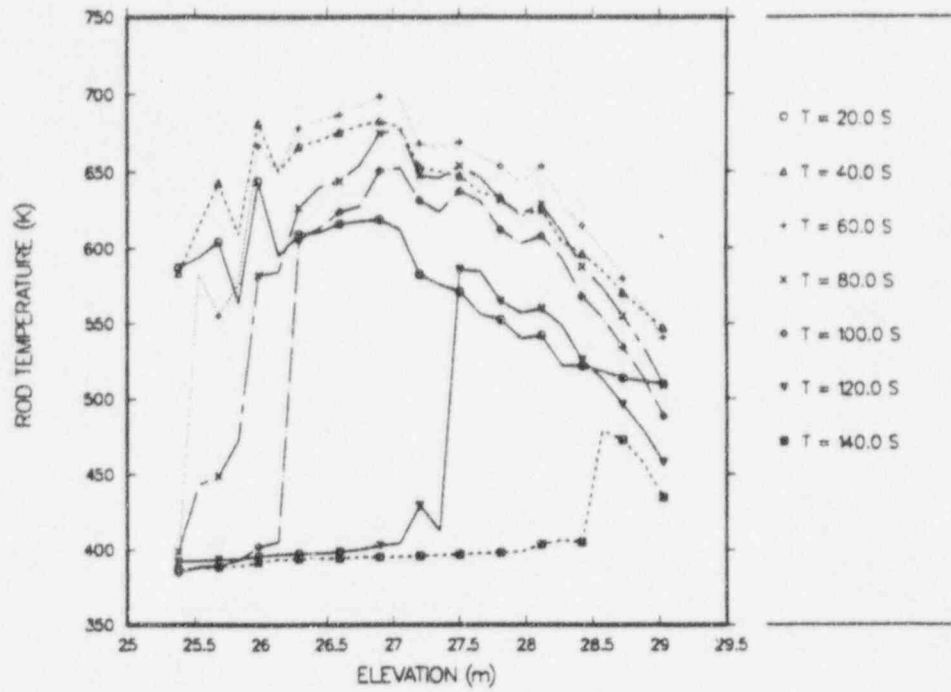


Fig. E-14b. Average-rod cladding temperatures vs core elevation at selected transient times from 20 to 140 s for core cell 14.

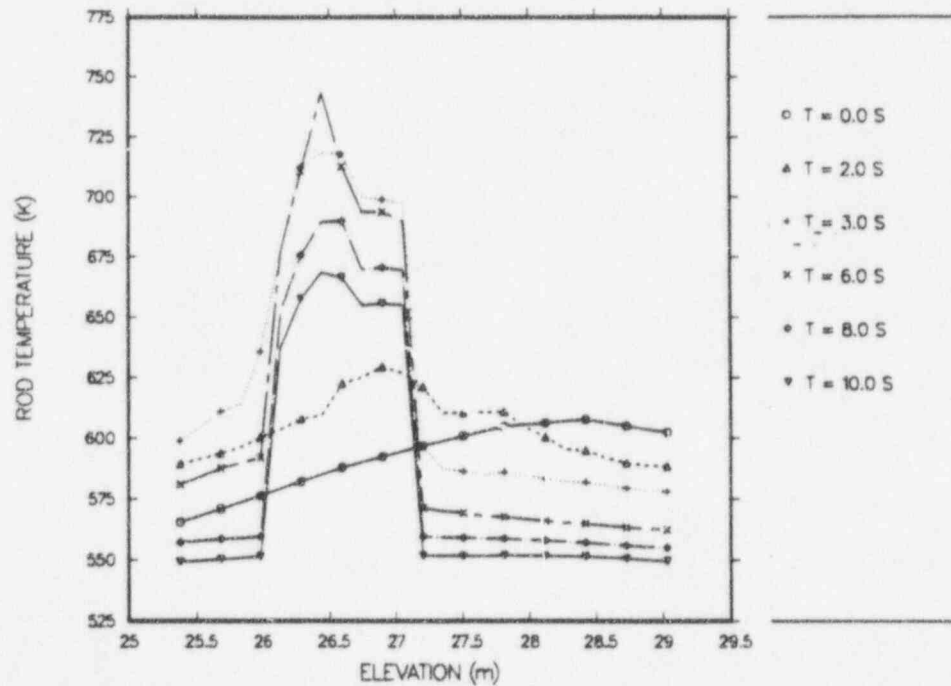


Fig. E-15a. Average-rod cladding temperatures vs core elevation at selected transient times from 0 to 10 s for core cell 15.

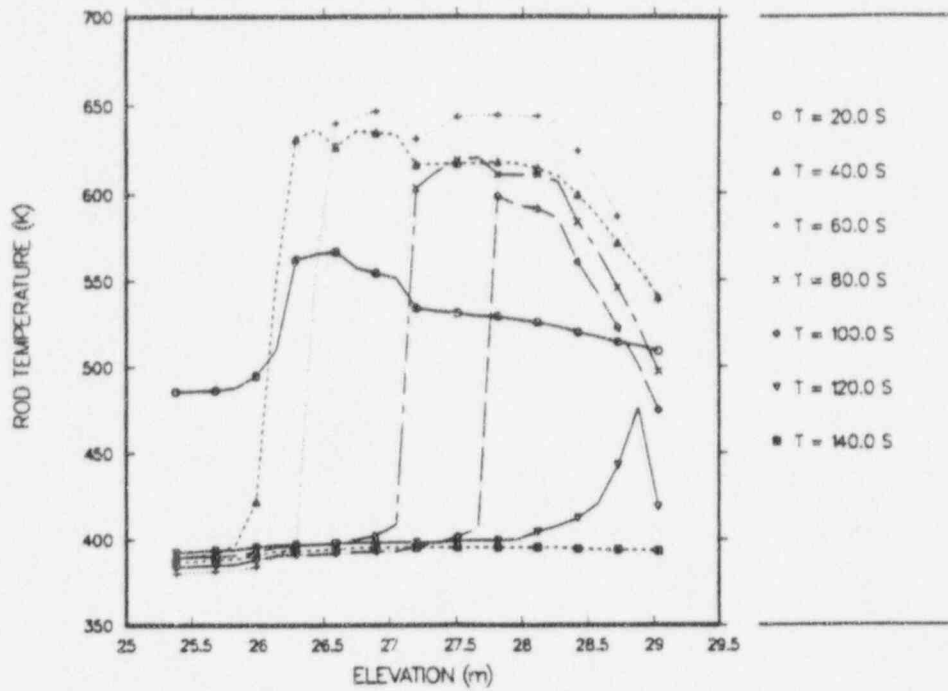


Fig. E-15b. Average-rod cladding temperatures vs core elevation at selected transient times from 20 to 140 s for core cell 15.

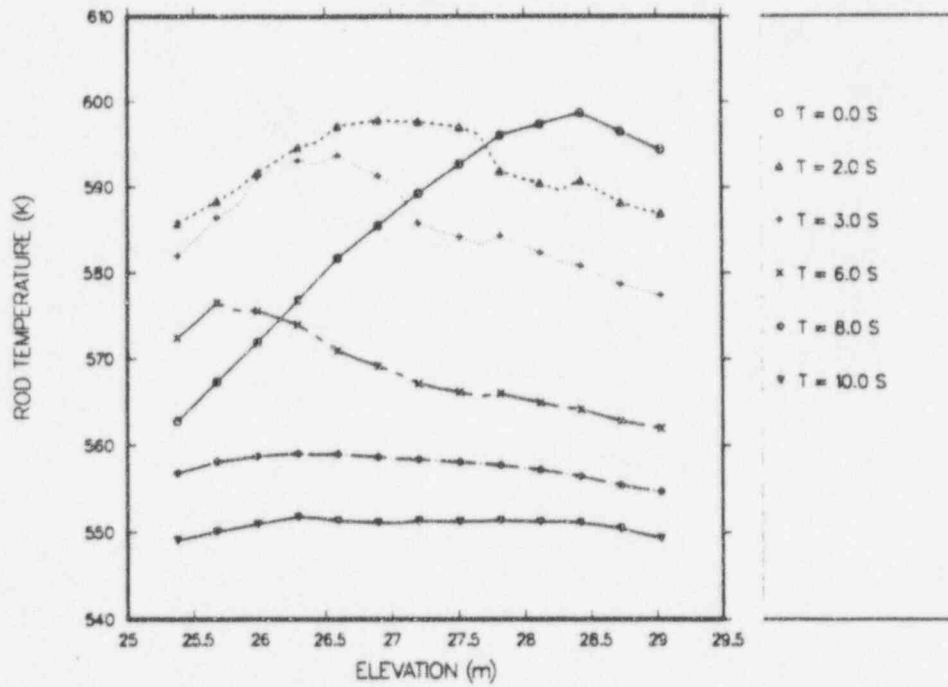


Fig. E-16a. Average-rod cladding temperatures vs core elevation at selected transient times from 0 to 10 s for core cell 16.

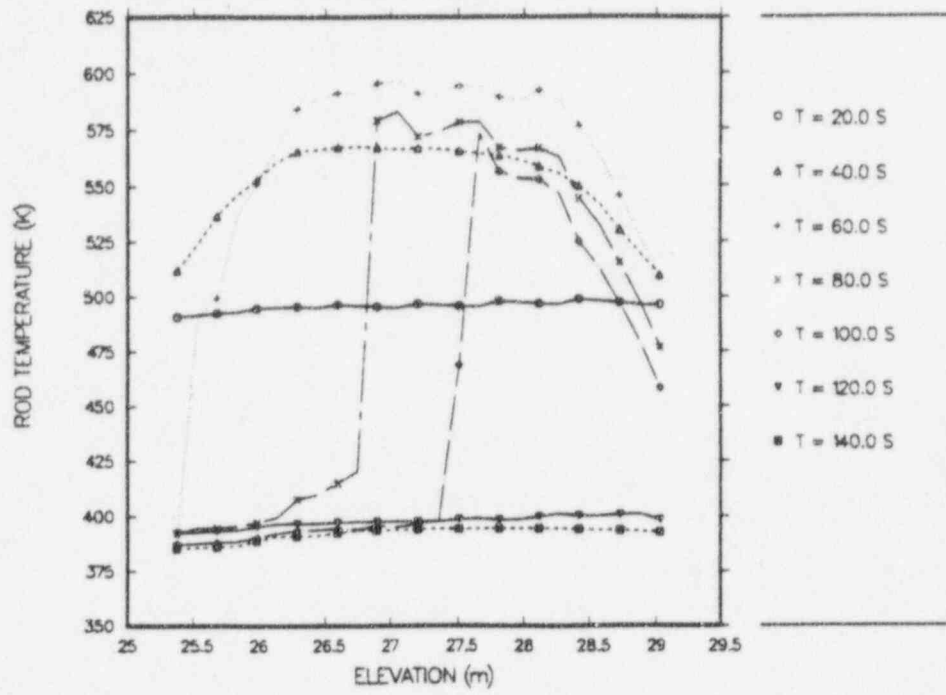


Fig. E-16b. Average-rod cladding temperatures vs core elevation at selected transient times from 20 to 140 s for core cell 16.

APPENDIX F

HOT-ROD CLADDING TEMPERATURES VS ROD ELEVATION AT SELECTED TRANSIENT TIMES

Figures F-1 through F-16 depict hot-rod cladding temperatures vs rod elevation at selected transient times are presented for each core sector cell. Two plots are presented for each core sector cell. The first plot is for transient times of 0, 2.0, 3.0, 6.0, 8.0, and 10 s. The second plot is for transient times of 20, 40, 60, 80, 100, 120, and 140 s. A noding diagram is provided in Fig. 6 of the main text.

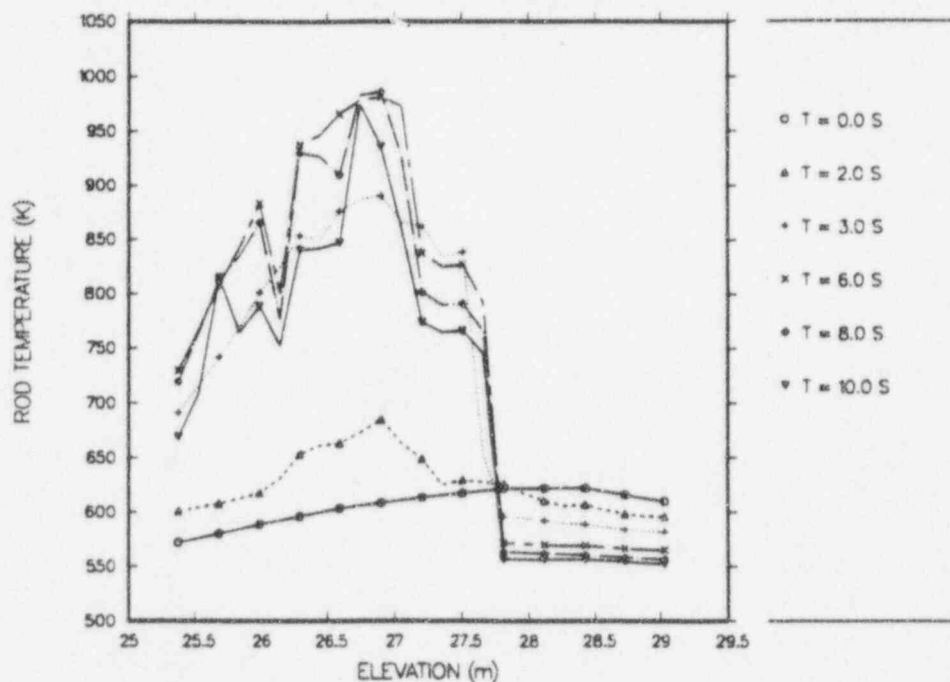


Fig. F-1a. Hot-rod cladding temperatures vs core elevation at selected transient times from 0 to 10 s for core cell 1.

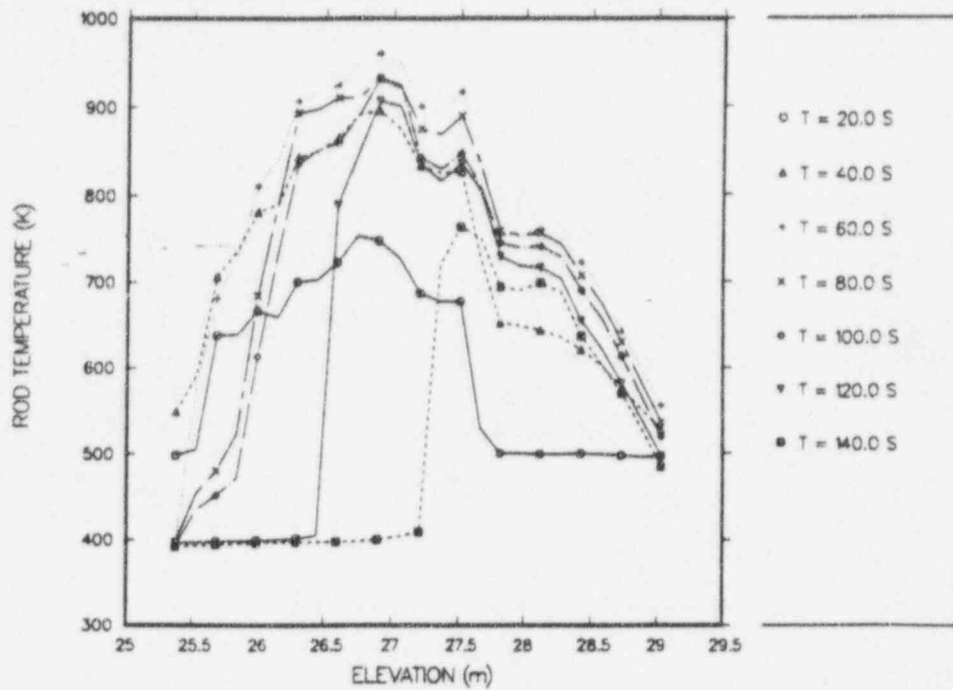


Fig. F-1b. Hot-rod cladding temperatures vs core elevation at selected transient times from 20 to 140 s for core cell 1.

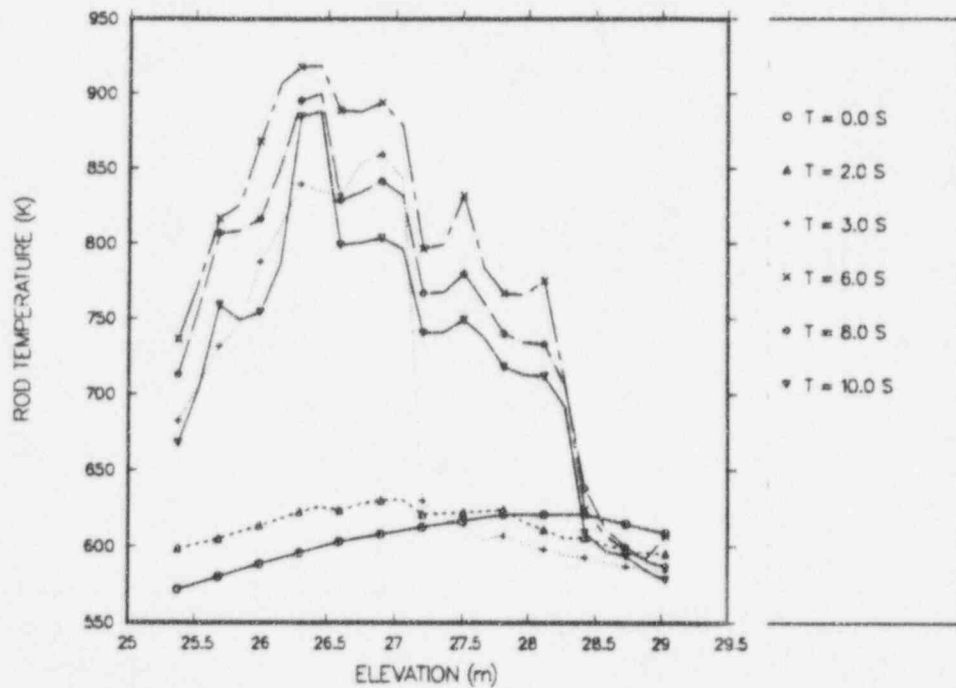


Fig. F-2a. Hot-rod cladding temperatures vs core elevation at selected transient times from 0 to 10 s for core cell 2.

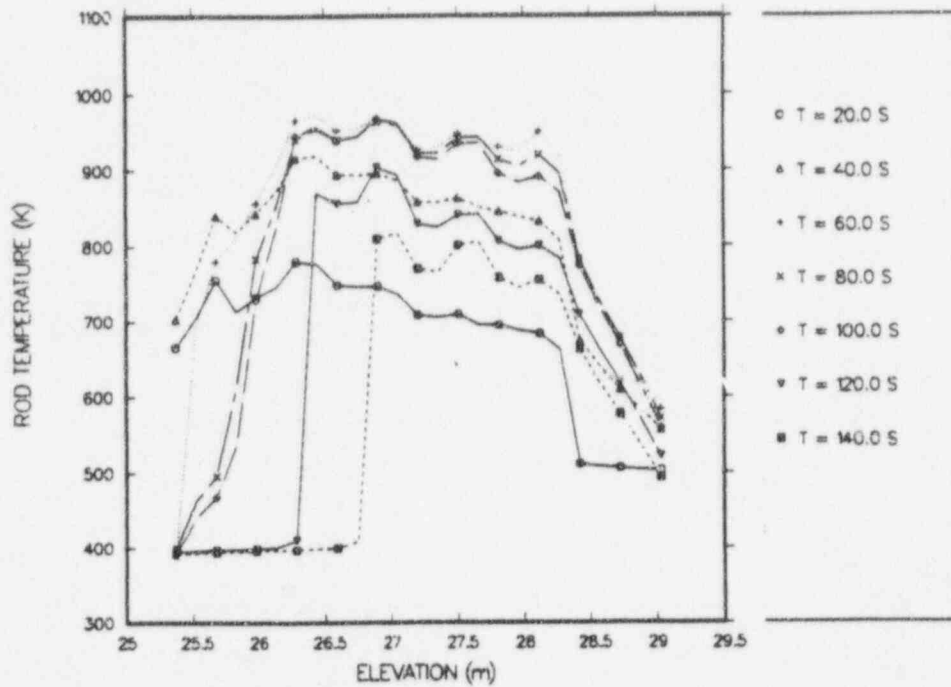


Fig. F-2b. Hot-rod cladding temperatures vs core elevation at selected transient times from 20 to 140 s for core cell 2.

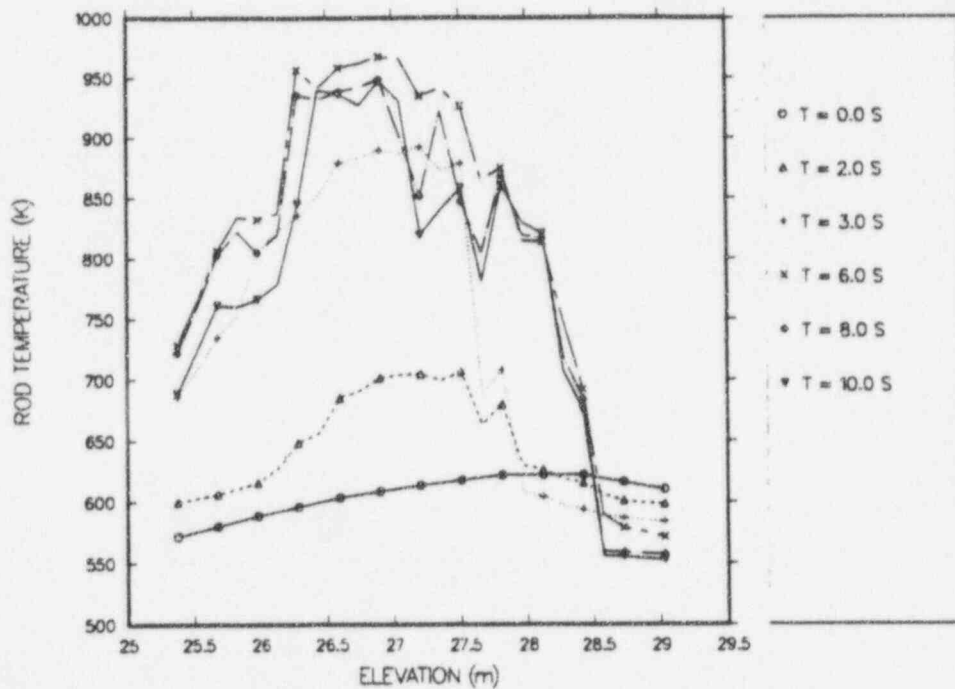


Fig. F-3a. Hot-rod cladding temperatures vs core elevation at selected transient times from 0 to 10 s for core cell 3.

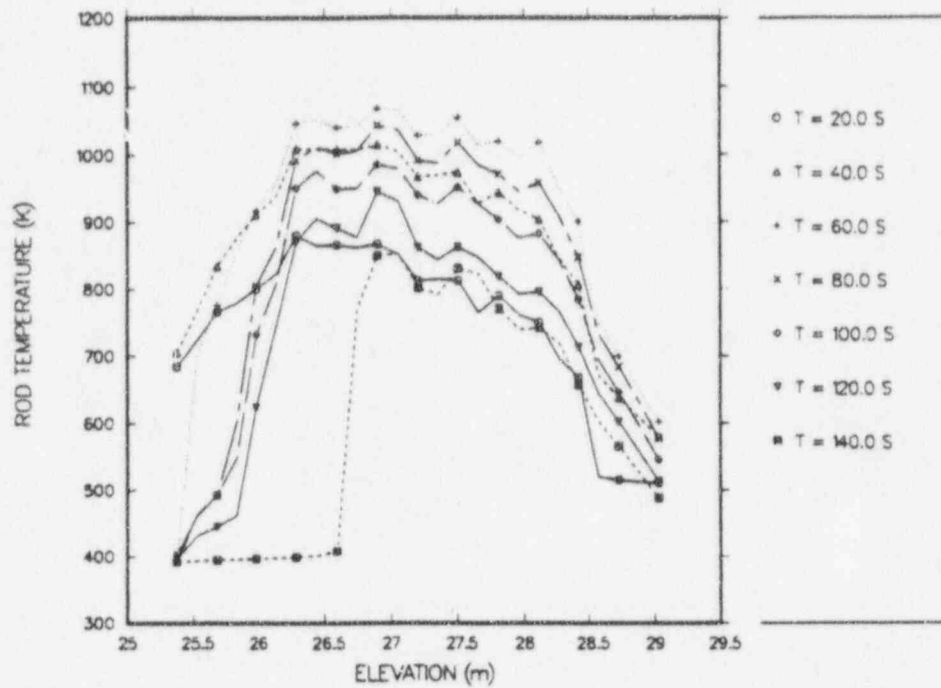


Fig. F-3b. Hot-rod cladding temperatures vs core elevation at selected transient times from 20 to 140 s for core cell 3.

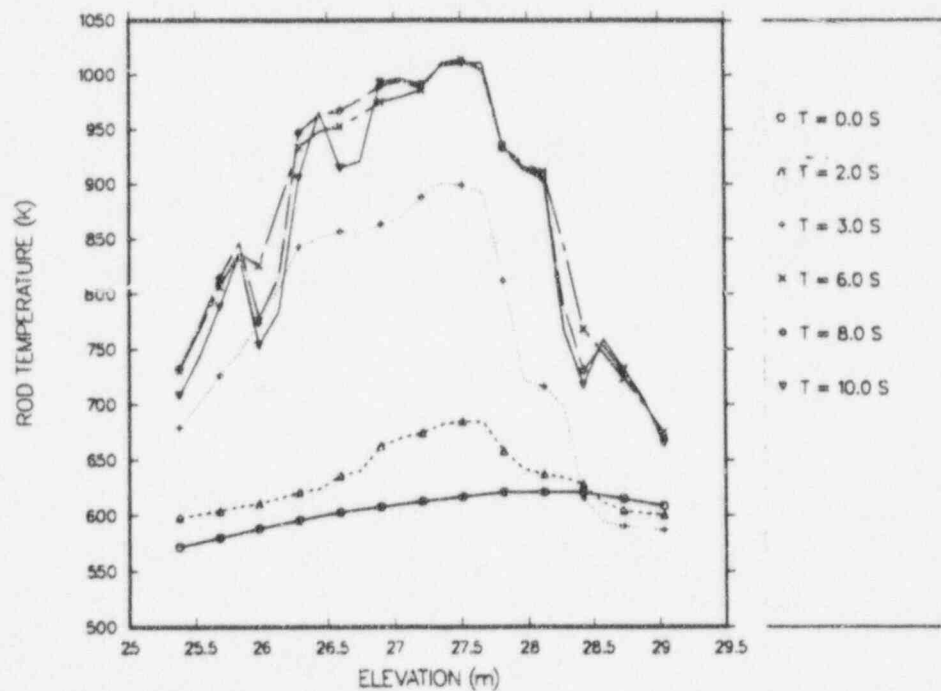


Fig. F-4a. Hot-rod cladding temperatures vs core elevation at selected transient times from 0 to 10 s for core cell 4.

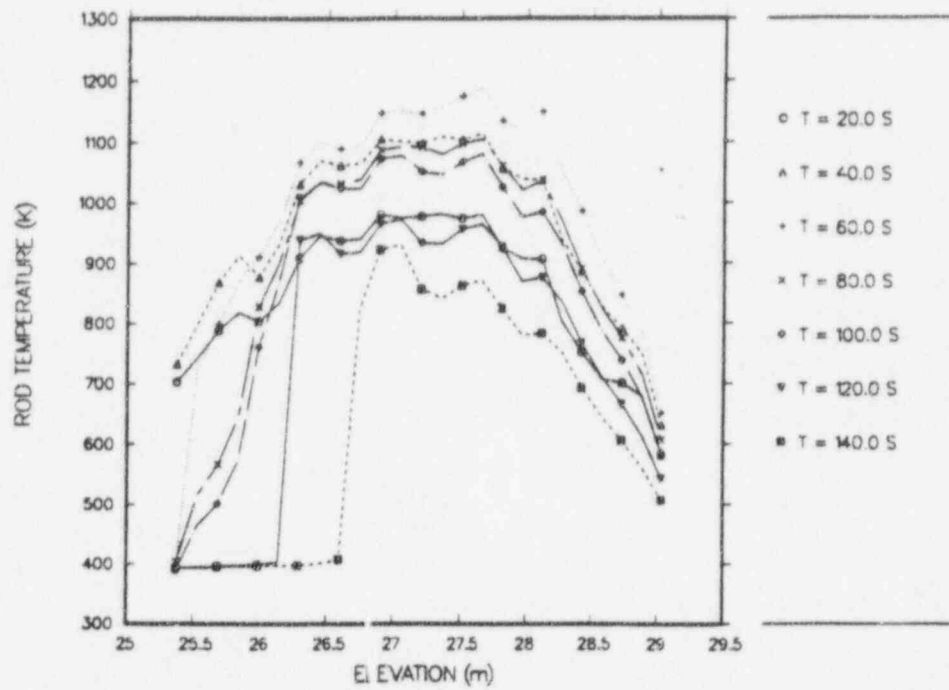


Fig. F-4b. Hot-rod cladding temperatures vs core elevation at selected transient times from 20 to 140 s for core cell 4.

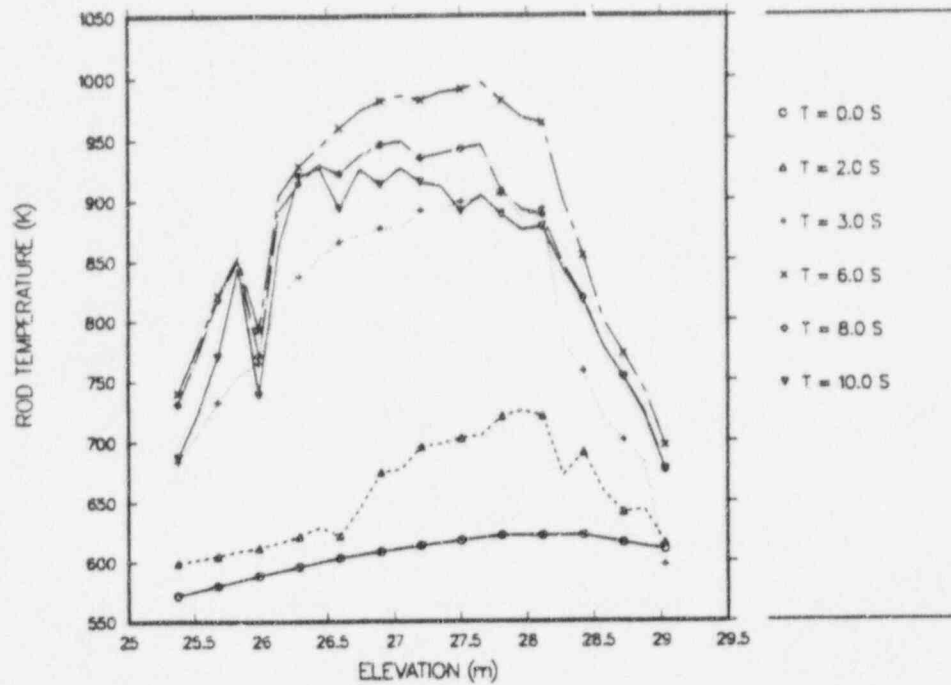


Fig. F-5a. Hot-rod cladding temperatures vs core elevation at selected transient times from 0 to 10 s for core cell 5.

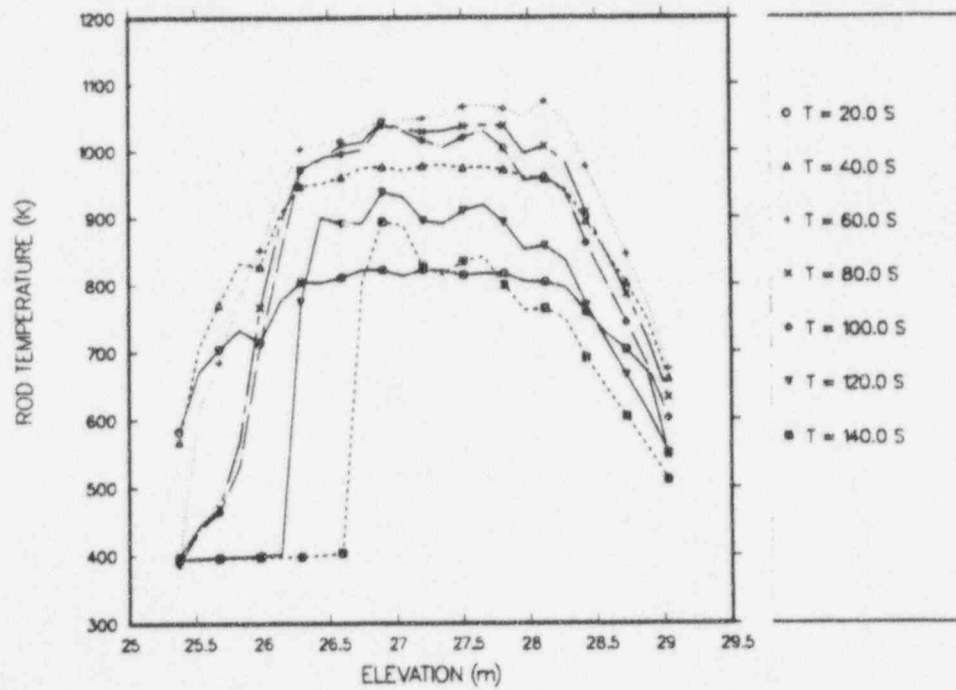


Fig. F-5b. Hot-rod cladding temperatures vs core elevation at selected transient times from 20 to 140 s for core cell 5.

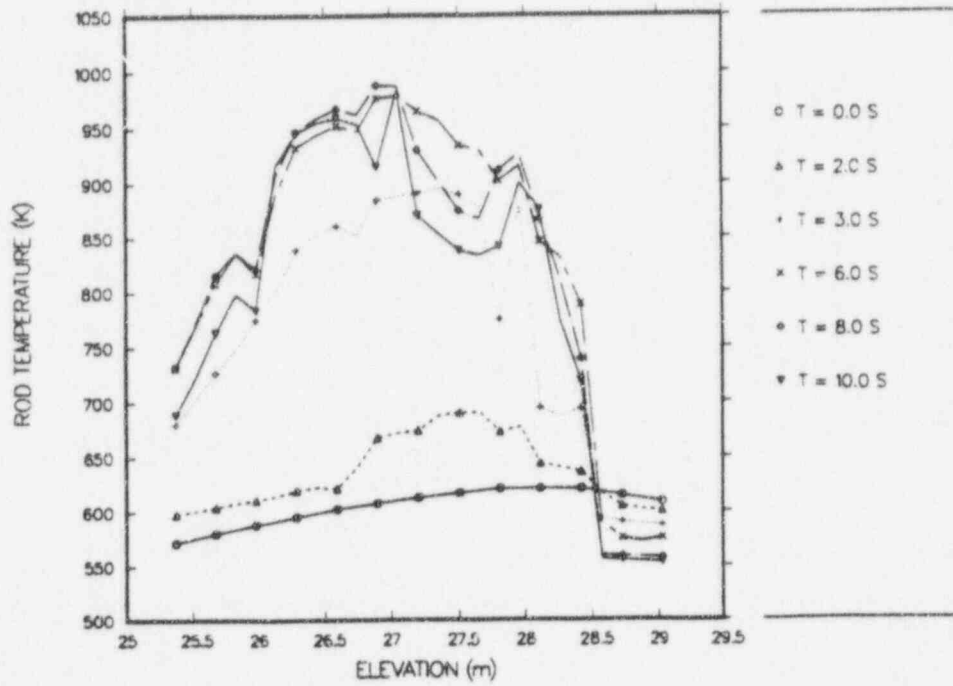


Fig. F-6a. Hot-rod cladding temperatures vs core elevation at selected transient times from 0 to 10 s for core cell 6.

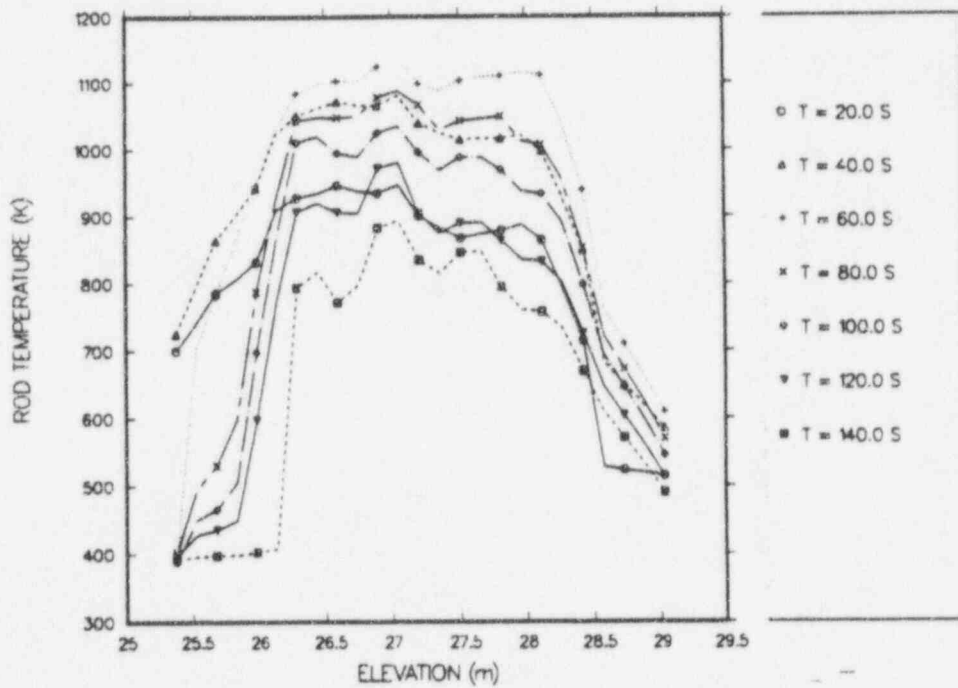


Fig. F-6b. Hot-rod cladding temperatures vs core elevation at selected transient times from 20 to 140 s for core cell 6.

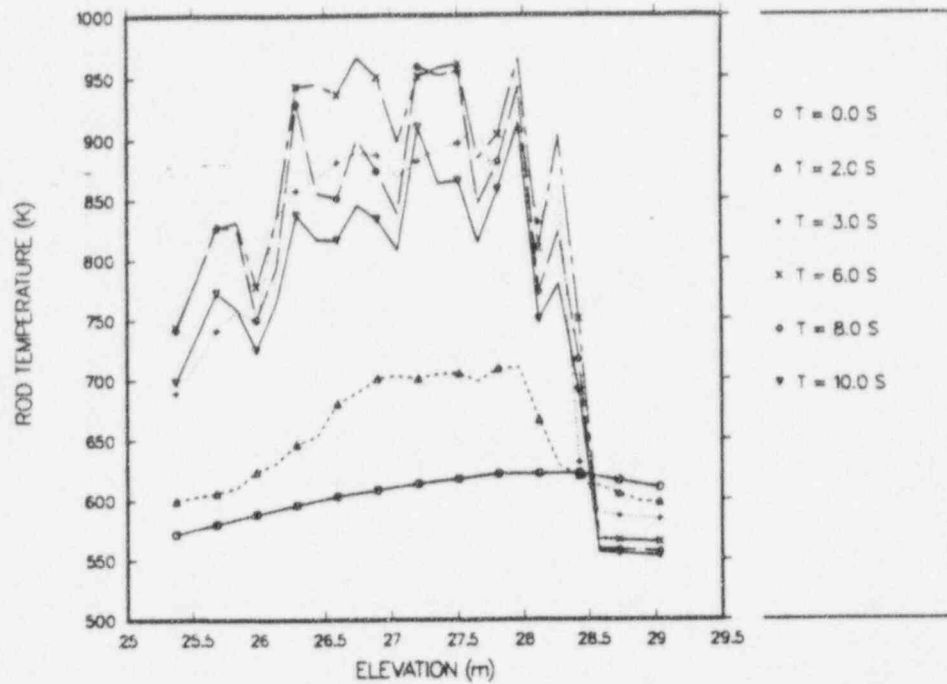


Fig. F-7a. Hot-rod cladding temperatures vs core elevation at selected transient times from 0 to 10 s for core cell 7.

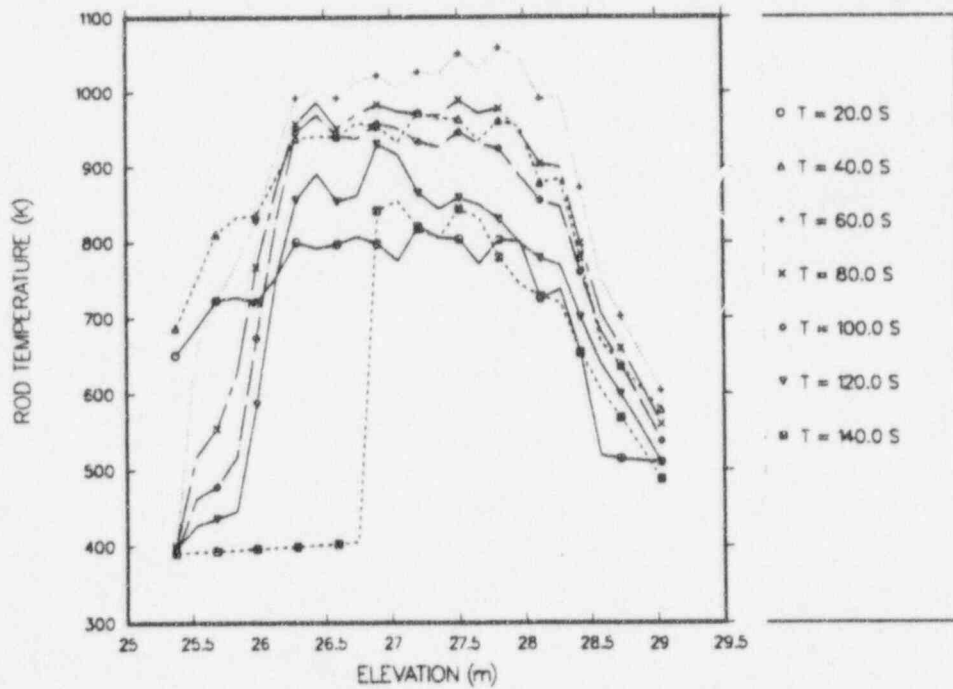


Fig. F-7b. Hot-rod cladding temperatures vs core elevation at selected transient times from 20 to 140 s for core cell 7.

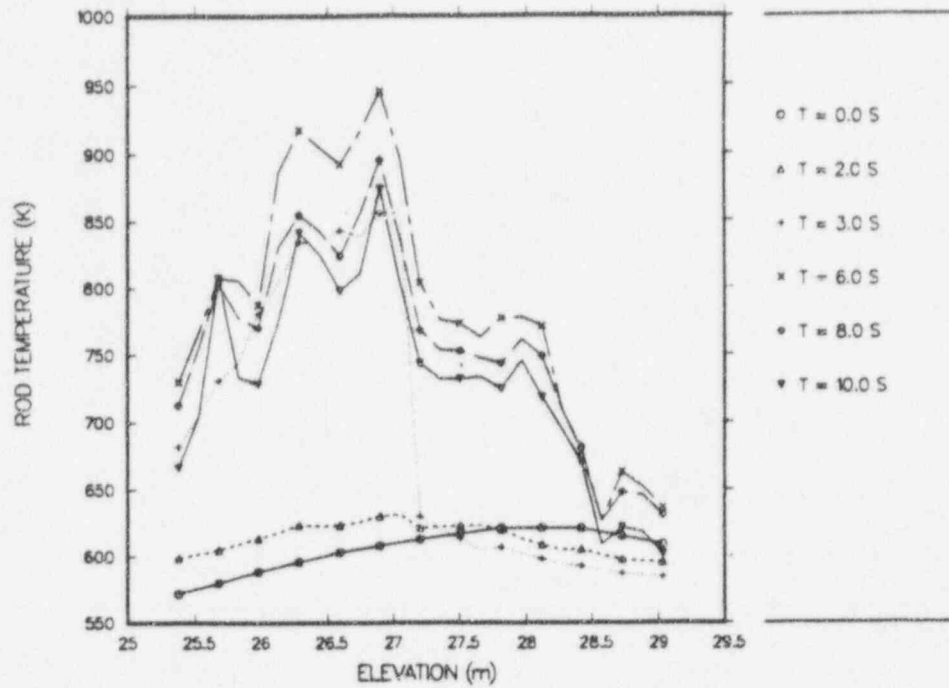


Fig. F-8a. Hot-rod cladding temperatures vs core elevation at selected transient times from 0 to 10 s for core cell 8.

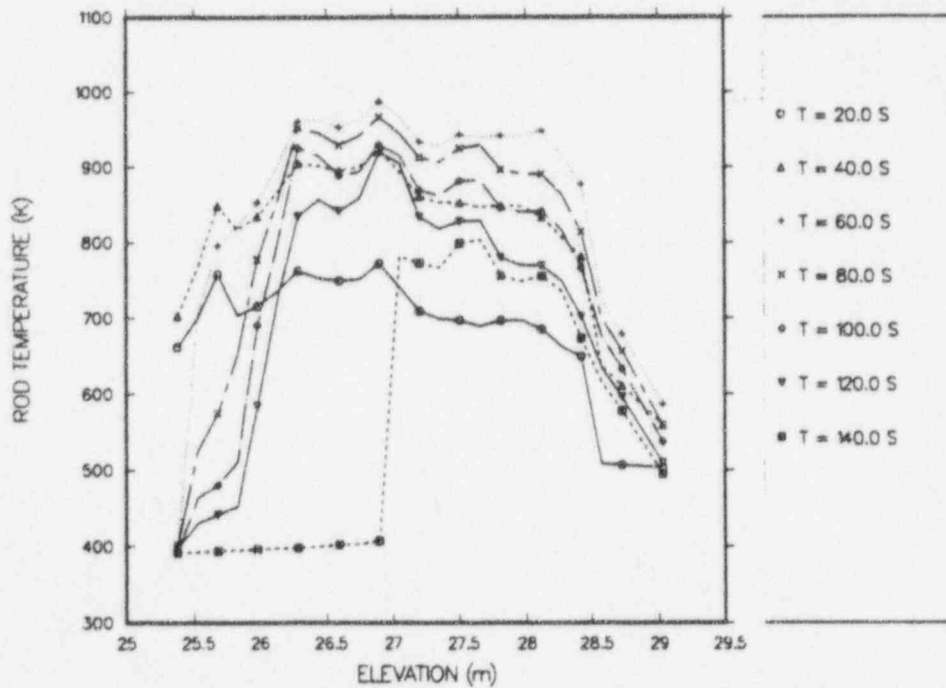


Fig. F-8b. Hot-rod cladding temperatures vs core elevation at selected transient times from 20 to 140 s for core cell 8.

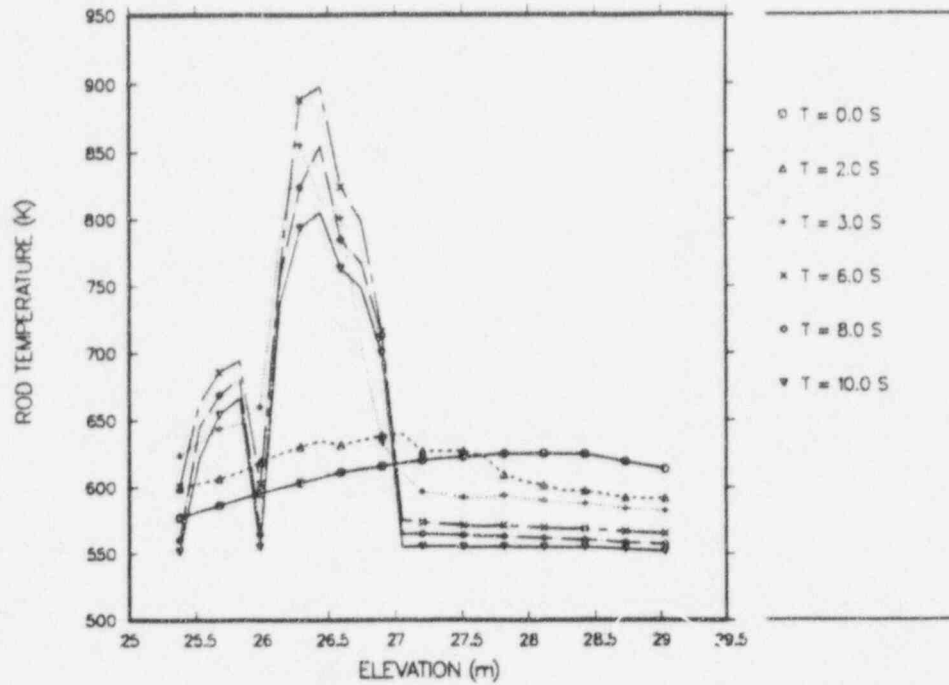


Fig. F-9a. Hot-rod cladding temperatures vs core elevation at selected transient times from 0 to 10 s for core cell 9.

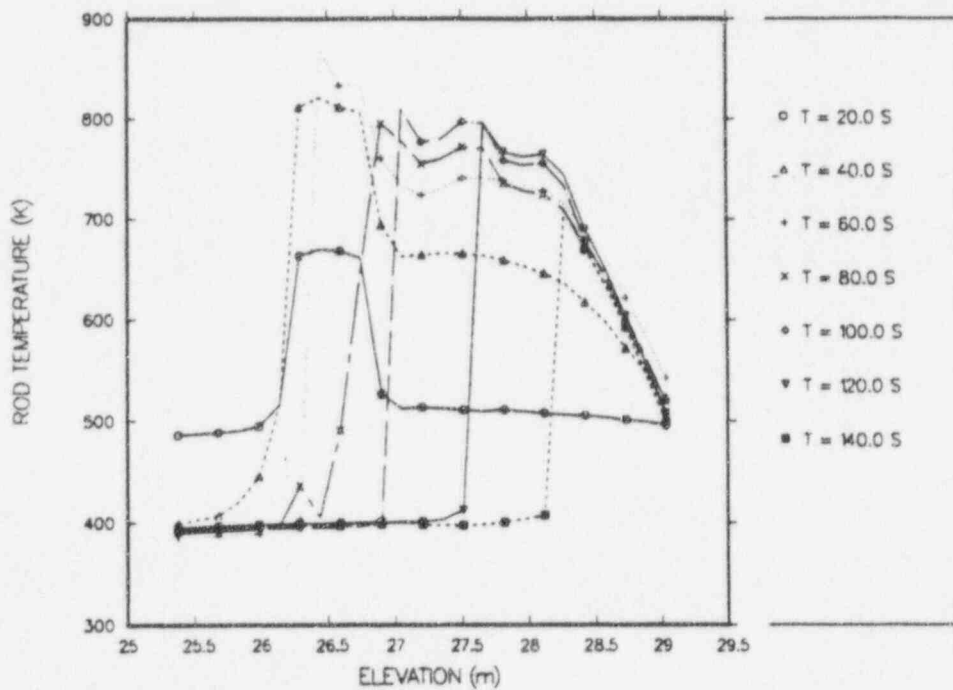


Fig. F-9b. Hot-rod cladding temperatures vs core elevation at selected transient times from 20 to 140 s for core cell 9.

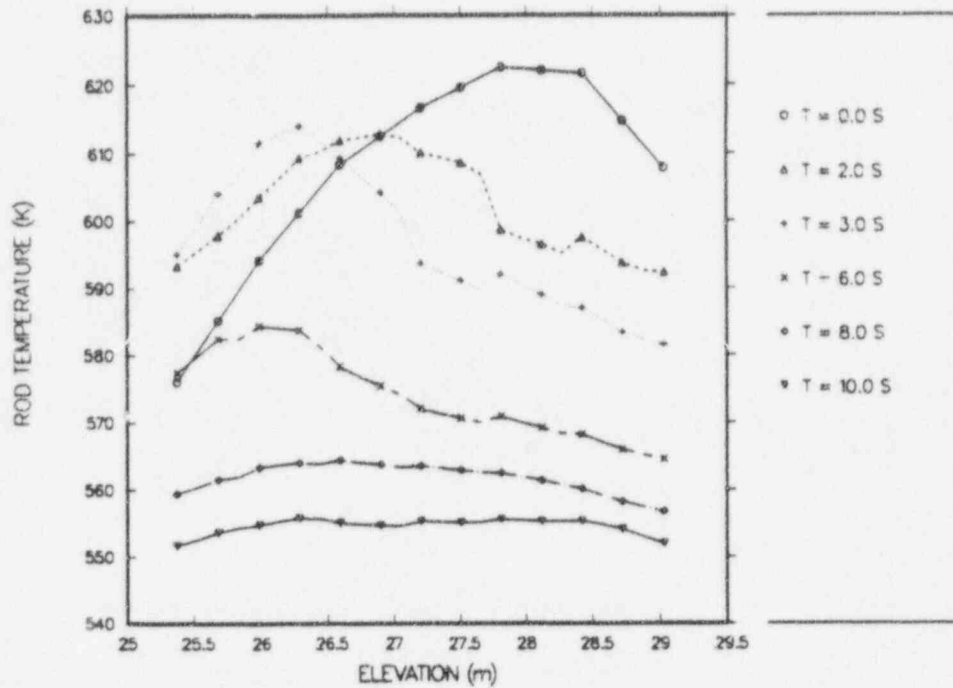


Fig. F-10a. Hot-rod cladding temperatures vs core elevation at selected transient times from 0 to 10 s for core cell 10.

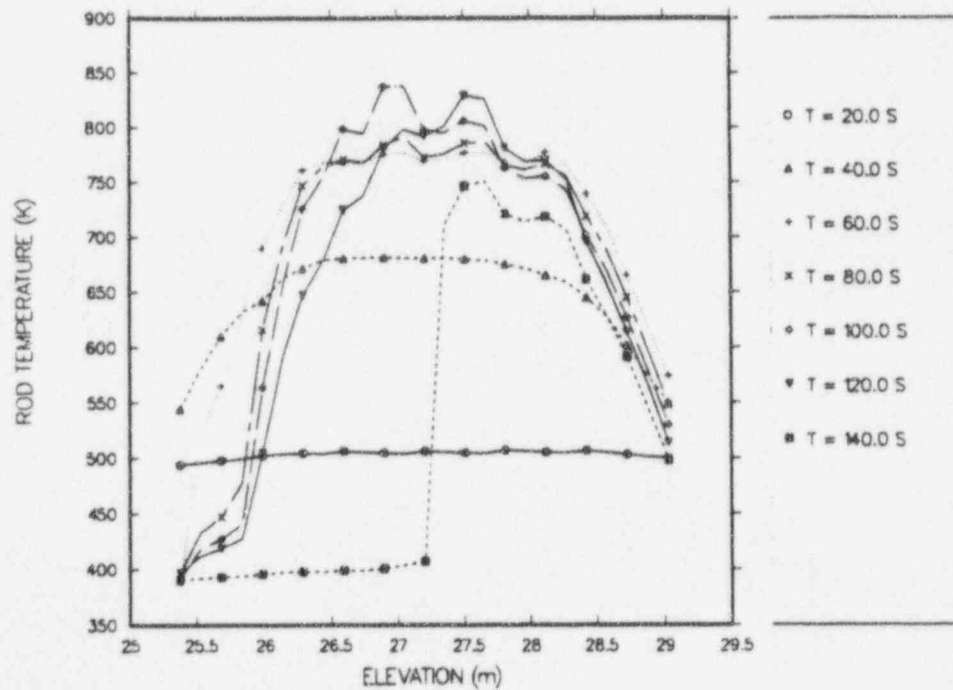


Fig. F-10b. Hot-rod cladding temperatures vs core elevation at selected transient times from 20 to 140 s for core cell 10.

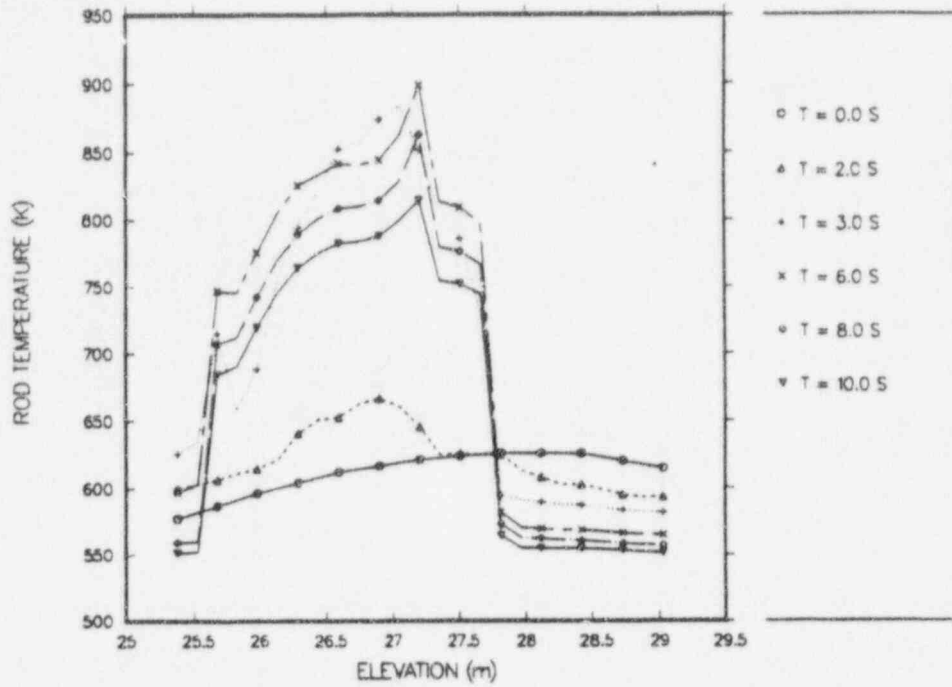


Fig. F-11a. Hot-rod cladding temperatures vs core elevation at selected transient times from 0 to 10 s for core cell 11.

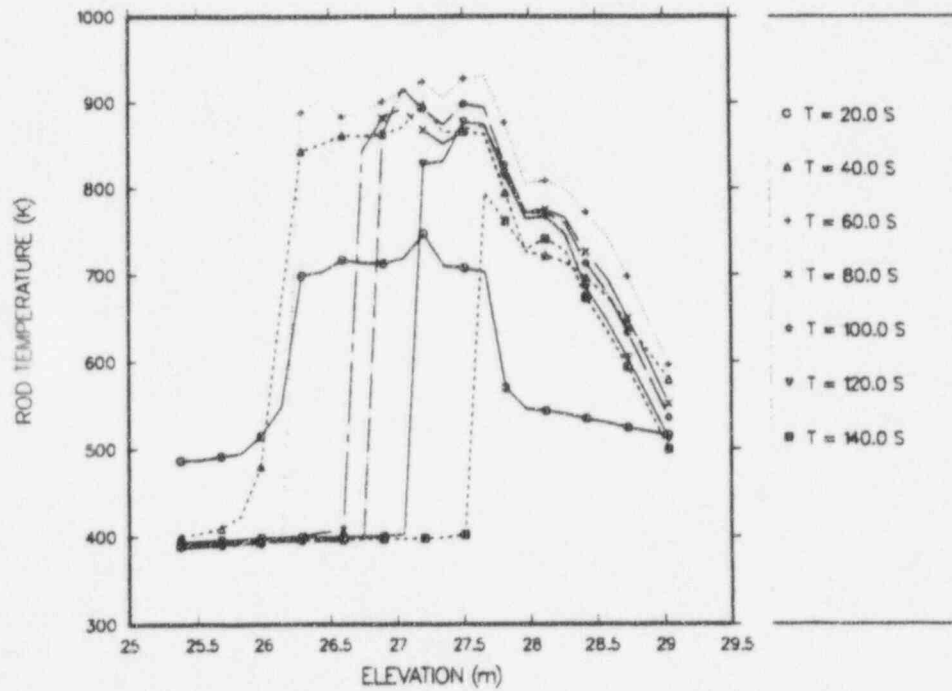


Fig. F-11b. Hot-rod cladding temperatures vs core elevation at selected transient times from 20 to 140 s for core cell 11.

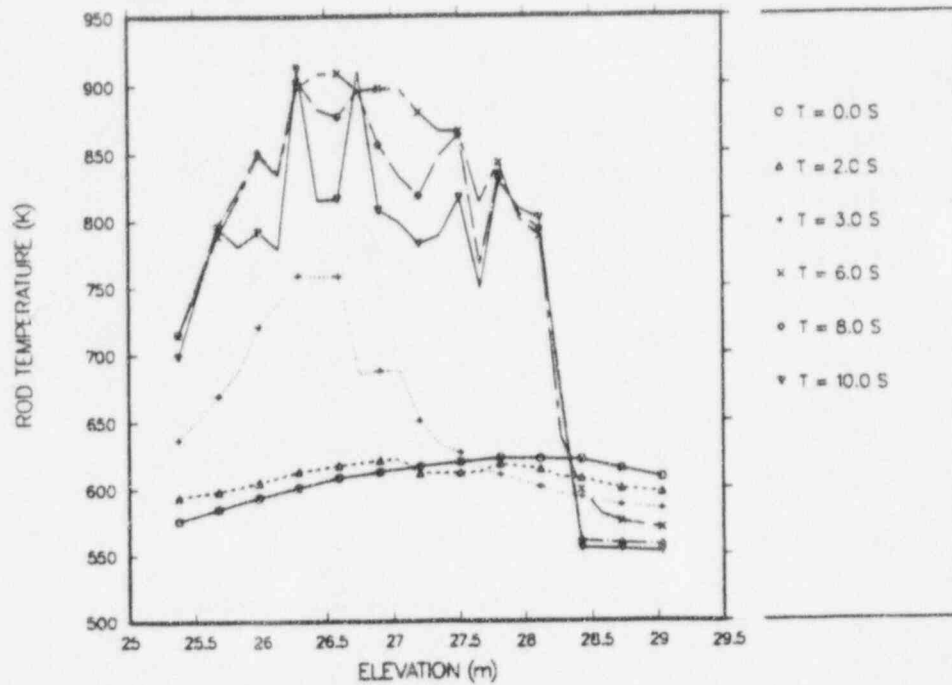


Fig. F-12a. Hot-rod cladding temperatures vs core elevation at selected transient times from 0 to 10 s for core cell 12.

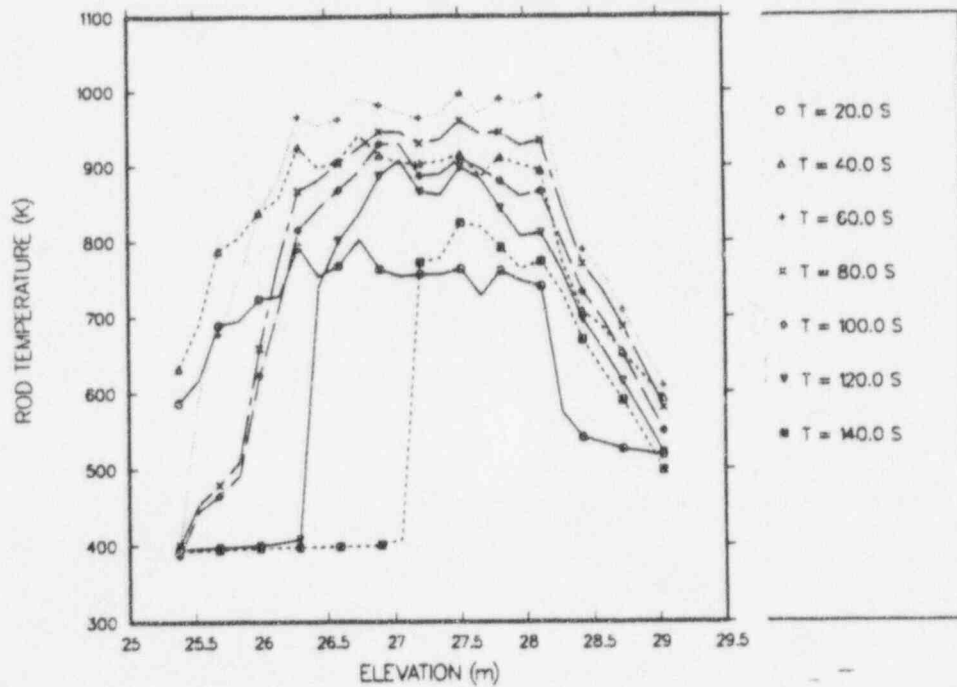


Fig. F-12b. Hot-rod cladding temperatures vs core elevation at selected transient times from 20 to 140 s for core cell 12.

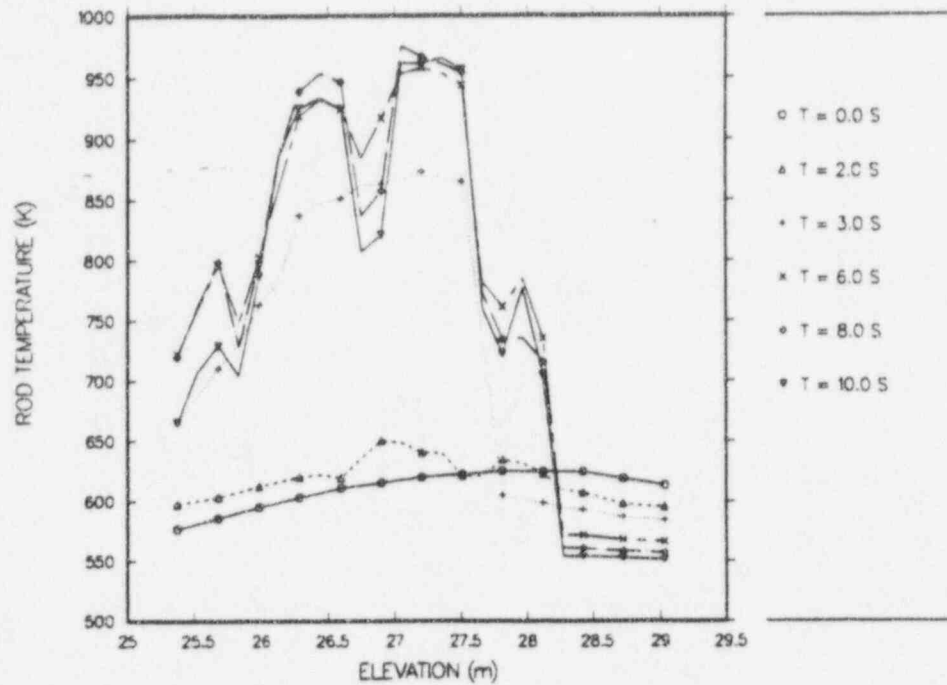


Fig. F-13a. Hot-rod cladding temperatures vs core elevation at selected transient times from 0 to 10 s for core cell 13.

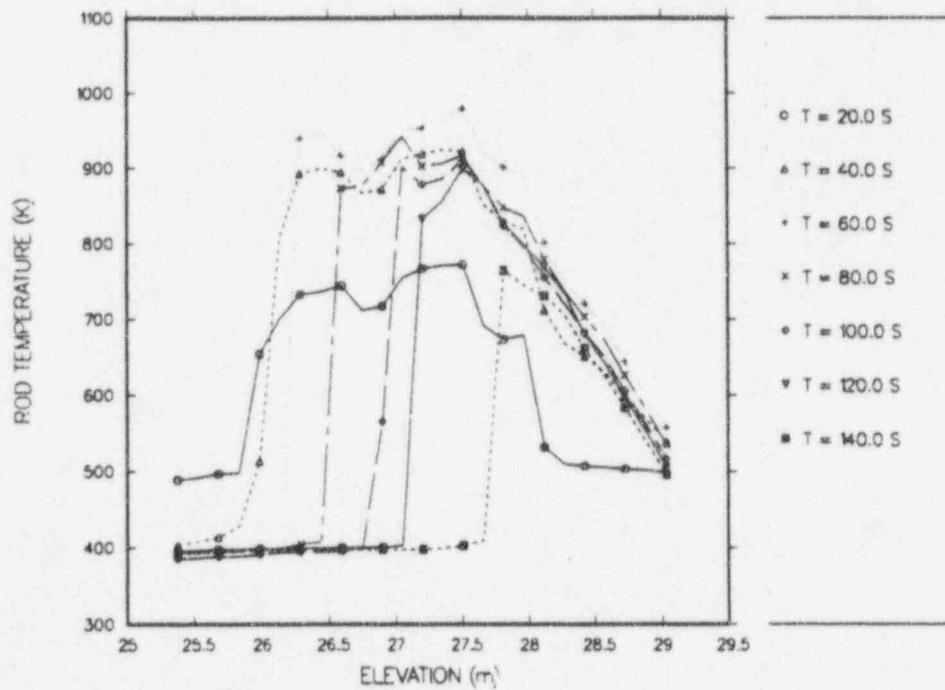


Fig. F-13b. Hot-rod cladding temperatures vs core elevation at selected transient times from 20 to 140 s for core cell 13.

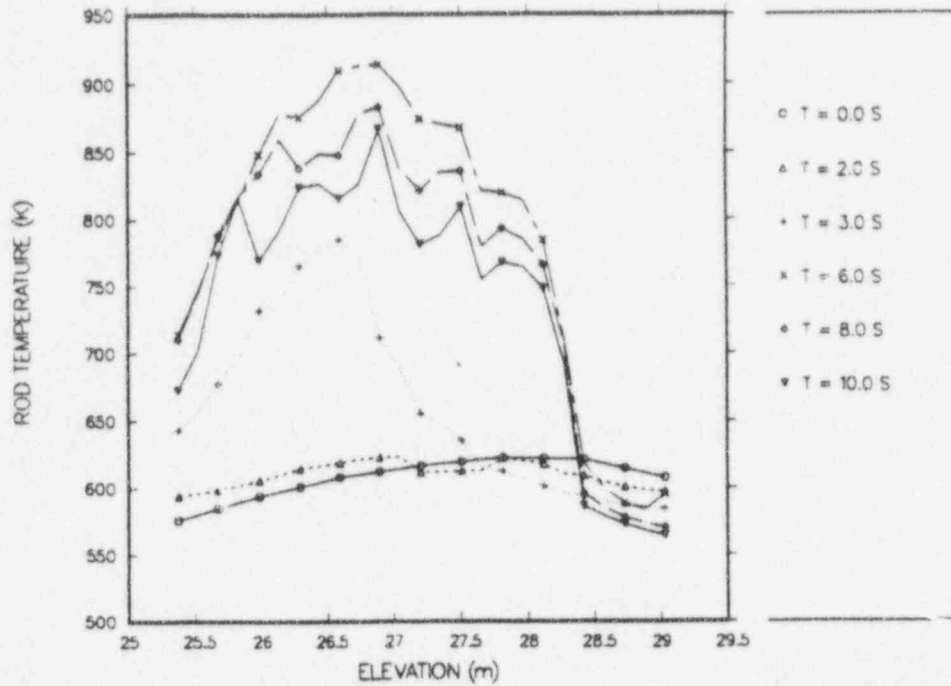


Fig. F-14a. Hot-rod cladding temperatures vs core elevation at selected transient times from 0 to 10 s for core cell 14.

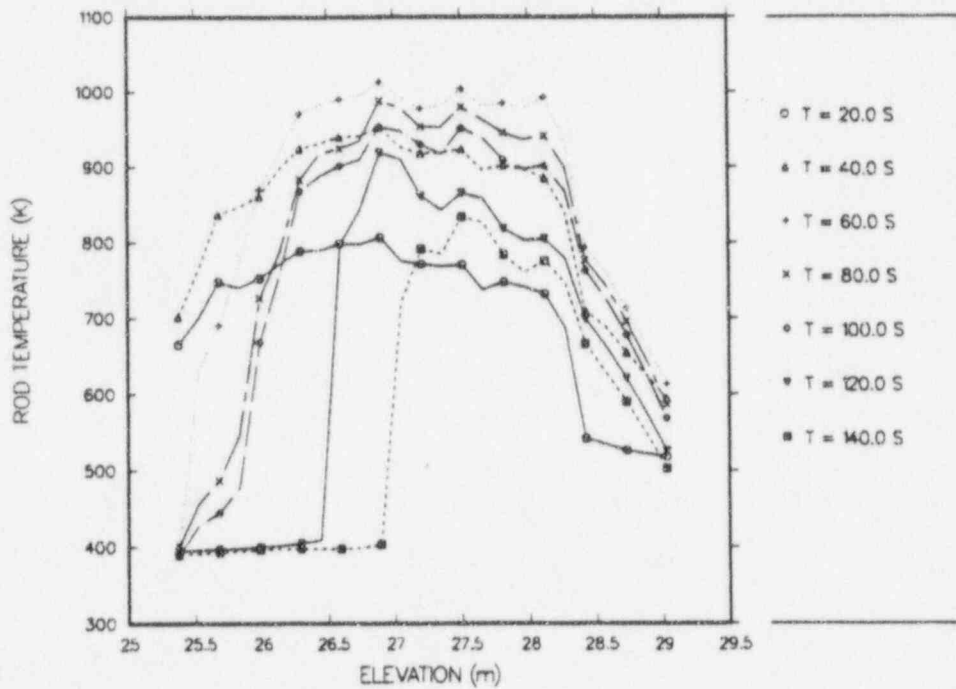


Fig. F-14b. Hot-rod cladding temperatures vs core elevation at selected transient times from 20 to 140 s for core cell 14.

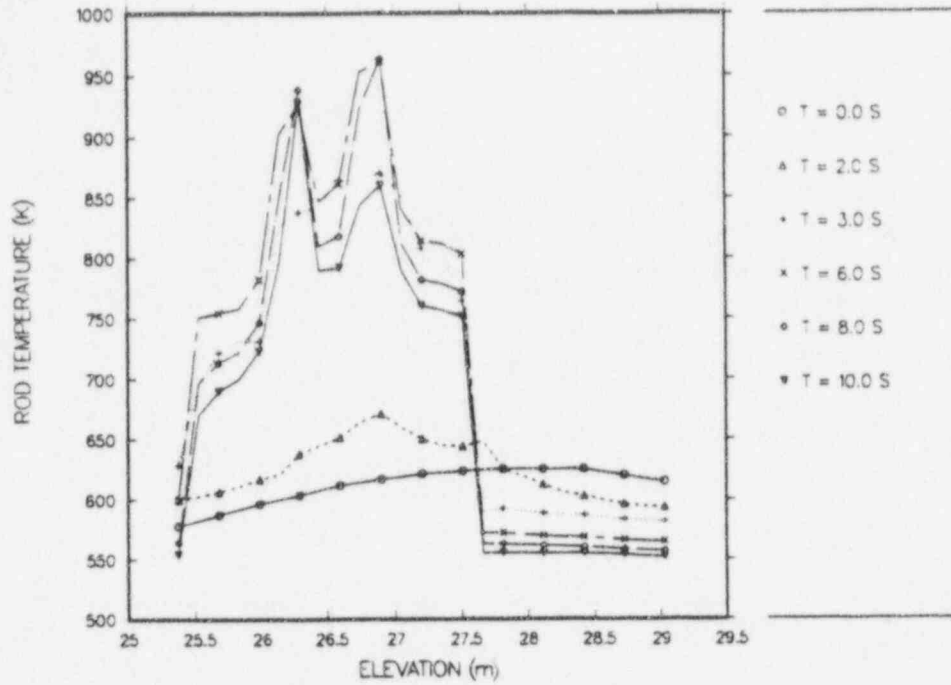


Fig. F-15a. Hot-rod cladding temperatures vs core elevation at selected transient times from 0 to 10 s for core cell 15.

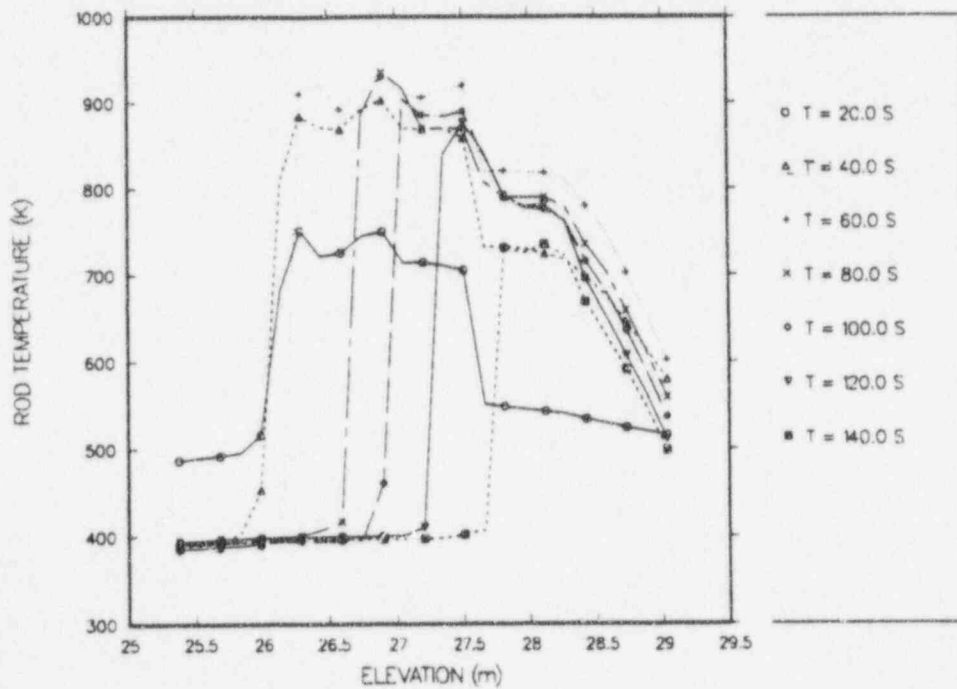


Fig. F-15b. Hot-rod cladding temperatures vs core elevation at selected transient times from 20 to 140 s for core cell 15.

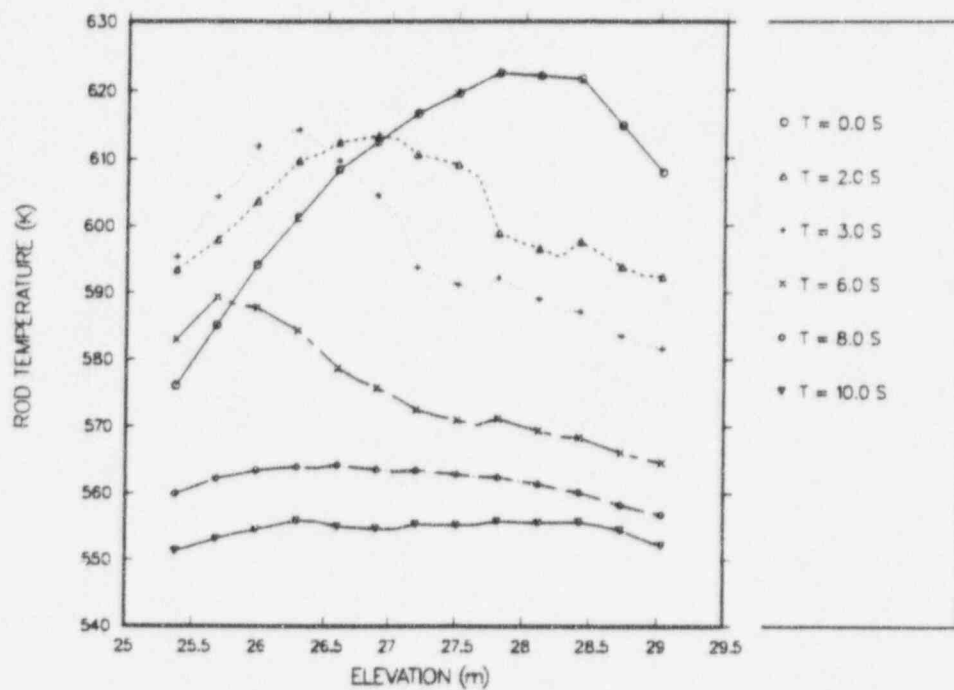


Fig. F-16a. Hot-rod cladding temperatures vs core elevation at selected transient times from 0 to 10 s for core cell 16.

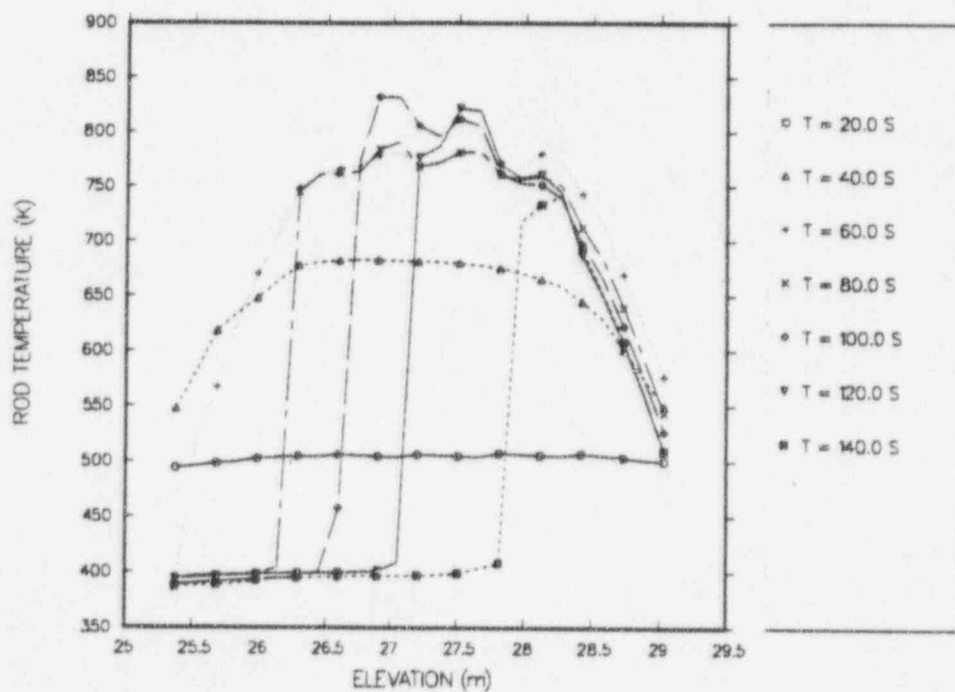


Fig. F-16b. Hot-rod cladding temperatures vs core elevation at selected transient times from 20 to 140 s for core cell 16.

APPENDIX G

LBLOCA TIMESTEP AND CPU TIME INFORMATION

The entire extended LBLOCA calculation was performed on the HP9000 workstation and required 48 separate calculation runs. Figures G-1 and G-2 show the timestep size and total CPU time per calculation run. The tabulation below shows more detailed information for each run. There were at least eight times when the calculation died because of code computation difficulties and had to be restarted using a smaller maximum timestep size. The code difficulties occurred primarily during the latter stages of reflood, between 140 and 230 s.

The total calculation required 6,375,074 CPU s, which is equivalent to 73.8 days of continuous computation on the HP workstation. Calculations 1 through 29 were performed with an unoptimized code. The rest of the calculation runs were performed with the same code version optimized at an optimization level 1 but with selected subroutines optimized at an optimization level 2. This optimized code was seven times faster than the unoptimized code for the AP600 LBLOCA calculation.

Calculation Run Number	Calculation End Time	Number of Time Steps	Total CPU Time (s)	Avg. Timestep Size (s)
1	5	1448	62,296	0.003453
2	10	1418	54,647	0.003526
3	15	1247	60,558	0.004010
4	20	1091	58,508	0.004583
5	25	1240	73,313	0.004032
6	30	1324	62,654	0.003776
7	35	1598	98,248	0.003129
8	40	1781	91,522	0.002807
9	45	4805	240,399	0.001041
10	50	3033	167,006	0.001649
11	55	2024	97,155	0.002470
12	60	1301	64,940	0.003843
13	70	2338	126,163	0.004277
14	80	4371	223,366	0.002288
15	90	4542	229,528	0.002202
16	100	4920	242,200	0.002033
17	110	8638	392,661	0.001158
18	120	7436	366,047	0.001345
19	130	8023	375,773	0.001246
20	140	7054	353,680	0.001418
21	144	3244	158,565	0.001235
22	147	3377	151,877	0.000888

Calculation Run Number	Calculation End Time	Number of Time Steps	Total CPU Time (s)	Avg. Timestep Size (s)
23	150	2977	133,028	0.001008
24	152	2080	95,180	0.000962
25	153	1574	60,845	0.000635
26	156	1786	82,310	0.001680
27	160	4983	212,729	0.000803
28	165	6310	186,818	0.000792
29	168	3960	124,084	0.000758
30	174	21,320	223,172	0.000281
31	180	17,808	174,103	0.000337
32	185	10,435	97,466	0.000479
33	189	6760	64,111	0.000592
34	195	13,366	120,028	0.000449
35	200	13,228	130,089	0.000378
36	205	10,438	85,025	0.000479
37	206	2000	16,723	0.000500
38	210	16,234	137,886	0.000246
39	212	8840	75,964	0.000226
40	215	15,302	130,688	0.000196
41	219	20,160	159,468	0.000198
42	225	15,026	132,682	0.000399
43	230	5056	39,997	0.000989
44	240	6562	53,675	0.001524
45	250	2819	24,212	0.003547
46	260	3072	27,488	0.003255
47	270	2016	16,745	0.004960
48	280	2282	19,452	0.004382
Total		292,647	63,75,074	0.000957

Summary:

Total number of time steps	292,647
Total CPU time (s)	6,375,074
Total CPU time (min)	106,251
Total CPU time (h)	1770.85
Total CPU time (days)	73.8
Average timestep size for total calculation	0.000957 s

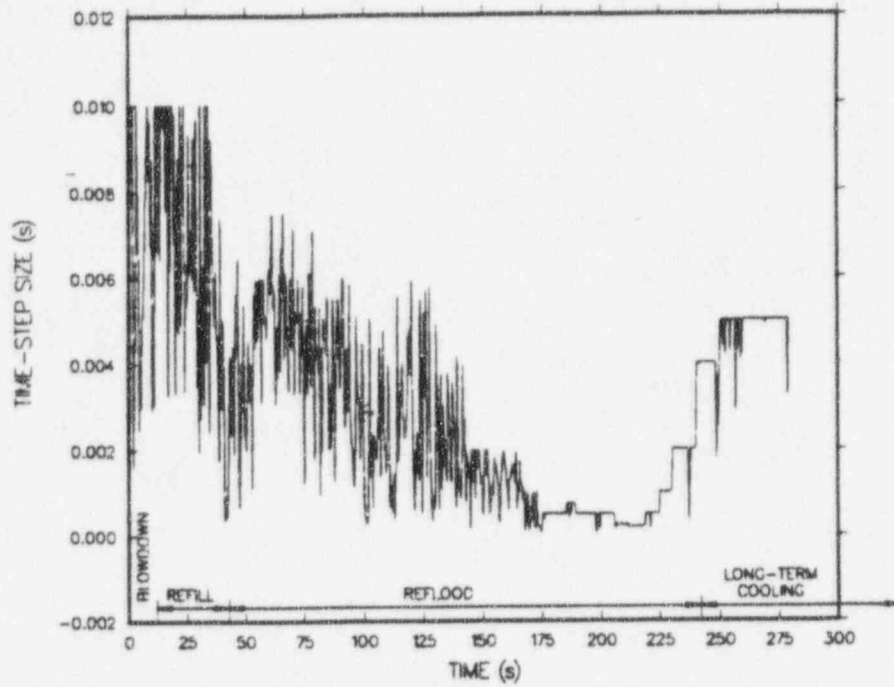


Fig. G-1. Timestep size.

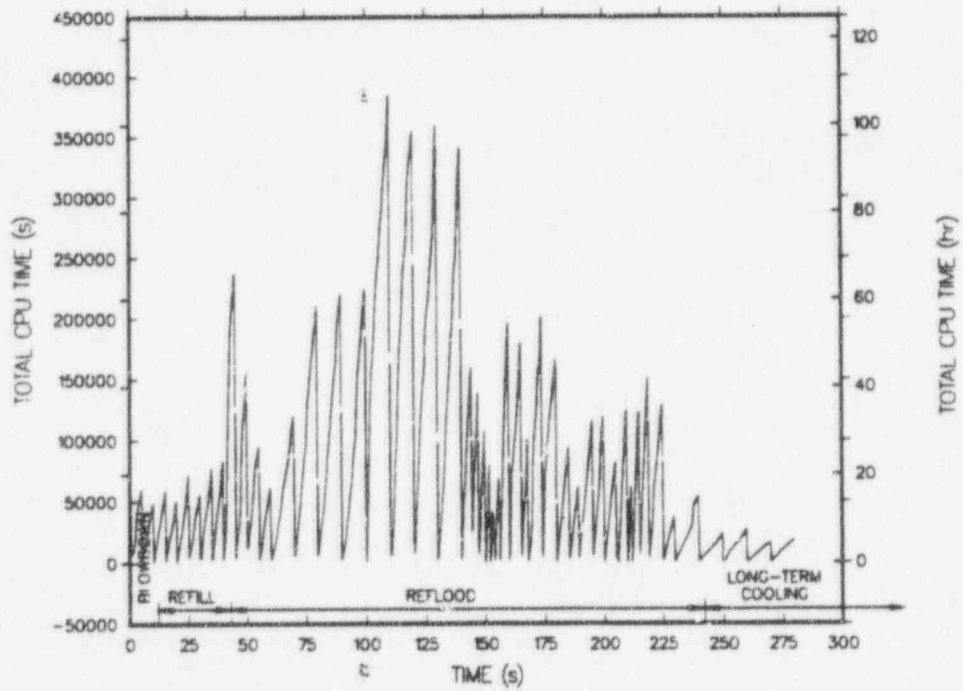


Fig. G-2. Total CPU time per calculation run.